ABSTRACT

Title of dissertation: STUDIES OF ULTRACOLD
                            STRONTIUM GASES

                            Benjamin Reschovsky, Doctor of Philosophy, 2017

Dissertation directed by: Professors Gretchen Campbell and Steve Rolston
                            Joint Quantum Institute,
                            National Institute of Standards and Technology,
                            and
                            Department of Physics, University of Maryland

We describe the operation and performance of an ultracold strontium apparatus that is capable of generating quantum degenerate gases. The experiment has produced Bose-Einstein condensates (BECs) of ^{84}Sr and ^{86}Sr as well as degenerate Fermi gases (DFGs) of ^{87}Sr with a reduced temperature of $T/T_F \simeq 0.2$ at a Fermi temperature of $T_F \simeq 55$ nK. Straightforward modifications could be made to allow for isotopic mixtures and BECs of the fourth stable isotope, ^{88}Sr.

We also report on a technique to improve the continuous loading of a magnetic trap by adding a laser tuned to the $^3P_1 \rightarrow {}^3S_1$ transition. The method increases atom number in the magnetic trap and subsequent cooling stages by up to 65 % for the bosonic isotopes and up to 30 % for the fermionic isotope of strontium. We optimize this trap loading strategy with respect to laser detuning, intensity, and beam size. To understand the results, we develop a one-dimensional rate equation model of the system, which is in good agreement with the data. We discuss the use of other transitions in strontium for accelerated trap

loading and the application of the technique to other alkaline-earth-like atoms.

Finally, we also report on an updated investigation of photoassociation resonances relative to the $^1S_0 + {}^3P_1$ dissassociation limit in bosonic strontium. Multiple new resonances for ^{84}Sr and ^{86}Sr were measured out to binding energies of -5 GHz and several discrepancies in earlier measurements were resolved. These measurements will allow for the development of a more accurate mass-scaled model and a better theoretical understanding of the molecular potentials near the $^3P_1$ state. We also measure the strength of the ^{84}Sr 0_u^+ transitions in order to characterize their use as optical Feshbach resonances.

STUDIES OF ULTRACOLD STRONTIUM GASES

by

Benjamin Reschovsky

Dissertation submitted to the Faculty of the Graduate School of the
University of Maryland, College Park in partial fulfillment
of the requirements for the degree of
Doctor of Philosophy
2017

Advisory Committee:
Professor Steven L. Rolston, Chair
Dr. Gretchen K. Campbell, Advisor
Professor Christopher Monroe
Professor Amy Mullin, Dean's Representative
Dr. James V. (Trey) Porto

Acknowledgments

When I first joined the project, the strontium lab consisted of a mostly empty room containing only a couple desks and storage cabinets. As a novice graduate student, I did not fully appreciate all the work ahead of us needed to build the apparatus and coax it into functioning. Though there were plenty of frustrations along the way, I am immensely grateful for the experience of building a new lab since it exposed me to the full variety of experimental techniques needed for an ultracold atomic physics lab.

Many people have contributed directly to the construction of the strontium apparatus. We have had a number of talented undergraduate students over the years who tackled a wide variety of projects, including Patrick McKenna, Tyler McKay, Eliot Bohr, and Peter Zhou. In the early days, we had valuable help from Guilherme Miranda, who designed the vacuum chamber, and post-doc Joe Pechkis, who built the initial dipole traps and computer control systems. Though he was only with us for a short time, the insights that Joe shared with us were particularly helpful given his experience and outside perspective. In addition, graduate students Avinash Kumar, Erin Marshall, Madison Anderson, and Swarnav Banik built a number of electronics and optics projects before they started working full-time for other labs. Alessandro Restelli has been an invaluable resource and has vastly improved the quality of our home-built electronics projects. Many of our lab's capabilities would not have been possible without his expertise and guidance. The next generation of strontium graduate students, Ananya Sitaram and Peter Elgee, have also contributed to data taking in addition to assembling a "rebooted" strontium apparatus. The new system also got a significant jump start thanks to Alex Hesse's efforts during the year he spent visiting our

Table of Contents

List of Tables

List of Figures

List of Abbreviations

a_0	Bohr radius
c	Speed of light
ϵ_0	Vacuum permittivity
$\hbar$	Planck's constant, reduced
k_B	Boltzmann's constant
μ_B	Bohr magneton divided by $\hbar$
AC	Alternating Current
AE	Alkaline-Earth-like
AOM	Acousto-Optic Modulator
AR	Anti-Reflection
AWG	American Wire Gauge
BEC	Bose-Einstein Condensate
bMOT	blue Magneto-Optical Trap
CCD	Charge-Coupled Device
CF	Conflat
CG	Clebsch-Gordan
CTE	Coefficient of Thermal Expansion
DAC	Digital to Analog Converter
DAQ	Data Acquisition
DDS	Direct Digital Synthesis
DFG	Degenerate Fermi Gas
DMD	Digital Micromirror Device
DVR	Discrete Variable Representation
ECDL	External Cavity Diode Laser
EDM	Electrical Discharge Machining
EOM	Electro-Optic Modulator
FALC	Fast Analog Linewidth Control
FPGA	Field Programmable Gate Array
FPI	Fabry-Pérot Interferometer
FSR	Free Spectral Range
IR	Infrared
JILA	JILA
JQI	Joint Quantum Institute
LMA	Large Mode Area

LTRF	Loading Time Reduction Factor
LWP	Long Wave Pass
MOSFET	Metal-Oxide-Semiconductor Field-Effect Transistor
MOT	Magneto-Optical Trap
NI	National Instruments
NIST	National Institute of Standards and Technology
ODT	Optical Dipole Trap
OFR	Optical Feshbach Resonance
OSG	Optical Stern-Gerlach
OPLL	Optical Phase Locked Loop
PAS	Photoassociation Spectroscopy
PBS	Polarizing Beamsplitter
PD	Photodiode
PDH	Pound Drever Hall
PID	Proportional Integral Differential
PI	Proportional Integral
PM	Polarization Maintaining
ppb	Parts Per Billion
ppm	Parts Per Million
PZT	Piezoelectric Transducer
RF	Radiofrequency
rMOT	red Magneto-Optical Trap
rms	Root Mean Square
SHG	Second Harmonic Generation
SRS	Stanford Research Systems
STIRAP	Stimulated Raman Adiabatic Passage
SWP	Short Wave Pass
TA	Tapered Amplifier
TOF	Time Of Flight
TSP	Titanium Sublimation Pump
UHV	Ultra-High Vacuum
ULE	Ultra-Low Expansion glass
UMD	University of Maryland
USAF	U.S. Air Force
USB	Universal Serial Bus
VI	Virtual Instrument
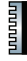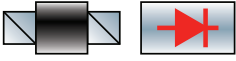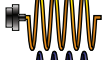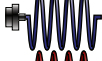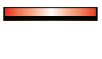
Flat Mirror:		Polarizing Beamsplitter Cube:	
Curved Mirror:		Glan Laser Polarizer:	
Diffraction Grating:		Optical Isolator:	
Mirror w/ PZT:		Faraday Rotator:	
Grating w/ PZT:		Half-Wave Plate:	
Lenses:		Quarter-Wave Plate:	
Beam Dump:		Bichromatic Wave Plate:	
Iris:		Non-Linear Crystal:	
Flipper Mirror:		Acousto-Optic Modulator:	
Solenoid Shutter:		Electro-Optic Modulator:	
SRS Shutter:		Fiber Electro-Optic Modulator:	
Laser Diode:		Liquid Crystal Variable Waveplate:	
Photo Diode:		Digital Micromirror Device:	
PID Controller:		Single Mode Fiber:	
PDH Module:		Polarization Maintaining Fiber:	
FALC Module:		Large Mode Area Fiber:	
SWP Dichroic:		Tapered Amplifier:	
LWP Dichroic:			

Figure 1: List of optical components and associated symbols. These symbols are taken or adapted from Alexander Franzen's *ComponentLibrary* (version 3, available at http://www.gwoptics.org/ComponentLibrary/), which is licensed under the Creative Commons Attribution-NonCommercial 3.0 Unported License (http://creativecommons.org/licenses/by-nc/3.0/).

Chapter 1: Introduction

1.1 History of Laser Cooling

Shortly after the first demonstration of the laser in 1960 [1], several groups proposed ideas to use this new invention to exert radiation pressure on atoms in order to trap and slow them [2–5]. These ideas were motivated by the prospect of reducing the atomic thermal motion to perform more accurate spectroscopy, or frequency metrology. The first experimental demonstrations of laser cooling was performed by Wineland *et al.* and Neuhauser *et al.* in 1978 on ions confined in Penning or Paul traps [6, 7]. However, these methods could not immediately be applied to neutral atoms because the kinetic energy of atoms from an atomic beam was much larger than the depth of the available trapping methods. To solve this problem, researchers developed two methods for slowing an atomic beam. The Zeeman slower, which used a tapered magnetic field to compensate for the varying Doppler shift of atoms in an atomic beam as they were slowed, was first demonstrated by Phillips and Metcalf [8] and succeeded in slowing atoms all the way down to rest in 1985 [9]. An alternative method based on laser frequency sweeps, or chirp cooling, was proposed by Letokhov in 1976 [10] and demonstrated a few years later [11, 12].

With the tools needed to produce sufficiently slow samples of neutral atoms, researchers quickly realized other cooling and trapping methods. Doppler cooling in an "optical molasses" was first demonstrated by Chu *et al.* in 1985 [13] and magnetic trapping was accomplished by Migdall *et al.* in the same year [14]. The first hybrid magneto-optical

trap (or MOT) was demonstrated shortly thereafter in 1987 [15]. Finally, trapping neutral atoms in 3D using the dipole force from a focused laser, proposed by Ashkin in 1978 [5], was first realized by Chu *et al.* in 1986 [16]. The importance of this early work in laser cooling was recognized by the 1997 Nobel Prize, which was awarded to Bill Phillips, Steven Chu, and Claude Cohen-Tannoudji.[1] These tools were developed, refined, and expanded over the next couple of decades, giving researchers unprecedented control over atomic systems. Laser cooling not only led to important advances in atomic clocks and spectroscopy [19–21], but also led to completely new avenues of research, such as the study of Bose-Einstein condensates (BECs) [22,23], degenerate Fermi-gases (DFGs) [24], many body physics [25], atomic interactions [26], quantum simulation [27], and quantum information processing [28].

1.2 Alkaline-Earth Elements

The initial laser cooling work used alkali atoms, which have only a single valence electron and relatively simple electronic structure. More recently, these techniques have been applied to alkaline-earth (AE) elements, such as strontium, calcium, and ytterbium.[2] The AE elements, being one electron more complicated, have properties that make them more challenging to laser cool but also allow for new experiments not possible with alkalis.

The second valence electron leads to both singlet and triplet electronic states (see Fig. 1.1 for the Sr level structure, which is similar to that of other AE elements). Under the LS coupling scheme, transitions between singlet and triplet states are forbidden because of the $\Delta S = 0$ selection rule. However, a small breakdown of the spin-orbit coupling leads to mixing between the $^1P_1$ and $^3P_1$ wavefunctions [29]. Therefore, AE atoms have transi-

---

[1]The brief timeline of laser cooling presented here is based on the Nobel lectures of Bill Phillips and Steven Chu [17, 18].

[2]Ytterbium, a member of the lanthanide series, has two valence electrons and therefore a similar electronic structure to alkaline earth elements. It is often described as alkaline-earth-like. In this thesis, all descriptions of AE elements will include ytterbium.

tions between the $^1S_0$ ground state and the $^3P_1$ state with narrow linewidths ($\Gamma/2\pi = 0.37$, 7.5, and 182 kHz for Ca, Sr, and Yb respectively [30]). These transitions, known as intercombination transitions because they mix singlet and triplet states, allow for laser cooling down to $\approx \mu$K temperatures [31–38], and for one experiment in strontium, all the way to degeneracy [39]. Researchers have also used these narrow linewidth transitions for photoassociation spectroscopy with kHz precision [40–45], the manipulation of atomic interactions [46–49], production of ground state molecules [50–52], detection and manipulation of spin state populations [53], and the creation of highly excited Rydberg states [54–56].

Furthermore, AE atoms have even narrower $^1S_0 \rightarrow {}^3P_{0,2}$ transitions that violate the $J = 0 \nleftrightarrow J = 0$ or $\Delta J = 0, 1$ selection rules [29] and are therefore "doubly forbidden." For the fermionic AE isotopes, the $^1S_0 \rightarrow {}^3P_0$ transition acquires a non-zero line strength because hyperfine interactions cause mixing among the various $^{2S+1}P_J$ states with the same value of F yielding linewidths on the order of mHz [57]. The $^1S_0 \rightarrow {}^3P_2$ transition has a non-zero linewidth due to higher order magnetic quadrupole transitions [58]. In addition, since the $^1S_0 \rightarrow {}^3P_0$ transition is insensitive to first order Zeeman shifts, there has been considerable effort to use this transition as the basis for the next generation of optical clocks [21, 59–62]. A recent effort was able to reduce atomic interactions by using degenerate Fermi gas in a 3D lattice to demonstrate a clock with the unprecedented precision of 5×10^{-19} [63]. In addition to frequency metrology, these incredibly accurate clocks could be used for gravitational wave detectors or searches for dark matter [64–67].

Another key difference between AE elements and the alkalis are that AE atoms have no electronic angular momentum ($J = 0$) in the ground-state. This is a disadvantage in some respects since it means that ground state AE atoms cannot be trapped magnetically and we cannot tune the atomic interactions using a magnetic Feshbach resonance [26]. However, the magnetic field insensitivity is also an advantage for atomic clocks and other precision measurement applications [68–70]. While the bosonic AE isotopes are

completely spinless in the ground state, the fermionic isotopes have non-zero nuclear spin. This leads to a nearly complete decoupling between the nuclear spin and electronic angular momentum between the $^1S_0$ ground state and $^3P_0$ metastable state [71]. This decoupling means that the atomic interactions are independent of the projection of nuclear spin onto the quantization axis, resulting in a system with $SU(N)$ symmetry, where N is the number of populated spin states. Since $I = 9/2$ for ^{87}Sr, (see Table 1.2) $N = 2I + 1$ can be as large as 10 in our experiment. This highly symmetric system has led to a number of theoretical proposals to study $SU(N)$ quantum magnetism, [72–81], as well as synthetic gauge fields [82–84] and quantum information processing [85, 86].

1.3   Strontium Properties

The level diagram for strontium, the AE element that we chose to work with, is shown in Fig. 1.1. As will be discussed in more detail in Chapter 3, ultracold strontium experiments typically use the broad 461-nm $^1S_0 \rightarrow {}^1P_1$ transition to pre-cool the atoms to $\simeq$ mK temperatures and then use the narrow 689-nm $^1S_0 \rightarrow {}^3P_1$ line to cool to $\simeq \mu$K temperatures. We also perform repumping on several transitions from the ^3P manifold to the $^3S_1$ state. As mentioned above, the fermionic ^{87}Sr isotope possesses a nuclear spin, which leads to hyperfine splittings of the various levels illustrated in Fig. 1.1. The splittings are given in Table 1.1 and can be calculated according to [57]

$$\Delta E_{\mathrm{HFS}}/h = \frac{A}{2}K + \frac{Q}{2}\frac{\frac{3}{4}K(K+1) - I(I+1)J(J+1)}{I(2I-1)J(2J-1)}, \qquad (1.1)$$

where $I = 9/2$ is the nuclear spin, A and Q are the magnetic and electric quadrupole interaction constants, and $K = F(F+1) - I(I+1) - J(J+1)$.

Some properties of the four stable isotopes of strontium are shown in Table 1.2. One of the isotopes, ^{88}Sr, is by far the most abundant and is therefore the easiest to use for spectroscopy and optimizing laser cooling performance. However, due to its nearly
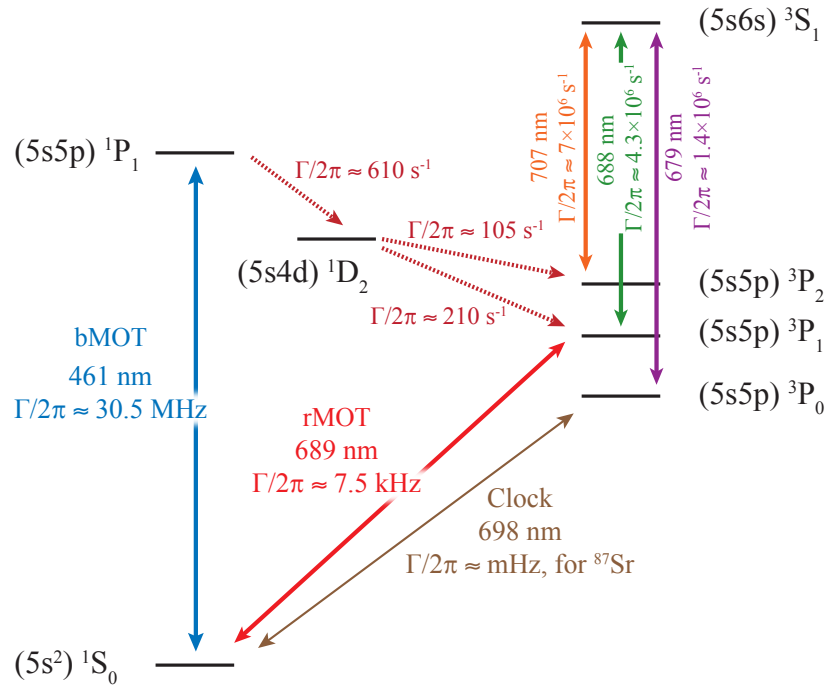
Figure 1.1: The strontium energy levels and transitions relevant for this thesis. Linewidths and decay rates are from [87–91]. The broad $^1S_0 \rightarrow ^1P_1$ transition is used to slow an atomic beam and trap Sr atoms in a MOT down to $\simeq$ mK temperatures. A slow leak through the intermediate $^1D_2$ state populates the metastable $^3P_2$ state, which can be repumped by excitation to the $^3S_1$ level. A second MOT on the narrow $^1S_0 \rightarrow ^3P_1$ transition cools atoms down to $\simeq \mu$K temperatures. The extremely narrow ($\Gamma/2\pi \approx$ mHz) "clock" transition between $^1S_0$ and $^3P_0$ allows for extremely precise spectroscopy for frequency metrology or manipulation of quantum degenerate gases.

Table 1.1: Calculated hyperfine splittings for [87]Sr states relevant to this thesis. The A and Q parameters are the magnetic dipole and electric quadrupole interaction constants and are used to calculate the hyperfine splittings, ΔE_{HFS}, relative to a theoretical isotope with $I = 0$. The g_F factors ignore the effect of the nuclear g factor. The Zeeman shift in the $^1\mathrm{S}_0$ and $^3\mathrm{P}_0$ states are ≈ 200 Hz/G $\times m_F$ [57].

State	A (MHz)	Q (MHz)	F	g_F	$\Delta E_{\mathrm{HFS}}/h$ (MHz)
$^1S_0$	0	0	9/2	0	0
$^1P_1$	-3.334(25) [92]	-40.29(21) [92]	7/2	-2/9	36.8
			9/2	4/99	-23.5
			11/2	2/11	-4.9
$^3P_0$	0	0	9/2	0	0
$^3P_1$	-260.084(2) [93]	-35.658(6) [93]	7/2	-1/3	1414.12
			9/2	2/33	283.86
			11/2	3/11	-1179.29
$^3P_2$	-212.765(1) [94]	67.215(15) [94]	5/2	-6/7	2371.22
			7/2	-1/7	1597.14
			9/2	2/11	618.69
			11/2	51/143	-551.52
			13/2	6/13	-1898.08
$^3S_1$	542.0(1) [95]	-0.1(5) [95]	7/2	-4/9	2981
			9/2	8/99	542
			11/2	4/11	-2439

Table 1.2: Properties of the naturally occurring isotopes of strontium. Scattering lengths are from [42, 96] and relative abundances are from [97].

Isotope	Spin Statistics	Relative Abundance	Nuclear Spin	Scattering Length
^{84}Sr	Boson	0.56%	0	$123a_0$
^{86}Sr	Boson	9.86%	0	$823a_0$
^{87}Sr	Fermion	7.00%	9/2	$96a_0$
^{88}Sr	Boson	82.58%	0	$-2a_0$

vanishing scattering length, ^{88}Sr cannot be directly evaporatively cooled. The low natural abundance of the other isotopes, especially ^{84}Sr, initially hindered efforts to achieve degeneracy, but can be overcome by optimizing trap loading (see Chapter 3). Since the scattering length of strontium cannot be tuned with magnetic Feshbach resonances, it is fortuitous that the natural scattering lengths of the three bosonic isotopes neatly fall into three different regimes of strong, intermediate, and extremely weak interactions for ^{86}Sr, ^{84}Sr, and ^{88}Sr respectively.

1.4 Thesis Outline

This thesis will describe several intermediate studies we have performed as we work towards the long term goal of simulating of quantum magnetism with ^{87}Sr. Since almost all the proposals for laser-cooled AE atoms require, or benefit from, degenerate samples, when we first started constructing the strontium lab our initial goal was to achieve a strontium Bose-Einstein condensate and then degenerate Fermi gas. I will first discuss the theory of ultracold gases and highlight the key differences between thermal gases, BECs, and DFGs in Chapter 2. Next, in Chapter 3, I will describe the specific laser cooling processes that we use in our lab and describe the accomplishment of our initial goal of generating quantum degenerate gases. Chapter 4 contains the details of the vacuum system, laser systems, and other equipment that we have built in order to perform our experiments. While optimizing the performance of our apparatus in order to reach

degeneracy, we investigated a technique to improve the loading of our magnetic trap which resulted in our lab's first publication. Those results are described in Chapter 5. Finally, Chapter 6 discusses more recent photoassociation studies of the excited-state molecular potentials near the $^1S_0 + {}^3P_1$ dissassociation limit for several bosonic isotopes.

Chapter 2:   The Theory of Trapped Atomic Gases

2.1   Trapped Atomic Gases

This chapter will briefly cover the statistical mechanics of trapped atomic gases, both at thermal temperatures and at near-zero temperatures for bosons and fermions. In our experiment, we typically acquire data by imaging the atomic density profile either in-situ or after releasing the atoms and allowing them to freely expand for a variable time-of-flight (TOF). I will discuss the expected density profiles for these various regimes and the related fit functions that we use to extract physical information from our samples.

To illustrate the properties of trapped atomic gases, let us first consider a system in the grand canonical ensemble. For non-interacting particles at a temperature T, the average occupation of the state i with energy E_i is

$$\langle n_i \rangle = \frac{1}{e^{(E_i - \mu)/k_B T} \mp 1} \tag{2.1}$$

where the upper sign gives the Bose-Einstein distribution for bosonic particles and the lower sign gives the Fermi-Dirac distribution for fermions. Typically our samples have a fixed number of particles, N, so the chemical potential, μ, is constrained such that $N = \langle N \rangle = \sum_i \langle n_i \rangle$.

Instead of working with the full quantum expression, which requires knowledge of the wavefunctions for a given trapping potential, we can approximately describe the system with a semi-classical distribution, $f(\mathbf{r}, \mathbf{p})$. This simplification, also known as the Thomas-Fermi approximation, is valid in the limit of large particle number, N, when a

localized portion of the gas has the same properties as the sample as a whole [98, 99]. This description is not valid for atoms in the ground state, but it is a good approximation for the excited states. The semi-classical distribution is defined such that the average number of particles in the phase-space volume $\mathrm{d}\mathbf{p}\mathrm{d}\mathbf{r}$ is given by $f(\mathbf{r}, \mathbf{p})\mathrm{d}\mathbf{p}\mathrm{d}\mathbf{r}/(2\pi\hbar)^3$ and

$$f(\mathbf{r}, \mathbf{p}) = \frac{1}{e^{\left(\frac{p^2}{2m} + V(\mathbf{r}) - \mu\right)/k_B T} \mp 1} \tag{2.2}$$

for the trapping potential $V(\mathbf{r})$. The density distribution of the thermal gas can be found by integrating over all momenta

$$n_{th}(\mathbf{r}) = \int \frac{f(\mathbf{r}, \mathbf{p})}{(2\pi\hbar)^3}\mathrm{d}^3\mathbf{p} = \pm\frac{1}{\lambda_{dB}^3}\mathrm{Li}_{3/2}\left(\pm e^{(\mu - V(\mathbf{r}))/k_B T}\right), \tag{2.3}$$

where $\lambda_{dB} = (2\pi\hbar^2/mk_B T)^{1/2}$ is the de Broglie wavelength and $\mathrm{Li}_n(z)$ denotes the nth-order polylogarithm function (see App. A for the definition and some properties of this function) [99–102]. So far we have made no assumptions about the trapping potential, $V(\mathbf{r})$. We can similarly find the momentum space distribution by integrating over all real space $n_{th}(\mathbf{p}) = (2\pi\hbar)^{-3}\int f(\mathbf{r}, \mathbf{p})\,\mathrm{d}^3\mathbf{r}$, which does depend on the specifics of the trapping potential. The total atom number can be found by integrating the spatial density distribution

$$N_{th} = \int \mathrm{d}^3\mathbf{r}\, n_{th}(\mathbf{r}), \tag{2.4}$$

which, assuming N_{th} is fixed, places a constraint on μ.

Cold atom traps are typically well approximated as harmonic, so we will consider trapping potentials of the form

$$V(\mathbf{r}) = \frac{1}{2}m(\omega_x^2 x^2 + \omega_y^2 y^2 + \omega_z^2 z^2). \tag{2.5}$$

In this case, Eq. (2.4) evaluates to[1]

$$N_{th} = \pm \left(\frac{k_B T}{\hbar \bar{\omega}}\right)^3 \text{Li}_3 \left(\pm e^{\mu/k_B T}\right) \tag{2.6}$$

where $\bar{\omega} = (\omega_x \omega_y \omega_z)^{1/3}$ is the geometric mean of the harmonic trapping frequencies.

2.2 Thermal Atoms

Let us first consider the case of thermal atoms in a harmonic trap at (relatively) high temperatures. At high temperatures, μ becomes very small[2] and $(E_{min} - \mu)/k_B T \gg 1$ where E_{min} is the energy of the lowest single-particle state [99]. In this case, the argument to the polylogarithm in Eq. (2.3) is very small and we can use the fact that $\text{Li}_n(z) \xrightarrow{z \ll 1} z$, to find $n_{th}(\mathbf{r}) \propto e^{-V(\mathbf{r})/k_B T}$. After normalizing according to Eq. (2.4) we have

$$n_{th}(\mathbf{r}) = \frac{N_{th}}{\pi^{3/2} r_x r_y r_z} e^{-x^2/r_x^2 - y^2/r_y^2 - z^2/r_z^2} \tag{2.7}$$

where $r_i = (2k_B T/m\omega_i^2)^{1/2}$ is the in-situ width in the ith direction. We could have also reached this result by starting with the Maxwell-Boltzmann distribution,

$$f_{MB}(\mathbf{r}, \mathbf{p}) = e^{-\left(\frac{p^2}{2m} + V(\mathbf{r}) - \mu\right)/k_B T}, \tag{2.8}$$

which is the limiting form of the Bose-Einstein and Fermi-Dirac distributions when $(E - \mu) \gg k_B T$.

We typically release our clouds from the trapping potential and let them expand for a short time-of-flight before imaging them. Ignoring atomic collisions during the expansion, an atom initially at position $\mathbf{r}_0$ with momentum $\mathbf{p}_0$ will end up at position $\mathbf{r} = \mathbf{r}_0 + \mathbf{p}_0 t/m$

---

[1]This integral can be performed easily using the relationship given by Eq. (A.8).

[2]More specifically, in the thermal approximation $\mu < 0$ and $|\mu| \gg k_B T$

after an expansion time t. We can calculate the density after expansion as

$$n(\mathbf{r}, t) = \int d^3\mathbf{r}_0 \int \frac{d^3\mathbf{p}_0}{(2\pi\hbar)^3} f(\mathbf{r}_0, \mathbf{p}_0) \, \delta\left(\mathbf{r} - \mathbf{r}_0 - \frac{\mathbf{p}_0}{m}t\right)$$
$$= \int \frac{d^3\mathbf{p}_0}{(2\pi\hbar)^3} f\left(\mathbf{r} - \frac{\mathbf{p}_0}{m}t, \mathbf{p}_0\right). \tag{2.9}$$

This expression can be evaluated analytically for a harmonic potential. We can also simplify the algebra by recognizing the fact that for expansion from a harmonic trap, evaluating the integral above is equivalent to re-scaling the density by the factors $b_i(t) = \sqrt{1 + \omega_i^2 t^2}$ where i denotes either the x, y, or z direction, resulting in [100, 103]

$$n(\mathbf{r}, t) = \frac{1}{b_x(t)b_y(t)b_z(t)} n\left(\frac{x}{b_x(t)}, \frac{y}{b_y(t)}, \frac{z}{b_z(t)}, t = 0\right). \tag{2.10}$$

Finally, to obtain a column density that we can compare directly to images of our samples, we integrate over the imaging direction, (see Sec. 4.3 for more imaging details) which here we will take to be $\hat{z}$, giving

$$\tilde{n}_{th}(x, y, t) = \frac{N_{th}}{\pi r_x(t)r_y(t)} e^{-x^2/r_x(t)^2 - y^2/r_y(t)^2}, \tag{2.11}$$

where $r_i(t) = r_i\sqrt{1 + \omega_i^2 t^2}$. We can fit our thermal clouds to 2D or 1D Gaussian fits with the form of Eq. (2.11) and extract the atom number from the amplitude. The corresponding temperature can be determined by

$$T = \frac{m\omega_i^2 r_i(t)^2}{2k_B(1 + \omega_i^2 t^2)}, \tag{2.12}$$

or, if $t \gg \omega_i^{-1}$,

$$T \simeq \frac{m r_i(t)^2}{2k_B t^2}. \tag{2.13}$$

Ideally, the gas is fully thermalized and the temperatures are the same in each dimension. In practice, the fitted temperatures often slightly disagree in the various directions and we

take an average for the overall temperature.

In the long time-of-flight limit, we can ignore the initial size of the cloud, or for an individual atom $\mathbf{r}(t) = \mathbf{r}_0 + \mathbf{p}_0 t/m \simeq \mathbf{p}_0 t/m$. Since we are replacing the spatial dependence with a momentum dependence, imaging after a long time-of-flight is equivalent to taking a Fourier transform. Since the momentum distribution is isotropic for thermal atoms, it makes sense that for $t \gg \omega_i^{-1}$, $r_i(t) \simeq t\sqrt{2k_B T/m}$ and the spatial distribution is isotropic.

2.3 Bosons

Bosons will form a Bose-Einstein Condensate when the mean interparticle spacing, $n^{-1/3}$, is comparable to the thermal de Broglie wavelength, λ_{dB}. I will first derive an expression for T_c, the critical temperature at which a BEC forms. Then, I will discuss some of the properties of a BEC in the Thomas-Fermi limit and the fitting functions that we use to characterize it.

Neglecting the zero-point energy[3], the number of excited state atoms is given by

$$N_{ex} = \sum_{i \neq 0} f_{BE}(E_i) \approx \int_0^\infty dE \; g(E) \; f_{BE}(E), \tag{2.14}$$

where $f_{BE}(E) = 1/(e^{(E-\mu)/k_B T} - 1)$ is the Bose-Einstein distribution function and $g(E)$ is the density of states. For a 3D harmonic oscillator, the density of states is [99]

$$g(E) = \frac{E^2}{2\hbar^3 \bar{\omega}^3}. \tag{2.15}$$

Above the critical temperature, the number of atoms in the ground state, N_0 is negligible compared to N. At the critical temperature, the number of excited atoms is maximized for

---

[3]In a harmonic potential, considering the zero-point energy leads to corrections to the critical temperature $\Delta T_c/T_c \propto N^{-1/3}$, which is about 2% for $N = 10^5$ atoms [99].

$\mu = 0$, so we have

$$N = N_{ex}(T_c, \mu = 0) = \int_0^\infty dE \frac{g(E)}{e^{E/k_B T_c} - 1} = \frac{1}{2\hbar^3 \bar{\omega}^3} \int_0^\infty dE \frac{E^2}{e^{E/k_B T_c} - 1}$$
$$= \left(\frac{k_B T_c}{\hbar \bar{\omega}} \right)^3 \zeta(3),$$
(2.16)

where $\zeta(x)$ is the Riemann zeta function and $\zeta(3) \approx 1.202$.[4] This result can be re-arranged to give

$$k_B T_c = \hbar \bar{\omega} \left(\frac{N}{\zeta(3)} \right)^{1/3}.$$
(2.17)

At T_c, the phase-space density, $\rho = n\lambda_{dB}^3$, satisfies the BEC condition in the center of the trap, as can be seen from Eq. (2.3) with $\mathbf{r} = 0$ and $\mu = 0$

$$n(0) = \frac{\mathrm{Li}_{3/2}(1)}{\lambda_{dB}^3} \approx \frac{2.612}{\lambda_{dB}^3}.$$
(2.18)

Below T_c, $N > N_{ex}$, leading to a large population in the ground state and a BEC will start to form at a non-zero temperature. This finite T_c is not trivial. For instance, in the case of the density of states being independent of energy, such as for a 2D gas in a uniform potential, the integral in Eq. (2.16) diverges and a BEC will only form at zero temperature [99].

The BEC can be described by the many-body ground-state wavefunction, $\psi(\mathbf{r})$, which obeys the time-independent Gross-Pitaevski equation,

$$-\frac{\hbar^2}{2m} \nabla^2 \psi(\mathbf{r}) + V(\mathbf{r}) \psi(\mathbf{r}) + g_0 |\psi(\mathbf{r})|^2 \psi(\mathbf{r}) = \mu \psi(\mathbf{r}).$$
(2.19)

The factor $g_0 \equiv 4\pi\hbar^2 a_s/m$, where a_s is the s-wave scattering length, captures the effect of two-body collisions. In the Thomas-Fermi approximation, we assume that the interaction term dominates and completely neglect the kinetic energy term. This simplification allows

---

[4]This integral can be evaluated by using the definition of the polylogarithm integral, Eq. (A.2), and the fact that $Li_n(1) = \zeta(n)$.

us to easily solve for the density,

$$n_{BEC}(\mathbf{r}) = |\psi(\mathbf{r})|^2 = \begin{cases} \frac{\mu - V(\mathbf{r})}{g_0}, & \mu - V(\mathbf{r}) > 0 \\ 0, & \mu - V(\mathbf{r}) \leq 0 \end{cases}. \tag{2.20}$$

In this approximation, the BEC fills up the potential up until the point when $\mu = V(\mathbf{R})$ and the density distribution takes on the shape of the potential $n_{BEC}(\mathbf{r}) \propto -V(\mathbf{r})$. The resulting in-situ Thomas-Fermi radius in the i direction is $R_i^2 = 2\mu/m\omega_i^2$. By integrating $n_{BEC}(\mathbf{r})$ over all space, we arrive at a relationship between the atom number and chemical potential,

$$N_{BEC} = \frac{8\pi\mu}{15g_0} \left(\frac{2\mu}{m\bar{\omega}^2} \right)^{3/2}. \tag{2.21}$$

We can express the in-situ density distribution in a more convenient form

$$n_{BEC}(\mathbf{r}) = \frac{15N_{BEC}}{8\pi R_x R_y R_z} \max\left(1 - \frac{x^2}{R_x^2} - \frac{y^2}{R_y^2} - \frac{z^2}{R_z^2}, 0 \right). \tag{2.22}$$

As with the thermal distribution, the expected column density after a time of flight is found by integrating Eq. (2.22) along the imaging axis, giving

$$\tilde{n}_{BEC}(\mathbf{r}) = \frac{5N_{BEC}}{2\pi R_x(t)R_y(t)} \max\left[\left(1 - \frac{x^2}{R_x(t)^2} - \frac{y^2}{R_y(t)^2} \right)^{3/2}, 0 \right], \tag{2.23}$$

where the Thomas-Fermi widths after a free expansion time of t, $R_i(t)$ can be described as a re-scaling of the in-situ widths [104]

$$R_i(t) = \beta_j(t)R_i(0). \tag{2.24}$$

The scaling factors, $\beta_j(t)$, obey the coupled differential equations

$$\ddot{\beta}_i = \frac{\omega_i(0)^2}{\beta_i\beta_x\beta_y\beta_z}, \tag{2.25}$$

15

with the initial conditions $\beta_i(0) = 1$ and $\dot{\beta}_i(0) = 0$.

To extract physical parameters from our BECs, we use a fitting function with the form of Eq. (2.23). The scaling factors are numerically calculated using equation Eq. (2.25) in order to back out the in-situ Thomas-Fermi widths. The number of atoms in the BEC can be measured from the amplitude of Eq. (2.23) allowing the chemical potential to be calculated using [99]

$$\mu = \frac{15^{2/5}}{2} \left(\frac{a_s N_{BEC}}{\bar{a}} \right)^{2/5} \hbar\bar{\omega}, \tag{2.26}$$

where $\bar{a} = \sqrt{\hbar/m\bar{\omega}}$ is the characteristic harmonic oscillator length.

However, since BECs tend to be very dense, the optical depth in the center of the cloud can be very large, even for large expansion times, potentially leading to systematic errors in measuring the amplitude of the BEC distribution. For very dense samples, we can also extract the atom number from the measured Thomas-Fermi radii using

$$N_{BEC} = \frac{\bar{a}}{15 a_s} \left(\frac{\bar{R}}{\bar{a}} \right)^5. \tag{2.27}$$

Here, $\bar{R} = (R_x R_y R_z)^{1/3}$ is the geometric mean of the in-situ Thomas-Fermi radii.

In the case of radially symmetric, elongated trap with $\omega_x = \omega_y \gg \omega_z$, the initial aspect ratio is $R_x(0)/R_z(0) = \omega_z/\omega_x$. Solving for the scaling parameters at lowest order using Eq. (2.25) yields

$$\begin{aligned} R_x(t) &= R_x(0)\sqrt{1 + \omega_x^2 t^2} \\ R_z(t) &= R_x(0)\frac{\omega_x}{\omega_z}\left(1 + \frac{\omega_z^2}{\omega_x^2}\left[\omega_x t \arctan(\omega_x t) - \ln\sqrt{1 + \omega_x^2 t^2} \right] \right). \end{aligned} \tag{2.28}$$

For large expansion times, $t \gg \omega_{x,z}^{-1}$, the aspect ratio approaches the limit $R_x(t)/R_z(t) = (2/\pi)(\omega_x/\omega_z)$. This relationship illustrates a key signature of BECs that distinguish them from thermal gases. Whereas thermal gases approach an isotropic density distribution after a long time-of-flight (as shown in Sec. 2.2), the aspect ratio of BEC released from

16

an anisotropic trap will invert. Another obvious signature of the onset of a BEC is the presence of a bimodal distribution. At $T < T_c$, but before all of atoms have condensed, the density distribution will have a high-density parabaloid superimposed on a Gaussian background and can be fit with the sum of Eq. (2.11) and Eq. (2.23) to extract information about both the BEC and thermal background.

2.4   Fermions

For fermions, the Pauli exclusion principle forbids two or more identical fermions from occupying the same quantum state. Therefore, there is no sudden transition, as with bosons, to a macroscopic population in the ground state as $T \rightarrow 0$. As illustrated in Fig. 2.1a, the Fermi-Dirac distribution function smoothly approaches its zero-temperature limit for which all states less than the chemical potential, μ, have unit occupation and all states above μ have zero population,

$$f_{FD}(E) = \frac{1}{e^{(E-\mu)/k_B T} + 1} \xrightarrow{T \rightarrow 0} \begin{cases} 1, & E < \mu \\ 0, & E > \mu \end{cases}. \tag{2.29}$$

The energy of the highest occupied state at zero temperature is also known as the Fermi energy, E_F, and $\mu \xrightarrow{T \rightarrow 0} = E_F$. The Fermi energy in a harmonic trap is fixed by the number of particles by

$$\frac{N}{M} = \int_0^\infty dE \, g(E) f_{FD}(E) = \frac{1}{2\pi \hbar^3 \bar{\omega}^3} \int_0^{E_F} dE \, E^2 = \frac{1}{6} \left(\frac{E_F}{\hbar \bar{\omega}} \right)^3$$
$$\Rightarrow E_F = \hbar \bar{\omega} \left(\frac{6N}{M} \right)^{1/3}, \tag{2.30}$$

where N is the total atom number evenly distributed among M spin states and we used the harmonic oscillator density of states from Eq. (2.15). We typically use the reduced temperature, or T/T_F where $T_F = E_F/k_B$ is the Fermi temperature, to describe how close
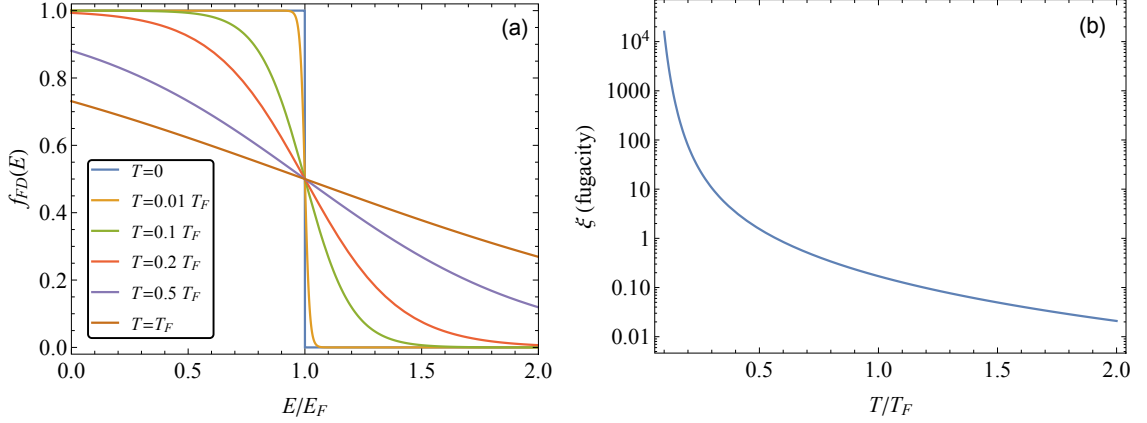
Figure 2.1: (a) Fermi-Dirac distribution function at various temperatures. At zero temperature, all states with energy below the Fermi energy are occupied and all states above E_F are unoccupied. At finite, but low temperatures, the distribution differs from the zero-temperature limit only in the vicinity of E_F. At higher temperatures, the distribution approaches the classical Boltzmann distribution. (b) Fugacity versus the reduced temperature.

our samples are to the $T = 0$ limit. Fermionic samples are said to form a degenerate Fermi gas when $T/T_F < 1$. It is also convenient to use a parameter known as the *fugacity*, denoted by ξ, to characterize the degeneracy of our fermionic samples. The fugacity is defined as

$$\xi = e^{\mu/k_B T}, \tag{2.31}$$

and ξ is small for high-temperature, classical gases and large as $T/T_F \to 0$, as shown in Fig. 2.1b. Using Eqs. (2.6) and (2.30), the relationship between the reduced temperature and fugacity is determined to be

$$\frac{T}{T_F} = [-6 \, \mathrm{Li}_3(-\xi)]^{-1/3} . \tag{2.32}$$

We can determine the time-of-flight density distribution of a fermionic sample by re-scaling the in-situ density, given by Eq. (2.3), using the same procedure as for thermal atoms and detailed by Eq. (2.10). This results in,

$$n_{FD}(\mathbf{r}, t) = -\frac{1}{\lambda_{dB}^3} \prod_{i=1}^{3} \left(1 + \omega_i^2 t^2\right)^{-1/2} \mathrm{Li}_{3/2} \left(-\xi e^{-x^2/r_x(t)^2 - y^2/r_y(t)^2 - z^2/r_z(t)^2}\right), \tag{2.33}$$

18

with $r_i(t)^2 = (1 + \omega_i^2 t^2)(2k_B T/\omega_i^2 m)$. Just as for a thermal gas, for long times-of-flight $r_i(t)^2 \approx 2k_B T t^2/m$ and the density distribution is isotropic. After integrating along the imaging axis, the column density is [100–102]

$$\tilde{n}_{FD}(x, y, t) = -\frac{m(k_B T)^2}{2\pi \omega_z \hbar^3 \sqrt{1 + \omega_x^2 t^2}\sqrt{1 + \omega_y^2 t^2}} \mathrm{Li}_2\left(-\xi e^{-x^2/r_x(t)^2 - y^2/r_y(t)^2}\right). \qquad (2.34)$$

Finally, we parameterize this equation by fitting our DGF clouds using

$$\tilde{n}_{FD}(x, y) = \frac{A}{\mathrm{Li}_2(-\xi)} \mathrm{Li}_2\left(-\xi e^{-(x-x_0)^2/w_x^2 - (y-y_0)^2/w_y^2}\right) + B, \qquad (2.35)$$

where A, x_0, y_0, w_x, w_y, ξ, and B are the fit parameters. The additional factor of $\mathrm{Li}_2(-\xi)$ in the denominator is not strictly necessary but helps the performance of the numerical fitting procedure. Atom number and temperature are extracted using the fit amplitude and widths according to

$$
\begin{aligned}
N &= \frac{A\pi w_x w_y \mathrm{Li}_3(-\xi)}{\mathrm{Li}_2(-\xi)} \\
T &= \frac{m}{4k_B t^2}(w_x^2 + w_y^2)
\end{aligned}
\qquad (2.36)
$$

and the reduced temperature, T/T_F, is determined by Eq. (2.32). Compared to a Gaussian thermal cloud with the same atom number and temperature, a deeply degenerate Fermi gas is flatter near the center of the cloud and broader in the wings. As illustrated in Fig. 2.2, the shape of a DFG is only subtlety different from that of a Gaussian, making it challenging to characterize these samples. Though we sometimes fit thermal gases and BECs using 1D fits to increase processing speed, we only use 2D fits for DFG fits because they allow us to use the whole image to extract information from the small deviations in the shape of the cloud.
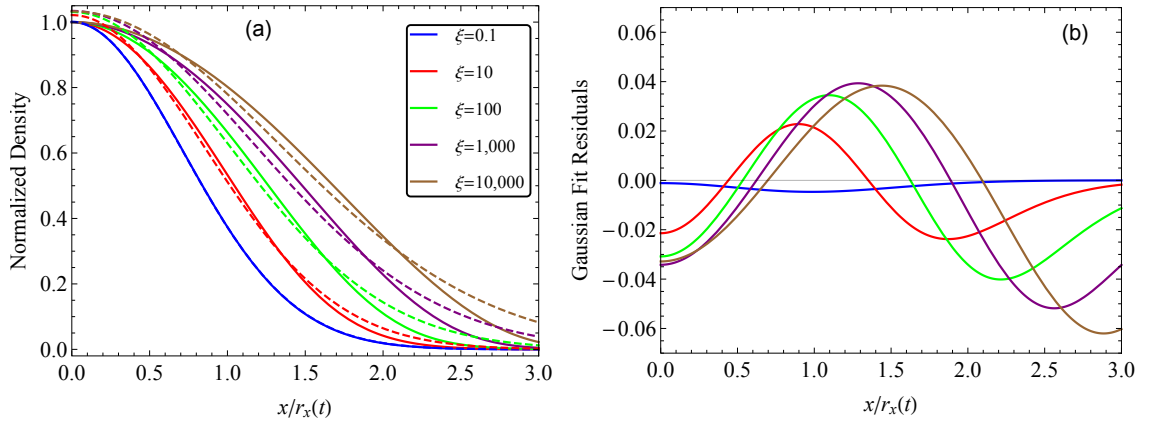
Figure 2.2: (a) Fermionic density distributions for various fugacity values. All curves are normalized to the same peak density and plotted against the width $r_x(t)$. Solid lines are the fermionic density distribution given by Eq. (2.34) and the dashed lines are Gaussian fits to the solid curves. (b) Residuals of the Gaussian fits from (a). For small fugacities, there is almost no deviation from a thermal Gaussian distribution. For larger values of ξ, the DFG distribution is slightly suppressed at the center of the cloud and rolls off more sharply towards the wings. Even for highly degenerate samples, the overall shape is not significantly different from a Gaussian, making it difficult to characterize DFGs.

Chapter 3: Achieving Quantum Degenerate Gases of Strontium

3.1 Overview

In order to generate quantum degenerate gases of strontium, we must cool our samples by roughly 10-12 orders of magnitude from their starting temperature of ≈ 1000 K. In this chapter, I will discuss how we accomplish this feat using the powerful laser cooling techniques of Doppler cooling, Zeeman slowing, magneto-optical traps, and evaporative cooling that were introduced in Sec. 1.1 and developed since 1975. The first step is to generate an atomic beam of strontium, which is collimated by a transverse cooling stage and decelerated by a Zeeman slower. The slow atomic beam is then captured in a 3D MOT, which we refer to as the "blue MOT" (or bMOT) since it operates on the broad $^1S_0 \rightarrow {}^1P_1$ transition at 461 nm. Though the bMOT has a large capture velocity due to the large linewidth ($\Gamma/2\pi = 30.5$ MHz) of the 461-nm transition, the minimum attainable temperature is Doppler limited to $\simeq 1$ mK. Therefore, we transfer the atoms to a second MOT, which we call the "red MOT" (or rMOT) since it addresses the narrow ($\Gamma/2\pi = 7.4$ kHz) $^1S_0 \rightarrow {}^3P_1$ transition at 689 nm. The rMOT allows us to cool our samples to $\simeq 1$ μK, at which point we load the atoms into an optical dipole trap (ODT) and perform further cooling by forced evaporation. Finally, I will also discuss the achievement of BECs and DFGs of multiple strontium isotopes in our lab.

3.2 Generating a Slow Atomic Beam

The first step to produce ultracold strontium gases is to generate an atomic beam that is slow enough to be captured by a MOT. We begin by heating solid strontium in our oven at $\simeq 600$ °C to generate a vapor of strontium atoms. As this vapor exits our oven, it is collimated by a nozzle consisting of an array of parallel hypodermic needles (the oven and nozzle is described in more detail in Sec. 4.1.1). After the oven, we use a 2D optical molasses stage to further collimate the atomic beam by damping the transverse momentum.

The basic operating principle of the molasses, which we call our transverse cooling stage, can be explained using Doppler cooling theory. In one dimension, the force on an atom with velocity $\mathbf{v}$ from a laser beam propagating in the plus or minus directions is [29, 105]

$$F_{\pm}(\mathbf{v}) = \pm \hbar k \Gamma \frac{s/2}{1 + s + \left[2 \left(\delta \mp |\mathbf{k} \cdot \mathbf{v}|\right)/\Gamma\right]^2}, \tag{3.1}$$

where $\mathbf{k} = 2\pi \hat{k}/\lambda$ is the laser's wavevector, Γ is the linewidth of the atomic transition, s is the saturation parameter $s = I/I_{sat}$ where $I_{sat} = 2\pi^2 hc\Gamma/3\lambda^3$, and $\delta/2\pi$ is the detuning of the laser beam. This simplified expression is only valid when the light intensity is low enough to ignore stimulated emission. When $|\mathbf{k} \cdot \mathbf{v}| \ll \Gamma$, the total force on the atoms can be approximated as

$$F_{tot} = F_+ + F_- \cong \frac{8\hbar k^2 \delta s}{\Gamma \left[1 + s + (2\delta/\Gamma)^2\right]^2} \mathbf{v} \equiv -\beta \mathbf{v}. \tag{3.2}$$

For $\delta < 0$, the Doppler shift decreases the total detuning of the beam opposing the atomic velocity so that photons are preferentially scattered from that beam over the counter-propagating beam. Thus the net force is directed against the atomic motion, and acts to damp the atomic velocity. The velocity damping time constant in the linear region is given by $\tau_{damp} = -\text{v}/\dot{\text{v}} = m/\beta$. Though the average velocity will damp to zero,

there are additional heating mechanisms that balance the cooling and result in a non-zero equilibrium rms velocity. The heating mechanisms stem from the statistical fluctuations in the rate of absorbing and emitting photons from the cooling beams. I will briefly discuss the resulting Doppler cooling limit in the next section.

Our transverse cooling beams consist of two counter-propagating pairs of beams in the horizontal and vertical directions, transverse to the direction of atomic flux. The beams are slightly detuned from the $^1S_0 \rightarrow {}^1P_1$ transition at 461 nm, which has a broad linewdith of $\Gamma/2\pi$ = 30.5 MHz and I_{sat} = 40.3 mW/cm^2. Each pair of beams contains between 10-15 mW, depending on the performance of the blue laser, with a detuning of $\delta/2\pi$ = −10 MHz. The beams are elliptical with $1/e^2$ radii of 3×9 mm with the long dimension oriented along the atomic beam to increase the interaction time. The net force as a function of transverse velocity is plotted in Fig. 3.1 for a typical saturation value s = 0.75. Picking the beam size for the transverse cooling involves a tradeoff between smaller beams to increase s or larger beams to increase the interaction time. For an operating temperature of 600 °C, the most probable velocity of an atom emitted from our oven is $v_p = \sqrt{2k_BT/m} \simeq 400$ m/s. Therefore the atoms will interact with the transverse cooling beams for approximately 23 μs, which is slightly longer than the damping time, $\tau_{\text{damp}} \simeq 18$ μs, for our parameters. As shown in Fig. 3.1, our 2D molasses beams are expected to efficiently damp transverse velocities $\lesssim$ 10 m/s with a maximum force for velocities $\simeq$ 6 m/s. The net effect of our transverse cooling beams is to improve the bMOT fluorescence by a factor of $\simeq$ 3.

Now that we have a well collimated atomic beam, the next step is to slow its axial velocity to $\lesssim$ 50 m/s for capture in the bMOT. The decelerating force is applied by a laser beam, also addressing the $^1S_0 \rightarrow {}^1P_1$ transition, counter-propagating the atomic beam direction. The force on an atom due to this beam is also described by Eq. (3.1). However, while we can pick a detuning to cancel the Doppler shift for a certain class of atomic velocities, the laser will only interact strongly with a narrow range of velocities with a
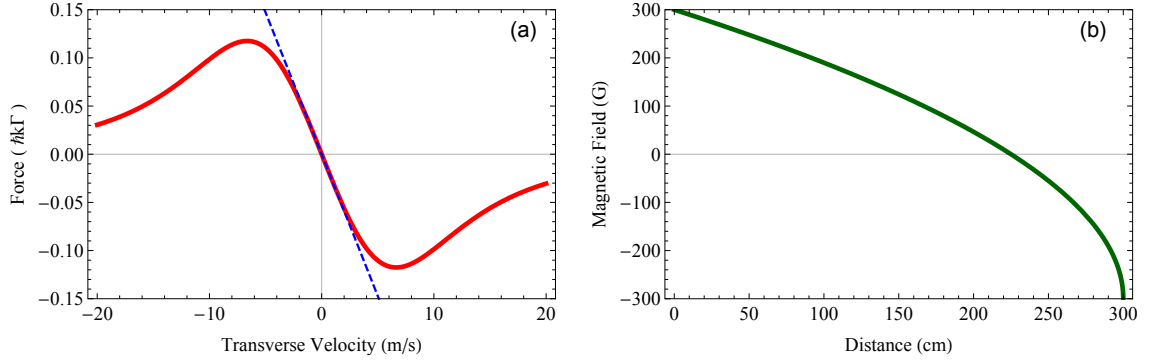
Figure 3.1: (a): The force (in units of $\hbar k \Gamma$) of the transverse cooling optical molasses beams vs. the atomic velocity. The red solid curve is full expression for $F_+ + F_-$ while the blue dashed line shows the linear approximation from Eq. (3.2). The curves use a detuning $\delta/2\pi = -10$ MHz and saturation parameter $s = 0.75$, similar to the experimental parameters of our transverse cooling beams. (b): Ideal Zeeman slower magnetic field profile. The shape is given by Eq. (3.3) and is designed to cross zero.

width $\Delta v \approx \Gamma/k$. Not only will we only be able to cool a small fraction of the thermal velocity distribution, the atoms that we can address will quickly slow down until their Doppler shift is no longer resonant with the laser. The solution is to use a Zeeman slower, which uses a spatially varying magnetic field to induce a Zeeman shift that cancels the changing Doppler shift as the atoms decelerate along the slower.[1]

To generate constant deceleration of the beam, the desired magnetic field profile is [8, 29, 105]

$$B(z) = B_0\sqrt{1 - z/L_0} + B_{\text{bias}} \tag{3.3}$$

where L_0 is the length of the slower region and B_{bias} is a bias magnetic field. The magnetic field magnitude, B_0, determines the maximum capture velocity, v_{max}, through the expression $B_0 = \hbar k(v_{\text{max}} - v_{\text{final}})/\mu'$, where v_{final} is the exit velocity at the end of the slower. The effective magnetic moment, μ', is defined as

$$\mu' \equiv (g_e m_e - g_g m_g)\mu_B, \tag{3.4}$$

---

[1]One can also compensate for the changing Doppler shift by chirping the laser frequency. However, this produces pulses of slow atoms instead of a constant flux. In addition, we don't have an easy method of generating an appropriate frequency sweep so we have not attempted to implement this technique.

with $g_{e,g}$ and $m_{e,g}$ being the Landé g-factors and magnetic quantum numbers for the ground and excited states, and μ_B is the Bohr magneton. For our slower, $L_0 \simeq 30$ cm and the designed field has a magnitude $B_0 \simeq 600$ G, which corresponds to $v_{max} - v_{final} \simeq 400$ m/s. The final velocity can be tuned by changing the detuning of the slower laser beam. Typically one would not operate with $v_{final} \simeq 0$ since the atoms need enough residual velocity carry them cleanly out of the slower and into the trapping region. Our slower implements a "spin-flip" design, which involves using multiple coils with currents flowing in opposite directions such that $B_{bias} \simeq -300$ G and the magnetic field goes through zero, as illustrated in Fig. 3.1.[2] In addition to reducing the magnitude of the field we need to generate, the zero-crossing design means that the contributions of the coils with opposite current tend to cancel out as the atoms leave the slowing region, allowing for a rapid decrease in the magnitude of the magnetic field. The abrupt change in magnetic field profile at the end of the slower is helpful to minimize further slowing of the atoms that may prevent them from reaching the MOT. The Zeeman slower beam has a detuning of -605 MHz and an initial $1/e^2$ radius of 6 mm. We slightly focus the slower beam on the oven nozzle in order to add a small transverse component to the laser's k-vector and provide a small amount of cooling in the transverse directions. The final Zeeman slower performance has not been measured directly, though it is expected to produce a beam of atoms with a velocity $v \lesssim 50$ m/s. The slower parameters are optimized by maximizing loading into the bMOT.

---

[2]The "spin-flip" name for Zeeman slowers with a magnetic field zero comes from the fact that these slowers were first used for alkali-metal atoms whose spins must flip directions to follow the changing quantization axis when the direction of the magnetic field switches. For strontium and other alkaline-earth elements, there is no spin in the ground state and therefore no spin flip.

3.3 Blue MOT and Metastable Reservoir

3.3.1 Bosonic Blue MOT

A magneto-optical trap operates on a similar principle to the optical molasses described above. In addition to counter-propagating laser beams, we also add a magnetic field gradient and set the two beams to have opposite circular polarizations. This creates a spatially dependent detuning such that the atom's position, as well as its velocity, undergoes damping.

In one dimension, the average force on an atom at position z with velocity $\mathbf{v}$ due to the MOT beams is [29, 105]

$$F(z, \mathbf{v}) = \frac{\hbar k \Gamma}{2} \left(\frac{s_+}{1 + s' + 4 \left(\delta - |\mathbf{k} \cdot \mathbf{v}| + \mu' dBz \right)^2 / \Gamma^2} \right.$$
$$\left. - \frac{s_-}{1 + s' + 4 \left(\delta + |\mathbf{k} \cdot \mathbf{v}| - \mu' dBz \right)^2 / \Gamma^2} \right), \tag{3.5}$$

where $s_\pm$ is the saturation of the positive, negative propagating beams respectively and $s' \geq s_\pm$ accounts for saturation due to cooling beams in the other axes [106]. We also have the magnetic field gradient, dB, and the effective magnetic moment, μ', as defined in Eq. (3.4). For bosonic strontium, $\mu' = \mu_B$.

The forces due to Eq. (3.5) lead to damped harmonic motion for both the position and velocity of the atoms. However, we cannot use this technique to cool the atoms all the way to zero temperature. Eq. (3.5) is only the average force on the atoms. Fluctuations in the actual force due to the random absorption and emission of photons from the cooling beams increase the atom's kinetic energy and lead to heating. According to Doppler cooling theory, the minimum attainable temperature is given by [106]

$$T = \frac{\hbar \Gamma^2}{8 k_B |\delta|} \left(1 + s_{\text{tot}} + 4\delta^2 / \Gamma^2 \right), \tag{3.6}$$
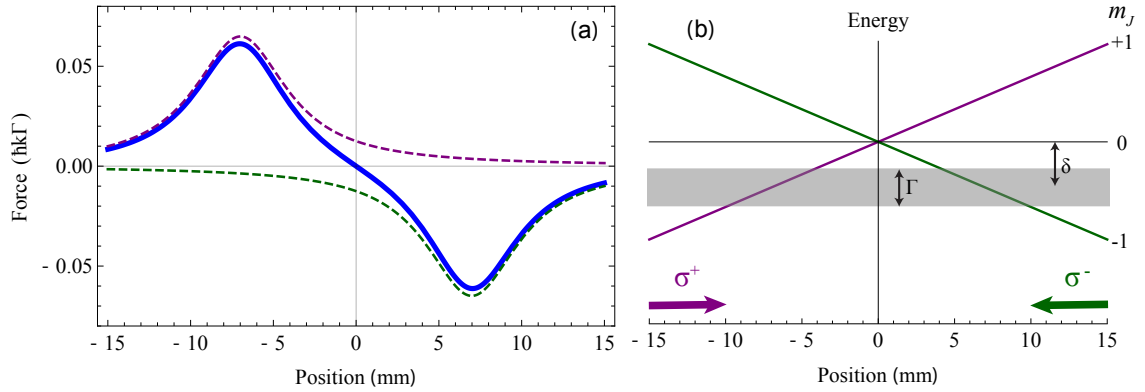
Figure 3.2: (a) Force on an atom due to a pair of MOT beams for typical bMOT parameters. The plot shows the average trapping force, given by Eq. (3.5), as a function of position for $s_\pm = 0.27$, $s' = 3s_\pm$, $dB = 46$ G/cm, v = 0, and $\delta/2\pi = -45$ MHz. For the bMOT, $\Gamma/2\pi = 30.5$ MHz and $k = 2\pi/461$ nm. The purple (green) dashed lines show the force from the positive (negative) propagating beam and the blue solid line shows the total force. (b) Schematic of the position dependent Zeeman splitting for the $m_J = \pm 1$ excited state sublevels for the bosonic bMOT. For an atom to the right (left) of the trap center, the Zeeman shift ensures that the atoms will scatter more photons from the σ^- (σ^+) polarized beam directed in the left (right). Thus an atom will always feel a force pushing it towards the center of the trap.

where s_{tot} is the total saturation from all MOT beams. For one-dimension, and assuming $s_{\text{tot}} \ll 1$, the minimum temperature is given by the well known Doppler temperature $k_B T_{\text{Doppler}} = \hbar\Gamma/2$ at a detuning of $\delta = -\Gamma/2$ [29, 105, 106]. For the strontium $^1S_0 \rightarrow {}^1P_1$ transition, $T_{\text{Doppler}} \simeq 730 \ \mu$K.

For alkali atoms, temperatures below the Doppler temperature can be obtained through polarization gradient cooling or other sub-Doppler cooling methods [29, 105, 106]. However, those cooling processes are not possible for the bosonic isotopes of strontium due to the lack of hyperfine structure in the ground state, so the Doppler temperature is the fundamental temperature limit in the bMOT. Furthermore, it has been shown that transverse spatial intensity modulations in the trapping beams give rise to local imbalances between the intensity of the counter-propagating beams and adds an additional heating mechanism [107]. The extra heating is dependent on the saturation of the MOT beams, so for typical MOT parameters with $s_{\text{tot}} > 1$ that are used to optimize the atom loading rate, the heating rate can be significant and bosonic bMOT temperatures are typically several times larger than the Doppler cooling limit [108]. In contrast to the bosons, the fermionic

isotope of strontium has a $F = 9/2$ ground state. The resulting magnetic degeneracy allows for sub-Doppler cooling and has been observed in at least one experiment [109].

Our bMOT consists of three retro-reflected beams with a $1/e^2$ radius of 8 mm, a maximum power of about 11 mW per beam, and a detuning of $\delta/2\pi = -45$ MHz. This gives us a saturation of $s_\pm \simeq 0.27$ per beam and $s_{\text{tot}} \simeq 1.6$. While loading, the magnetic field gradient is $dB \approx 46$ G/cm in the vertical direction and 23 G/cm in the horizontal directions. In order to estimate the capture velocity of the bMOT, I numerically evaluated the acceleration due to the four horizontal trapping beams given by Eq. (3.5) with the approximation that the MOT beams have a uniform saturation of $s = s_\pm/2 = 0.135$, a radius of 8 mm, and assumed $s' = 3s_\pm = 0.81$. The calculation gives a capture velocity of about 55 m/s. A plot of the trapping force as a function of position is shown in Fig. 3.2 for typical MOT parameters.

A typical bMOT loading procedure is illustrated in Fig. 3.3. We load the bMOT for a variable amount of time, t_{load}, that is typically between 1-10 s depending on the natural abundance of the isotope being used, see Table 1.2. During this load time, we use about 11 mW of power in each MOT beam and the vertical magnetic field gradient is about 46 G/cm. After accumulating enough atoms in the bMOT, we perform a Doppler cooling step for 75 ms. During this step, we linearly decrease the power in each MOT beam to ≈ 2 mW, which decreases to the temperature of the MOT to ≈ 1 mK and enhances the transfer efficiency to the rMOT, which is the next cooling step. Since the bMOT is substantially larger than the rMOT, we do not currently have an imaging system that is capable of collecting absorption images of the bMOT. Therefore, we do not optimize bMOT performance directly but instead select bMOT parameters to maximize the number of atoms collected in the rMOT.
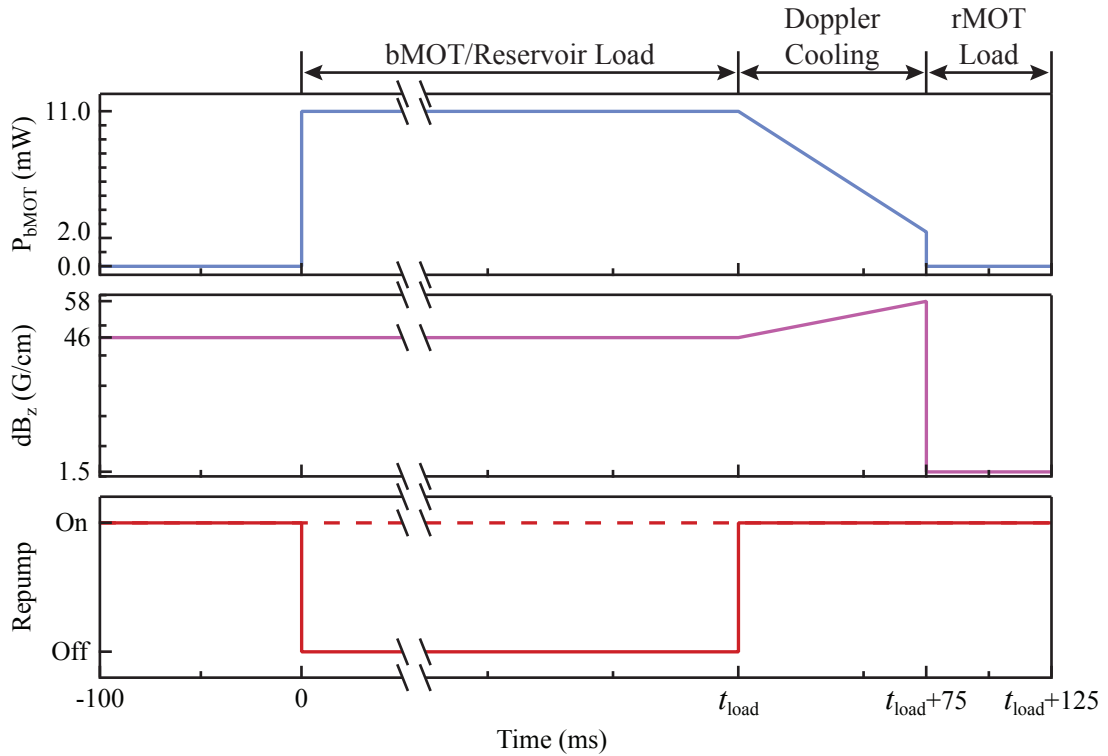
Figure 3.3: Power, magnetic field gradient, and repump ramps for bMOT operation. We load the bMOT or metastable reservoir at a power of 11 mW per MOT beam and a vertical magnetic field gradient of 46 G/cm for a variable time, t_{load}, that depends on the abundance of the isotope being used. The dashed red line indicates that repump lasers can be left on (off) to load the bMOT (metastable reservoir). After loading, the power in the bMOT beams is decreased to ≈ 2 mW per beam to cool the sample, while the field gradient is slightly increased for 75 ms. Then the bMOT beams are extinguished and the field gradient is snapped down to 1.5 G/cm in order to load the rMOT.

3.3.2 Repumping

Though the $^1S_0 \rightarrow\,^1P_1$ transition is nearly closed, there is a small leak (about 1 in 5×10^4 scattering events [88]) to the $^1D_2$ level. Those atoms then decay to either the $^3P_1$ or $^3P_2$ states (see Fig. 1.1). From the $^3P_1$ state, the atoms will quickly decay back to the ground state and are re-captured in the bMOT, but the $^3P_2$ state is metastable with a lifetime of about ≈ 500 s [110, 111][3]. Without repumping, this leakage to a dark, metastable state limits the lifetime of the bMOT to a few 10 ms. To return $^3P_2$ atoms to the bMOT we use a laser at 707 nm to excite the $^3P_2 \rightarrow\,^3S_1$ transition. Since the atoms can subsequently decay to any of the states in the ^3P manifold, we also need a second repump laser at 679 nm to depopulate the $^3P_0$ state.

We choose to repump using the $^3S_1$ state because the 679-nm and 707-nm wavelengths are relatively convenient to access using laser diodes. However, there is an infinite ladder of $^3D_2$ states that could also be used. For example, the Rice group has excited atoms to the $5s4d\;^3D_2$ state using infrared (IR) light at 3012 nm [112, 113] and the Innsbruck group uses the $5s5d\;^3D_2$ state at 497 nm [114, 115]. Another attractive option is the 5s6d $^3D_2$ state, because the associated transition wavelength of 403 nm could be accessible using laser diodes developed for Blu-ray devices [116]. One advantage of using one of these $^3D_2$ states is that they do not decay to the $^3P_0$ level and therefore do not require a second laser.

Fortuitously, the $^3P_2$ $m_J = 1$ and $m_J = 2$ sublevels are magnetically trapped by the bMOT quadrupole field [117]. The repump beams can optionally be turned off during bMOT loading (see bottom of Fig. 3.3) and the bMOT will continuously load atoms into this reservoir of metastable atoms. After loading for a long enough time, we can turn on the repump lasers and recapture the atoms in either the bMOT or rMOT. Though loading times tend to be longer than just collecting atoms in the bMOT, this turns out to

---

[3]The natural lifetime of the $^3P_2$ state is reduced by black-body induced transitions to upper-lying ^3D states and was found to depend on the ambient temperature [110].

be a convenient method of accumulating a sufficient quantity of atoms for some of the less abundant isotopes of strontium, particularly [84]Sr. Other groups have also used the metastable reservoir to sequentially load multiple isotopes of strontium [115]. In Ch. 5 we will investigate a method to enhance the loading rate into the metastable reservoir.

3.3.3 Fermionic Blue MOT

The hyperfine structure of the fermionic isotope, [87]Sr, slightly complicates the bMOT operation and repumping. The $^1P_1$ hyperfine splitting is on the same order as the transition linewidth of $\Gamma/2\pi = 30.5$ MHz (see Table 1.1 and Fig. 3.4). Stable MOT operation requires that $F_e = F_g + 1$, so we operate the bMOT laser beams relative to the $F = 9/2$, $^1S_0 \rightarrow F = 11/2$, $^1P_1$ transition. However, it is not possible to avoid also addressing the $F = 9/2$ excited level as it is only separated from the $F = 11/2$ state by about 19 MHz. This undesirable scattering will reduce the cooling efficiency of the bMOT beams.

The hyperfine structure also complicates repumping. As shown in Table 1.1, the $^3P_2$ and $^3S_1$ states split into five and three hyperfine levels respectively. Therefore, instead of addressing a single transition out of $^3P_2$, we have to worry about as many as nine allowed transitions spanning ≈ 5.4 GHz. We find that all five of the $^3P_2$ levels are populated by the bMOT, though the relative populations are not even. It is difficult to measure the relative populations of the various levels, but we seem to get the largest gains by repumping the $F = 13/2$, $11/2$, and $5/2$ states, which matches the observations of other groups [114]. The relative population between the various hyperfine states is affected by the various branching ratios during the $^1P_1 \rightarrow {}^1D_2 \rightarrow {}^3P_2$ decay process. In addition, because the g_F factors for the various $^3P_2$ hyperfine levels vary significantly (see Table 1.1), some levels are more likely to be magnetically trapped than others. We have tried a couple different methods to broaden the linewidth of our 707-nm laser in order to repump as many of the $^3P_2$ states as possible (see Sec. 4.2.2). We find that the atom number is highly

MHz | $^1P_1$
0 — ^{88}Sr
-7.8 — ^{87}Sr (F=7/2)
-49.5 — ^{87}Sr (F=11/2)
-68.1 — ^{87}Sr (F=9/2)
-126.3 — ^{86}Sr
-273.2 — ^{84}Sr

MHz | $^3P_1$
1351.97 — ^{87}Sr (F=7/2)
221.71 — ^{87}Sr (F=9/2)
0 — ^{88}Sr
-164.9 — ^{86}Sr
-352.6 — ^{84}Sr
-1241.44 — ^{87}Sr (F=11/2)

$^1S_0$
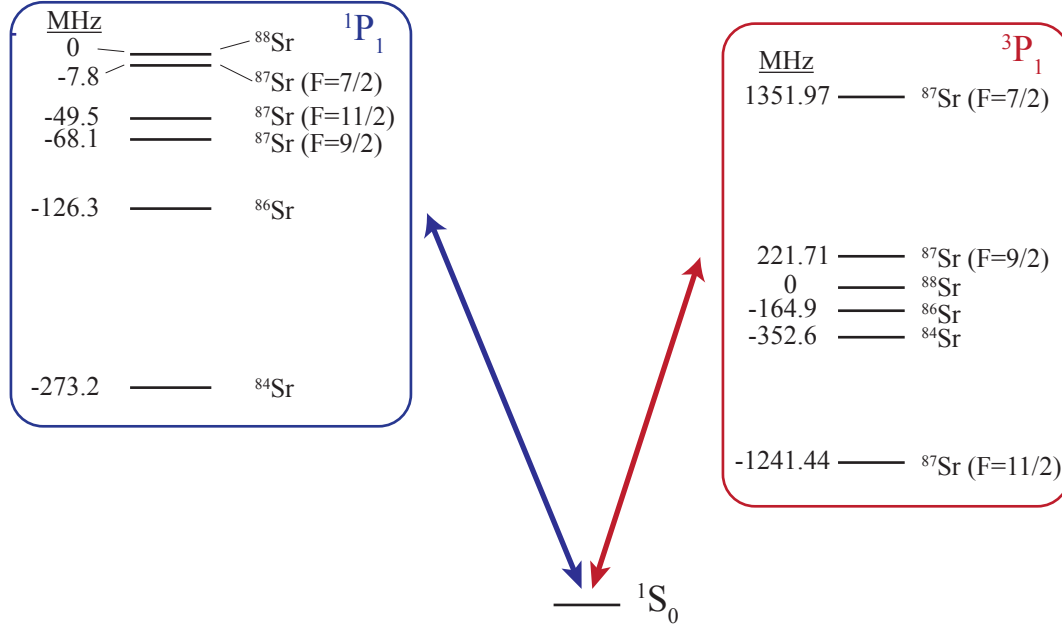
Figure 3.4: Isotope and hyperfine splittings for the $^1P_1$ and $^3P_1$ states relative to the ^{88}Sr transition frequencies. The splittings within each box are to scale relative to each other. For the $^1P_1$ state, the hyperfine splittings are small compared to the isotope shifts while the opposite is true for the $^3P_1$ state. Splitting values are based on [92, 93, 95, 118, 119].

dependent on the available 707-nm power, indicating that we have not saturated the ^{87}Sr repumping efficiency. Repumping at 679 nm remains straightforward, as we only address the $^3P_0$ ($F = 9/2$) $\rightarrow$ $^3S_1$ ($F = 11/2$) transition.

3.4 Red MOT

3.4.1 Bosonic Red MOT

The red MOT operates on the narrow $\Gamma/2\pi = 7.4$ kHz, $^1S_0 \rightarrow {}^3P_1$ transition. Due to the kHz linewidth, the rMOT operates in a very different regime than the bMOT or even typical alkali metal MOTs which have linewidths of about 5-10 MHz [105]. Since the maximum cooling force is $\hbar k\Gamma/2$, the reduced linewidth also means that the capture velocity of the rMOT is on the order of mm/s, which is four orders of magnitude lower than the capture velocity of the bMOT. Therefore, it is not feasible to capture atoms in the rMOT directly from the slowed atomic beam and we use the bMOT to pre-cool the atoms.
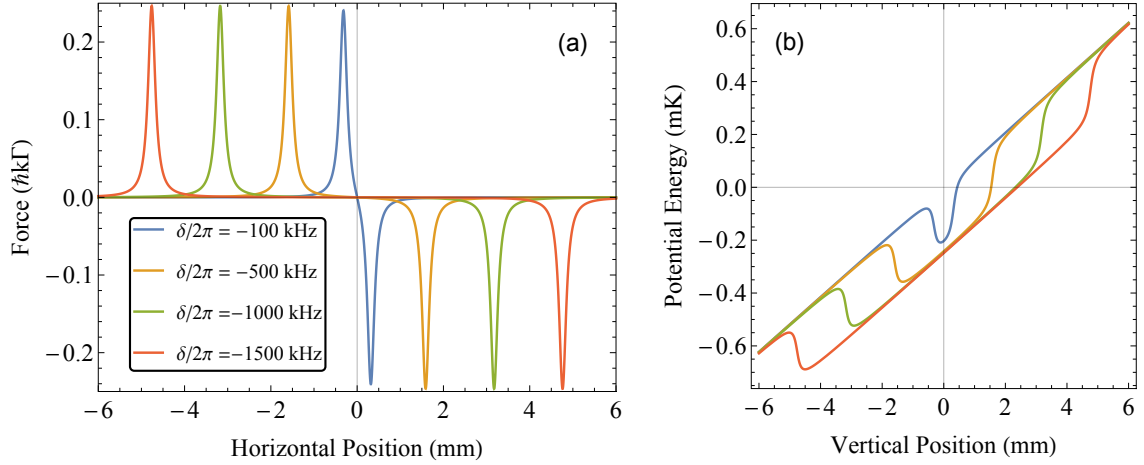
Figure 3.5: (a) Force as a function of horizontal position for various detunings. For large detunings, $\delta \ll -\Gamma_{\text{sat}}$, the cooling force has a very localized effect. For smaller detunings, $\delta \approx -\Gamma_{\text{sat}}$, the force has a dispersive shape. (b) The rMOT potential energy curves in the vertical direction. The effect of gravity, which causes a linear tilt to the curves, causes the position of the atoms to sag for large detunings. These plots were generated using Eq. (3.5) with $s = s' = 36$, v = 0, and $dBz = 1.5$ G/cm.

Conversely, the small linewidth means that we can achieve much lower temperatures in the rMOT. The Doppler temperature $T_D = \hbar\Gamma/2k_B$ is only ≈ 180 nK. In fact, this temperature is so low that we must consider another fundamental cooling limit known as the recoil temperature. The recoil temperature is related to the temperature corresponding to an average velocity that a single spontaneous emission event would give an atom, or $T_{\text{recoil}} = (\hbar k)^2/mk_B$. For the rMOT, $T_{\text{recoil}} \approx 460$ nK and the fundamental cooling limit is given by $T_{\text{recoil}}/2 \approx 230$ nK [33,34]. Since the saturation intensity of the 689-nm transition is so low ($I_{\text{sat}} = 3.0 \ \mu\text{W/cm}^2$) it is very common to operate in a highly saturated regime. In this case, an important parameter is the saturation broadened linewidth $\Gamma_{\text{sat}} = \Gamma\sqrt{1 + s'}$.

Instead of exerting a damping force on the atoms within the volume of an ellipsoid, as for the bMOT, the rMOT force only acts on the atoms over a thin region of position or velocity space. This localized force is illustrated in Fig. 3.5(a). The width of this region has a characteristic width of $w_z = \Gamma_{\text{sat}}/(\mu' dBz)$ in position space and $w_{\text{v}_z} = \Gamma_{\text{sat}}/k$ in velocity space. For $s' = 1$, these widths are only $w_z \simeq 33 \ \mu\text{m}$ and $w_{\text{v}_z} \simeq 7$ mm/s. Even for our maximum available laser intensity $s' = 2400$ the widths are $w_z \simeq 1.2$ mm and $w_{\text{v}_z} \simeq 250$ mm/s which are smaller than the spread of positions and velocities in the

bMOT. In order to simultaneously capture and cool atoms in the entire MOT volume, we frequency modulate the laser frequency at 30 kHz with an initial modulation depth of 2 MHz. This means that the trapping light consists of many frequency tones, each of which acts on slightly different slice of position or velocity space. The combination of the various frequencies exerts a trapping force out to a distance of about 6 mm or a velocity of 1.4 m/s, enabling us to capture a large fraction of the bMOT atoms.[4]

The rMOT capture and cooling procedure is illustrated in Fig. 3.6. The rMOT beams have a $1/e^2$ radius of about 2.5 mm and the laser used for the bosonic isotopes has a maximum power of about 700 μW per MOT beam, corresponding to a maximum saturation $s = 2400$. After snapping the magnetic field gradient down to 1.5 G/cm, the bMOT atoms are captured for 50 ms using the maximum available laser power and a broadband frequency profile that is broadened by about 2 MHz, as described above. Next, the broadband rMOT is compressed over 400 ms by linearly increasing the field gradient to 2.3 G/cm and linearly decreasing the depth of the frequency modulation. The center detuning is simultaneously decreased as well such that the laser's frequency component closest to resonance stays fixed, as illustrated in Fig. 3.6. As described in [33], in the regime where $\delta > \Gamma_{\text{sat}}$, the equilibrium rMOT temperature is

$$ T \propto \frac{\hbar \Gamma_{\text{sat}}}{2 k_B}. \tag{3.7} $$

Therefore the temperature is independent of detuning and proportional to $\sqrt{s}$. In addition to compressing the cloud, we also cool it by decreasing the laser intensity to approximately 40 μW. After compression, the broadband rMOT typically contains $\approx 1 \times 10^7$ atoms (depending on the loading time of the bMOT), at temperatures of about $1.5 - 2.5$ μK.

At this point, the rMOT is sufficiently compressed to be contained by a single fre-

---

[4]Though we were able to achieve transfer efficiencies of $\approx 40\%$ from the bMOT to the rMOT in the early days of the experiment when we were initially optimizing the rMOT, we believe that our current transfer efficiency is not as good and may be one of the factors limiting our achievable atom number. One way to improve this transfer efficiency would be to increase the optical power and size of the rMOT beams.
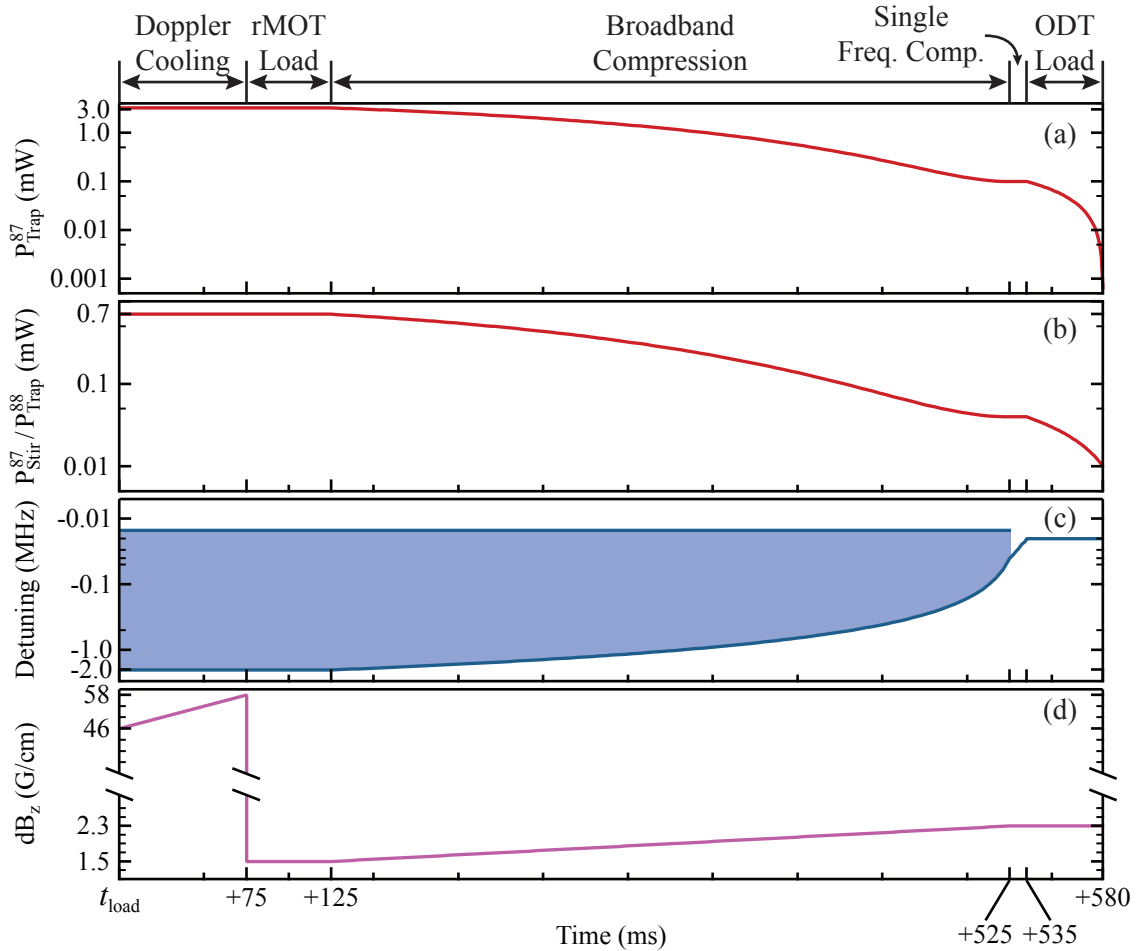
Figure 3.6: Optical power (a-b), detuning (c), and magnetic field gradient (d) ramps for rMOT operation. For the bosonic isotopes, only one laser is used with the optical power profile of P_{Trap}^{88}, see (b). The ^{87}Sr rMOT requires use two lasers. The power profile of the stirring laser, P_{Stir}^{87}, is also given in (b) while the profile of the trapping laser, P_{Trap}^{87}, is shown in (a). The rMOT is loaded from the compressed bMOT using the maximum available power and with a broadband detuning spanning nearly 2 MHz. After loading, the broadband rMOT is compressed over 400 ms by ramping down the laser power, increasing the field gradient from 1.5 to 2.3 G/cm, and decreasing the width of the detuning modulation. Next, we turn off the frequency modulation and compress the rMOT a little further by decreasing the detuning by 20 kHz for 10 ms. Finally, we further ramp down the laser powers while loading into the dipole trap.

quency tone and we switch from broadband to single frequency operation. The frequency modulation is switched off and the detuning is set at ≈ -40 kHz. The rMOT is further cooled and compressed for another 10 ms by ramping the detuning to ≈ -20 kHz. At this point the rMOT typically contains $\gtrsim 90\%$ of the atoms in the broadband rMOT at a temperature of about {1.0, 1.5, 0.6} μK for the {^{84}Sr, ^{86}Sr, ^{88}Sr} isotope and a typical phase space density of $\rho \gtrsim 10^{-2}$. The temperature of the ^{88}Sr rMOT is lower because of the extremely small scattering length for ^{88}Sr (see Table 1.2). For the final 45 ms of the rMOT, we further reduce the intensity of the laser to optimize loading into the dipole trap.

Another significant difference of the narrow line rMOT is that the maximum cooling force is only about 16$\times$ greater than the force of gravity. Therefore, gravity provides a strong perturbation to the MOT dynamics, as illustrated in Fig. 3.5(b). For large detunings, gravity tilts the MOT potential and changes the location of the potential minimum. The atoms tend to sag toward the point where the upward propagating cooling beam balances the force due to gravity and the rMOT takes on an oblate, pancake-like shape, as illustrated in Fig. 3.7. In addition, the vertical position of the rMOT varies with the laser detuning, which has important implications when transferring atoms from the rMOT to the dipole trap. In practice, we adjust the vertical position of the rMOT to match the vertical position of the dipole trap by slightly changing the magnitude of a constant magnetic field in the vertical direction.

3.4.2   Fermionic Red MOT

The hyperfine structure of ^{87}Sr also complicates the operation of the rMOT. Since the ground state has no electronic spin, its Zeeman shift is determined only by its nuclear magnetic moment and therefore has a small value of $\mu_g \approx 200$ Hz/G $\times m_F$ [57]. In contrast, the excited $^3P_1$, $F = 11/2$ state has a Zeeman shift sensitivity of $\mu_e = g_F \mu_B m_F \approx 380$ kHz/G $\times m_F$, which is almost 2,000 times larger. In order for a MOT to have a restoring force for all the spin sublevels, the position dependent Zeeman shift of
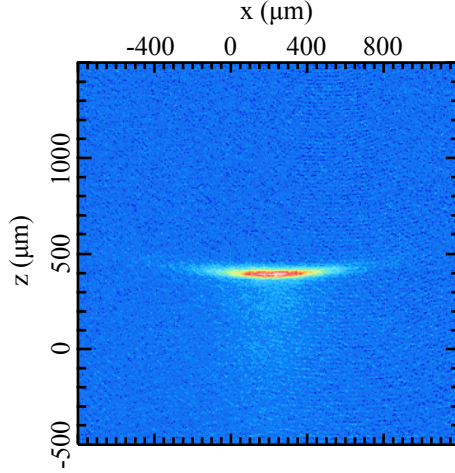
Figure 3.7: In-situ image of a ^{86}Sr rMOT sample at the end of the single frequency compression step. Due to gravity, the atoms sag to the bottom of the MOT ellipsoid and take on a pancake-like shape. To efficiently load these atoms into the dipole trap, we use pancake shaped dipole beams with an aspect ratio of about 10:1 to achieve good spatial overlap with the rMOT.

$\left[(m_F \pm 1)\mu_e - m_F\mu_g\right] dBz$ must have the same sign at a given position for all values of m_F. This condition is violated for ^{87}Sr, as is illustrated in Fig. 3.8(a). To elaborate on the problem, consider an atom in the $^1S_0$, $m_F = -9/2$ state. On the right side of the MOT, the atom could be excited to the excited $m_F = -11/2$ state by a σ^- photon, which would direct the atom back towards the center of the trap. However, at slightly larger distances, the atom will also be resonant with σ^+ light that would excite the atom to the excited $m_F = -7/2$ state. Unfortunately, the σ^+ beam is oriented such that it would push the atom out of the trap. Furthermore, if the atom is on the left side of the MOT it will not be resonant with either laser beam and it's residual momentum may carry it out of the trap.

However, as first demonstrated by [32], we can still achieve stable trapping in the ^{87}Sr rMOT by taking advantage of the relative line strengths of the various transitions. As shown in Fig. 3.8(b), the largest σ^+ (σ^-) Clebsch-Gordan coefficients are for transitions directed toward the excited magnetic sub-states with the largest (smallest) values of m_F. Consequently, on the left (right) side of the MOT, atoms are more likely to scatter σ^+ (σ^-) photons directed toward the center of the trap. Therefore, as long as the atomic population is continuously redistributed amongst all the Zeeman levels, the relative line

strengths yield a stable trapping force.

For transitions with larger linewidths, the trapping laser can provide both the confining force and optical pumping needed to rapidly randomize the magnetic state populations.[5] However, for the narrow $^1S_0 \rightarrow {}^3P_1$ transition, the linewidth Γ is less than the shift due to a single photon recoil kv_R, where v_R is the recoil velocity. Therefore the laser does not stay resonant for long enough to guarantee efficient optical pumping. To solve this issue, we use a second laser, which we call the "stirring" laser, that addresses the $F = 9/2 \rightarrow F = 9/2$ transition. The Landé g-factor for the stirring transition ($g_F = 2/33$, see Table 1.1) is 4.5× smaller than that of the $F = 9/2 \rightarrow F = 11/2$ transition. Therefore the atoms are resonant with the stirring laser over a larger volume, allowing for an efficient randomization of the magnetic state populations [32].

Our ^{87}Sr rMOT procedure is similar to that of the bosons described above and illustrated in Fig. 3.6. The main difference is that the laser used to trap the bosons is used for "stirring" on the $F = 9/2 \rightarrow F = 9/2$ transition, while we use a second 689-nm laser for trapping on the $F = 9/2 \rightarrow F = 11/2$ transition. The trapping laser initially has about 3 mW of power available, while the stirring laser starts with about 700 μW. The two lasers are combined using a fiber beamsplitter so that they counter-propagate along each rMOT axis with the same beam size and polarization. Both lasers have similar detuning and intensity ramp profiles. The ^{87}Sr rMOT has a typical temperature of about 1.5 μK and 1.0 μK after the broadband and single-frequency stages, respectively.

3.5 Optical Dipole Traps

Though we are able to achieve extremely low temperatures in the rMOT, we still need to increase the phase space density further in order to achieve quantum degeneracy. The MOTs that we used to achieve $T \approx 1$ μK have fundamental cooling limits due to the fact that they operate by continuously scattering photons. Our final cooling step is

---

[5]For example, this rapid randomization and trapping is provided by the 461-nm laser in the bMOT.
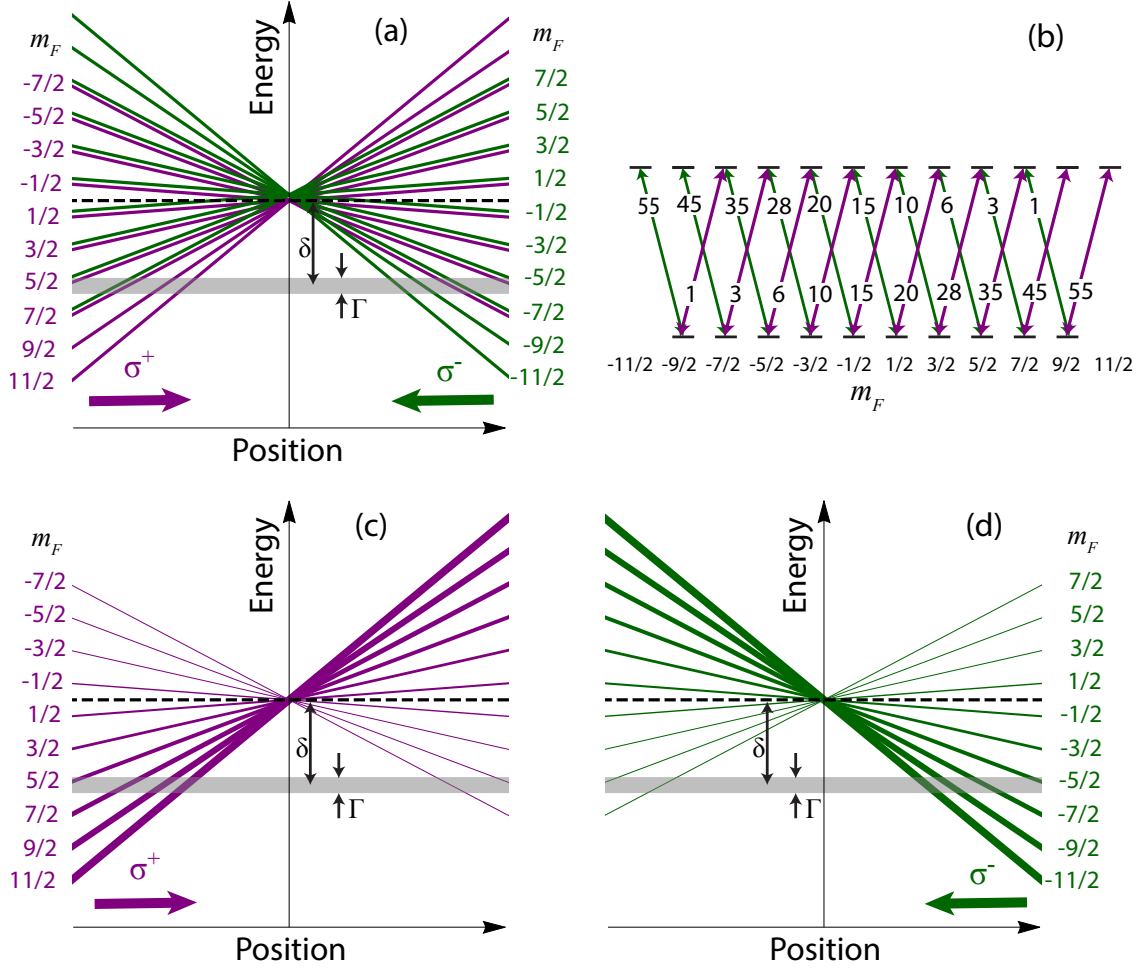
Figure 3.8: Fermionic rMOT Zeeman shifts. (a) Position dependent Zeeman shifts for σ^+ (purple) and σ^- (green) transitions. Due to the large mismatch between μ_e and μ_g, some of the slopes are negative and some are positive for each polarization. Therefore, the rMOT does not provide a confining force for all Zeeman sublevels. A small vertical shift has been introduced to the σ^- slopes for clarity. (b) The squared Clebsch-Gordan coefficients corresponding to the σ^+ and σ^- transitions of the $F = 9/2 \rightarrow F = 11/2$ manifold. The strongest σ^+ (σ^-) transitions are for the highest (lowest) m_F values. (c) and (d) show the same Zeeman shifts as in (a) for the σ^+ and σ^- transitions respectively. For (c) and (d) the thickness of the lines are proportional to the relative line strengths. Due to the various line strengths, the σ^+ (σ^-) beam will predominantly scatter more photons from the large (small) m_F states to the left (right) of the MOT center. Therefore, if we can rapidly randomize the atomic populations amongst all the Zeeman states, the Clebsch-Gordan coefficients will provide for stable operation of the rMOT. This state randomization is provided by a second laser operating on the $F = 9/2 \rightarrow F = 9/2$ transition.

performed in an optical dipole trap, which can have a very low photon scattering rate.

The trapping mechanism in dipole traps come from the interaction between an induced atomic dipole with the electric field of an intense, far-detuned laser beam. The potential at position $\mathbf{r}$ due to a dipole laser with intensity $I(\mathbf{r})$ and wavelength λ is given by [120]

$$V(\mathbf{r}) = \frac{-\mathrm{Re}\,[\alpha(\lambda)]\,I(\mathbf{r})}{2\epsilon_0 c}, \tag{3.8}$$

where $\alpha(\lambda)$ is the complex polarizability of an atom, ϵ_0 is the vacuum permittivity, and c is the speed of light. In addition, we also have a scattering rate of

$$\Gamma_{\mathrm{scat}}(\mathbf{r}) = \frac{\mathrm{Im}\,[\alpha(\lambda)]\,I(\mathbf{r})}{\hbar\epsilon_0 c}. \tag{3.9}$$

In the semi-classical picture, the atomic polarizability at the wavelength, λ is

$$\alpha(\lambda) = 6\pi\epsilon_0 c^3 \sum_j \frac{\Gamma_j/\omega_j^2}{\omega_j^2 - \omega^2 - i\Gamma_j(\omega^3/\omega_j^2)} \tag{3.10}$$

where the jth atomic transition has a natural decay rate Γ_j at frequency ω_j, and $\omega = 2\pi c/\lambda$.

If we simplify the expressions above by only considering the strongest atomic transition (two-level atom approximation) and also take the rotating-wave approximation, we find that $V \propto I/\delta$ and $\Gamma_{\mathrm{scat}} \propto I/\delta^2$, where $\delta = \omega - \omega_0$ is the detuning of the dipole beam relative to the atomic transition frequency, ω_0 [120]. These relationships illustrate two key characteristics of dipole traps. First, the sign of the interaction depends on the sign of δ. Therefore, red detuned traps are attractive whereas blue detuned traps are repulsive. Second, the scattering rate falls off more quickly than the potential as the magnitude of the detuning increases. This means that we can create traps with sufficient trap depths but low scattering rates and therefore low heating rates by operating at large intensities and large detunings.

The spatial profile of the dipole trap is determined by the laser's intensity profile.

For a trap consisting of a single beam propagating in $\hat{z}$, the confinement is determined by the transverse Gaussian $1/e^2$ waists, w_x and w_y and the Rayleigh range $z_R = \pi w^2/\lambda$. Since $z_R > w_{x,y}$, the intensity falls off much more slowly along the beam axis and the atoms are more weakly confined in that direction. We typically ensure tight trapping in all dimensions by crossing two or more dipole beams. As long as $k_B T$ is sufficiently small compared to the trap depth, we can Taylor expand the intensity profile near the focus of the beam(s) and express the trap as a harmonic oscillator potential

$$V(\mathbf{r}) \approx V_0 + \frac{1}{2}m\omega_x x^2 + \frac{1}{2}m\omega_y y^2 + \frac{1}{2}m\omega_z z^2, \tag{3.11}$$

where V_0 is the trap depth, m is the atomic mass, and ω_i is the trap frequency in the ith direction. Neglecting the effects of gravity, $V_0 \propto P$ and $\omega_{x,y,z} \propto \sqrt{P}$, where P is the power in the trapping beam.

For our beam sizes, available optical power, and wavelength $\lambda = 1064$ nm, the maximum scattering rate of our dipole trap is $\Gamma_{\text{scat}}/2\pi \lesssim 6 \times 10^{-3}$ s^{-1}. The corresponding heating rate is

$$\gamma_{\text{heat}} \leq 2E_r \Gamma_{\text{scat}} \lesssim 1 \text{ nK/s} \tag{3.12}$$

where E_r is the recoil energy of the trapping laser. This is sufficiently slow that in practice, we are limited by other heating mechanisms like pointing or intensity modulations of the trapping lasers.

Cooling in the ODT is accomplished by forced evaporation. To qualitatively understand how evaporation cools the atomic samples, let us assume that the gas has a Maxwell-Boltzmann energy distribution, $f_{MB}(E) \propto \exp\left[-E/k_B T\right]$, in a trap with a finite depth $V_0 \gg k_B T$. Due to the exponential tail of the Maxwell-Boltzmann distribution, an atom will occasionally gain enough energy such that $E > V_0$ and it will escape the trap. Since that lost atom carried more energy than the mean energy per particle, the average energy of the remaining particles is reduced and the atoms left in the trap will re-

thermalize at an overall lower temperature. Therefore, evaporative cooling trades overall atom number for lower temperatures [99, 105].

The evaporation rate depends on how quickly the atoms re-thermalize. We can estimate the elastic collision rate as $\gamma_{el} = n_0 \sigma_e \bar{v}_{rel}$ where n_0 is the peak density, σ_e is the elastic cross section, and $\bar{v}_{rel} = 4\sqrt{k_B T/\pi m}$ is the mean relative velocity. The atomic cross section can be estimated as $\sigma_e = 8\pi a_s^2$ for bosons and when the temperature is sufficiently low such that only s-wave collisions are relevant.[6] In this expression a_s is the atomic s-wave scattering length, see Table 1.2. The evaporation rate will then be given by [99]

$$\gamma_{evap} = \gamma_{el} \frac{V_0}{\sqrt{2}k_B T} e^{-V_0/k_B T}. \tag{3.13}$$

As the cooling progresses and the temperature of the cloud decreases, we must continuously turn down the trap depth so that the ratio of $V_0/k_B T$ doesn't get too large and slow down the evaporation. Evaporation in an ODT is complicated by the fact that as the trap depth is lowered the trap frequencies also decrease, which in turn reduces the peak density and γ_{el}.[7]

In order to increase the atoms' phase space density, the evaporation rate must be faster than the rate of other atomic loss mechanisms. For example, atoms knocked out of the trap due to collisions with background gas molecules lead to a one-body loss rate, γ_1. For our experiment, $\gamma_1 \simeq 0.1$ s^{-1}. There are also three-body recombination processes that lead to trap loss with a rate of $\gamma_3 \propto \sigma_e^2 n^2$. Since γ_{el} and γ_3 both depend on a_s and n_0, the evaporation of the various isotopes of strontium require different trap and evaporation parameters. I will go into specifics about the evaporation parameters used to make quantum degenerate gases of ^{84}Sr, ^{86}Sr, and ^{87}Sr in sections 3.6 and 3.7. We have not made ^{88}Sr BECs in our lab because it is not possible to directly evaporate that isotope

---

[6]For fermions, $\sigma_e = 4\pi a_s^2$ for particles in different spin states and approaches zero for fermions in the same spin state as the sample approaches Fermi degeneracy due to Pauli blocking.

[7]Independent control over the depth and trap frequencies of an ODT can be accomplished using a specialized technique of dynamically shaped traps [121].

Table 3.1: The Gaussian $1/e^2$ beam waists for the dipole trap beams. The waists are measured by fitting measured trap frequencies at various beam powers and the error is estimated to be $\simeq 10\%$ for most measurements. There are larger systematic errors for the cross pancake beam because it suffers from thermal effects in the optical setup and astigmatism.

Trapping Beam	Beam Waist		
	w_x	w_y	w_z
Main Pancake	228 μm	–	22.8 μm
Cross Pancake	–	270 μm	16 μm
Tight Vertical	72 μm	72 μm	–
Loose Vertical	230 μm	230 μm	–

due to its nearly vanishing scattering length (see Table 1.2).[8]

Our dipole trap consists of up to three intersecting beams at 1064 nm. The beam waists are summarized in Table 3.1. As illustrated in Fig. 3.7, the atoms are tightly compressed in the vertical direction but are spread out over a large area horizontally at the end of the rMOT sequence. We use two highly elliptical, pancake-shaped beams in the horizontal plane to provide good spatial overlap with the atom distribution in the rMOT. The primary beam, which we dub the "main pancake" beam, has a vertical waist of 22.8 μm and horizontal waist of 228 μm. The second horizontal beam, called the "cross pancake," intersects the main beam at 45° and has a vertical (horizontal) waist of 16 (270) μm. In order to increase confinement in the horizontal directions, we also have two different ODT beams oriented in the vertical direction. The "loose vertical" beam has a waist of about 230 μm and is used for ^{86}Sr, as discussed in Sec. 3.6.1. The "tight vertical" beam has a waist of about 72 μm and is used for all the other isotopes. Only one of the two vertical beams can be used at a time since they are sourced from the same beam arm (see Sec. 4.2.5 for more details). Each beam is individually intensity controlled and we perform evaporation by ramping down the powers and therefore overall depth of the dipole trap.

_____

[8]It is possible to make small BECs of ^{88}Sr via sympathetic cooling with other isotopes [115, 122].

3.6 Generating Bose-Einstein Condensates

3.6.1 ^{86}Sr BEC

The first isotope that we cooled to degeneracy was ^{86}Sr. Since ^{86}Sr has a large s-wave scattering length ($a_s = 823a_0$ [42]), achieving a BEC requires limiting the peak density of the gas to $\approx 10^{12}$ cm^{-3} in order to avoid excessive three-body recombination losses [115, 123, 124]. Our first ^{86}Sr BECs were generated in a trap consisting of the main pancake beam and the loose vertical beam. This combination of beams means that the sample is tightly confined in the vertical direction due to the small (≈ 23 μm) vertical waist of the main beam, allowing for fast evaporation and confinement against gravity. However, the sample is not tightly confined in the horizontal directions since the transverse waist of the main beam and the waist of the loose vertical beam are about 230 μm. This large volume trap is crucial to avoid the rapid loss of atoms due to three-body recombination. We transferred about 3×10^6 atoms into the dipole trap with $P_{\text{main}} = 3$ W and $P_{\text{vert}} = 10$ mW. Next, we held the atoms at a constant power for 100 ms, after which the samples had a temperature of ≈ 600 nK. Finally, we performed forced evaporation by exponentially ramping down the power in the main beam for 2.5 s with a time-constant of 1.0 s. During this ramp, we also linearly increased the power in the vertical beam to 75 mW to maintain sufficient horizontal confinement. The BEC starts to form after about 1.75 s of evaporation at a temperature of about 50 nK. After the full evaporation sequence, we have a nearly pure BEC with about 2×10^4 atoms and a chemical potential of $\mu/h \approx 300$ Hz.

We have more recently generated ^{86}Sr BECs in a slightly different trap consisting of the main and cross pancake beams instead of the vertical dipole trapping beam. We loaded the trap with $P_{\text{main}} = 1.6$ W and $P_{\text{cross}} = 0.8$ W. After holding for 100 ms our samples have about 3×10^6 atoms at $T \approx 900$ nK. Similar to the procedure described above, the evaporation sequence also consisted of an exponential ramp lasting for 2.5 s with a time-constant of 1.0 s for both beams. Examples of BECs using this procedure are
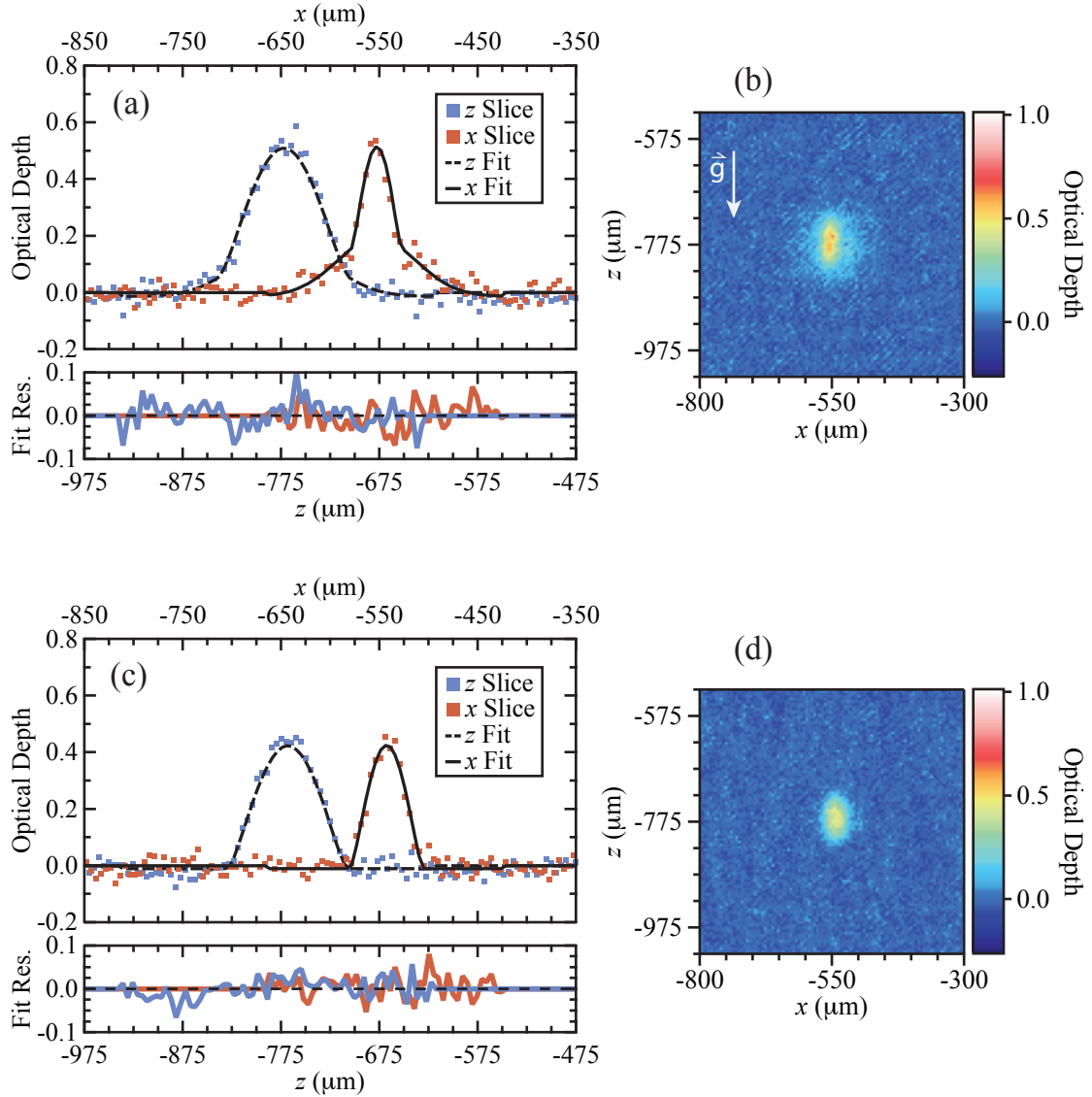
Figure 3.9: Bose-Einstein condensation of ^{86}Sr. Plots on the left show horizontal and vertical slices for the images on the right. These images were taken after a time-of-flight of 25 ms. (a) and (b) depict a partially condensed sample. The slices in figure (a) are fit using a sum of a thermal and BEC density profile resulting in a bimodal profile in the x direction. The thermal component has a temperature of about 30 nK. (c) and (d) depict a nearly pure BEC with $\simeq 1 \times 10^4$ atoms. Given the dipole trap beam waists, the in-situ BEC is much smaller vertically than horizontally. After the 25 ms time-of-flight these images show a clear inversion of the aspect ratio.

shown in Fig. 3.9. The bimodal density distribution in the top figures and the inversion of the aspect ratio are clear evidence of the formation of a BEC. We did not spend as much time optimizing the evaporation sequence for this trapping configuration, so our final BECs were a bit smaller with about 1×10^4 atoms.

3.6.2 ^{84}Sr BEC

Due to its convenient scattering length (a_s = 123a_0 [42]), ^{84}Sr was the first isotope to be cooled to degeneracy [125, 126]. The main challenge to working with ^{84}Sr is its low natural abundance of 0.58% (see Table 1.2). However, once the cooling steps described in Secs. 3.2, 3.3, and 3.4 are sufficiently optimized to load $\gtrsim 10^6$ atoms into the dipole trap, the moderate scattering length ensures rapid thermalization without excessive loss due to three-body recombination and evaporation is very efficient. We can make ^{84}Sr BECs using any combination of two (or more) of our main pancake, cross pancake, and tight vertical ODT beams.

Fig. 3.10 shows an example of a ^{84}Sr BEC created in our lab using the main and cross pancake beams. After loading the dipole trap at P_{main} = 1.8 W and P_{cross} = 0.8 W, the powers were snapped up to P_{main} = 3.2 W P_{cross} = 1.6 W to compress the cloud. We then performed forced evaporation by exponentially decreasing the powers in the dipole beams with a time constant of 1.0 s. After evaporating for about 2.4 s, the cloud contains about 9×10^5 atoms at 200 nK. As shown in Fig. 3.10a and Fig. 3.10b, the cloud is well described by a thermal atom distribution and appears isotropic after a long expansion time. After evaporating a little bit further, a BEC starts to form and the atom distribution becomes bimodal as it contains both thermal and condensed atoms. Finally, after evaporating for 3.3 s, we create a nearly pure BEC, as shown in the bottom plots of Fig. 3.10.

Due to the large optical depths in the center of these BEC images, technical noise, or "flat topping," contribute to systematic errors in the measured densities at the center of the sample. Therefore, measuring the total atom number using the amplitude of
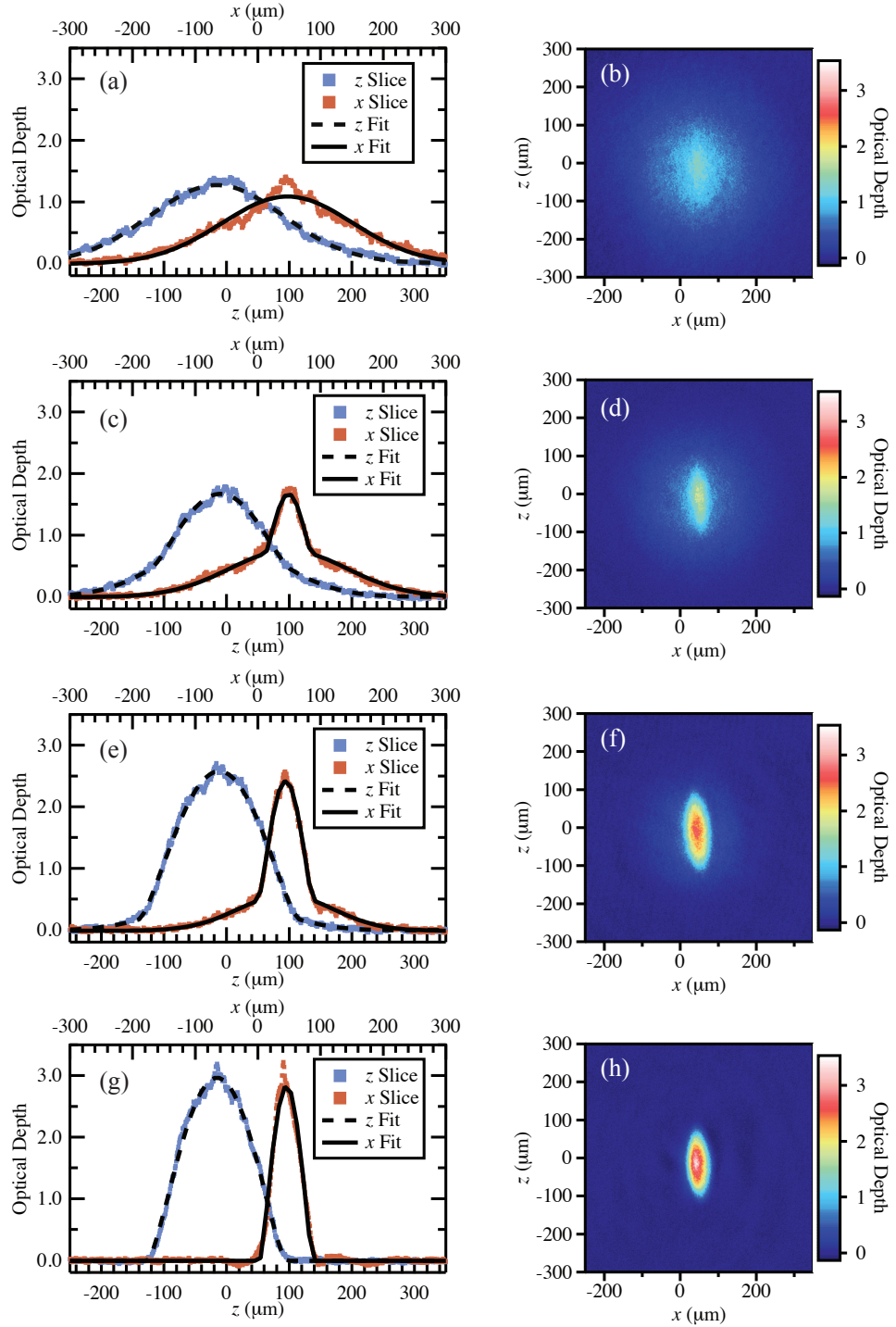
Figure 3.10: Bose-Einstein condensation of ^{84}Sr. Plots on the left show horizontal and vertical cross sections for the images on the right, taken after a time-of-flight of 25 ms. From top to bottom the evaporation sequence was truncated after 2.4 s, 2.7 s, 3.0 s, and 3.3 s. (a) and (b) depict a thermal sample just before condensation at a temperature of $\simeq 200$ nK. The slices in figure (a) are fit using a thermal density profile. (c-f) show bimodal samples with both thermal and BEC components. The slices in figures (c) and (e) are fit using a sum of a Gaussian and Thomas-Fermi profiles. (g) and (h) show a nearly pure BEC with $\simeq 1.3 \times 10^5$ atoms. The slices in (g) are fit with a Thomas-Fermi profile only. The thermal cloud in (b) is nearly isotropic while the BEC shows a clear inversion of the aspect ratio from its initial tight vertical confinement.

the Thomas-Fermi fit or integrating the total optical depth over the region of interest is likely to underestimate the actual atom number. We can obtain a better estimate for the atom number and chemical potential using the extracted Thomas-Fermi radii, as given by Eq. (2.27). In our experiment, we typically make ^{84}Sr BECs with a few times 10^5 atoms and $\mu/h \approx 1$ kHz. Though this atom number is perfectly sufficient for our purposes, ^{84}Sr BECs with atom numbers up to 10^7 have been demonstrated [115].

In addition to their other interesting attributes, BECs of ^{84}Sr are useful for a variety of calibration tasks. For instance, we often use BECs to measure dipole trap frequencies by observing center of mass or width oscillations (see Sec. 4.2.5.1). Though thermal clouds can also be used, BECs usually give cleaner results because their small size and large optical density make it easier to extract small changes in position or width. We have also used Kipitza-Dirac diffraction of ^{84}Sr BECs to measure optical lattice depths (see Sec. 4.2.5.2) and to calibrate the magnification of imaging systems.

3.7 Generating Degenerate Fermi Gases

For fermions, as the temperature approaches the quantum degenerate regime, the Pauli exclusion principle prohibits fermions in the same spin state from interacting via the s-wave collision channel [24]. Thus, the rate of elastic collisions will rapidly decrease making evaporative cooling increasingly difficult. Two techniques that are commonly used to overcome this challenge are sympathetic cooling of the fermionic isotope with a bosonic species [102, 115, 127, 128] or direct evaporation using elastic collisions of fermions in different spin states [101, 115, 129]. For ^{87}Sr, there are up to 10 spin states that can be populated, so the fraction of interactions that are forbidden as $T \to 0$ can be small. Since we have not yet attempted isotopic mixtures with our experiment, we choose to evaporate ^{87}Sr directly using all 10 spin states.

Our evaporation procedure is as follows. We first load about 9×10^6 atoms into the dipole trap with $P_{\text{main}} = 1.6$ W, $P_{\text{cross}} = 0.8$ W, and $P_{\text{vert}} = 0.1$ W. Next, the ODT

powers were adiabatically increased to $P_{\text{main}} = 3.2$ W, $P_{\text{cross}} = 1.6$ W, and $P_{\text{vert}} = 0.6$ W using a sinusoidal shaped ramp over 200 ms. We perform this ramp in order to compress the cloud and increase the elastic scattering rate [130]. Then, we perform evaporation by exponentially decreasing the power in the main and cross beams for 7.5 s using a time-constant of 2.5 s. After this first ramp, the sample approaches quantum degeneracy and the efficiency of the evaporation slows down. In order to continue cooling deeper into the degenerate regime, we perform a slower, second evaporation sequence for up to 3.9 s with a time constant of 5.5 s.

The resulting samples are imaged after a time-of-flight of 25 ms. We fit the clouds using Eq. (2.35) and extract the reduced temperature T/T_F from the fitted fugacity using Eq. (2.32). We supply starting points for the least-squares fitting routine by performing a preliminary fit using a 2D Gaussian function. The initial guess for the fugacity parameter, $\xi = e^{\mu/k_B T}$, is set to a conservative value of 1 to avoid biasing the fits to colder temperatures. Fig. 3.11 shows an example of a degenerate sample. The 2D image is shown in Fig. 3.11(c), while Figs. 3.11(a) and (b) show 1D slices and 2D residuals generated by fitting the image to a 2D thermal distribution of the form of Eq. (2.11). Figs. 3.11(d) and (e) show the corresponding fits to a 2D Fermi-Dirac distribution fit function of the form of Eq. (2.35). The thermal residuals exhibit a clear bullseye pattern, indicating that this form does not capture the shape of the cloud. The Fermi-Dirac fit successfully reproduces the density distribution and yields a fugacity of $\simeq 100$, corresponding to $T/T_F = 0.19$. Another method of visually comparing the two fitting methods is shown in Fig. 3.12. For this plot, we show the azimuthally averaged optical depth at a radius r and also display the corresponding average of the thermal (green) and Fermi-Dirac (purple) fits. Similar to Fig. 2.2, the results show that the thermal fit overestimates the optical depth at the center of the cloud and underestimates it at intermediate values of the radius.

We also performed a sanity check on the fitted fugacities by calculating the reduced temperature, T/T_F, directly. To do this, we measured the trap frequencies at the end
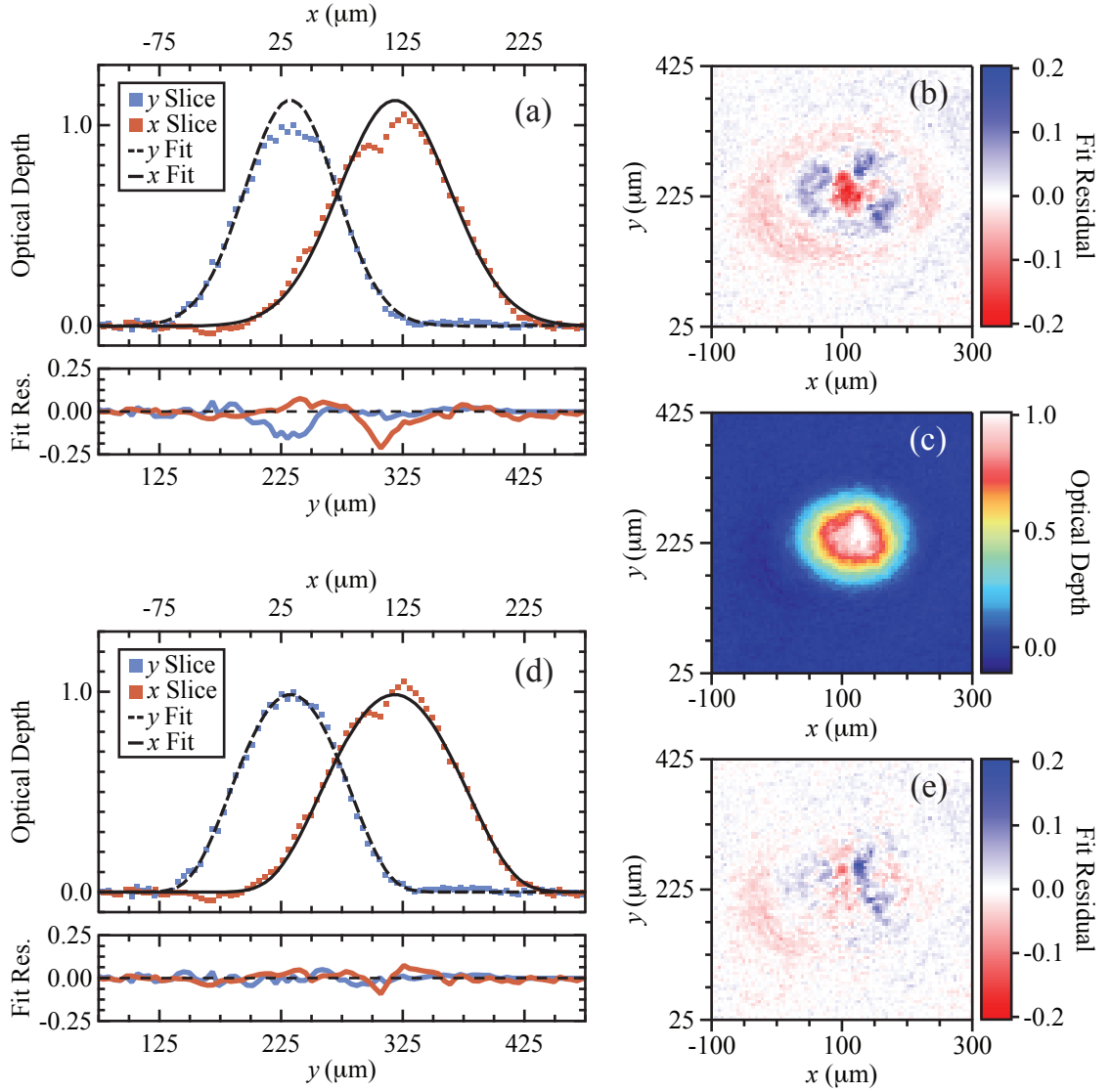
Figure 3.11: Degenerate Fermi-Gas of of ^{87}Sr. Figures (a) and (d) show 1D slices through the image depicted in (c). The image is captured from the vertical direction after a TOF of 25 ms. We attempt to fit the image using a 2D thermal distribution with the form of Eq. (2.11). The resulting cross sections of the thermal fit are shown in the top part of (a) and the fit residuals are shown in (b) and the bottom of (a). We also fit the image with a 2D Fermi-Dirac distribution. The corresponding results and residuals are shown in (d) and (e). The Gaussian fit overestimates the density at the center of the cloud and underestimates the density in the wings of the profile, indicating that it does not fully capture the correct shape. In contrast, residuals for the Fermi-Dirac fit have no structure, indicating that it is a better representation of the actual density profile. The fitted shape corresponds to $T/T_F = 0.19$. We confirm this measurement by extracting temperature from the Fermi-Dirac fit and calculating T_F according to Eq. (2.30)
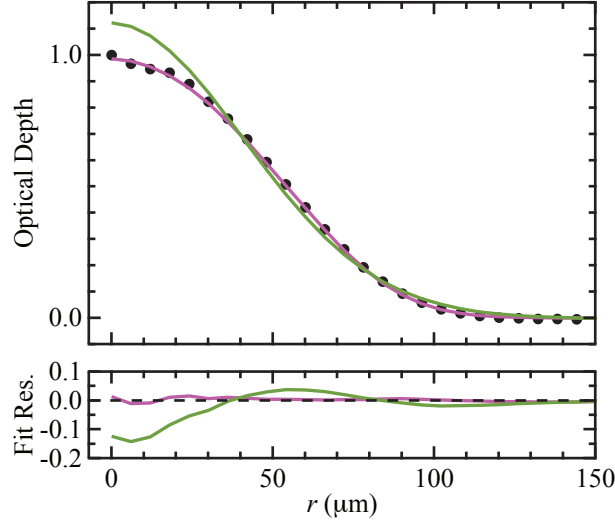
Figure 3.12: The radial profile of the same image detailed in Fig. 3.11 and corresponding thermal and DFG fits. The profile is created by azimuthally averaging all points at a distance r from the center of the cloud. The thermal Gaussian fit (green) does not reproduce the measured optical depth as well as the Fermi-Dirac (purple) fit.

of the second evaporation sequence by making a ^{84}Sr BEC in an identical trap and measuring oscillations in the center of mass and width to give $\omega_z = 2\pi \times 283(28)$ Hz, $\omega_x = 2\pi \times 9.8(1.0)$ Hz, and $\omega_y = 2\pi \times 20(2)$ Hz. For a detailed discussion of these trap frequency measurements, see [131]. Given the trap frequencies, we can use $k_B T_F = \hbar\bar{\omega}(6N/M)^{1/3}$, see Eq. (2.30), to calculate T_F for N, the number of atoms in a sample. In this calculation, we assume $M = 10$ and all ten spin states are evenly populated. We can also extract the temperature of the sample from the width of the cloud, giving us an independent measure of the degeneracy parameter. Since the expansion time of 25 ms is not large compared to $\omega_{x,y}^{-1}$, we used Eq. (2.12) to determine the temperature instead of the simpler form in Eq. (2.13). Fig. 3.13 shows T/T_F against evaporation time using both the fitted fugacity (blue circles) and direct calculation (red triangles). The two methods of determining the degeneracy parameter are in excellent agreement, confirming our results.

For this work we assumed that the 10 spin states were evenly populated. This is a good approximation, since the ^{87}Sr rMOT randomizes the spin state population (see Sec. 3.4.2) and, if the samples were heavily spin polarized, the reduced evaporation efficiency would make it very difficult to achieve such low temperatures. However,

subsequent efforts to optically pump the spin populations for other studies suggest that AC Stark shifts, induced by the dipole trap as we transfer the atoms from the rMOT, lead to slightly imbalanced spin state populations. Since we did not directly measure the spin state population for the data presented in this section, the reduced temperatures presented here have significant uncertainty. The various spin states should be in thermal equilibrium with each other, however, if they do not have the same number of atoms, each spin state will have a different Fermi temperature and therefore degeneracy parameter. The fitted fugacity samples the average degeneracy parameter of the entire cloud and therefore is an upper limit on the reduced temperature of the highest populated spin state. Similarly, the direct calculation of T_F assumes evenly populated spin states and therefore is also an upper limit on the T/T_F value for the highest populated state. In the future, we can ensure the spin populations are equal by slowly ramping the bias magnetic field, which sets the quantization axis, through zero during the evaporation sequence which effectively randomizes the atoms among the various spin states. This section demonstrates that we have produced degenerate gases of ^{87}Sr with $T/T_F \simeq 0.2$ and $T_F \simeq 55$ nK.
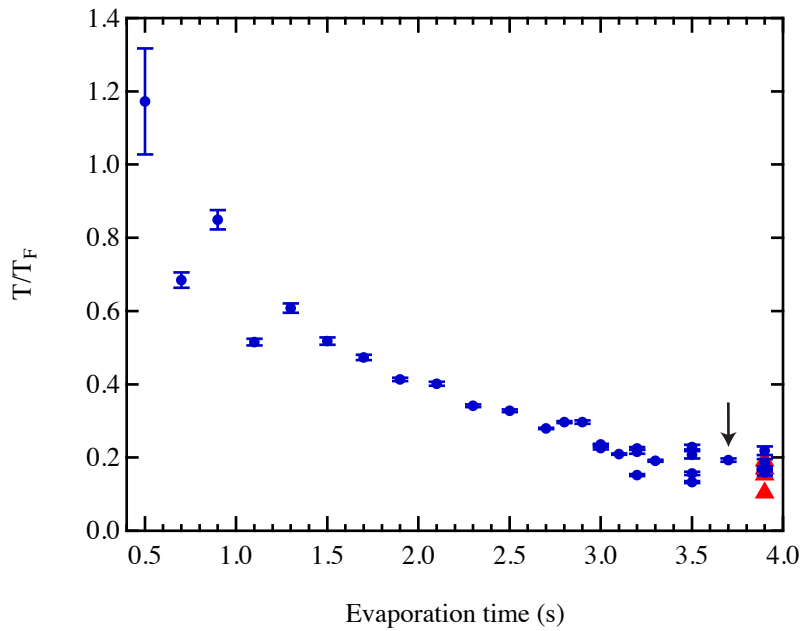
Figure 3.13: Evaporation Progression of the DFG Reduced Temperature. The blue circles show the degeneracy parameter, T/T_F, extracted from the fugacity of after fitting the images with Eq. (2.35) and are plotted against time during the second exponential evaporation step. The error bars show the statistical uncertainty in the fit. The data shows a clear progression to colder samples up until evaporation times of about 3.0 s. For the samples with an evaporation of 3.9 s, a direct calculation of T/T_F, shown in red triangles, agrees well with the fitted fugacity. The black arrow indicates the image shown in more detail in Figs. 3.11 and 3.12.

Chapter 4: Experimental Apparatus Details

In this chapter, I will describe the experimental apparatus that we use to generate degenerate gases of strontium. The optical traps that we use to confine our atomic samples have depths that are much less than the thermal energy of a particle at room temperature. Therefore, atoms will not remain in our traps after colliding with a background particle and it is very important to limit the rate of these collisions. As a result, cold atom experiments typically operate at "ultra-high vacuum" (UHV, $< 10^{-9}$ Torr) or similar environments. I will first discuss the vacuum system that we use to generate our atomic beam and also to achieve low pressures in the region used to trap the atoms. I will also discuss the various laser systems and magnetic field coils that we need to perform the various laser cooling steps described in Ch. 3. Finally, I will also describe the imaging systems we use to extract density profiles of our atomic clouds and the computer control systems that synchronize the timing of our cooling cycles.

4.1 Vacuum System

There are three main sections to our vacuum system, which is shown in Fig. 4.1. The highest pressures are found in the atomic source or oven section, which we heat to ≈ 600 °C in order to generate a hot beam of strontium. Next, we have an intermediate section, which we call the transverse cooling section where we apply a 2D optical molasses to cool the transverse velocity of the atomic beam. Finally, after the Zeeman slower, we have the main chamber vacuum section where we capture the atomic beam and cool the atomic samples down to quantum degeneracy. This section will describe these parts of
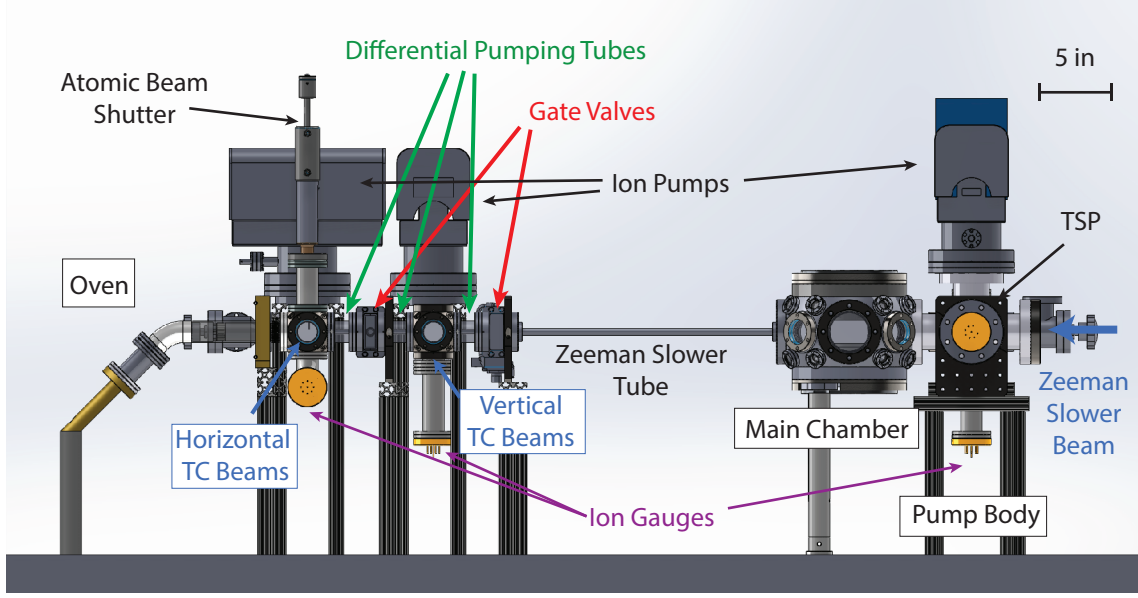
Figure 4.1: Side-view schematic of the vacuum chamber. Horizontal and vertical transverse cooling beams are applied at different locations (see 4.1.2). The relatively high pressures in the oven region are reduced by 3 differential pumping stages and we are able to achieve pressures of $\simeq 5 \times 10^{-11}$ Torr in the main chamber.

the vacuum system in more detail.

4.1.1   Atomic Source

The first step toward producing a sample of ultracold strontium is to generate a beam of hot atoms. I will first discuss some of the considerations that went into the design of the nozzle, which is crucial to collimating the atomic beam, and then I will describe the construction of the oven assembly.

4.1.1.1   Nozzle Design

The flux of atoms from a thin aperture source with area A into a solid angle $d\omega$ at angle θ from the aperture normal is [132]

$$dN = \frac{d\omega \, n\bar{v} A \cos\theta}{4\pi},$$

(4.1)

where $n = P/k_B T$ is the density particles on the source side of the aperture and $\bar{v} = \sqrt{8k_B T/\pi m}$ is the mean atomic velocity as given by the Maxwell-Boltzmann distribution. We can control the strontium vapor pressure, P, by varying the temperature, T, in the oven according to [133]

$$\log(P) = 14.232 - 8572/T - 1.1926 \log(T). \tag{4.2}$$

The large angular spread of the simple, cosine emitter means that most of the atomic flux will not be captured in our MOT. However, we can increase the fraction of atoms emitted on-axis by using a tube of length L and radius a where $L \gg a$ instead of a thin aperture. Let us first consider the collision-free regime, where the mean free path $\lambda_{\text{MFP}} = 1/(2^{1/2}\pi n\sigma^2)$ satisfies the condition that $\lambda_{\text{MFP}} \gg L, a$. In this expression, $\sigma = 0.498$ nm is the atomic diameter of strontium [134]. Under these conditions, a theoretical estimate for the angular half-width at half-maximum, $\theta_{1/2}$, is [135, 136]

$$\theta_{1/2} = 1.68a/L. \tag{4.3}$$

Therefore, the degree to which the atomic beam peaks on axis is directly related to the ratio of L/a and suggests that an efficient nozzle design should use a long, narrow aperture.

However, we cannot win simply by arbitrarily increasing the ratio L/a. In addition to practical considerations in the fabrication of tubes with extreme L/a ratios, as the cross section of the tube decreases, the total flux also decreases. In order to generate enough total flux, it is often necessary to increase the atomic density in the oven such that $a < \lambda_{\text{MFP}} < L$. In this, so called, opaque regime, it is no longer possible to ignore interatomic collisions in the nozzle. The details of the atomic collisions are complicated [135], but they have the effect of reducing the peaking factor relative to that of the same nozzle in the collision-free

regime. One estimate of the half-width in this regime is [136]

$$\theta_{1/2} \approx 4.74\sigma a\sqrt{n/L}, \tag{4.4}$$

which clearly broadens as the atomic flux $\dot{N}_{tot} \propto n$ increases.

In order to retain directionality without sacrificing total flux, arrays of multiple, narrow nozzles are commonly used [132]. This allows one to generate the necessary atomic flux without reducing the aspect ratio of the nozzles or increasing the density too far into the opaque regime. However, with a large number of nozzles, the half-width of the beam could be limited by difficulties in aligning all the nozzles to each other. Imperfect mutual alignment has been identified as a performance limiting factor in previous nozzle designs [137].

Our nozzle design consists of an array of 496 hypodermic needles clamped in place using a geometry that forces them to be parallel to each other. The general idea is based on [138] and it involves mounting the tubes in a precisely machined slot shaped like an equilateral triangle (see Fig. 4.2 inset). This geometry forces the circular tubes into a hexagonal packing arrangement which eliminates gaps due to dislocations and ensures their mutual alignment. In order to make a precise 60° corner without a radius from machining tools, the feature is fabricated using wire-cut electrical discharge machining (EDM). The hypodermic needles have an inner diameter of about 100 μm and a length of 15 mm for a large ratio $L/a = 300$. They are made from 304 stainless steel and were purchased from Microgroup.[1] The tubes are clamped into their triangular groove by wedge, also precisely machined, and secured by 4 bolt-nut pairs.

Though we have not directly measured the performance of the oven, the expected total flux is [136]

$$\dot{N}_{\text{tot}} = \frac{2\pi}{3}\frac{n\bar{v}a^3}{L}N_{\text{tubes}} \approx 9 \times 10^{15} \text{ s}^{-1} \tag{4.5}$$

---

[1]Note that it is important to use a burr-free method of machining when cutting the tubes to the desired length. Microgroup cut ours using EDM.
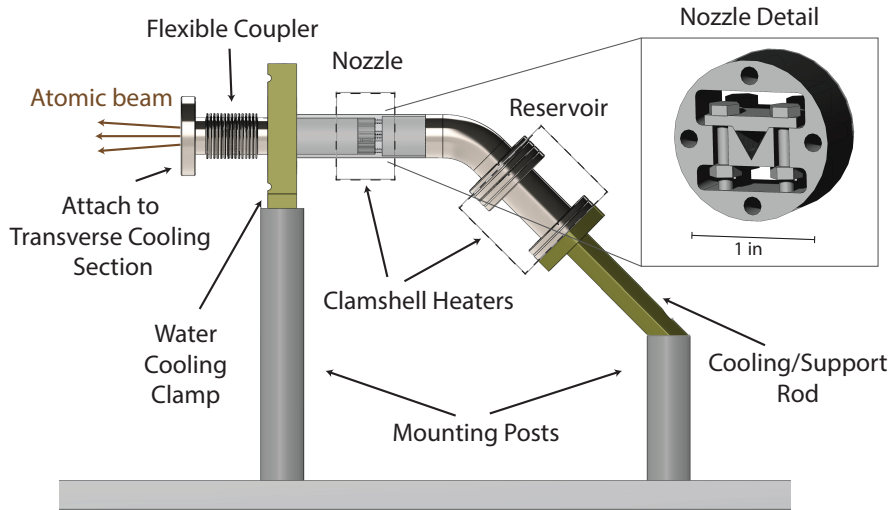
Figure 4.2: Side-view schematic of the oven. The reservoir, containing 10 g of strontium, is separated from the nozzle section by a 45° bend. Two clamshell heaters heat the reservoir and nozzle sections to 600 and 675 °C, respectively. The nozzle itself consists of 496 hypodermic needles with an inner diameter of 100 μm clamped in a triangular pattern. The equilateral triangle geometry of the clamping region ensures tight packing and therefore mutual alignment of the individual tubes. The nozzle section is connected to the rest of the chamber via a flexible coupler to allow for adjustments to the alignment of the atomic beam. We water cool the Conflat (CF) connection between the nozzle and the flexible coupler to prevent it from getting too hot. The reservoir is supported via a cooling rod and mounting post. A water-cooled block (not shown) can be clamped onto the cooling rod at the end of a day in order to reduce the time it takes for the oven to cool from the operating to idling temperature. We found it helpful to add insulation between the cooling rod and the mounting post in order to maintain high temperatures when operating. Not shown: thermocouples used to maintain constant temperatures and many layers of moldable ceramic insulation.

at an operating temperature of 650 °C. At this temperature, we should be in the opaque regime and the estimated angular width is $\theta_{1/2} \approx 2.5°$. If we were able to operate in the transparent regime, our half angle would be reduced by about a factor of 10.

4.1.1.2   Oven Design

The oven consists of a reservoir and nozzle section separated by a 45° elbow (see Fig. 4.2). The reservoir contains about 10 g of solid strontium which should be enough for several years of operation. We heat the nozzle and reservoir regions using two pairs of clamshell heaters (Mellen Company Inc. 11C-2403.5-TC and 11C-1302-TC) that are clamped around the outside of the vacuum components. The temperatures of the two regions are monitored by high temperature thermocouples (OMEGA XC-24-K-12) and

stabilized using a commercial proportional-integral-derivative (PID) controller (OMEGA CNi16D44-EIT) which regulates the power supply of the heaters via solid state relays (OMEGA SSRL240DC25). We typically operate the nozzle at 650-675 °C and the reservoir at 600 °C. The reservoir is rigidly supported by a support rod and mounting post. A water-cooled block can be clamped onto the cooling rod to help the reservoir cool down faster at the end of the day. There are several layers of insulation between the cooling rod and the mounting post to help the reservoir maintain its operating temperature when running. The nozzle and reservoir sections are insulated with many layers of moldable ceramic sheets (Cotronics #372-2). The oven is connected to the rest of the vacuum system via a flexible coupler, which allows us to tweak the alignment of the atomic beam with respect to the Zeeman slower and bMOT in order to optimize loading rates. The CF connection closest to the nozzle is water-cooled to prevent the rest of the vacuum chamber from getting too hot.[2]

The atomic beam can be blocked using a pneumatic atomic beam shutter (MDC 662006, see Fig. 4.1) mounted just after the oven. We block the beam at all times except for bMOT loading to avoid collisions between our cold samples and the hot atomic beam and also to minimize coating our Zeeman slower viewport with strontium. The pressure immediately outside of the oven is maintained by a 75 L/s ion pump[3] (Gamma Vacuum 75S-CVX-6S-SC-220-N) and monitored by and ion gauge (Varian UHV-24). Operating pressures are typically $\simeq 7 \times 10^{-9}$ Torr when the oven is operational and $\simeq 3 \times 10^{-10}$ Torr when in standby mode.

---

[2]Cooling this connection is also important if you ever want to be able to remove and replace the oven.

[3]Our current oven design replaced a similar one in December 2015. The original nozzle design was constructed with a vacuum-compatible epoxy. We believe that the epoxy, when exposed to the extreme temperatures of our oven, outgassed some material that slowly poisoned this vacuum pump. We had to replace it twice prior to upgrading the oven.

4.1.2   Transverse Cooling Section

The transverse cooling section of our vacuum chamber immediately follows the oven. As described in Sec. 3.2, the addition of an optical molasses to cool the transverse velocity of the atomic beam increases atom number in the bMOT by about a factor of 3. Originally, we applied cooling beams both horizontally and vertically on the same six-way cross, which is about 35 cm from the nozzle. However, when trying to brainstorm ways to increase atomic flux to our main chamber, we realized that it would be better to apply the transverse cooling as close as possible to the nozzle before the atomic beam has spread out as far. Unfortunately, given the location of the atomic beam shutter and the orientation of our ion pumps, we could not easily move both cooling axes to the six-way cross immediately after the oven. We settled for only moving the horizontal cooling beams closer and leaving the vertical beams in their original position, which slightly improved atom number ($\simeq 15\%$).

There is a second ion pump for the transverse cooling section which helps maintain a pressure of about 2×10^{-10} Torr when the oven is hot. In the vicinity of the transverse cooling stage, a series of three differential pumping tubes, each with a diameter of 0.25 inches and length of 3 inches, separate the comparatively high pressures immediately after the oven from the main chamber. We have also installed a pneumatic gate valve immediately after the transverse cooling stage that automatically closes in the event of a power failure to help protect the vacuum quality in the main chamber.

4.1.3   Main Chamber and Pump Body

We capture and cool our atomic samples in the main chamber. Thus the most important considerations for this section of the vacuum system are to maintain a very low pressure to maximize trap lifetimes and to provide good optical access for our many laser beams. The main chamber is connected via a six-way pump body to a 75 L/s ion

pump, ion gauge (Varian UHV-24P), residual gas analyzer (MKS Instruments e-Vision2), and titanium sublimation pump (TSP, VGScienta ST22). The TSP was very helpful in reducing the pressure from $\simeq 1 \times 10^{-10}$ Torr after baking to the current operating pressure of about $\simeq 5 \times 10^{-11}$ Torr. The differential pumping stages provide adequate isolation between the main chamber and the oven so that there is no measurable change to the pressure near the main chamber when the oven is turned on.

The pump body also houses the viewport used to launch the Zeeman slower beam. This viewport is heated to 150 °C in order to slow the rate that strontium from the atomic beam coats it. This heater is turned off after loading the bMOT so that magnetic fields from the AC power supply do not interfere with our experimental cycles. We have also chosen to use sapphire for this viewport because of its enhanced resistance to many corrosive materials compared to standard glasses. After upgrading our oven in December 2015, we observed a gradual decline in atom number performance over the course of many months. After observing that we could recover some atom number by diverting blue laser power from the transverse cooling and MOT arms to the Zeeman slower arm, we concluded that the new oven had an increased atomic flux and was coating the slower window much faster. We switched from operating with the atom beam shutter almost always open to closing it except for when loading the bMOT, which has slowed the coating rate significantly. We also added an injection locked 461-nm laser in order to maximize the power in the Zeeman slower beam (see Sec. 4.2.1).

The main chamber is a Kimball Physics spherical octagon. Custom recessed viewports were installed at the top and bottom of the chamber that allow for the installation of magnetic coils close to the location of the atoms and increase the numerical aperture of the vertical imaging system.[4] The viewports are anti-reflection (AR) coated for 461 nm and 689 nm plus broadband near-IR (Spectrum Thin Films). The 2.75 and 4.5 inch view-

---

[4]Due to a communication error, the recessed viewports were manufactured in such a way that they block optical access from the 1.33 inch flanges. This is one of the many mistakes that has been fixed in the upgraded strontium experiment.

ports are mounted with custom designed washers that allow Thorlabs cage systems to be attached directly to the chamber.

4.2   Laser Systems

The process of capturing and cooling alkaline-earth elements is complicated and requires a variety of laser systems. Our lab currently uses over 10 individual lasers and we have plans for more. The 461-nm lasers address the broad ($\Gamma/2\pi$ = 30.5 MHz) $^1S_0 \rightarrow {}^1P_1$ transition for the transverse cooling, Zeeman slower, bMOT, and imaging probes. The slow leak out of the bMOT necessitates several repump lasers to depopulate the $^3P_2$ and $^3P_0$ states. Since the bMOT is Doppler limited to $\approx$mK temperatures, we need several lasers at 689-nm to further cool the atoms in the rMOT using the narrow ($\Gamma/2\pi$ = 7.4 kHz) $^1S_0 \rightarrow {}^3P_1$ line. We also have several 689-nm slave lasers for further atomic manipulation, such as photoassociation and spin state pumping and readout. In addition, we are in the process of building a clock laser to address the extremely narrow ($\Gamma/2\pi \approx$ mHz) $^1S_0 \rightarrow {}^3P_0$ line. Finally, we use a high power 1064-nm laser for dipole traps and optical lattices. In this section, I will describe these various laser systems.

4.2.1   461-nm Lasers

In order to generate enough optical power and easily switch between isotopes, we use three different lasers at 461 nm. The master laser is locked to a ^{88}Sr $^1S_0 \rightarrow {}^1P_1$ spectroscopy signal to provide an absolute frequency reference. We use a beatnote lock to reference a Toptica TA-SHG pro laser system to this master. The TA-SHG system provides most of the optical power needed. However, since our Zeeman slower viewport is partially coated with strontium, we have also added a second slave that is injection locked in order to increase the power in the Zeeman slower arm.

The 461-nm master laser (see Fig. 4.3) is a Toptica DL pro HP that generates
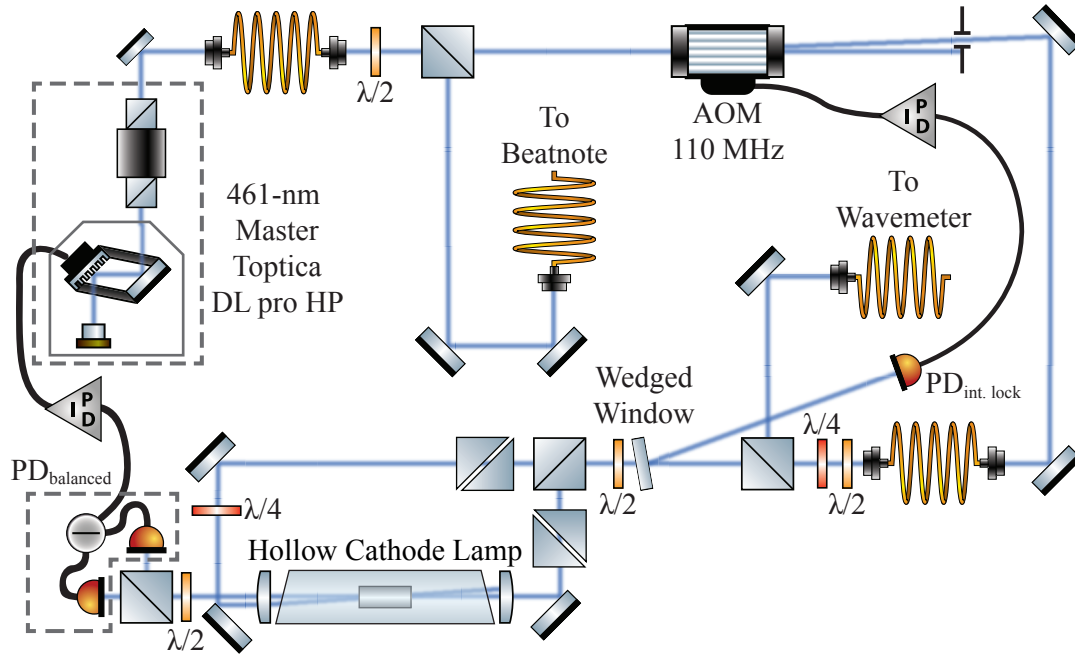
Figure 4.3: Schematic of the 461-nm master laser and spectroscopy lock.

≈ 60 mW of light, of which only about 13 mW are used for locking. In the past we have also used a home-built laser consisting of a Littman-Metcalf external cavity mount and a AR coated diode (Nichia NDBA116T) as the master.[5] The master light is split into two arms; one for a spectroscopy lock and the other for a beatnote lock with the TA-SHG system.

Approximately 350 μW is delivered to the spectroscopy portion of the setup via a single mode fiber. A small portion of the light is picked off to be monitored on a wavemeter (High Finesse WS7). The beam is then split into a weak probe and stronger pump beam by a polarizing beam splitter (PBS). The two beams counterpropagate through a strontium vapor created in a hollow cathode lamp (Hamamatsu L2783-38NE-SR).[6]

---

[5]We switched because long term drift in cavity alignment or diode aging made it increasingly difficult to generate enough laser power at the necessary wavelength.

[6]The hollow cathode lamp consists of two electrodes containing strontium and a buffer gas. When a large voltage is applied to the electrodes, electrons are emitted from the cathode and travel toward the anode. In the process, the electrons collide with the buffer gas and produce ions. The ions are accelerated toward the cathode and collide with enough kinetic energy to sputter individual strontium atoms creating a dilute strontium vapor [139]. Unfortunately, Hamamatsu has discontinued their line of see through lamps, but similar lamps may be available from Photron Pty. Ltd.

The error signal is generated using a polarization rotation technique [140]. The pump is converted to circular polarization which differentially saturates the σ^+ and σ^- components of the $^1S_0 \rightarrow {}^1P_1$ transition depending on the laser detuning. This anisotropic saturation causes a birefringence that rotates the polarization of the linearly polarized probe beam. We measure this rotation of the probe polarization using a polarimiter consisting of a PBS and balanced photodiode (PD). We always lock to the ^{88}Sr feature because of the much larger natural abundance of ^{88}Sr compared to all of the other isotopes. We lock the master laser to this spectroscopy signal using a proportional-integral lock circuit[7] feeding back to the laser cavity's piezo.

Though the linewidth of the 461-nm transition is 30.5 MHz, we find that we are sensitive to drifts of the blue lasers on the order of several MHz. Therefore, we took a number of precautions to improve the stability of the spectroscopy error signal. Like most of our lasers, the spectroscopy setup is shielded from air currents by putting the whole setup in a box. We minimize shifts due to laser intensity fluctuations by stabilizing optical power through active feedback to an acousto-optic modulator (AOM). We also found that it was important to use Glan-Laser polarizers to ensure clean polarizations of the probe and pump beams. Finally, in order to mitigate Zeeman shifts due to stray magnetic fields, we installed several pieces of MuMetal around the hollow cathode lamps. These precautions allowed us to achieve a lock stability of $\approx$ 1 MHz or better over the timescale of several hours. We check for longer term drifts to the lockpoint daily, but corrections are rarely needed.

The other arm of the master laser goes to a 50/50 single mode fiber beamsplitter (Thorlabs FC488-50B-APC) where it is combined with light from the Toptica TA-SHG pro slave laser. The beatnote corresponding to the frequency difference between the two lasers is measured using a fast photodiode (Thorlabs DET02AFC, bandwidth = 1 GHz).

---

[7]The circuit that is used for this, and many of our other locks, was designed by J. Tiamsuphat with contributions from A. Restelli and N. Pisenti. See https://github.com/JQIamo/analog-pi for details.

The offset of the two lasers is compared to an external frequency source using an optical phase-locked-loop (OPLL) circuit based on [141]. The OPLL signal is used to lock the slave laser frequency relative to the master. We select the lockpoint such that the TA-SHG laser is 205 MHz to the red of the $^1S_0 \rightarrow {}^1P_0$ transition. This beatnote lock is extremely flexible, as we can easily switch between various setpoints to, for instance, change between the different isotopes of strontium.

Since the fast feedback paths of the TA-SHG laser are used to lock the master oscillator to the doubling cavity, the only feedback path available is to the piezo of the master oscillator. In order to make the lock stable, we found it necessary to low-pass filter the feedback signal at ≈ 1 Hz. As a result, the two lasers are not phase locked and the beatnote lock only provides low bandwidth frequency stability. Nevertheless, this is sufficient for our needs because high frequency noise in the TA-SHG laser is suppressed by locking to the doubling cavity. At the moment, the limited bandwidth and dynamic range of the beatnote lock feedback preclude us from switching between the various isotopes during an experimental cycle. However, it should be easy to implement a feed-forward circuit to get around this limitation if it ever becomes necessary.

The details of the 461-nm slave lasers are shown in Fig. 4.4. The Toptical TA-SHG Pro generates about 500 mW of optical power which is divided into a variety of different arms. A low power arm transmits through the first beam cube after the laser. After an AOM operating at 211 MHz (IntraAction ATM-3001A1), we couple the unshifted light into a fiber for the beatnote lock described above. The shifted light is used as an imaging probe beam. We use a manual flipper mirror to switch between imaging using the low-magnification horizontal imaging axis ("Flea Imaging") and the high magnification vertical imaging axis ("PIXIS Imaging," see Sec. 4.3.1).

The majority of the optical power reflects from the first PBS and is divided into three different arms for the Zeeman slower, bMOT, and transverse cooling. Two pairs of waveplates and PBS cubes balance the relative power in these three arms. The Zeeman
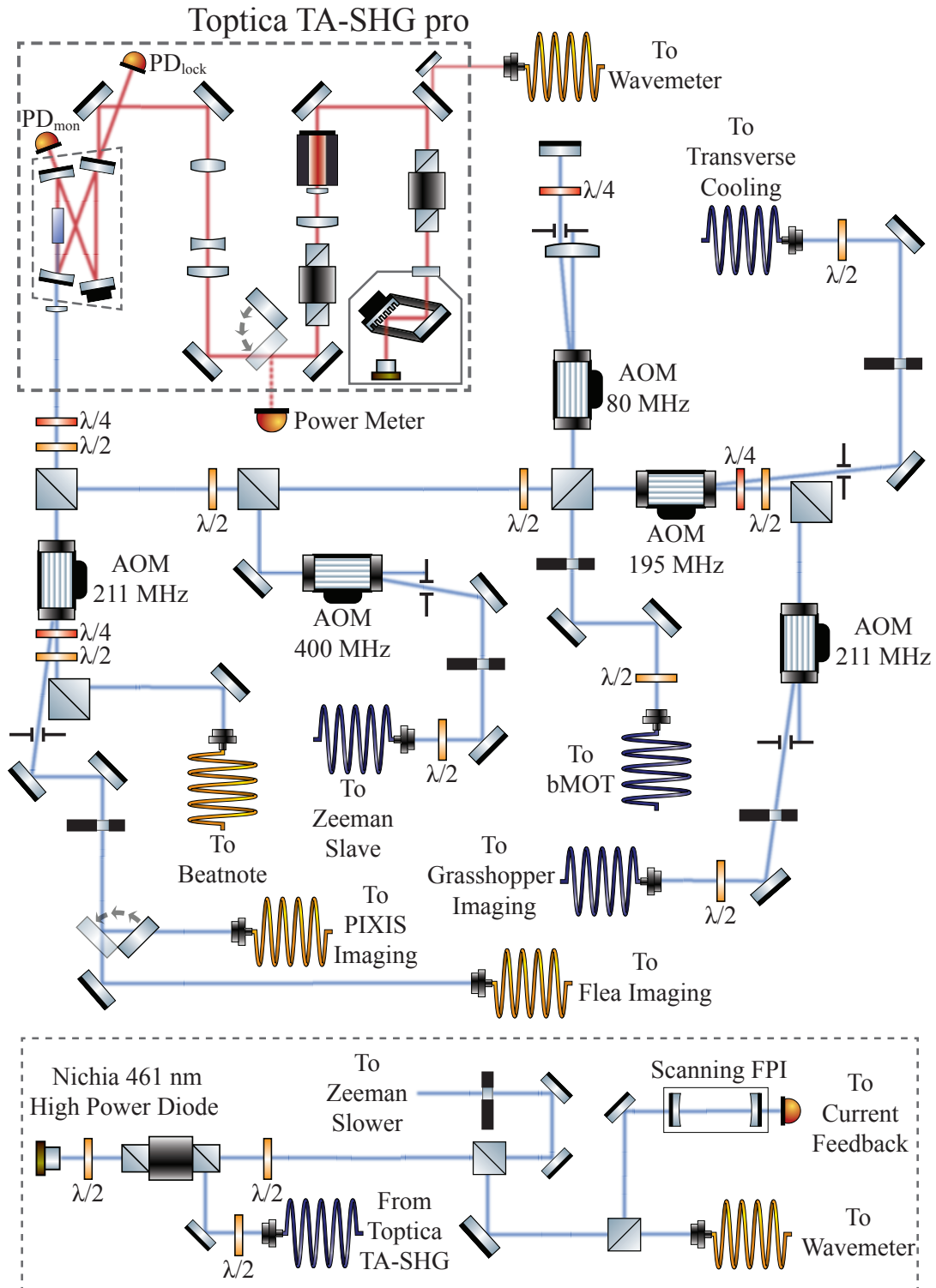
Figure 4.4: Schematic of the 461-nm slave lasers. The Toptica TA-SHG pro is beatnote locked to the 461-nm master laser and generates ≈ 500 mW of power that is split into a variety of different arms for imaging, transverse cooling, cooling the bMOT, and seeding the Zeeman slower slave laser. The Zeeman slower laser, shown on the bottom of the figure, is injection locked using light from that TA-SHG and provides about 60 mW of light for cooling. Most beam shaping optics are omitted for clarity.

slower light is shifted by 400 MHz by an AOM (Brimrose TEM-400-100-461) to a total detuning of -605 MHz and coupled into a single-mode polarization maintaining (PM) fiber. This fiber delivers $\lesssim$ 10 mW of power to injection lock a secondary slave laser, described below.

Light for the bMOT is double-passed through an 80 MHz AOM (IntraActionATM-801A1) and coupled into a custom 1×3 fiber splitter (Evanescent Optics). Each of the 3 outputs of the fiber splitter are used to launch an axis of the bMOT. Each MOT axis is expanded to a $1/e^2$ waist of 8 mm and typically contain $\approx$ 11 mW of power before entering the main chamber. We intensity lock the optical power in the MOT arms in order to compress the bMOT by ramping down the bMOT laser intensity after loading.

The third arm is used for transverse cooling. The light is blue shifted by 195 MHz (Brimrose TEM-200-50-461) to a final detuning of -10 MHz and delivered to the experiment using a single-mode PM fiber. After the fiber, $\approx$ 25 mW of power is split into two arms for cooling the atomic beam in the horizontal and vertical directions separately. The beams are expanded using a cylindrical telescope to a $1/e^2$ waist of 9 mm × 3 mm where the long axis of the beam is parallel to the atomic beam to maximize the cooling region. The unshifted light from the transverse cooling AOM is sent through another AOM at 211 MHz (IntraAction ATM-2001A1) and used as the probe light for the high-magnification horizontal imaging ("Grasshopper Imaging") system.

In order to increase the amount of power available for the Zeeman slower, we injection lock a secondary slave laser consisting of a high power 461-nm diode (Nichia NDB4216E, see bottom of Fig. 4.4). We inject $\lesssim$ 10 mW from the Toptica TA-SHG using the rejection port of an optical isolator (Thorlabs IO-5-461-HP). The injection lock is only stable for a narrow range of applied diode currents. Furthermore, the stable region drifts over time and with small changes in the temperature of the diode. In order to stabilize the lock, we use a custom, Arduino based circuit[8] inspired by [142]. The mode of the laser

---

[8]The Arduino circuit was built and programmed by N. Pisenti. More details can be found at `https:`

is monitored on a scanning Fabry-Pérot Interferometer (FPI, Thorlabs model SA200-3B). When the laser is in the process of unlocking, the amount of light in the desired optical mode declines and we can observe the heights of the Fabry-Pérot peaks decrease. The Arduino circuit monitors the these peak heights and adjusts the diode current in order to keep them above a tunable threshold. To avoid fiber coupling losses, the output of this laser is aligned over free space to the experiment. The Zeeman slower beam has $\simeq 60$ mW before entering the chamber, though it is attenuated by an unknown amount due to the strontium coating on the viewport. The beam has a $1/e^2$ waist of 6 mm as it enters the chamber and is slightly converging in order to focus onto the oven nozzle.

4.2.2 Repump Lasers

As described in Sec. 3.3.2, there is a slow leak in the bMOT that leads to atoms populating the metastable $^3P_2$ state. We repump out of this state using the $^3P_2 \rightarrow {}^3S_1$ transition at 707 nm. Since some atoms decay from the $^3S_1$ level to the $^3P_0$ state, which is also metastable, we use an additional laser at 679 nm to repump that state as well. The linewidths of these transitions are relatively broad, $\Gamma/2\pi \approx 7\,(1.4)$ MHz for the 707 (679)-nm transition, so we don't need a fast bandwidth lock to stabilize these lasers. Instead, we rely on a slow feedback method using our wavemeter.

For all of our lasers, including these repumps, we fiber couple a small amount of light from the laser into a 16×1 fiber switch (Laser Components USA, Inc.). The output of the fiber switch goes to our wavemeter (HighFinesse WS7) which has a specified resolution of 10 MHz but, in our experience, can distinguish frequency drifts of about 1 MHz. I wrote a custom Labview program that monitors the frequencies of multiple lasers by continuously cycling through the desired channels on the fiber switch with a switching speed on the order of 100 ms. For the lasers that we lock using this method, the software compares the measured frequencies to some user-specified setpoints and generates analog feedback

---

`//github.com/JQIamo/injection-ffwd`.
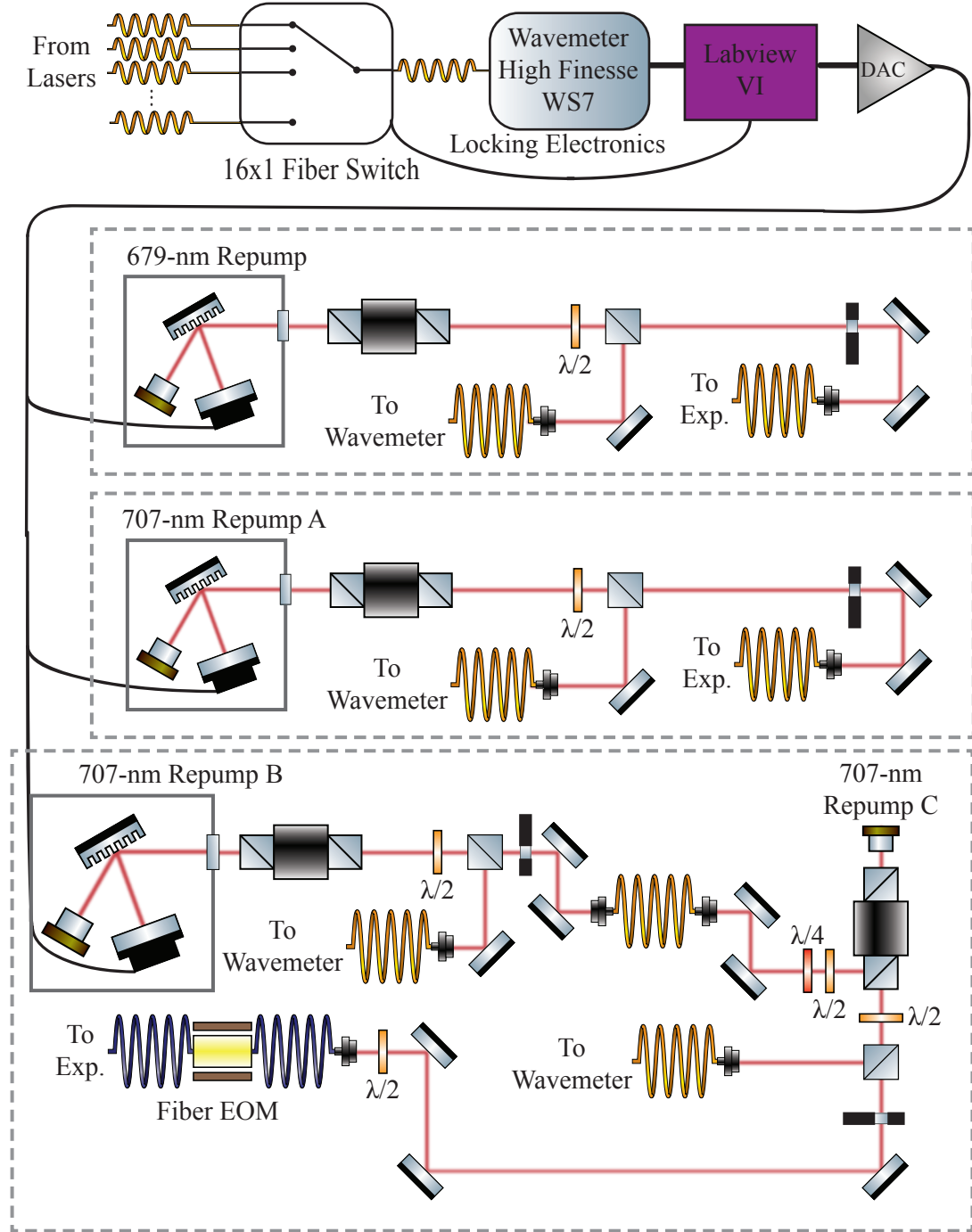
Figure 4.5: Schematic of repump lasers. The 688-nm depumping laser used in chapter 5 is not shown, but its setup is similar to that of the 679-nm repump or 707-nm repump A. The wavelength of the 679-nm laser as well as 707-nm repumps A and B are stabilized within 5 MHz by slow feedback from a wavemeter. Since the fiber EOM has a large injection loss, the amount of 707-nm power used to repump [87]Sr is increased by injection locking a non-AR coated diode.

signals via a multi-channel digital-to-analog converter (DAC),[9] which are routed to the laser cavity piezo to stabilize long term frequency drifts. We use this wavemeter lock to stabilize our repump lasers to within $\lesssim 5$ MHz, which is much less than the sensitivity of the bMOT to repump drift.

Three of the repump lasers use a very similar design (see Fig. 4.5). The 679-nm repump and 707-nm repumps A and B are all homebuilt external cavity diode lasers (ECDLs) using a Littman-Metcalf mount based on a JILA design. The 707-nm diodes are commercial AR coated diodes (Toptica LD-0705-0040-AR-1), while the 679-nm diode is an Opnext HL6738MG diode that we AR coated ourselves using the UMD fabrication facility. In the past we have also used a non-AR coated diode (similar to SDL7311) for the 679-nm repump, but the AR coated diode is much more stable and easier to tune to the right mode. We do not need precise timing control of the repump lasers, so we turn on/off these beams using SRS optical shutters. The 679-nm and 707-nm repump A both provide ≈ 5 mW of power after the optical fiber. For the bosonic isotopes, we repump using only these two lasers.

Repumping for the fermionic isotope of strontium is more complicated. Instead of a single transition, the added hyperfine structure of ^{87}Sr means that there are 9 different $^3P_2 \rightarrow {}^3S_1$ transitions spanning about 5.4 GHz (see Table 1.1). In the past we have solved this issue by modulating the piezo and current of the 707-nm repump in order to broaden its linewidth and address as many of the repumping transitions as possible. This technique worked well and was used to produce our first DFGs, as discussed in Sec. 3.7. However, it could be difficult to find the optimum repump settings and they were not always repeatable day to day. Furthermore, we could not use the wavemeter lock to stabilize long term drifts of the laser throughout the day because the laser was multimode. To address this issue, we switched to a different, more stable, solution to broaden the spectrum of the 707-nm

---

[9]This DAC circuit was built and designed by N. Pisenti. In the future, we would like to move to a digital feedback system where the Labview software would communicate directly with the piezo driver electronics over a local network.

repump laser using a fiber electro-optic phase modulator (EOM) phase modulator.

The fiber EOM (Jenoptik PM705) has a large bandwidth (up to about 2 GHz) and can drive a large modulation depth at reasonable voltages ($V_\pi \approx 4$ V). Since the EOM has a large injection loss of 4.5 dB, instead of using the roughly 6 mW output of 707-nm repump B directly, we use that light to injection lock a third laser (uncoated laser diode, Opnext HL7001MG) in order to increase the optical power available. Repump C gives us roughly 45 mW before fiber coupling, though we limit the amount of power used to $\lesssim 5$ mW after the EOM to avoid damaging the optical interfaces between the crystal and the fiber.[10]

To generate our repumping spectrum, we lock the center frequency of the repump B at the $^3P_2$, $F = 13/2 \rightarrow \, ^3S_1$, $F = 11/2$ transition. We drive the EOM with a high speed direct digital synthesizer (DDS) (Analog Devices AD9914 evaluation board) which is capable of generating frequencies up to 1750 MHz. In order to generate multiple modulation frequencies, we rapidly switch (delay time = 20 μs) between 4 different frequencies at 655, 1240, 1510, and 1720 MHz. The radio frequency (RF) power of each tone is different, but they are all in the range of 15-23 dBm.[11] These settings were chosen based on an empirical optimization and they are highly dependent on the laser frequency and optical power. A different optimization procedure would likely find another set of parameters that also work well. Though the EOM scheme has not been rigorously compared to the direct modulation method, they offer similar performance. We observe that our atom number increases with increased 707-nm laser power, indicating that we have not saturated our repump efficiency for ^{87}Sr and further improvements are possible.

The various repump lasers are delivered to the experiment by single mode fibers

---

[10]Though our full power (6.5 mW after the EOM) should be below the specified optical damage threshold of the device (20 mW), we destroyed one EOM in this manner so we now run with a more conservative total power.

[11]The idea to "mix" a number of frequencies by switching quickly between them was based on a tip from M. Norcia at JILA.

and are directed into the main chamber either through the Zeeman slower viewport or the viewport above the main chamber. Since we do not have enough power in 707-nm repump C to saturate the atom number in our ^{87}Sr bMOTs, we make sure to launch this laser using the vertical viewport to avoid the partially coated Zeeman slower viewport.[12]

4.2.3 689-nm Lasers

The $^1S_0 \rightarrow {}^3P_1$ transition at 689 nm has a very narrow linewidth of $\Gamma/2\pi = 7.5\,\text{kHz}$. In order to maximize the performance of our rMOT, we would like our 689-nm lasers to have linewidths narrower than the natural width of the transition. The 689-nm laser system consists of a master laser locked to an ultra-high finesse cavity which provides both short term and long term stability. In order to generate enough optical power and easily switch between the various isotopes, we operate 3 slave lasers that are referenced to the master.

4.2.3.1 689-nm Master Laser

The master laser (see Fig. 4.6) is a Toptica DL pro laser. When free-running, it has a linewidth of $\simeq 100\,\text{kHz}$, which was measured using the delayed self-heterodyne technique and a 2 km fiber delay line. We stabilize it using a Pound-Drever-Hall (PDH) lock to an ultra-high finesse cavity that we purchased from Advanced Thin Films (ATF-6010-4). The cavity is 10 cm long with a free spectral range (FSR) of 1.5 GHz. The cavity finesse, as measured by the cavity ring-down time, is about 240,000 which corresponds to a linewidth of just over 6 kHz.

Since the resonance frequency of a cavity depends on its length, we would like to minimize length fluctuations due to vibrations and thermal changes. With this goal in mind, the mirrors and spacer are made out of Ultra-Low-Expansion (ULE) glass. ULE glass is manufactured by Corning to have a very small coefficient of thermal expansion

---

[12]In the upgraded strontium experiment, these lasers can be launched into the chamber using the mini-viewports which should minimize the number of optics between the fiber and bMOT and therefore reduce optical power losses.
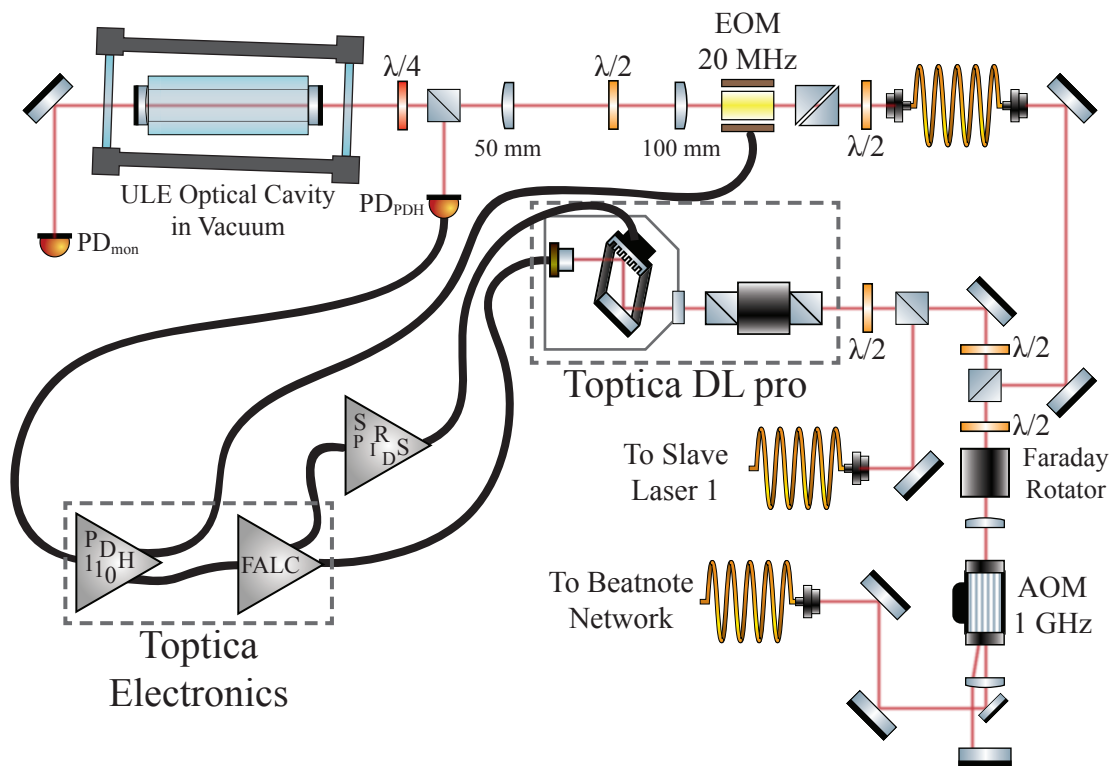
Figure 4.6: Schematic of the 689-nm master laser. A Toptica DL pro is stabilized with a short-term linewidth of < 200 Hz by a PDH lock to an ultra-high finesse cavity. The master is then used as a reference for several slave lasers.

(CTE). For example, the CTE for ULE is less than 30 ppb/K [143], which is about three orders of magnitude smaller than common glasses such as fused silica (CTE $\approx$ 0.5 ppm/K [144]) or BK7 (CTE $\approx$ 7 ppm/K [145]). Furthermore the CTE of ULE glass varies as a function of temperature and typically changes sign in the vicinity of room temperature. One can minimize the CTE of the cavity by operating it at a temperature near this zero crossing. It is somewhat painful to measure the zero crossing given the long thermalization time between the vacuum chamber and the cavity, so we have not bothered to do so for our 689-nm cavity. However, we have measured the zero crossing at 30.2 °C for an identical cavity that we are using to stabilize a laser at 698 nm to address the clock transition (see Sec. 4.2.4) and we could do a similar measurement for the 689-nm cavity if desired.

In order to provide additional stability, the cavity is placed in a vacuum chamber and evacuated to less than $\approx 5 \times 10^{-8}$ Torr. There are several advantages to placing the cavity under vacuum. First, the vacuum improves temperature stability by reducing heat transfer to the cavity from convection or conduction. In addition, the vacuum acts as an acoustic barrier, shielding the cavity from vibrations due to airborne acoustic waves. Finally, the vacuum chamber also reduces variations in pressure. These pressure changes have the same effect as slight variations in cavity length [146].

We maintain the vacuum of our cavity chamber with a 3 L/s ion pump (Gamma Vacuum 3S-CV-1V-5K-N-N). The pump is mounted so there is no line of sight between the pump and the cavity to reduce heating of the cavity by black body radiation. The cavity rests on several viton spacers and the vacuum chamber is also mounted on rubber feet to provide vibration damping. The outside of the vacuum chamber is actively temperature stabilized to about 29 °C.

Since the cavity is completely passive, we use a double passed, high speed 1 GHz AOM (Brimrose GPF-1000-500-689) to tune the absolute frequency of the master laser relative to a nearby cavity mode. Our original plan was to use a spectroscopy signal
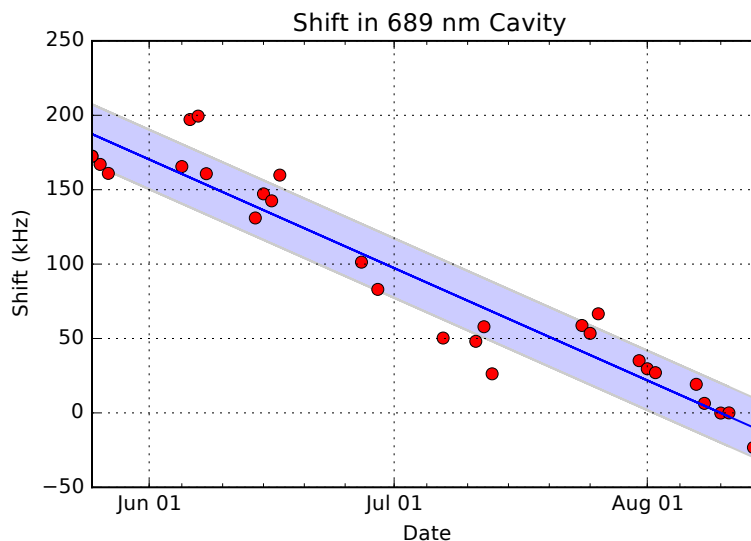
Figure 4.7: Plot of the long term drift of the 689-nm lasers. This data was measured by tracking the shift of the $^1S_0 \rightarrow {}^3P_1$ transition frequency in a ^{84}Sr BEC over several months. The dark blue line is a linear fit to the data and the light blue filling indicates a region ± 20 kHz from the linear trend. The average drift is 2.4 kHz/day or about 30 mHz/s. There are shorter term fluctuations about the average on the order of 10s of kHz.

as an absolute frequency reference to cancel the long term drift of the ULE cavity, but we found that the cavity's long term stability is good enough to make the spectroscopy feedback unnecessary. ULE cavities typically exhibit a long term linear drift in their resonance frequency that is attributed to a settling or creep of the glass. A recent measure of the cavity drift is shown in Fig. 4.7. We observe a linear drift of about 2.4 kHz/day or 30 mHz/s, which is slow enough to only require the occasional correction every couple days. However, we see day-to-day fluctuation on the order of 10s of kHz, which suggests that the stability of the master laser is limited by medium timescale fluctuations on the order of hours. Though we are sensitive to frequency changes of about 5-10 kHz, these fluctuations have not been a big problem for our experiment because we can simply calibrate them out once or twice a day. Given the timescale, it is likely that these fluctuations are thermal in nature. If that is the case, we may be able to suppress them by operating the ULE cavity at the CTE zero crossing temperature as discussed above.

The DL pro laser produces about 16 mW of optical power. We divert about 2 mW

immediately after the laser to injection lock slave laser 1 (see Sec. 4.2.3.2). The remainder of the light is double-passed through the GHz AOM. Since the Brimrose AOM is more efficient for horizontally polarized light, we use a Faraday rotator to ensure the polarization is horizontal in both directions through the AOM but rotated by 90° upon returning to the pickoff PBS. The AOM has a specified diffraction efficiency of about 30%, though we are only able to achieve about 25% single-passed and 3% double passed efficiency.[13] Despite the poor efficiency, we still have about 350 μW immediately after the AOM and 60 μW at the cavity input, which is sufficient for the PDH lock. The majority of the light is not diffracted by the AOM. This arm is picked off and sent to a network of fiber beamplitters, which is illustrated in Fig. 4.8. The fiber network sends about 1% of the light to the wavemeter and the rest is used to generate beatnote signals with several slave lasers.

The PDH lock uses the standard setup to generate an error signal [147, 148]. A single-mode fiber delivers the light to the cavity to decouple cavity alignment from that of the rest of the system. After the fiber, we phase modulate the light using a free-space EOM (Thorlabs EO-PM-R-20-C1) that is driven using a 20 MHz RF signal from a Toptica PDH 110 module. After a couple of mode matching optics, the beam is aligned into the cavity. To avoid forming an etalon between the vacuum chamber viewports and the cavity mirrors, the cavity is mounted inside the cavity at a 4° angle. The light reflected from the cavity is measured by an amplified photodiode (Thorlabs PDA10A) and demodulated by the PDH 110 module. We then send the error signal to the Toptica Fast Analog Linewidth Control (FALC) module, which provides feedback to the master diode current with a bandwidth > 1 MHz. We also use a second loop filter (SRS SIM960) that feeds back to the laser cavity piezo in order to cancel long term drifts and keep the FALC output from railing. A photodiode after the chamber monitors the cavity transmission and provides a useful diagnostic.

---

[13] Other groups have found that Brimrose doesn't always do a great job lining up the optical aperture on the case with the optimum location for the beam. If better double-passed efficiency is needed, it may be helpful to remove the case and enlarge the holes.
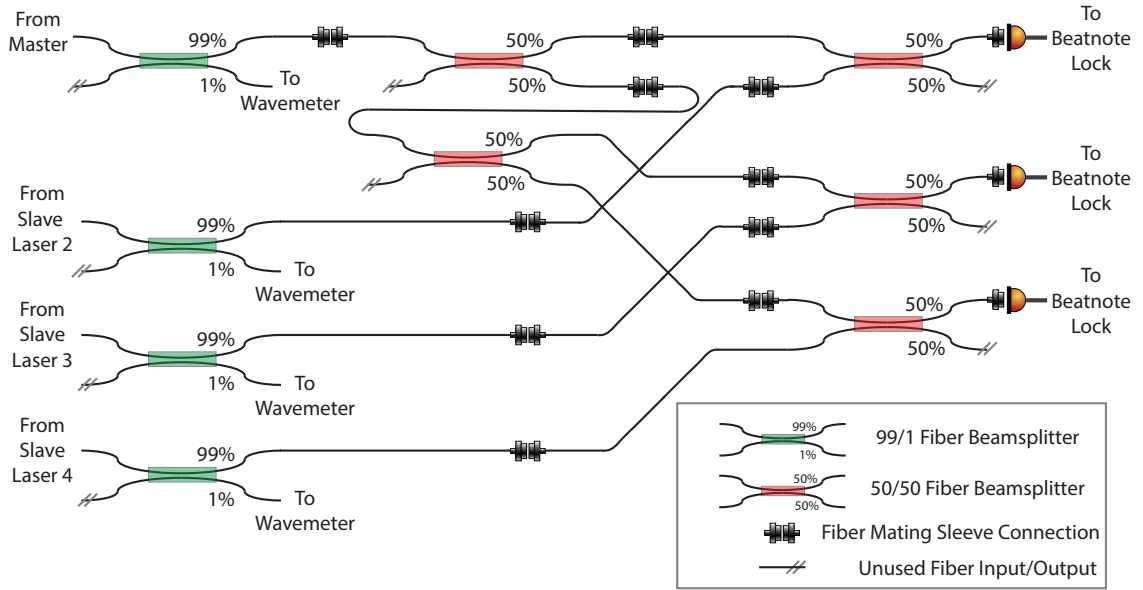
Figure 4.8: Schematic of beatnote network based on a series of fused fiber optic beamsplitters (Thorlabs TW630R5A2, TW630R1A2 or similar). Slave laser 4 is still under construction, so it is not shown in Fig. 4.9.

It can be very challenging to measure laser linewidths $\lesssim 10$ kHz. We initially tried to measure the linewidth using the delayed self-heterodyne method and a 2 km fiber delay line, but the delay time of ≈ 10 μs was only long enough to constrain the linewidth to less than ≈ 50 kHz. Recently, we took advantage of the fact that we are constructing another narrow linewidth laser using an identical cavity. This laser, which I will describe in more detail in Sec. 4.2.4, will be only 9 nm away at 698 nm. While optimizing the new cavity lock, we locked a second 689-nm diode to it in order to measure the beatnote between the two lasers and found their joint linewidth to be ≈ 200 Hz. The joint linewidth is an upper limit on the linewidth of the 689-nm laser since it is a measure of the sum of the two lasers' individual linewidths. This means that our 689-nm master is much narrower than our goal of 7.5 kHz!
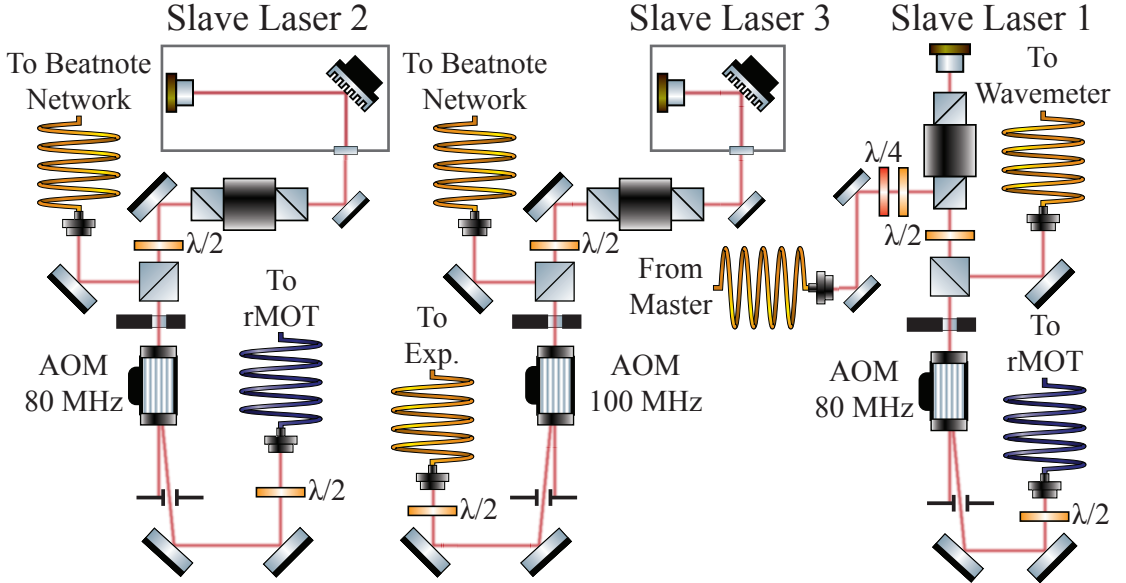
Figure 4.9: Schematic of the 689-nm slave lasers. Slave Laser 1 is used as the trapping laser for the ^{87}Sr rMOT. Slave Laser 2 is used as the stirring laser for the ^{87}Sr rMOT and the rMOT laser for all bosonic isotopes. Slave Laser 3 is used for other purposes, such as spin state optical pumping, photoassociation, and optical Stern-Gerlach.

4.2.3.2   689-nm Slave Lasers

We currently operate three slave lasers at 689 nm for various purposes and we have plans for a fourth. Slave laser 1 consists of an uncoated Opnext HL6750MG laser diode that we injection lock with about 1 mW of light from the master. This laser is used as the trapping laser for our ^{87}Sr rMOT to address the $^1S_0$, $F = 9/2 \rightarrow {}^3P_1$, $F = 11/2$ transition [32]. Slave lasers 2 and 3 are home build Littrow configuration ECDLs based on the design of [149]. Slave laser 2 uses a commercial AR coated diode (Sacher SAL-690-025) and is a longer cavity (10 cm), while laser 3 uses a Opnext HL6738MG diode AR coated in-house[14] and a shorter cavity (2.2 cm), but they are otherwise the same design. We divert a small amount of light ($\approx$ 100 μW) from each of these two lasers to the fiber beatnote network (see Fig. 4.8) where the light is combined with light from the

---

[14]Our AR coating recipe, inspired by [150] includes a layer of Al_2O_3 up to a retardation of $\lambda/2$ and a second layer of HfO_2 up to a thickness of $\lambda/4$. The deposition was performed in an electron beam evaporator in the UMD fabrication facility while monitoring the diode's threshold current in-situ.

master laser and the resulting beatnote is measured on a fast photodiode (either Thorlabs DET02AFC or Hamamatsu G4176-03). These signals are then used to lock the frequency difference between the slaves and master with an OPLL circuit based on [141]. The flexibility of these beatnote locks means we can quickly change the lockpoint for these lasers to switch between different isotopes or detunings. The reference signals for the beatnote locks are supplied by homebuilt DDS circuits, which are in turn programmed by an Arduino micro-controller and our computer control software, which gives us the ability to sweep or change the lockpoints within an experimental cycle. We use slave laser 2 for the "mixing" laser that addresses the $^1S_0$, $F = 9/2 \rightarrow {}^3P_1$, $F = 9/2$ transition during the ^{87}Sr rMOT and also as the rMOT laser for all the bosonic isotopes. We have used slave laser 3 for photoassociation relative to the $^3P_1$ dissociation limit (see Ch. 6) and for optically pumping the ^{87}Sr ground state spin populations. We could also use this laser for optical Stern-Gerlach (OSG) spin state detection [53] or to generate a second rMOT frequency for experiments with isotopic mixtures. We are planning to build a fourth slave laser (not pictured in Fig. 4.9) with a similar setup for even more flexibility.

The optical setup for each slave laser is very similar. We use AOMs (IntraAction ATM-801A1) at $\approx$ 80 MHz for fast switching and intensity control. The beams can be completely extinguished using optical shutters. We use a custom 4×4 fiber splitter (Evanescent Optics) to deliver the beams from slave lasers 1 and 2 to the three rMOT axes. Currently, we waste 25% of the light by not using the fourth fiber splitter output. On the new experiment, we may have two separate fiber launches for the upward and downward propagating rMOT beams since the downward rMOT beam is not strictly necessary during the final stages of the rMOT [39]. Lasers 1 and 2 produce $\approx$ 2.8 mW and $\approx$ 750 μW respectively per MOT arm at the experiment. The rMOT beams are expanded to a $1/e^2$ radius of 2.5 mm and combined with the bMOT beams using a dichroic mirror before entering the chamber.

Minus-K Vibration Isolation Stage

PD_{PDH}

$\lambda/4$

$\lambda/2$

ULE Cavity Under Vacuum

PD_{mon}

Fiber EOM

PDH 110

PID

Ω_{offset}

Power Combiner

Slow feedback path

PD_{mon}

Invar Pre-Stab. Cavity

To Exp.

To Wavemeter

$\lambda/4$

AOM 80 MHz

AOM 80 MHz

PD_{PDH}

$\lambda/4$

EOM 20 MHz

$\lambda/2$

$\lambda/2$

$\lambda/2$

$\lambda/2$

$\lambda/2$

$\lambda/2$

Clock Laser

PID

PDH 110
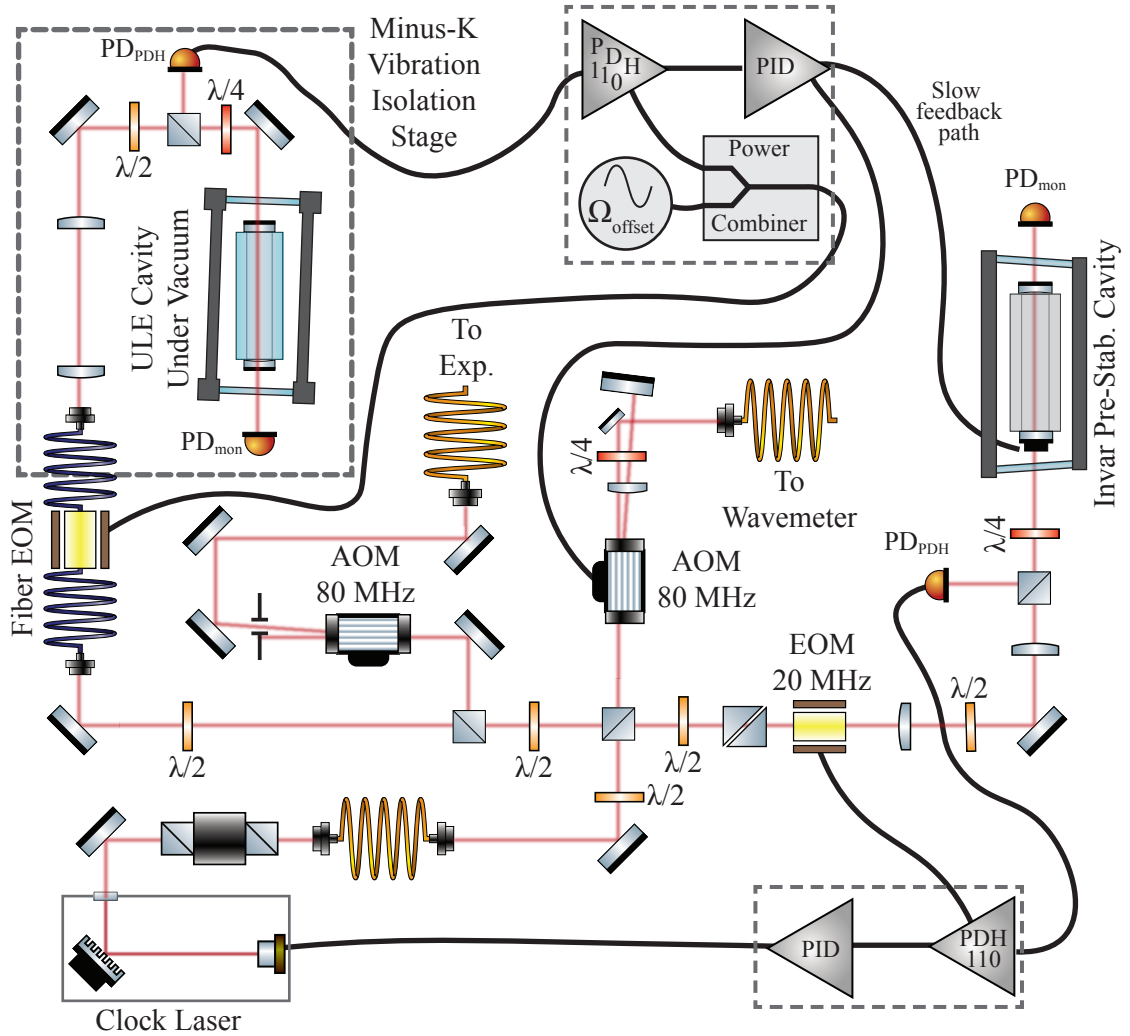
Figure 4.10: Schematic of the clock laser setup. The laser is first locked to a pre-stabilization cavity of finesse ≈ 1200 using fast feedback to the laser current. The laser is then locked to the ultra-high-finesse, ULE cavity by feeding back to the frequency of an intermediate AOM.

4.2.4 Clock Laser

Many proposals to use strontium to study quantum magnetism involve addressing the ultra-narrow, $^1S_0 \rightarrow {}^3P_0$, clock transition. A few groups have successfully built lasers whose linewidth is similar to the natural linewidth of the transition, $\Gamma/2\pi \simeq$ mHz (for example, see [151, 152]). However, these systems typically require a tremendous amount of effort to minimize thermal and vibrational perturbations of the cavity. Our goal is to spend a medium amount of effort (and money) to build a laser with a linewidth below

100 Hz, which should be narrow enough so that we will be able to individually address different ^{87}Sr m_F levels if we use a magnetic field to apply a Zeeman shift. The Zeeman sensitivity of the clock transition is $\approx 109 \times m_F$ Hz/G [57]. To reduce cost and to build upon our earlier experience, the clock laser uses a ULE cavity that is identical to the one used to stabilize the 689-nm master.

Our clock laser is currently under construction, so I will only briefly summarize its design (see Fig. 4.10). The laser diode is commercially AR coated (Sacher SAL 0705-020) and installed into a Littrow configuration mount (based on [149]). The laser is first locked to a homemade pre-stabilization cavity (finesse $\approx$ 1200) with a spacer made from Invar. The pre-stabilization cavity is not strictly necessary (indeed we forego one for the 689-nm master), but it is much easier to diagnose and optimize the lock to the ultra-stable cavity if the laser is first narrowed to $\lesssim$ 1 kHz. The pre-stabilization lock has a fast bandwidth (> 1 MHz) and feeds back to the laser diode current. A separate optical path is double-passed through an 80 MHz AOM and then sent through a fiber EOM to a vibration isolation stage that holds the ultra-narrow cavity. The PDH lock to the ULE cavity uses the fiber EOM to generate the phase modulation and feeds back to the frequency of the double-passed 80 MHz AOM. A slow feedback path to the piezo of the pre-stabilization cavity cancels long term drifts. The finesse of the ULE cavity is about 150,000 as measured by the cavity ringdown time. The output of the laser is shifted by a second 80 MHz AOM for intensity control and fast switching. In the future, we should also be able to use the second AOM for fiber phase noise cancellation [153].

By using a fiber EOM with large bandwidth (Jenoptik PM705), we can use an offset lock technique to tune the frequency difference between the laser and a nearby cavity mode. We drive the EOM with two RF frequencies, a larger frequency Ω_{offset} supplied by tunable RF source, and a slower frequency $\omega_{\text{PDH}} = 18$ MHz supplied by a Toptica PDH 110 module. We then lock a sideband of the laser, offset from the carrier by Ω_{offset}, to the cavity using the modulation at ω_{PDH}. This technique will give us the flexibility to tune
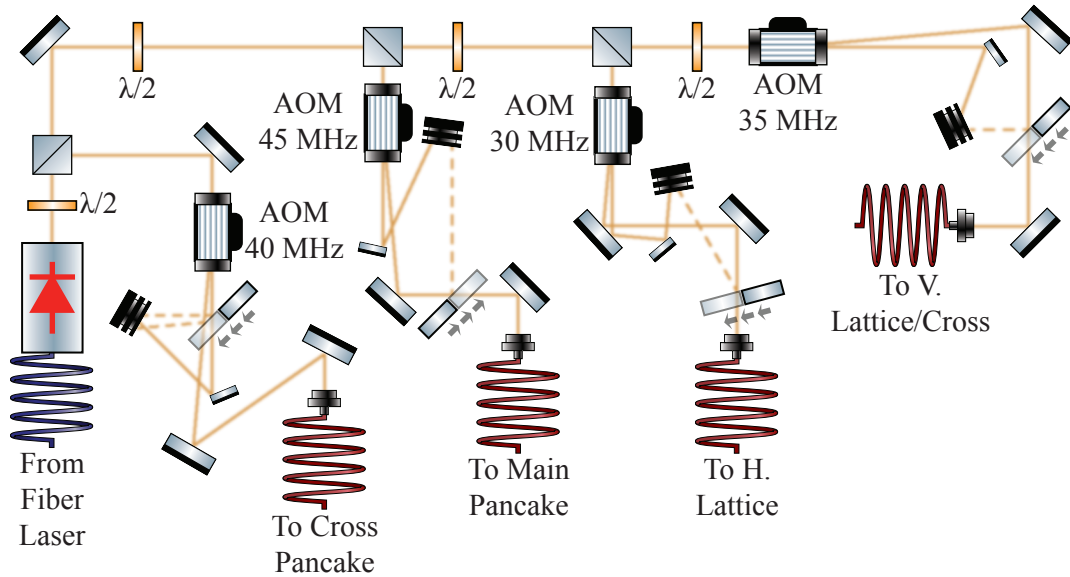
Figure 4.11: Schematic of the 1064-nm dipole trap laser. The light is divided into four different arms that are used for four different dipole traps. Each arm has an AOM for intensity control and fast switching as well as a solenoid shutter.

the absolute frequency of the laser by changing Ω_{offset} while remaining locked to a single cavity mode.

Though the ULE cavity is identical to the one used for the 689-nm master laser, we took a few extra steps to minimize thermal and vibrational perturbations. First, N. Pisenti performed finite element analysis simulations to determine the optimum geometry to mount the cavity in order to minimize sensitivity to mechanical vibrations [154]. In addition, the cavity is mounted on an isolation stage (Minus-K 100BM-8) that provides up to 60 dB of attenuation to vibrations at $\simeq 100$ Hz. We also placed the stage in a box lined with several inches of foam insulation to provide further acoustic and thermal isolation. Finally, we measured the cavity's CTE as a function of temperature and operate it near the point where the CTE vanishes, as discussed in Sec. 4.2.3.1. Initial results are encouraging, as the measured joint linewidth with the 689 master was $\simeq 200$ Hz, as mentioned above.

4.2.5 1064-nm Laser

To cool our strontium samples beyond the $\approx 1 \ \mu$K temperatures that we obtain in the rMOT, we must perform evaporative cooling. Since magnetic trapping isn't an option for strontium due to its $J = 0$ ground state, we perform evaporation using a crossed-beam optical dipole trap at 1064 nm. The light for the dipole traps is generated by a 30 W fiber laser (IPG YLR-30-1064-LP-SF), which we divide into four different arms that are used for four individual trapping beams (see Fig. 4.11). The intensity of each trap is controlled by an AOM (IntraAction AOM-402AF4 or AOM-302AF4) and can be fully extinguished by a home-built shutter. The shutters are actuated using solenoids from computer speakers and are based on the design in [155]. To avoid unwanted interference effects between the various trapping beams, we ensure that the drive frequencies of the various AOMs are well separated from each other. We couple the light from the laser breadboard to the experiment using large-mode-area (LMA) optical fibers (Coastal Connections S-FAmkFAmk-10nx/130/3-7.6). The LMA fibers can handle up to 10 W of power in their core[15] and are cheaper than other options based on photonic crystals. One challenge with the LMA fibers is that the cladding forms a multi-mode waveguide, so initial alignment can involve a significant amount of trial and error to properly align the beams through the core. The maximum power available at the experiment for the [main pancake, cross pancake, vertical ODT, horizontal lattice] arm is [3.2 W, 2.3 W, 1.0 W, 1.0 W] when the IPG is set to 15 W.

Since the ODT trap depth is proportional to the intensity, we implement intensity locks to stabilize the optical power in each beam. Before the mode-shaping optics that focus each beam onto the location of the atoms, we sample a small fraction of the beam intensity by either a back-side polished mirror (Thorlabs NB1-K14-SP) or AR coated

---

[15]Though the fibers can handle a large amount of power in their core, they can still be easily damaged if the light is not aligned into the core. Coarse alignment should be performed at low laser power and only fine-tuned with small adjustments after turning the power up. This also applies to aligning the retro-reflected beam of an optical lattice.

wedged window (Thorlabs WW11050-C14). The power in the sampled light is measured by a photodiode (Thorlabs DET10C) and stabilized by a PI loop filter circuit that feeds back to the AOM. One source of instability comes from the fact that the LMA fibers are not polarization maintaining, so the polarization after the fiber may drift due to mechanical or thermal perturbations to the fiber. To minimize these effects, we clean up the polarization of each beam immediately after the fiber using a Glan laser polarizer (Thorlabs GL10-C26). We also try to align our wedged windows close to normal incidence so that the proportion of light that is reflected is as insensitive to polarization as possible. Fast intensity fluctuations are reduced to $\lesssim 1\%$ when the locks are operational. However, for some of our dipole traps, we observe long term (timescales on the order of many minutes/hours) drifts of $\simeq 10\%$. We have tried to pinpoint the source of these drifts without success. My best guess is some residual polarization dependence, for example from an improperly aligned Glan laser polarizer, or some thermally induced drift in the response of either the photodiode or locking electronics.

The optics used to launch the dipole beams in the vertical and horizontal directions are shown in Figs. 4.14 and 4.15. Since efficient evaporation of different strontium isotopes requires different trap parameters due to the isotopic differences in scattering legnths, there are two vertical dipole beam launches and we can switch between the two by changing which optical fiber is plugged into the launch after the AOM. The loose vertical beam forms a $1/e^2$ radius of about 230 μm and is used for ^{86}Sr when large trap volumes are necessary to avoid three-body loss (see Sec. 3.6.1). We use the other vertical launch for all the other isotopes, which gives a $1/e^2$ waist of about 72 μm. Below the chamber, the vertical dipole beam transmits through a liquid crystal variable waveplate (Meadowlark Optics SRC-200-IR2), which can be used to adiabatically rotate the beam from a beam dump onto a retro-reflecting mirror and switch from a single beam dipole trap to an optical lattice configuration.

There are three different dipole beams in the horizontal plane. The main pancake
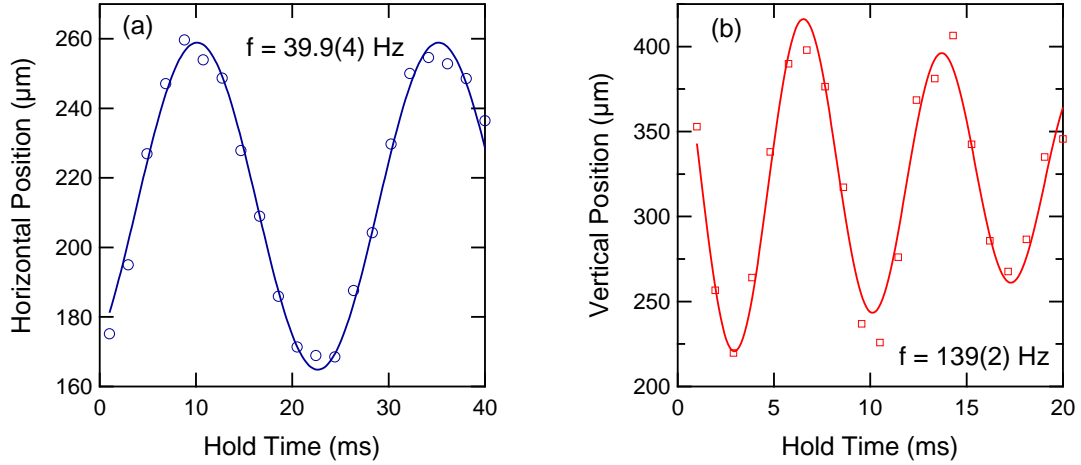
Figure 4.12: Example of measuring trap frequencies using center of mass oscillations. We excite oscillations in the dipole trap by briefly pulsing one of the trapping beams to a higher power and then measure the position of a ^{84}Sr BEC as a function of hold time. We extract trap frequencies by fitting the BEC position to a decaying sinusoid function for one of the horizontal directions (a) and vertical direction (b).

and cross pancake beams both use cylindrical lenses to generate beam waists that are much larger in the horizontal direction than the vertical direction. These pancake shapes mimic the spatial mode of the atoms in the rMOT after compression and also provide strong vertical confinement. These beams cross at a 45° angle and we can use one or both of them to load atoms from the rMOT. The main beam has a vertical (horizontal) waist of 22.8 (228) μm and the cross pancake has a vertical (horizontal) waist of 16 (270) μm. There is also a lattice beam that co-propagates with the cross pancake beam that can be used to form a lattice in the horizontal direction. The horizontal lattice beam has a design radius of 100 μm though this has not been measured.

4.2.5.1 Trap Frequency Measurement

The trap frequencies are a very useful parameter to describe the shape and depth of the ODT. Knowledge of trap frequencies is often needed in order to extract physical parameters from our atomic samples. We have measured trap frequencies in two different ways. One method, known as parametric heating, involves modulating the setpoint of the ODT intensity lock at a frequency, ω_{mod}. When $\omega_{\text{mod}} = 2\omega_{\text{trap}}$, atoms are parametrically

heated out of the trap. There can also be similar features at sub-harmonic frequencies, $\omega_{\text{mod}} = 2\omega_{\text{trap}}/n$, where n is an integer [156]. The disadvantages of the parametric heating method are that the sub-harmonic features and asymmetric lineshapes may complicate the analysis. In addition, the technique is more sensitive at higher trap frequencies, making it difficult to use for low trap frequencies ($\lesssim 20$ Hz). Another method involves perturbing the atomic sample, typically by displacing it in the trap using a different dipole trap beam or by suddenly changing the intensity of the beam. We can then image the center of mass or breathing mode oscillations as a function of time, as depicted in Fig. 4.12. We prefer using center of mass oscillations as their interpretation is the simplest.

4.2.5.2 Lattice Depth Calibration

An optical lattice is formed by retro-reflecting an optical dipole trap beam on itself. The resulting standing wave forms a periodic potential with the form $V_0 \cos^2 kz$, where V_0 is the trap depth, $k = 2\pi/\lambda$ is the wavenumber of the trapping light, and z is the distance along the lattice. In this approximation I am neglecting the Rayleigh divergence of the lattice beams which reduces the lattice depth away from the waist. Many properties of the lattice depend on the depth, so it is an important parameter to calibrate. In this section I will describe a method to calibrate the lattice depth using diffraction of a BEC.

In the presence of the lattice (and ignoring mean-field interactions), the BEC is subject to the Hamiltonian [157]

$$\hat{H} = -(\hbar^2/2m)\partial_z^2 + V_0 \cos^2 kz. \tag{4.6}$$

We can expand the condensate wave function in the plane wave basis as $\Psi(t) = \sum_n c_n(t)e^{i2nkz}$ where n is an integer and $c_n(t = 0) = \delta_{n,0}$. The time-dependent Schrödinger equation can
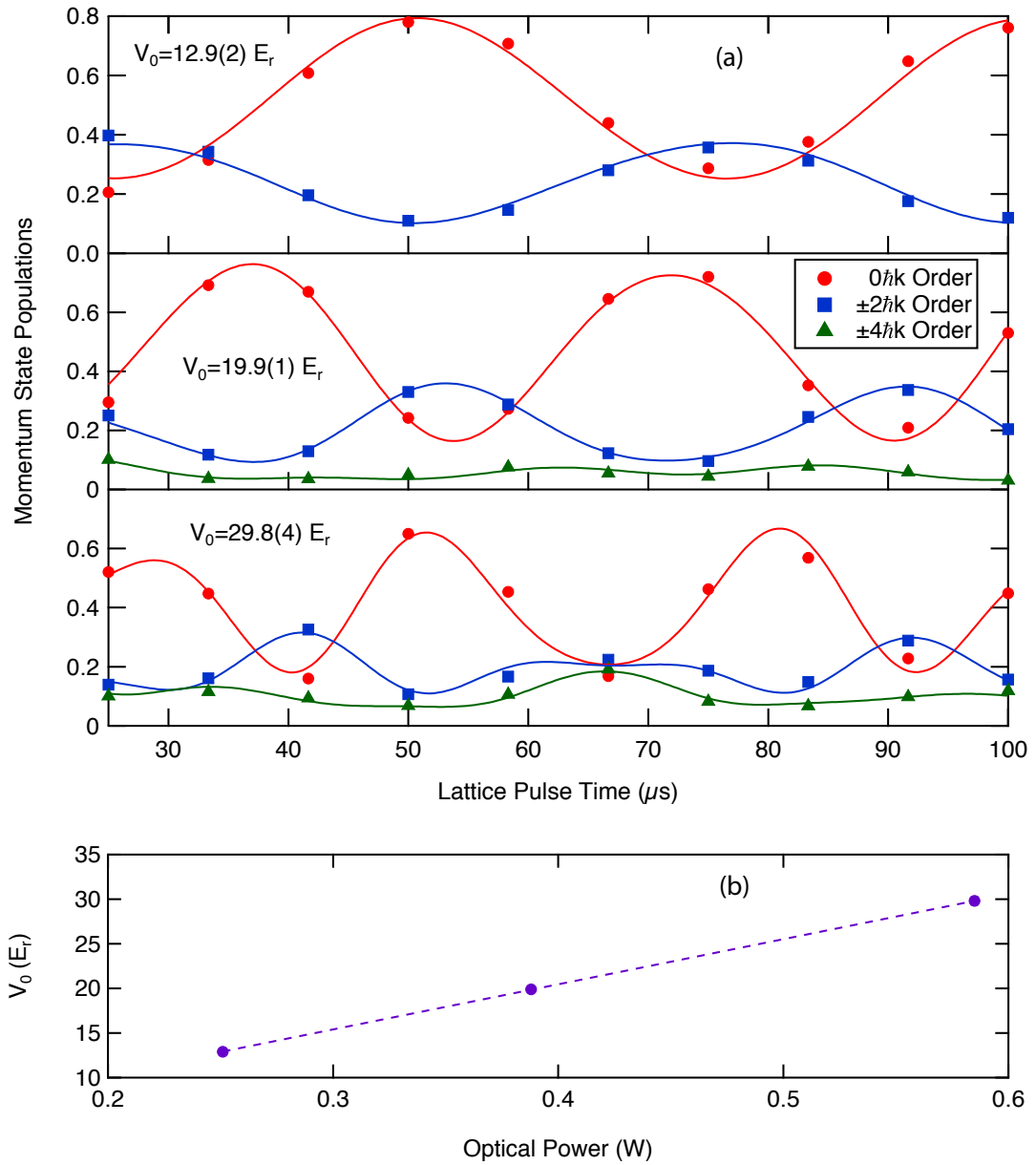
Figure 4.13: (a) Example calibration of optical lattice depth. The lattice beam is pulsed on for a variable amount of time between 25 and 100 μs and the population in the $0\hbar k$ (red circles), $\pm 2\hbar k$ (blue squares), and $\pm 4\hbar k$ (green triangles) orders are measured. The populations are fit using the numerical solutions to Eq. (4.7) (solid lines). The population of each order are fit independently and typically yield depths that are consistent within 2%. Since the populations in the $\pm 4\hbar k$ orders are smaller and therefore slightly noisier, our extracted trap depth is an average of the results from the $0\hbar k$ and $\pm 2\hbar k$ orders. (b) Calibration results from (a) versus power in the lattice beam. The lattice depth varies linearly with power with a slope of 50.6(2) E_r/W. The error bars are smaller than the markers.

be transformed into a set of coupled differential equations given by

$$i\frac{\mathrm{d}c_n}{\mathrm{d}t} = \frac{4E_r n^2}{\hbar}c_n + \frac{V_0}{4\hbar}(c_{n-1} + 2c_n + c_{n+1}), \tag{4.7}$$

where the energy of photon-recoil, E_r is defined as $E_r = (\hbar k)^2/(2m)$. The problem can be solved approximately in the Raman-Nath regime, which is valid when the pulse time, τ, is much shorter than the harmonic oscillation period of a potential well, or $\tau\omega_{\mathrm{trap}} \ll 1$, where $\omega_{\mathrm{trap}} = 2[V_0 E_r]^{1/2}/\hbar$. In this regime, we can ignore the first term on the right hand side of Eq. 4.7 and the population in the nth diffracted order is given by

$$P_n = |c_n|^2 = J_n^2\left(\frac{V_0\tau}{2\hbar}\right), \tag{4.8}$$

where J_n are Bessel functions of the first kind. However, it can be challenging to pulse the lattice with times short enough to satisfy the Raman-Nath criteria but with significant population in the diffracted orders. Therefore, we would like to develop a calibration method based on this description of the system that is not constrained to short pulses.

The method that I developed involves taking a sequence of images using the same lattice depth while varying the lattice pulse time (see example in Fig. 4.13). In order to avoid issues of integrator windup, the lattice beam AOM is operated at a constant RF power instead of using the intensity lock. One could also use a loop filter circuit that incorporates an integrator hold feature. We can then measure the population in the various diffracted orders as a function of pulse time and compare the curves to the numerical solution to the coupled differential equation (Eq. 4.7). We use a curve fitting routine to find the trap depth that best fits the data for the population of each order. The trap depth varies linearly with lattice beam intensity, so once we measure the depth at a few powers we can extrapolate to any other power.
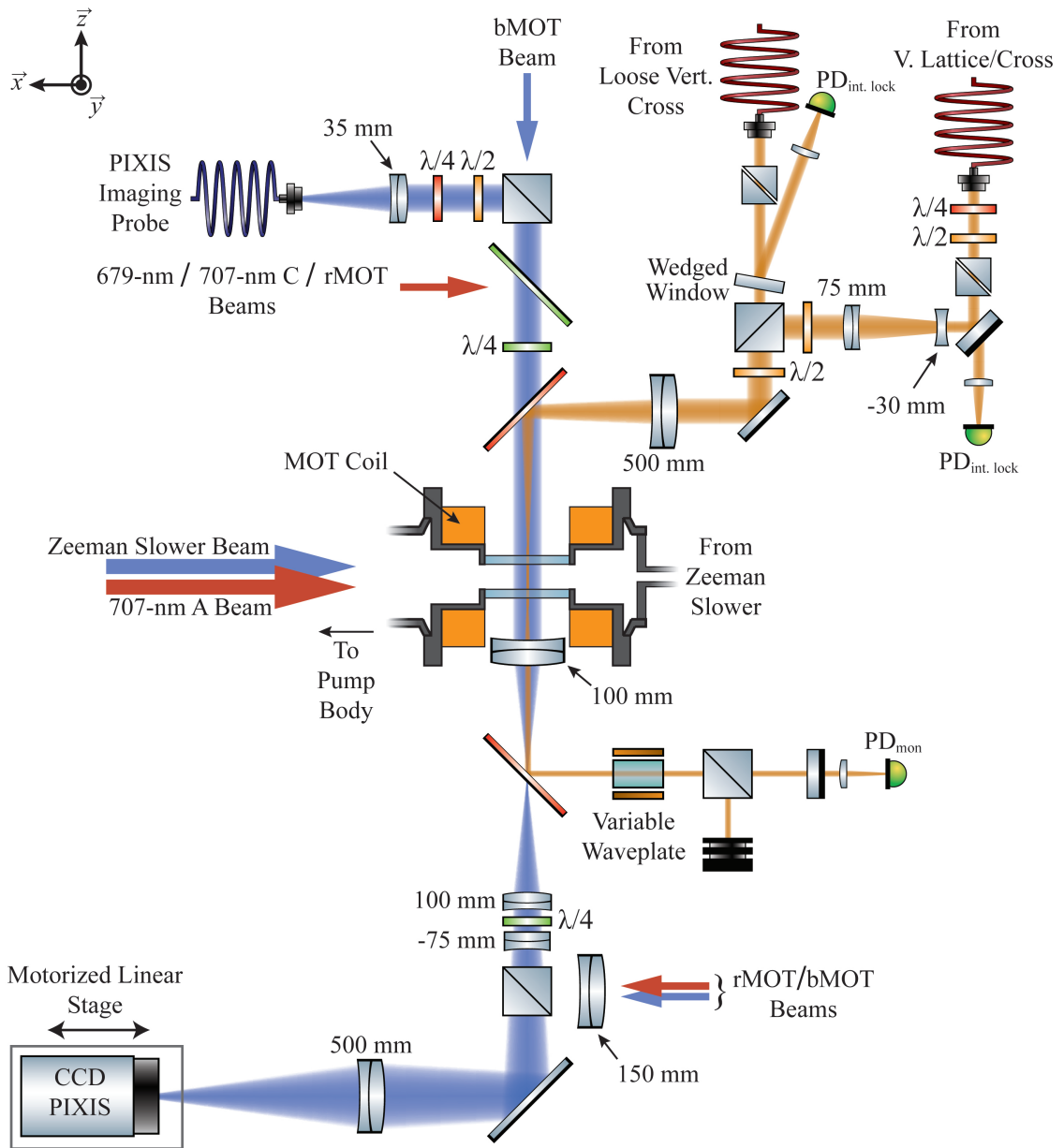
Figure 4.14: Schematic of the vertical dipole trap and imaging optics. The loose vertical ODT arm is used for ^{86}Sr while the other ODT arm is used for the other isotopes. A variable waveplate below the chamber can be used to adiabatically transform between a single-passed ODT and a retro-reflected lattice. The vertical imaging system has a large magnification (5.48×) and a resolution of a few μm. The PIXIS camera is mounted on a motorized linear motion stage to compensate for the fact that the imaging plane of the system needs to move depending on how long the atoms fall before imaging.
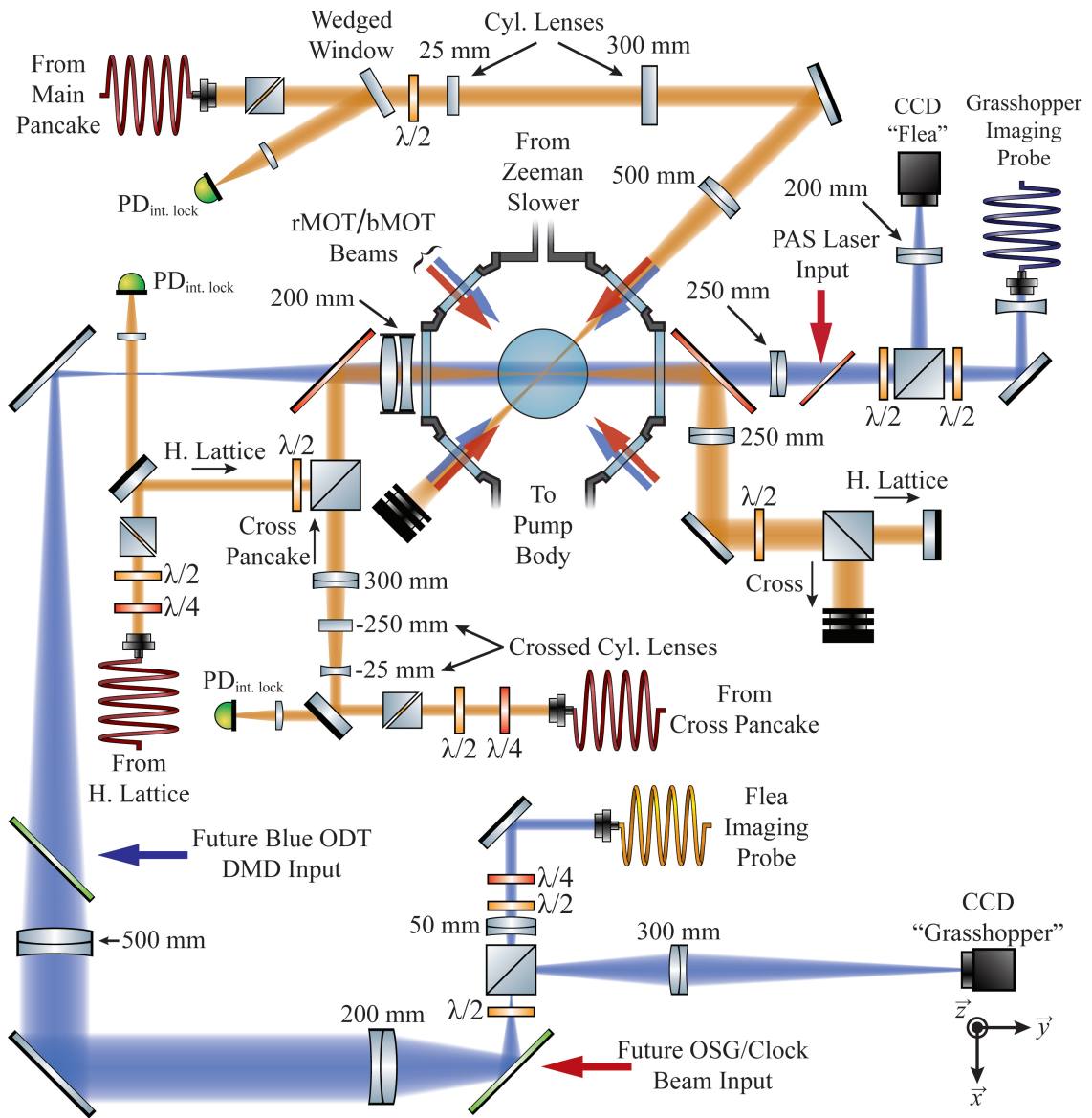
Figure 4.15: Schematic of the horizontal dipole trap and imaging optics. Two pancake shaped dipole traps ("Main Pancake" and "Cross Pancake") cross at 45°. There is also a separate beam that co-propagates with the Cross Pancake that can be used to make an optical lattice. There are two imaging systems in the horizontal direction. The Flea imaging system has a low magnification (0.898×) and is used to image large clouds. The Grasshopper imaging system has a larger magnification (3.85×) and is able to capture more detailed images of small samples.

90

4.3   Imaging Systems

To generate data and extract physical information about our atomic samples, we use absorption imaging techniques to capture pictures of our atomic clouds. In this section I will describe the hardware, performance, and methods that we use to take these images. The fitting functions that we use to analyze and extract physical information about our samples have been discussed in Ch. 2.

4.3.1   Hardware

We currently have three imaging systems installed and in use. See Table 4.1 for a summary of their key parameters. The Flea and Grasshopper imaging systems are both oriented in the horizontal direction (see Fig. 4.15) while the PIXIS captures data from below the atoms (see Fig. 4.14). The Flea imaging system has a low resolution/magnification with a large field of view that is useful for imaging the rMOT and thermal clouds after a time-of-flight. The Grasshopper and PIXIS systems both have larger magnifications and resolutions of a few μm, which makes them more useful for in-situ imaging and analyzing smaller clouds of BECs or DFGs. The resolutions reported in Table 4.1 were measured by D. Barker using a USAF test pattern and represent the Rayleigh criteria for defining the resolution.[16] The resolution for the Grasshopper imaging system was not measured because the objective lens was already installed on the vacuum chamber, but is expected to be similar to or smaller than that of the PIXIS.

The magnifications of the horizontal imaging systems are calibrated by imaging a cloud of atoms after dropping them for a variable amount of time and comparing the measured acceleration of the cloud with the known value due to gravity. We determined the PIXIS imaging system magnification by using an optical lattice to diffract a ^{84}Sr BEC

---

[16]The Rayleigh criteria defines the minimum resolution of an imaging system as the distance between the center and first null of the Airy diffraction pattern of an object.

Table 4.1: Details of the three imaging systems currently in use. The measured resolution is based on the Rayleigh criteria and the uncertainty is the 1σ statistical fitting error, see [131] for details. The resolution was not measured for the Grasshopper imaging system because the objective lens was already installed on the main chamber.

	Imaging System		
	Flea	Grasshopper	PIXIS
Imaging Direction	Horizontal	Horizontal	Vertical
Measured Magnification	0.898	3.85	5.48
Measured Resolution	$16 \times 11.3(9)\ \mu$m	–	$4.3 \times 4.8(6)\ \mu$m
Field of View	6.00×7.96 mm	1.85×1.39 mm	2.43×2.43 mm
Camera	Point Grey FL3-FW-20S4M-C	Point Grey GS3-U3-28S4M	Princeton Instruments PIXIS Excelon 1024B

(using the same method as described in Sec. 4.2.5.2) and measuring the separation of atoms in different momentum states after a time-of-flight. Since the vertical position of the atoms changes as a function of the time-of-flight, we need to move the PIXIS camera in order to keep the atoms at the focus of the imaging system depending on how long the atoms fall before being imaged. To handle this correction automatically, we mount the PIXIS camera on a linear translation stage that is controlled by a motorized linear actuator (Newport CONEX-LTA-HS). The computer control software calculates the necessary correction to the camera position depending on the time-of-flight being used and commands the linear actuator to move to the appropriate position.

4.3.2 Methods and Calibration

The absorption of a probe beam with intensity I as it propagates in the z-direction through a cloud of atoms, known as the Beer-Lampert law, is given by [29, 158, 159]

$$\frac{\mathrm{d}I(x, y, z)}{\mathrm{d}z} = -n(x, y, z)\sigma_{\text{eff}} \frac{I(x, y, z)}{(2\delta/\Gamma)^2 + 1 + I(x, y, z)/I_{\text{sat}}^{\text{eff}}}, \quad (4.9)$$

where n is the atom density, $\delta/2\pi$ is the detuning of the probe beam, Γ is the linewidth of the transition, $\sigma_{\text{eff}} = \sigma_0/\alpha$ is the effective cross-section, and $I_{\text{sat}}^{\text{eff}} = \alpha I_{\text{sat}}$ is the effective saturation intensity.[17] The effective cross-section and saturation intensity are modified from the ideal values from a two-level system, $\sigma_0 = 3\lambda^2/2\pi$ and $I_{\text{sat}} = \pi hc\Gamma/3\lambda^3$, by a factor $\alpha \geq 1$ that captures corrections due to the structure of the ground and excited states, imperfections in the imaging beam polarization, and deviations of the magnetic field orientation.

Let us first consider the simplest case of a low intensity, resonant probe with $\alpha = 1$, ($I \ll I_{\text{sat}}, \delta = 0$). In this case, the Beer-Lampert law simplifies to

$$\frac{\mathrm{d}I(x, y, z)}{\mathrm{d}z} = -n(x, y, z)\sigma_0 I(x, y, z), \tag{4.10}$$

which can be integrated to find

$$\ln\left(\frac{I_f(x, y)}{I_0(x, y)}\right) = -n_{\text{2D}}(x, y)\sigma_0 = -D_{\text{opt}}(x, y), \tag{4.11}$$

where I_0 and I_f are the intensities before and after the atomic sample respectively. We have introduced the column density, $n_{\text{2D}}(x, y) = \int n(x, y, z)\mathrm{d}z$ and defined the optical depth, $D_{\text{opt}}(x, y) \equiv n_{\text{2D}}(x, y)\sigma_0$.

We measure the optical depth by taking a series of three images at the conclusion of an experimental cycle. First, we measure $I_A(x, y)$, the intensity of the probe laser after transmitting the atomic sample. Then we take a second image to give $I_P(x, y)$, the intensity of the probe in the absence of atoms. Finally, we take the last shot, $I_{BG}(x, y)$, to measure the background intensity at the camera when the probe is off. The column density can then be extracted by processing the images according to

$$D_{\text{opt}}(x, y) = n_{\text{2D}}(x, y)\sigma_0 = -\ln\left(\frac{I_A(x, y) - I_{BG}(x, y)}{I_P(x, y) - I_{BG}(x, y)}\right). \tag{4.12}$$

---

[17]The σ_{eff} and $I_{\text{sat}}^{\text{eff}}$ parameters are modified by the same α factor because for a two-level atom, $\sigma_0 \propto I_{\text{sat}}^{-1}$.

This method of measuring optical depth is known as absorption imaging. One downside of this technique is that the measurement of large optical densities is noisy as the fraction of photons transmitting the cloud decreases. One way to get around this problem is to increase the light in the probe pulse. However, this requires considering the full form of the Beer-Lampert law to properly account for the effects of saturation.

Integrating the full form of Eq. (4.9) results in [158, 159]

$$D_{\mathrm{opt}}(x, y) = n_{\mathrm{2D}}(x, y)\sigma_0 = -\alpha(1 + 4\delta^2/\Gamma^2)\ln\left(\frac{I_A(x, y) - I_{BG}(x, y)}{I_P(x, y) - I_{BG}(x, y)}\right) + \frac{I_P(x, y) - I_A(x, y)}{I_{\mathrm{sat}}}.$$
(4.13)

If $I_A, I_P \ll I_{\mathrm{sat}}$, we can neglect the second term and recover the low intensity form of Eq. (4.12). However, for large intensities the second term becomes significant and we must consider the intensities relative to the saturation intensity. In this regime, accurately determining $n_{\mathrm{2D}}(x, y)$ requires calibrating two values: α and the camera counts that correspond to I_{sat}.

We can attempt to calibrate or control α and I_{sat} using offline methods that don't require atomic samples. For example, we can estimate I_{sat} by placing a small aperture in the probe beam such that the entire beam can be imaged by the CCD. We then measure the total counts on the camera as well as the steady state power in the beam using a power meter as close to the main chamber as possible. Using the known magnification of the imaging system and camera pixel size, we can back out the approximate counts per camera pixel that corresponds to $I = I_{\mathrm{sat}}$ at the atoms. Unfortunately, this method is prone to systematic errors from various sources such as optical losses between the location we place the power meter and the center of the vacuum chamber, or deviations from an ideal square wave of the 10 μs imaging pulse. We can also attempt to minimize α by using a cleanly polarized probe beam and a well defined magnetic field. However, it would be helpful to develop some techniques that use the atomic sample to calibrate these parameters.

Other groups have used a couple different approaches to this problem. Reinaudi *et*
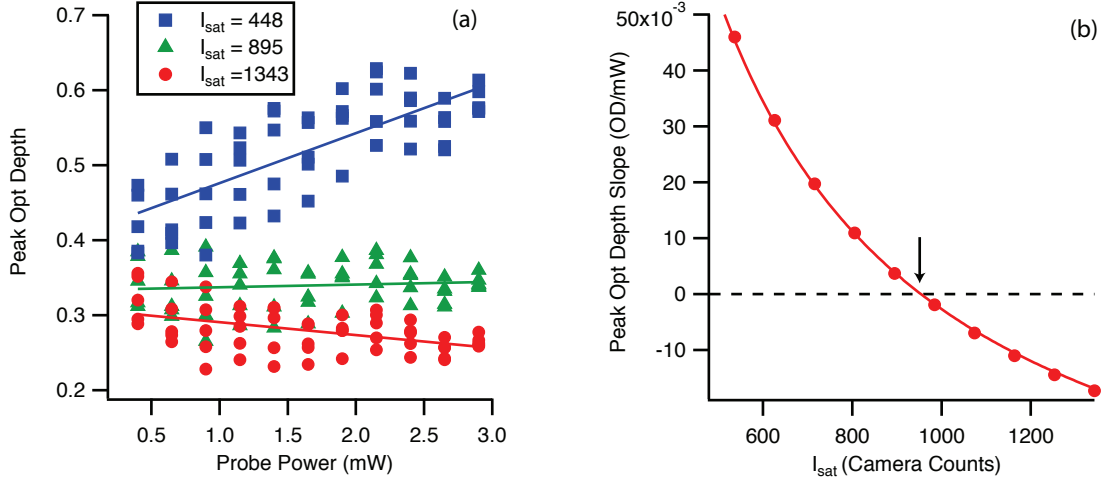
Figure 4.16: Example calibration of I_{sat}. We image a cloud of ^{84}Sr atoms at various probe powers. The optical depth is computed using Eq. (4.13) with $\delta = 0$, $\alpha = 1$, and various parameters for I_{sat}. (a) The peak optical depth of the cloud as a function of probe power for three different I_{sat} values. (b) The slope of optical depth vs probe power as a function of I_{sat}. The curve crosses zero at $\simeq 950$, indicated by the arrow, which is the calibration result. This is a 10% correction from the estimated value of I_{sat} measured by placing a pinhole in the path of the probe beam such that the entire beam is incident on the camera and comparing the counts recorded on the camera to the power in the beam measured by a power meter.

al. calibrated I_{sat} using offline methods and determined α by imaging their atomic sample with different probe intensities and found the value of α that gave peak optical densities that were independent of probe intensity [158]. Hueck *et al.* took a different approach that used other techniques to carefully purify the polarization and alignment of their magnetic field to justify using $\alpha = 1$. They then calibrated I_{sat} by measuring the momentum transferred to an atomic cloud as a function of probe intensity using an auxiliary imaging system with an orthogonal orientation [159].

Luckily for us, the atomic structure of bosonic strontium is very simple. There is only one $m_J = 0$ ground state so we don't have to worry about the ground state spin population. In addition, if we do a careful job shimming stray magnetic fields, the three Zeeman levels in the excited, $^1P_1$ state will be degenerate and the scattering cross section, σ_{eff}, will be independent of probe polarization. Therefore we can safely take $\alpha = 1$. To calibrate the remaining parameter, I_{sat}, we use a similar technique to [158]. We take a series of images using different probe intensities and find the I_{sat} value that yields a

peak optical density that is independent of probe power, see Fig. 4.16. This approach successfully avoids the systematic errors inherent in measuring I_sat directly.

Imaging of ^{87}Sr is more complicated. As shown in Table 1.1, the splittings between the various hyperfine states in the $^1P_1$ level are only 17 and 43 MHz, which are not large compared to the 30.5 MHz linewidth of the transition. D. Barker has performed numerical simulations of the optical Bloch equations governing the optical pumping dynamics during the imaging pulse. His work is described in Appendix A of his thesis [131], and also builds on a similar calculation in P. Mickelson's thesis [113]. These simulations show that the effective cross section of ^{87}Sr is reduced from that of the bosons by a factor that depends on the imaging beam detuning, intensity, and polarization. We generated lookup tables based on these results that are referenced by our imaging analysis software in order to correct for the reduced cross section. The calculation of these corrections is the equivalent of determining the correction factor α as described above. This method, along with a direct measurement if I_sat, was used to analyze the results in Sec. 3.7.

In the future, we could adapt the technique described above to determine α empirically. After calibrating I_sat using a bosonic sample, we could similarly image a fermionic sample with varying probe powers and find the value of α that yields a peak optical depth that is independent of probe intensity. This technique should do a better job of capturing effects that are not considered in the optical Bloch equation simulations, such as imperfect probe polarization or unbalanced ground state spin populations.

Another important consideration when choosing imaging parameters is to ensure that blurring due to atomic motion is smaller than the imaging system resolution. The velocity of an atom transverse to the probe beam is random with a rms value given by $v_\text{rms} = \sqrt{N_p} v_\text{rec}$ where N_p is the number of photons scattered during the imaging pulse of duration τ_p and $v_\text{rec} = \hbar k / m \approx 9.8$ mm/s for the 461-nm transition in strontium. This random velocity leads to a random displacement of $r_\text{rms} = v_\text{rms} \tau_p / \sqrt{3}$ [130]. The scattering rate depends on the probe detuning and intensity, but has a maximum value of $\Gamma/2$ for zero

detuning and $I \gg I_{\text{sat}}$. Therefore $r_{\text{rms}} \lesssim \text{v}_{\text{rec}}\sqrt{\Gamma \tau_p^3/6}$. We use imaging pulses of 10 μs which yields $r_{\text{rms}} \lesssim 2$ μm. This displacement is less than the resolution of our imaging systems.

4.4   Magnetic Field Coils

We use several sets of electromagnetic coils to carefully control the magnetic fields used in our experiment. High-current coils generate the magnetic field profiles used for the Zeeman slower and MOT. In addition, we have three pairs of low current "shim" coils that are used to cancel residual magnetic fields in the main chamber.

The Zeeman slower, as described in Sec. 3.2, uses a variable magnetic field profile to compensate for the changing Doppler shift as a hot atomic beam is decelerated by a counter-propagating laser. The designed magnetic field profile in the slowing region is illustrated in Fig. 3.1b and is generated by two variable pitch magnetic field coils. The coils are operated with currents in opposing directions in order to generate a field zero in the slowing region. As mentioned earlier, there are two advantages to this design. First, a smaller overall field magnitude is needed which reduces the maximum currents needed. Second, the field outside the slowing region damps to zero much faster so that the atoms can exit the slower cleanly. We also include a third coil that is used to cancel residual fields at the location of the MOT. The Zeeman slower was designed by D. Barker and more details about the designed and measured field profiles can be found in his thesis [131].

We constructed the slower using hollow, square profile tubing 0.427 cm wide (purchased from Small Tube Products with a Kapton coating by S&W Wire Co.). The tubing was wound onto an aluminum form with a 1.51 inch diameter and held in place with a high temperature epoxy. We use high current power supplies (Sorenson XG 8-100 or XG 12-70) to drive each of the three Zeeman slower coils with 30-40 A of current.

The quadrupole MOT fields are generated by a pair of coils mounted in the recessed viewports above and below the main chamber and operated with current flowing in opposite

directions (anti-Helmholtz configuration). Each coil consists of 6 layers of 8 turns of the same tubing that was used for the Zeeman slower. The coils are separated by 9.18 cm and generate a field gradient of 0.96 G cm^{-1} A^{-1} in the vertical direction. Our experimental cycle uses up to $\simeq$ 60 A of current during the bMOT to generate a gradient of $\simeq$ 58 G/cm. The power supply for the MOT coils is a TDK-Lambda GEN40-125.

The current in each of the Zeeman slower and MOT coils is monitored by Hall sensors (F.W. Bell CSLM-50LA or CSLM-100LA). We actively stabilize the measured current using feedback to the gate voltage of a bank of N-type power MOSFETs (STMicroelectronics STE250N510). The transition from the bMOT/metastable reservoir to the rMOT requires quickly changing the MOT gradient from 58 G/cm to 1.5 G/cm. Unfortunately, the switching speed of the coils is limited by their large inductance ($\approx$ 375 μH). We facilitate fast switching by using a snubber circuit, consisting of a flyback diode and a 5 Ω resistor, that reduces the time constant of the LR-circuit to $\approx$ 75 μs. To avoid heating due to the large currents being used, we actively cool each coil and the MOSFET banks using chilled water. See [131] for more details about the water cooling and measured magnetic field profiles.

In addition to the high-field coils described above, we also have three pairs of low-current "shim" coils that we use to precisely cancel residual magnetic fields or apply small bias fields at the center of the main chamber. These coils were constructed by simply wrapping 16 AWG wire directly around the main chamber CF viewports. The coils for the x and y axes are wrapped onto 4.5 inch viewports using two layers of 13 turns each, while the z direction coils are wrapped onto the 8 inch recessed viewports with a single layer of 26 turns. We can apply up to 6 A of current to each pair of coils using Agilent E3614A power supplies. This means we can supply up to $\approx$ 4 G in the x and y directions and up to $\approx$ 9 G in the z direction. The field profile in the z direction is more uniform because the geometry of those coils is closer to the Helmholtz configuration. We find calibrate the fields by measuring the Zeeman shifts of the $^1S_0 \rightarrow {}^3P_1$ transition in a ^{84}Sr BEC.

4.5 Computer Control

Each run of our experiment consists of a recipe of steps that must be performed with a timing accuracy of $\approx \mu$s. Like many of the other atomic physics labs in the JQI, we use a Labview program called Setlist to generate the list of parameters and to precisely disseminate the timing signals to the various equipment around the lab. Early versions of Setlist were written by I. Spielman, though an updated, object-oriented version was written by Z. Siegel, J. Tiamsuphat, and C. Herold in 2014. The newer version included many usability improvements and also modularized the code in order to make it easier add new devices. Additional fixes, features, and devices have been added by Z. Smith, N. Pisenti, D. Barker, and myself.[18] The main Setlist interface is a table where each column describes the settings of a particular piece of equipment (e.g. the frequency of a DDS or the voltage of an analog output channel) and each row of the table is a timestep with a variable duration. Settings can be ramped using arbitrary shapes during a single row of the table. A master device provides timing information to the various slave devices so that they can synchronously cycle through their programmed states specified in the Setlist table. In our case, the master device is an FPGA-based PulseBlaster USB by Spincore Technologies, which provides pulses as short as 50 ns with 10 ns resolution. We have a variety of slave devices, including National Instruments DAQ cards (with digital and analog output channels), a linear actuator (Newport CONEX-LTA-HS, described in Sec. 4.3.1), external function generators (SRS DS345), a Digital Micromirror Device (DMD, Texas Instruments DLP Lightcrafter 3000), and a number of homebuilt Arduino controlled DDS's. The analog and digital output channels are buffered, and the digital channels are opto-isolated. These outputs are then distributed around to lab to trigger tasks such as turning on/off AOMs, opening/closing beam shutters, changing intensity lock setpoints, etc.

---

[18]The Setlist software can be found at https://github.com/JQIamo/SetList.

99

The images from our Flea, Grasshopper, and PIXIS cameras are captured using separate Labview programs. The acquisition of PIXIS images also involves a plug-in, written by D. Barker, to the Princeton Instruments Lightfield software. The raw data from these cameras are saved to the disk in Igor binary format. We use custom scripts in Igor Pro to import, process (see Sec. 4.3.2), and analyze the images.[19]

---

[19]Our analysis software can be found at https://github.com/JQIamo/sr-scripts.

Chapter 5:   Enhanced Magnetic Trap Loading

In our effort to optimize the experiment in order to generate degenerate gases of ^{84}Sr and ^{87}Sr, we investigated a technique to increase the loading rate of the magnetic trap. This work resulted in our group's first publication [160], which I reproduce here. See [131] for a short discussion of other methods of applying the depump laser that we investigated before settling on the approach used in the paper. Though we have changed our experimental procedure to load the rMOT directly from a repumped bMOT for our recent work, this technique could still be useful in the future, especially if we do any work involving isotopic mixtures.

The published work was a collaboration between Dan Barker, Neal Pisenti, Gretchen Campbell, and me. I built the experimental setup and designed the measurement procedure along with Dan. I also wrote the software that we used to lock the depump laser to the wavemeter. Neal, Dan and I took the experimental data while Dan wrote the first manuscript draft and developed the rate equation model. All the authors discussed the results and edited the manuscript.

5.1   Publication: Enhanced magnetic trap loading for atomic strontium

5.1.1   Abstract

We report on a technique to improve the continuous loading of atomic strontium into a magnetic trap from a Magneto-Optical Trap (MOT). This loading enhancement is achieved by adding a depumping laser tuned to the $^{3}P_1 \rightarrow {}^{3}S_1$ (688-nm) transition.

The depumping laser increases atom number in the magnetic trap and subsequent cooling stages by up to 65 % for the bosonic isotopes and up to 30 % for the fermionic isotope of strontium. We optimize this trap loading strategy with respect to the 688-nm laser detuning, intensity, and beam size. To understand the results, we develop a one-dimensional rate equation model of the system, which is in good agreement with the data. We discuss the use of other transitions in strontium for accelerated trap loading and the application of the technique to other alkaline-earth-like atoms.

5.1.2 Introduction

Alkaline-earth-like (AE) atoms have received a great deal of recent interest due to the distinctive properties of their level structure [30, 91]. The largely disconnected singlet and triplet states in these atoms give rise to forbidden optical transitions, which could form the basis for an improved time standard [161, 162]. These transitions are also advantageous in a wide variety of other applications. For example, their low photon-scattering rates allow for the production of highly-excited Rydberg atoms with reduced decoherence compared to alkali metals [54]. Magnetic-field-insensitive singlet and triplet levels make AE atoms attractive for precision measurement and quantum sensing applications [68, 70]. In fermionic isotopes, these states manifest $SU(2I + 1)$ spin symmetry, where I is the nuclear angular momentum, allowing quantum simulation of Hamiltonians that are inaccessible with alkali atoms [73, 78, 80]. All of these applications require or benefit from a combination of large atom number and short experimental cycle times.

Recent advances in cooling and trapping techniques enabled production of the first strontium degenerate gases [122, 123, 125, 126, 129]. The small negative s-wave scattering length of the most abundant isotope, ^{88}Sr, hampered initial efforts to create Bose-Einstein condensates [42, 124, 163–165]. While the other stable isotopes (^{87}Sr, ^{86}Sr, and ^{84}Sr) possess favorable scattering lengths, their low natural abundance initially prevented Magneto-Optical Traps (MOT) from collecting enough atoms to reach degeneracy. Fortu-

(5s6s) $^3S_1$

(5s5p) $^1P_1$ $\Gamma/2\pi \approx 610$ s^{-1}

$\Gamma/2\pi \approx 105$ s^{-1}

(5s4d) $^1D_2$

$\Gamma/2\pi \approx 210$ s^{-1}

(5s5p) $^3P_2$
(5s5p) $^3P_1$
(5s5p) $^3P_0$

707 nm $\Gamma/2\pi \approx 7\times10^6$ s^{-1}
688 nm $\Gamma/2\pi \approx 4.3\times10^6$ s^{-1}
679 nm $\Gamma/2\pi \approx 1.4\times10^6$ s^{-1}

bMOT
461 nm
$\Gamma/2\pi \approx 30.5$ MHz

rMOT
689 nm
$\Gamma/2\pi \approx 7.5$ kHz

(5s^2) $^1S_0$
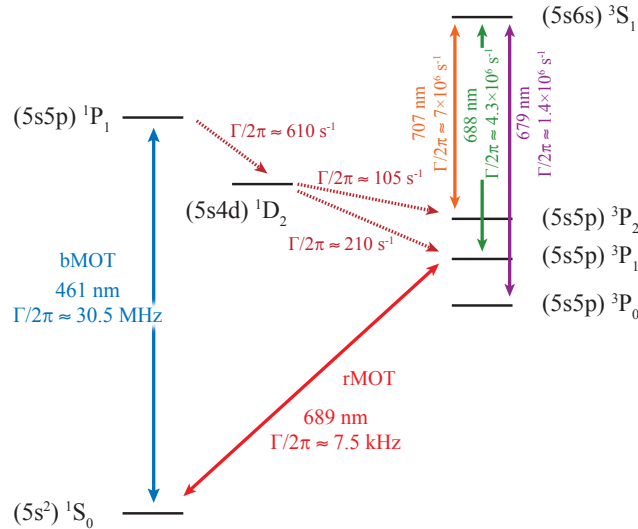
Figure 5.1: The low-lying energy levels of bosonic strontium with linewidths and natural decay rates taken from [87–91]. A Magneto-Optical Trap operating on the blue, 461-nm transition (bMOT) captures atoms from a Zeeman-slowed beam. Atoms in the bMOT continuously leak into the long-lived $^3P_2$ state, which is magnetically trapped by the bMOT quadrupole field. Two lasers at 688 nm and 679 nm increase the magnetic trap loading rate by pumping atoms that populate $^3P_1$ into $^3P_2$. The 679-nm laser and a 707-nm laser return atoms to the ground state via the $^3P_1$ state once magnetic trap loading is complete. A Magneto-Optical Trap operating on the red, 689-nm transition (rMOT) then cools the sample to ≈ 1 μK.

itously, laser cooling of strontium on the 461-nm line populates a magnetically-confined, metastable reservoir of atoms in the $^3P_2$ state (see Fig. 5.1) [117]. The long lifetime of this reservoir (typically $\gtrsim$10 s) compared to the MOT allows for the accumulation of sufficient populations of ^{87}Sr, ^{86}Sr, or ^{84}Sr for forced evaporation or sympathetic cooling of ^{88}Sr [122, 123, 125, 126, 129]. The ≈ 1 μK temperatures attainable with laser cooling on the 689-nm, intercombination transition (Fig. 5.1) lead to short evaporation times to reach degeneracy. Given the low abundance of the interacting isotopes, the short evaporation time means that the reservoir loading time usually dominates the experimental cycle [115, 122, 126, 129].

Typical Sr degenerate gas experiments first use a MOT operating on the $^1S_0 \rightarrow {}^1P_1$, 461-nm transition (bMOT) to capture atoms from a Zeeman-slowed atomic beam and cool them to ≈ 1 mK. Atoms slowly leak out of the bMOT cooling cycle (1:50,000 branching ratio) and into the metastable ^3P manifold, where they populate the $^3P_2$ and $^3P_1$ states in a
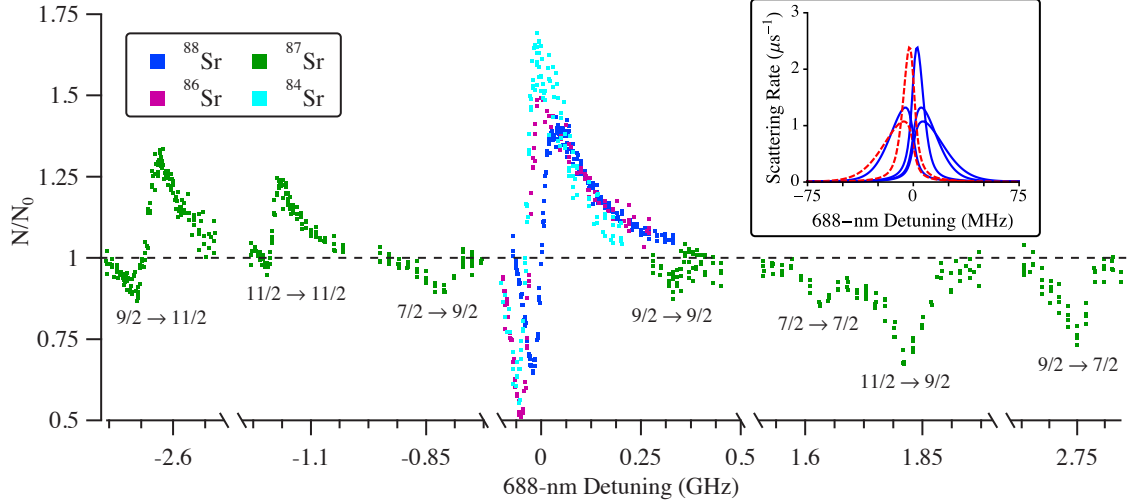
Figure 5.2: Measured atom number enhancement as a function of 688-nm laser detuning, Δ_{688}, for all strontium isotopes. The detuning zero is referenced to ^{88}Sr. For the data shown, the rMOT recaptures the less abundant isotopes and the bMOT recaptures ^{88}Sr. The depumper saturation parameter was $s_{688} \approx 35$ (≈ 50) for ^{88}Sr (^{87}Sr, ^{86}Sr, ^{84}Sr) and the 679-nm laser detuning, Δ_{679}, was set to maximize bMOT fluorescence. We label the fermionic hyperfine transitions with $F \rightarrow F'$, where F is the total angular momentum quantum number for $^3P_1$ and F' the corresponding quantum number for $^3S_1$. Inset: The detuning-dependent scattering rate for each transition between $^3P_1$ and $^3S_1$ Zeeman levels, averaged over the volume of a one-dimensional bMOT with $s_{688} = 1$ (see Sec. 5.1.5). Solid blue curves pump to a $^3S_1$ Zeeman level that can decay to a magnetically trappable $^3P_2$ Zeeman state, but dashed red curves do not. Asymmetric lineshapes arise in the atom number enhancement because the dashed red scattering rate curves dominate at negative detuning.

1:2 ratio [87,88]. The bMOT quadrupole field can magnetically trap atoms in the $^3P_2$ state (the Landé g-factor is $g_J = 3/2$ for bosonic isotopes, where J is the electronic angular momentum). Repumping lasers return $^3P_2$ atoms to the ground state once magnetic trap loading is complete, which, depending on the isotope, can take 30 s or more [115,126,129]. Loading times are also long for experiments with isotopic mixtures, since the isotope shifts of the 461-nm transition are on the same order of magnitude as the linewidth [115, 122]. Such small isotope shifts prohibit efficient simultaneous loading of the magnetic trap. A second stage Magneto-Optical Trap using the 689-nm, intercombination line (rMOT) cools these atoms to $\approx 1 \ \mu$K and facilitates loading into an optical dipole trap. Evaporation proceeds quickly due to the low initial temperature and degeneracy can be reached in ≈ 1 s for most isotopes [115].

Here we present a technique to reduce the reservoir loading time or, equivalently, increase the atom number for experiments with strontium, as first suggested in [114]. The

method relies on continuous optical pumping of atoms from the short-lived $^3P_1$ state into the magnetically trapped $^3P_2$ reservoir using the $^3P_1 \rightarrow {}^3S_1$, 688-nm transition. This optical pumping greatly reduces the steady-state atom number in the bMOT, but increases the flux of low-field seeking atoms into the metastable reservoir. Although the $^3P_2{:}^3P_1$ branching ratio from the $^1D_2$ state suggests that atom number should be enhanced by a factor of three (see Fig. 5.1), we show that this estimate is incorrect since it does not consider the reduction in bMOT atom number caused by the 688-nm laser.

We describe our experimental apparatus in Sec. 5.1.3 with an emphasis on the details relevant for the accelerated loading scheme. Sec. 5.1.4 explains the measurement procedure and results. In Sec. 5.1.5, we develop a rate equation model and demonstrate that our data is in agreement with expectations. We also simulate the trap loading enhancement for several other transitions in strontium and two in calcium. Sec. 5.1.6 is a summary of our results and give an outlook for future advances.

5.1.3   Apparatus

Our experimental setup is similar to other strontium apparatuses designed for optical clock and degenerate gas experiments [57,113,114,146]. An oven with a microtubule array nozzle, heated to 600 °C, creates an atomic strontium beam. Two stages of differential pumping prevent the pressure in the experiment chamber (6×10^{-11} Torr) from rising while the oven is in operation. The atomic beam passes through a transverse cooling stage, which consists of two orthogonal, retroreflected 461-nm laser beams. Each beam has ≈ 10 mW of power, a 1:3 aspect ratio ($1/e^2$ radius of 9 mm along the atomic beam axis), and -10 MHz detuning from the $^1S_0 \rightarrow {}^1P_1$ transition. The Zeeman slower is a 35-cm long, multilayer, variable-pitch coil located immediately after the transverse cooling stage. The Zeeman slower is pumped with ≈ 48 mW of -600 MHz detuned 461-nm light, which is focused onto the oven nozzle with an initial $1/e^2$ radius of 5 mm.

The bMOT has a standard retroreflected, three-beam configuration. Each beam
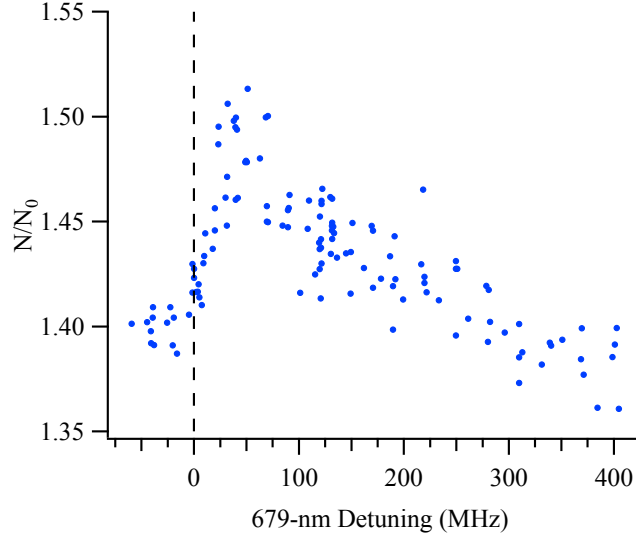
Figure 5.3: N/N_0 for ^{88}Sr recaptured in the bMOT as a function of Δ_{679}. The 688-nm laser has $s_{688} \approx 35$ and $\Delta_{688} \approx 30$ MHz. We reference the 679-nm detuning to the bMOT fluorescence maximum, indicated by the dashed vertical line. As shown in the inset to Fig. 5.2, the asymmetry arises from detuning-dependent scattering rates. Transitions to $^3S_1$ Zeeman levels that can decay into the magnetic trap are predominately blue detuned, whereas red detuned transitions populate levels that decay to high-field seeking $^3P_2$ Zeeman states.

has a $1/e^2$ radius of 8 mm, a detuning $\Delta_{461} = -45$ MHz, and contains either ≈ 7 mW (for bosonic isotope data) or ≈ 9 mW (for ^{87}Sr data) of power. These parameters give $s_{461} = I/I_{sat} \approx 0.16$ per beam for the bosons and $s_{461} \approx 0.21$ per beam for the fermion. The quadrupole coil has a vertical axis of symmetry and produces a magnetic field gradient of 6 mT/cm along that axis during bMOT operation. The bMOT field gradient is sufficient for magnetically trapping of $^3P_2$ atoms in the low-field-seeking $|m_J = 1\rangle$ and $|m_J = 2\rangle$ Zeeman sublevels. In our vacuum chamber, the position of two recessed viewports along the symmetry axis of the coils limits the trap depth for the $|m_J = 1\rangle$ state to ≈ 5 mK. This limitation is unimportant for us since our bMOT loads ≈ 1 mK atoms into the magnetic trap, but it suggests that experiments with larger vacuum chambers may find that a higher temperature bMOT optimizes magnetic trap loading [114].

Two repumping lasers addressing the 679-nm, $^3P_0 \rightarrow {}^3S_1$ and the 707-nm, $^3P_2 \rightarrow {}^3S_1$ transitions are used to return $^3P_2$ atoms in the magnetic trap to the ground state. The two beams co-propagate with the Zeeman slower beam, share a $1/e^2$ radius of ≈ 1 cm,

and contain $\approx$2.5 mW (679 nm) and $\approx$4.5 mW (707 nm) of power. For experiments with the bosonic isotopes, we lock the repump laser frequencies using slow feedback from a HighFinesse WS7 wavemeter.[1] The locking stability is $\pm$5 MHz, which is much narrower than the observed bosonic repumping linewidth.[2] The presence of hyperfine structure in the fermion complicates repumping on the $^3P_2 \rightarrow {}^3S_1$ transition. In order to cover as much of the $\approx$5.5 GHz hyperfine spectrum of the transition as possible, we modulate the 707-nm laser frequency at $\approx$700 Hz. To increase coverage of the hyperfine spectrum further, we use a second 707-nm laser that we modulate at $\approx$600 Hz. When optimized, application of the second laser to the experiment increases the ^{87}Sr atom number by about 10 %. For the fermionic data, the 679-nm laser is locked to the $|^3P_0, F = 9/2\rangle \rightarrow |^3S_1, F = 11/2\rangle$ transition (where $F = I + J$) using the wavemeter.

The linewidth of our 689-nm master oscillator is stabilized below the natural linewidth of the $^1S_0 \rightarrow {}^3P_1$ resonance using a Pound-Drever-Hall lock to an optical cavity (finesse $\approx$240, 000) [147]. We injection lock a slave laser diode to the master to obtain sufficient power for trapping (for the fermion, this laser pumps the $|^1S_0, F = 9/2\rangle \rightarrow |^3P_1, F = 11/2\rangle$ transition). Dichroic beamsplitters overlap the 689-nm light for the rMOT with the bMOT beams. In each rMOT arm, the power is $\approx$3.5 mW and the $1/e^2$ radius is 2.5 mm. The quadrupole field gradient switches to 0.16 mT/cm for rMOT operation. For the first 100 ms of rMOT operation, we frequency modulate the trapping laser at 30 kHz with a modulation depth of 1 MHz to increase the capture velocity of the rMOT. Over the next 400 ms, we linearly reduce the modulation depth to 100 kHz while simultaneously ramping the optical power to 100 μW with a half-Gaussian temporal profile. In this work, we terminate rMOT operation at this stage ($T \approx 2\ \mu$K), but we can cool further by turning off the frequency modulation and reducing the intensity.

---

[1] The identification of commercial products is for information only and does not imply recommendation or endorsement by the National Institute of Standards and Technology.

[2] The WS7 wavemeter resolution is specified to be 10 MHz, but we find that it can reliably detect 1 MHz frequency offsets.

The hyperfine structure of the fermion requires the use of a second slave laser to make a stable rMOT [32]. A beatnote lock to the master stabilizes the second laser to the $|^1S_0, F = 9/2\rangle \rightarrow |^3P_1, F = 9/2\rangle$ line [141]. The second slave laser provides $\approx 800\ \mu$W of light per rMOT beam to the experiment. Aside from the reduction in initial power, the intensity and modulation ramps are identical to those for the trapping laser. We also linearly increase the rMOT magnetic field gradient to 0.24 mT/cm during the final 400 ms of the rMOT when trapping ^{87}Sr to increase the atomic density.

To enhance magnetic trap loading, a 688-nm laser resonant with the $^3P_1 \rightarrow {}^3S_1$ transition pumps atoms that decay to $^3P_1$ out of the bMOT cycle and into $^3P_2$. We call this laser the depumper because it makes the bMOT transition less closed. The depumper is a Littman-Metcalf configuration laser that we built using a laser diode (model HL6738MG[1]) that was AR-coated in-house.[3] The laser provides up to 2.8 mW of light to the experiment, which corresponds to $s_{688} = I/I_{sat} \approx 50$. The 688-nm beam enters the chamber horizontally and perpendicular to the Zeeman slower axis. This beam has a $1/e^2$ radius $w_{688} = 1.35$ mm except where otherwise noted. We stabilize the 688-nm laser detuning, Δ_{688}, to within ± 3 MHz by locking to the wavemeter.

We measure the magnetic trap loading enhancement by interleaving shots with the 688-nm laser on and off. The 679-nm repumping laser closes the $^3S_1 \rightarrow {}^3P_0$ leak to increase the depumper's effect. This repumping laser remains on during both shots of a depumper on/off pair of experimental runs, but does not affect trap loading when the 688-nm laser is off since the bMOT does not populate $^3P_0$. After 0.5 s to 30 s of reservoir loading, an acousto-optic modulator extinguishes the 688-nm beam and optical shutters open to allow 707-nm light to reach the experiment. Either the bMOT or the rMOT can recapture atoms from the magnetic trap for detection and imaging. However, rMOT recapture greatly improves signal-to-noise for ^{87}Sr, ^{86}Sr, and ^{84}Sr, so we use the rMOT

---

[3] The anti-reflection coating is comprised of two layers, as suggested in [150]: one layer of Al_2O_3 to bring the facet coating to $\lambda/2$, and a final $\lambda/4$ layer of HfO_2. The deposition was done via electron beam evaporation, and monitored in-situ by scanning the diode current across the lasing threshold.
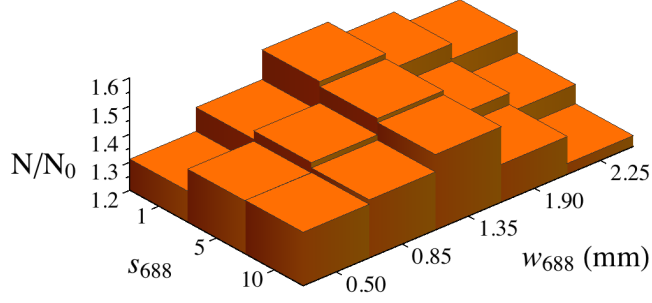
Figure 5.4: N/N_0 for ^{88}Sr recaptured in the bMOT versus s_{688} and w_{688}, where w_{688} is the $1/e^2$ radius of the depump beam. The standard errors are omitted for clarity, but are $\lesssim 0.03$. The optimal trap enhancement occurs when w_{688} roughly matches the $1/e$ radius of the bMOT and $s_{688} \approx 1$. Δ_{688} and Δ_{679} are both ≈ 30 MHz (corresponding to the maxima in Figs. 5.2 and 5.3).

exclusively for recapture of these isotopes. The bMOT recapture stage lasts 100 ms and rMOT recapture consists of the full rMOT cycle described above. We take an absorption image after a 1 ms (25 ms) ballistic expansion for bMOT (rMOT) recapture using a resonant, 10 μs pulse of 461-nm light with $I/I_{sat} \approx 0.04$. Numerical integration of the image yields the atom number for each shot.

5.1.4 Results

We study the magnetic trap loading enhancement as a function of isotope, power, detuning, and beam size. The enhancement is measured by comparing the atom number recaptured in the rMOT or bMOT with and without the 688-nm laser. We find that the depumper's effect is independent of which MOT we use for atom recapture. The magnetic trap loading enhancement is given by the normalized atom number, N/N_0, where N is the atom number with the depumper on and N_0 the number with it off.

We investigate the loading enhancement as we scan the depumper across the 688-nm transition. For this data set, we set $s_{688} \approx 35$ for ^{88}Sr and $s_{688} \approx 50$ for all other isotopes. The repump laser frequencies are locked to maximize bMOT fluorescence. The magnetic trap loading time, t_{load}, for $\{^{88}$Sr, ^{87}Sr, ^{86}Sr, ^{84}Sr$\}$ is $\{1.5$ s, 10 s, 6 s, 7.5 s$\}$ resulting in typical N_0 of $\{2 \times 10^7, 5 \times 10^6, 1 \times 10^7, 8 \times 10^5\}$ in the rMOT. Adjustment of the wavemeter
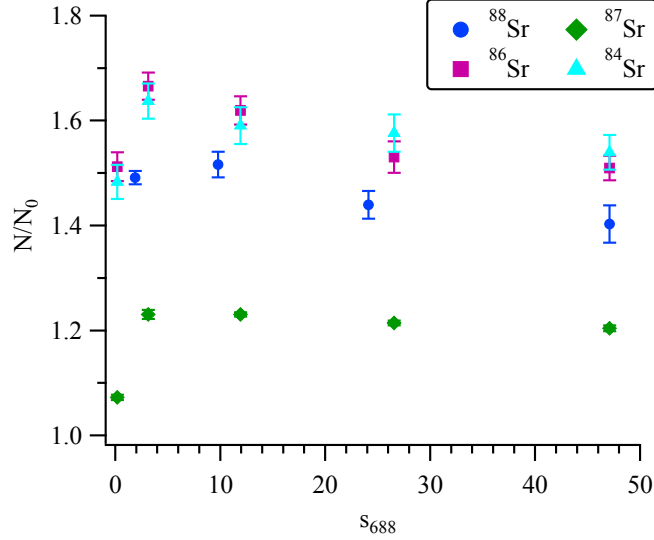
Figure 5.5: Atom number enhancement versus s_{688} with $w_{688} = 1.35$ mm. ^{87}Sr data are for the $F = 11/2 \rightarrow F' = 11/2$ transition and all isotopes are recaptured in the rMOT. Error bars represent the standard error in the mean for ≥ 10 measurements. The 688-nm and 679-nm laser detunings are set to ≈ 30 MHz.

lockpoint allows us to scan Δ_{688}. Fig. 5.2 shows the depumping spectrum for all isotopes and hyperfine transitions, the locations of which are in good agreement with [95]. On average, we observe trap loading improvements of ≈ 50 % for bosonic isotopes and ≈ 25 % for the fermionic isotope even without detailed optimization of the depumping parameters. The peak enhancement for each isotope occurs when $\Delta_{688} \approx 30$ MHz from resonance. In Fig. 5.2 we also see that the choice of hyperfine transition is crucial for atom number gains in ^{87}Sr. Pumping to $|{}^3S_1, F = 7/2\rangle$ and $|{}^3S_1, F = 9/2\rangle$ is always detrimental because these manifolds decay with ≥ 60 % probability to $|{}^3P_2, F = 7/2\rangle$ and $|{}^3P_2, F = 9/2\rangle$, which have Landé g-factors too small for magnetic trapping at the bMOT field gradient. Pumping to $|{}^3S_1, F = 11/2\rangle$ yields a lineshape similar to that of bosonic isotopes, but with reduced amplitude.

The asymmetric lineshapes observed in Fig. 5.2 are due to the non-uniform magnetic fields in the bMOT. Quadrupole fields shift low-field-seeking states to higher energy and high-field-seeking states to lower energy. Because the Landé g-factor for $^3S_1$ is larger than for $^3P_1$, this effect causes a blueshift for most transitions to $^3S_1$ states that can decay to

$|^3P_2, m_J = 1\rangle$ or $|^3P_2, m_J = 2\rangle$ (see inset to Fig 5.2). For the same reason, transitions to $^3S_1$ states that can only populate untrapped $^3P_2$ Zeeman states are redshifted. As a result, trap loading is enhanced to the blue of resonance and reduced to the red of resonance.

For this depumping scheme, application of the 679-nm laser during the bMOT is crucial; removing the 679-nm laser results in $\approx 50\%$ reduction of the enhancement. The effect of the 679-nm laser was studied by varying its detuning, Δ_{679}. As shown in Fig. 5.3, setting $\Delta_{679} \approx 30$ MHz (relative to the detuning that maximizes the bMOT fluorescence) adds an additional $\approx 10\%$ to the enhancement. The asymmetric lineshape is caused by the same mechanism discussed above for the 688-nm transition.

With Δ_{688} and Δ_{679} stabilized at their optimized values, we study the trap loading enhancement for ^{88}Sr as a function of s_{688} and w_{688}. Slight focusing/defocusing of the 688-nm beam changes the waist at the location of the bMOT, but the Rayleigh range is always larger than the bMOT $1/e$ radius, r_{bMOT}, for the parameter range we study. Fig. 5.4 shows that trap loading enhancement increases with s_{688} provided $w_{688} \lesssim r_{\text{bMOT}}$, with the optimal enhancement occurring when $w_{688} \simeq r_{\text{bMOT}}$. High s_{688} increasingly reduces N/N_0 for larger beam waists. The data suggest that, for our bMOT parameters, a substantial number of atoms populate the ^3P manifold before being fully captured by the bMOT. These atoms exist outside the bMOT radius and are too hot for magnetic confinement, but they are cold enough that they do not leave the bMOT capture volume during the ≈ 1 ms decay time for the $^1P_1 \rightarrow {}^1D_2 \rightarrow {}^3P_1 \rightarrow {}^1S_0$ path. The effect of varying s_{688} and w_{688} in the other isotopes was similar to the ^{88}Sr results. In Fig. 5.5, we plot N/N_0 for a wider range of the saturation parameter at the optimum w_{688}. All isotopes exhibit a steep rise in trap loading enhancement for $s_{688} \lesssim 1$, followed by a shallow rolloff for $s_{688} > 1$. We find that the enhancement is sensitive to the 688-nm beam alignment and that the peak at $s_{688} \approx 1$ is present only when the beam traverses the center of the bMOT.

Before recapturing atoms from the magnetic trap, we do not first discard ground-state atoms remaining in the bMOT. Keeping the ground-state atoms increases both N and

N_0, but decreases their ratio. This choice biases our results toward lower enhancement values, particularly for short load times and for ^{88}Sr. However, the reduced N/N_0 is the appropriate metric for evaluating the loading enhancement in most experiments, since the cycle time is typically limited by N. In experiments with isotopic mixtures, in which bMOT atoms are lost before recapturing from the magnetic trap, the depumping technique is even more useful. If we remove the bMOT atoms before imaging, N/N_0 increases by up to 15 %.

Our technique reduces the trap loading time necessary to achieve a given atom number. For short trap loading times, N/N_0 is a measure of the increased loading rate achieved with the depumping laser. This regime is shown in Fig. 5.2. For longer trap loading times, the atom number will saturate. Experiments requiring atom numbers close to the saturation limit can expect even greater reductions in loading time than suggested by the initial loading rate. We demonstrate this effect by fitting $N(t)$ and $N_0(t)$ with $N(t) = N^{\mathrm{max}}(1 - e^{-\alpha t})$, where α is the loading time constant and N^{max} is the saturated atom number (see inset to Fig. 5.6). Inverting the fitted function yields the loading time necessary to reach a given atom number with the depumper on, $t(N)$, or with the depumper off, $t_0(N_0)$. We plot the loading time reduction factor, $\mathrm{LTRF}(N/N_0^{\mathrm{max}}) = t_0(N_0{=}N)/t(N)$, for ^{88}Sr and ^{84}Sr in Fig. 5.6. The loading time reduction diverges as $N \rightarrow N_0^{\mathrm{max}}$ since $N^{\mathrm{max}} > N_0^{\mathrm{max}}$. For example, to reach an atom number of $\approx N_0^{\mathrm{max}}$, the depumping technique can reduce the loading time by a factor of ≈ 3.

5.1.5   Simulation

To understand the enhancement better, we develop a one-dimensional rate equation model to simulate the bMOT depumping process. This was motivated by two features of our data: the asymmetric lineshapes depicted in Fig. 5.2, and the discrepancy between the observed performance and the 3× initial estimate given by the $^3P_2$:$^3P_1$ branching ratio. A simple calculation, based on analysis of the cascade of Clebsch-Gordan (CG) coefficients
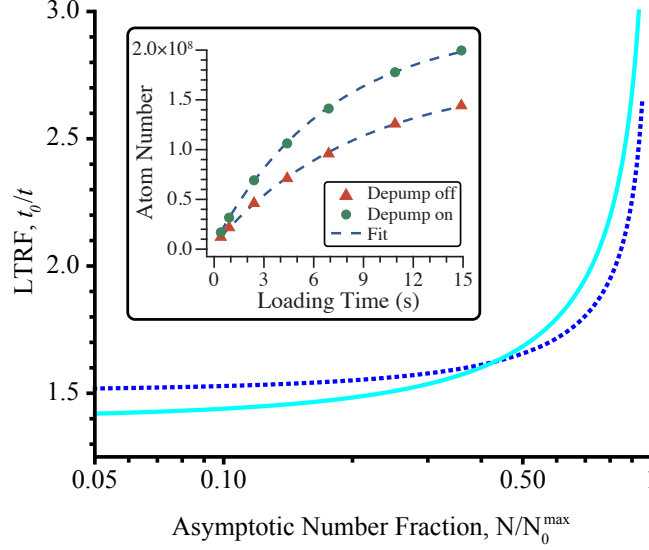
Figure 5.6: The Loading Time Reduction Factor (LTRF) for ^{88}Sr (dotted blue line) and ^{84}Sr (solid cyan line). The saturated atom number, N_0^{max}, is the asymptote of the trap loading curve with the 688-nm laser off (for ^{88}Sr, red triangles, inset). The loading time necessary to transfer N atoms into the rMOT with the depump laser on (off) is given by t (t_0). Inset: The raw data and fits associated with the ^{88}Sr (dotted blue) LTRF curve. The standard error is smaller than the data points. We find t and t_0 by inverting the appropriate fit function (see text).

connecting $^1P_1$ to $^3P_1$ and $^3P_2$, suggests that 3× trap loading enhancement is unlikely. However, this CG calculation depends sensitively on the relative populations of the $^1P_1$ Zeeman sublevels, which are position dependent, and the steady-state atom number in the bMOT. Both of these complications prevent analysis of experimental performance by this method. A full simulation of the optical pumping dynamics resolves both of these issues, allowing direct comparison of data with theory. Straightforward modifications of the rate equation model allow us to compare our technique to alternative depumping transitions.

In the rate equation model, we track the population, P_{i,m_i}, in each magnetic sublevel of $i \in \{^1S_0, {}^1P_1, \ldots, {}^3S_1\}$, with m_i the spin projection along the axis of a one-dimensional bMOT. Each level decays at a rate given by the appropriate linewidth, γ_{ij}, from Fig. 5.1,

$$\Gamma^{decay}_{|i,m_i\rangle \rightarrow |j,m_j;\ m_\gamma\rangle} = \gamma_{ij} \left| \langle j, m_j; 1, m_\gamma | i, m_i \rangle \right|^2 , \qquad (5.1)$$

where $\langle i, m_i; 1, m_\gamma | j, m_j \rangle$ is the CG coefficient. In addition to the transitions shown in

113

Fig. 5.1, we also include the $^1D_2 \to {}^1S_0$ quadrupole decay because its linewidth is non-negligible compared to decay rates into the ^3P states [87]. Since we are not interested in individual atom trajectories, we average the driven excitation rate for $|i, m_i\rangle \to |j, m_j\rangle$, $\Gamma^{exc}_{|i,m_i;\ m_\gamma\rangle \to |j,m_j\rangle}$, over the position and velocity distribution of the MOT,

$$\rho(x, v) = \frac{e^{-mv^2/2k_bT} e^{-(x/r_{bMOT})^2}}{\pi r^2_{bMOT}\sqrt{2\pi k_B T/m}} \ . \tag{5.2}$$

For the $^3P_0 \to {}^3S_1$ and $^3P_1 \to {}^3S_1$ transitions, we arrive at

$$\begin{aligned}
&\Gamma^{exc}_{|i,m_i;\ m_\gamma\rangle \to |j,m_j\rangle} = \\
&\int\limits_{0,\ -v_{max}}^{x_{max},\ v_{max}}\!\!\!\!\!\rho(x,v)\frac{s_{ij}\ \gamma_{ij}\ \sigma(m_\gamma)\left|\langle i, m_i; 1, m_\gamma|j, m_j\rangle\right|^2}{1 + s_{ij} + 4(\Delta_{m_i m_j}/\gamma_{ij})^2}dx\,dv\,,
\end{aligned} \tag{5.3}$$

where s_{ij} is the saturation parameter, $\sigma(m_\gamma)$ is the fraction of s_{ij} with polarization $m_\gamma \in \{-1, 0, 1\}$, and the effective detuning between $|i, m_i\rangle$ and $|j, m_j\rangle$, $\Delta_{m_i m_j}$, includes Doppler and Zeeman shifts. We choose x_{max}, v_{max} to be much larger than the characteristic scale of $\rho(x, v)$. The symmetry of a one-dimensional MOT permits us to model only the $x > 0$ region with all scattering rates then multiplied by two. This choice simplifies the tracking of magnetically trapped atoms because the magnetic field does not change sign in the simulation volume. Taking the transformation $s_{ij} \to 2s_{ij}$ in Eq. (5.3) while maintaining $\Sigma_{m_\gamma}\sigma(m_\gamma) = 1$ gives the correct scattering rate for the two bMOT beams. We assume a pure circular polarization for both bMOT beams and a random polarization for the repumper and depumper.

We describe the evolution of the populations, $\{P_{i,m_i}\}$, with a system of coupled
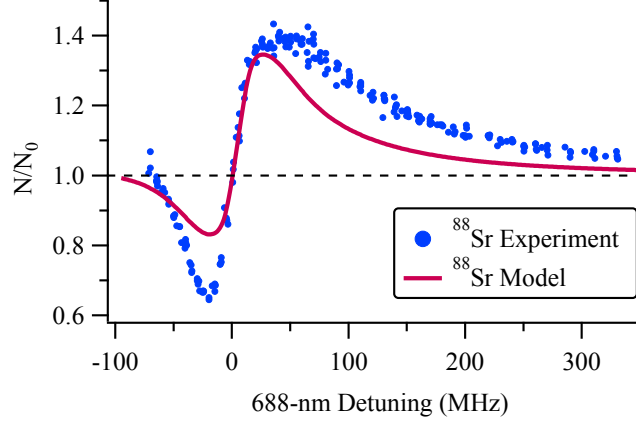
Figure 5.7: The ^{88}Sr curve from Fig. 5.2 (blue circles) plotted with simulation results (magenta line) from the one-dimensional rate equation model described in Sec. 5.1.5. Parameters for the simulation are identical to experimental conditions (see Sec. 5.1.3). The model reproduces the qualitative lineshape and the peak enhancement of the data. The difference in the amplitude and width between the curves implies that our one-dimensional model does not accurately capture the full three-dimensional nature of our experiment.

differential equations,

$$
\begin{aligned}
\dot{P}_{i,m_i} = &\; \mathcal{F}_{^1S_0}\delta_{i,^1S_0} - \beta(\delta_{i,^1S_0} + \delta_{i,^3P_2})P_{i,m_i} \\
&+ \sum_{j,m_j,m_\gamma} \left(\Gamma^{exc}_{|j,m_j;\, m_\gamma\rangle \to |i,m_i\rangle} P_{j,m_j} - \Gamma^{exc}_{|i,m_i;\, m_\gamma\rangle \to |j,m_j\rangle} P_{i,m_i} \right. \\
&+ \left. \Gamma^{decay}_{|j,m_j\rangle \to |i,m_i;\, m_\gamma\rangle} P_{j,m_j} - \Gamma^{decay}_{|i,m_i\rangle \to |j,m_j;\, m_\gamma\rangle} P_{i,m_i} \right),
\end{aligned}
\tag{5.4}
$$

where $\delta_{i,j}$ is the Kronecker delta, $\mathcal{F}_{^1S_0}$ is the atomic flux from the Zeeman slower, and $\beta \approx 0.1\,\mathrm{s}^{-1}$ is the experimentally measured 1-body loss rate (the effect of which is negligible for states with short lifetimes). Without repumping, the bMOT loading time ($\lesssim 100$ ms) is short compared to the magnetic trap loading time, so we take $\dot{P}_{i,m_i} = 0$ for all $i \neq {}^3P_2$. We solve algebraically for $\{\dot{P}_{^3P_2,-2}, \ldots, \dot{P}_{^3P_2,2}\}$ and numerically integrate the resulting first-order equations from $t = 0$ to $t = t_{\mathrm{load}}$. The sum $(P_{^3P_2,2} + P_{^3P_2,1} + P_{^1S_0,0})$ gives the total atom number at $t = t_{\mathrm{load}}$ (the population of other states is negligible), which we equate with N or N_0 depending on whether the 688-nm laser is on or off. A fit of the model to the ^{88}Sr, N_0 versus t_{load} data, with $s_{^3P_1{}^3S_1} \equiv s_{688} = 0$ and $\mathcal{F}_{^1S_0}$ as the only free parameter, matches the experiment to better than 4 % for all reservoir loading times (all

other parameters are taken from Sec. 5.1.3). We use the extracted value of $\mathcal{F}_{1S_0}$ for all subsequent simulations, but we find that the results are independent of $\mathcal{F}_{1S_0}$ and β.

We plot the simulated and measured N/N_0 for ^{88}Sr in Fig. 5.7. Parameters for the simulation are taken from Sec. 5.1.3 except for s_{688} and Δ_{679}, which are the same as given in Figure 5.2. The simulation agrees reasonably well with experiment given the simplicity of the model and the absence of free parameters. The simulation approximately reproduces the asymmetric lineshape and the magnitude of the peak trap loading enhancement. The one-dimensional model also qualitatively replicates the behavior of N/N_0 as a function of s_{688} and Δ_{679}. The difference in dimensionality between the 1D simulation and 3D experiment likely causes the mismatch in both the width and amplitude of the lineshapes in Fig. 5.7. The three-dimensional MOT beam configuration and magnetic quadrupole field complicate the optical pumping dynamics.

The choice of a $J = 1 \rightarrow J' = 1$ transition as our depumping line potentially limits the trap loading enhancement, since the 688-nm line has position-dependent dark states and small CG overlap with $|^3P_2, m_J = 2\rangle$. Furthermore, this transition requires a secondary laser to depopulate the $^3P_0$ state. Many repumping strategies exist for strontium and each of these possesses a nearby depumping resonance [112, 114, 116, 166]. We assess the relative merit of the various schemes by simulating them with optimum parameters (Fig. 5.8). The $5s5p\,^3P_1 \rightarrow 5s5d\,^3D_2$ line at 487 nm and the $5s5p\,^3P_1 \rightarrow 5s6d\,^3D_2$ line at 397 nm have similar performance to the 688-nm line. All other transitions for which linewidth data are available give less enhancement. For the $5s5p\,^3P_1 \rightarrow 5p^2\,^3P_2$ transition, unfavorable relative Landé g-factors between the excited state and $^3P_1$ marginally reduce the trap loading improvement. The linewidth of the $5s5p\,^3P_1 \rightarrow 5s4d\,^3D_2$ transition is too narrow for efficient optical pumping at bMOT temperatures.

We investigate the utility of the depumping scheme for other AE atoms. For Cd, Hg, Yb, Be, and Mg, the $^1D_2$ state lies above the $^1P_1$ state, so efficient continuous loading of the metastable reservoir does not occur [30, 114]. Direct pumping to the magnetically

trapped state is possible for these atoms [167]. The $^1D_2$:$^1S_0$ branching ratio in Ba and Ra is very large, which means that cooling to temperatures below the magnetic trap depth may not be possible without repumping [168, 169]. The level structure of calcium combines several features that make depumping more effective than in strontium (see Fig. 5.8). The $^3P_2$:$^3P_1$ branching ratio is $\approx$ 1:3 and, more importantly, the $^1D_2 \rightarrow {}^1S_0$ quadrupole transition linewidth is comparable to $^1D_2 \rightarrow {}^3P_J$ decay rates. Ca can be trapped in a MOT operating on $^3P_2 \rightarrow {}^3D_3$ transition [170], the loading of which could also benefit from this depumping technique. The loading enhancement for MOTs does not benefit from the detuning-dependent asymmetry seen for magnetic trap loading, which limits the simulated improvement in Ca to $\approx$50 %.

5.1.6 Conclusions

We have demonstrated that the 688-nm transition can be used to reduce cycle time and increase atom number in ultracold strontium experiments. For the bosonic isotopes, applying both a 688-nm and a 679-nm laser to the bMOT increases atom number in the metastable reservoir by up to 65 % regardless of loading time. If an experiment requires large atom number relative to experimental limits, the trap loading time can be reduced by a factor of three or better. The enhancement is less for ^{87}Sr due to complications arising from hyperfine structure and smaller Landé g-factors for the $^3P_2$ state. If a second frequency component to simultaneously pump $|F = 11/2\rangle \rightarrow |F' = 11/2\rangle$ and $|F = 9/2\rangle \rightarrow |F' = 11/2\rangle$ were added to the depumping beam, we believe performance comparable to the bosonic isotopes would be achievable. This improvement might make the depumping technique a useful method to reduce dead time in ^{87}Sr atomic clocks [21].

Comparison with a one-dimensional rate equation model shows that our results for the bosons are consist with expectations. The initial prediction of 3$\times$ increased atom number, based on the branching ratio from $^1D_2$ into $^3P_2$ and $^3P_1$, is not feasible. Simulations of alternative enhancement schemes indicate that pumping on either the
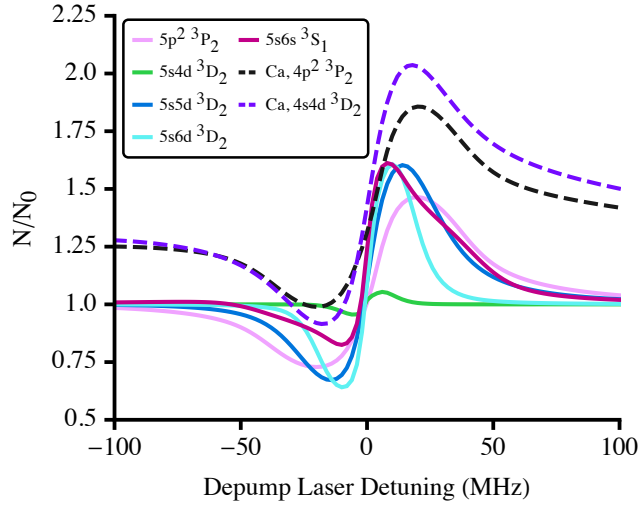
Figure 5.8: Simulations of several depumping schemes for bosonic strontium (solid lines) and calcium (dashed lines), which we label with the depumping transition excited state (the lower state is always $5s5p\,^3P_1$ for Sr and $4s4p\,^3P_1$ for Ca). In all simulations, we use our ^{88}Sr values for r_{bMOT}, t_{load}, s_{461}, Δ_{461}, $\mathcal{F}_{^1S_0}$, and β. The depumper saturation parameter is $s_{depump} = 1$ except for the simulation of $5s4d\,^3D_2$, where $s_{depump} = 2000$, which requires much higher saturation due to the narrow transition linewidth. For the simulation of $5s6s\,^3S_1$, Δ_{679} is set to its optimal value. The Sr $5s5d\,^3D_2$, Sr $5s6d\,^3D_2$, Sr $5p^2\,^3P_2$, Ca $4p^2\,^3P_2$, and Ca $4s4d\,^3D_2$ states may indirectly decay to $^3P_0$ via intermediate states outside of the ^3P manifold. The model ignores these processes, but atoms decaying into $^3P_0$ can be recovered using *e.g.* a 679-nm laser (for Sr). The apparent offset of the enhancement for Ca is a Gaussian pedestal with a full width at half maximum of approximately 500 MHz. The linewidths necessary for these simulations can be found in [30, 91, 112, 171].

$5s5p\,^3P_1 \rightarrow 5s5d\,^3D_2$ transition or the $5s5p\,^3P_1 \rightarrow 5s6d\,^3D_2$ transition, which are also accessible with diode lasers, offers similar performance to the approach pursued in this work. Regardless of the exact implementation, the trap loading enhancement scheme can substantially increase atom number independent of the bMOT loading rate or vacuum lifetime. We expect that this method will be helpful for experiments benefitting from high atom number or faster cycle times.

118

Chapter 6: Photoassociation of ^{84}Sr and ^{86}Sr

6.1 Background: Hund's Cases and Notation

Before discussing the photoassociation experiments, I will first give a short explanation of Hund's cases for diatomic molecules and the molecular term notation which will be relevant for this chapter. For diatomic molecules, the quantization axis is taken to be the internuclear axis. There are a number of different angular momentum vectors for the various spin and orbital sources of angular momentum, which are defined in Table 6.1. The spin and orbital angular momenta will couple due to magnetic interactions in several different ways [172]. The spin-orbit interaction couples $\mathbf{L}$ and $\mathbf{S}$ with the form $\bar{A}\mathbf{L} \cdot \mathbf{S}$ and the magnitude of the interaction is given by $A = |\bar{A}\hbar^2|$. There is also a spin-rotation coupling between $\mathbf{N}$ and $\mathbf{S}$ with a rotational constant of $B = \hbar^2/(2\mu R_0^2)$, where μ is the reduced mass of the molecule and R_0 is the distance corresponding to the minimum of the molecular potential. The way that the angular momentum vectors couple and add to form the total angular momentum, $\mathbf{J}$, depends on the relative magnitude of A, B, and the electrostatic interaction between the electrons and the nuclei. One way to quantify the electrostatic energy is by $|\Delta E|$, the splitting between two adjacent electronic levels with different values of Λ. There are five different Hund's cases that correspond to different relative magnitudes of A, B, and $|\Delta E|$. I will only describe cases (a) and (c), illustrated in Fig. 6.1, since those are the two that are applicable for this thesis.

Table 6.1: Notation for the various angular momentum vectors for diatomic molecules and their projections onto the internuclear axis. Since $\mathbf{N}$ is perpendicular to the internuclear axis, it's projection is 0, and $\mathbf{J}_a$ and $\mathbf{J}$ have the same projection. For each Hund's case, a different subset of these values are good quantum numbers.

Angular Momentum Vector	Projection	Definition
$\mathbf{L}$	Λ	electronic orbital ang. mom.
$\mathbf{S}$	Σ	electronic spin ang. mom.
$\mathbf{J}_a$	Ω	total electronic ang. mom., $\mathbf{J}_a = \mathbf{L} + \mathbf{S}$
$\mathbf{N}$	0	orbital ang. mom. of relative motion of nuclei
$\mathbf{J}$	Ω	total ang. mom.
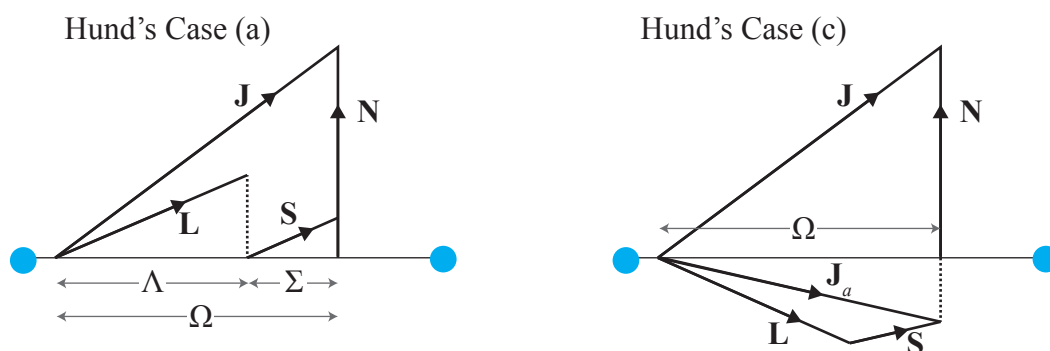
Figure 6.1: Schematic of Hund's coupling cases (a) and (c).

6.1.1 Hund's Case (a)

Hund's case (a) applies when $|\Delta E| \gg A \gg B$. In this case, $\mathbf{L}$ and $\mathbf{S}$ precess about the internuclear axis and the projections of $\mathbf{J}$, $\mathbf{L}$, and $\mathbf{S}$ obey $\Omega = \Lambda + \Sigma$. The good quantum numbers are Λ, S, Σ, J, and Ω. For strontium dimers, this is typically a good approximation at small internuclear distances and has been used for *ab initio* calculations [173].

Molecular states in Hund's case (a) are denoted by the molecular term symbol $^{2S+1}\Lambda_{g/u}^{+/-}$. Instead of denoting orbital angular momentum values of 0, 1, 2, 3 etc. with the usual atomic labels of S, P, D, F, etc., we use the equivalent Greek letters of Σ, Π, Δ, Φ, etc. The +/- in the superscript describes the symmetry of the molecular state with respect to reflection about a plane containing the internuclear axis. States that are unchanged are labeled + while states whose wavefunctions flip signs with the reflection are labeled -. This symmetry is only specified for $\Lambda = 0$ states since $\Lambda > 0$ states are (approximately) degenerate with the reflected wavefunction. Homonuclear molecules have an additional symmetry property denoted by the *g* for *gerade* (German for even) or *u* for *ungerade* (odd) in the subscript. This symmetry refers to whether the wavefunctions are even or odd with respect to inverting the electron coordinates about the midpoint between the two nuclei. Due to Laporte's selection rule, electric dipole transitions are only allowed between states of different parity. Another typical notation convention is to prepend the term symbol of the ground state with an X (for example $X^1\Sigma_u^+$). Excited states with the same spin multiplicity as the ground state are labeled by A, B, C, etc. (for example $C^1\Delta_g$), and those of different multiplicity are labeled by a, b, c, etc. (for example $b^3\Pi_u$) [172].

6.1.2 Hund's Case (c)

Hund's case (c) applies when $A \gg |\Delta E| \gg B$. Since the spin-orbit coupling is so strong, $\mathbf{L}$ and $\mathbf{S}$ add to form $\mathbf{J}_a$, which precesses about the internuclear axis. In this case

Ω is the projection of both $\mathbf{J}_a$ and $\mathbf{J}$ and the good quantum numbers are J_a, J, and Ω. In Hund's case (c), the states are denoted by the notation $\Omega_{g/u}^{+/-}$, where the symmetry labels are the same as above except the +/- label is only used for $\Omega = 0$ states (for example 0_u^+, 1_g, 2_u, etc.) [172, 174]. Due to the large spin-orbit coupling in strontium, Hund's case (c) is a good representation for excited dimers [175, 176] and coordinate transformations can be used to switch between the various Hund's case representations.

6.2 Introduction

Photoassociation, as illustrated in Fig. 6.2, is a process that couples two free ground-state atoms to a weakly bound molecular state corresponding to one excited, and one ground state atom [176]. The natural decay rate, ignoring stimulated broadening, of the excited molecular states is given by twice the atomic decay rate. Therefore, photoassociation relative to the narrow $^1S_0 \rightarrow {}^3P_1$ transition in Sr can be performed with precisions on the order of kHz. Previous narrow line photoassociation spectroscopy (PAS) has been performed in ^{88}Sr [40, 43], ^{86}Sr [177], and in ^{84}Sr [50]. In addition, two-color photoassociation of the $^1S_0 \rightarrow {}^3P_1$ line in ^{88}Sr was used to measure the scattering lengths of all the strontium isotopes [42] and several subradiant 1_g states have been probed in ^{88}Sr [178]. The ground [96, 179] and excited [180] state molecular potentials have also been explored by Fourier transform spectroscopy.

In addition to probing the shapes of the molecular potentials, photoassociation efforts are motivated by interest in creating ground-state molecules. Ground state molecules have been proposed as a platform for precision measurements, for example to study deviations of the proton-electron mass ratio [181, 182], and/or the fine structure constant [183]. The production of ground state molecules has been demonstrated by decay from excited-molecular states in ^{88}Sr [51] and by using stimulated Raman adiabatic passage (STIRAP) in ^{84}Sr [50, 52, 184]. In particular, the technique in [184] may offer a path towards creating a molecular BEC.

Another motivation for studying narrow line photoassociation resonances stems from the prospect of using them as optical Feshbach resonances (OFRs) to tune the s-wave scattering length of ground state atoms. The application of OFRs to strontium and other alkaline-earth elements is particularly interesting because the spinless ground-state of the bosonic isotopes precludes the use of magnetic Feshbach resonances. In addition, OFRs offer the possibility of controlling atomic interactions with increased temporal and spatial resolution compared to magnetic resonances. Early theoretical work suggested that the narrow intercombination lines of alkaline-earth atoms should reduce the atom loss associated with OFRs due to photoassociation while still allowing for useful modifications to the background scattering length [185]. There was hope that this technique could be applied to ^{88}Sr, which is the most abundant isotope of strontium but whose nearly vanishing scattering length ($a_{bg} = -1.4a_0$ where a_0 is the Bohr radius [42]) prevents it from being evaporatively cooled directly. Two groups successfully used an OFR to modify the scattering length of ^{88}Sr, however these results were associated with rapid atom loss, limiting the experimental lifetime to the order of a few ms or less [48, 49]. Nevertheless, OFRs may still prove to be useful in other situations or systems. For example, OFRs were used to modify the scattering lengths ^{176}Yb and ^{172}Yb by more than 10 nm with minimal loss rates [46].

In [177], Borkowski *et al.* took realistic, *ab initio* potentials from [173] and fit them to the known photoassociation resonances of the bosonic isotopes of strontium. They developed independent potentials for each isotope (see Sec. III) that were based on the same overall shape but included different quantum defect parameters tuned to the spectrum of each isotope. These potentials did an excellent job of reproducing most of the known lines, but also pointed to some open questions. Though the binding energy spectrum of ^{88}Sr was well measured with 11 known lines, they only had four resonances each for ^{84}Sr and ^{86}Sr. Their model could not reproduce one of the observed ^{84}Sr 0_u^+ lines, only included one ^{86}Sr 1_u resonance, and did not consider any ^{84}Sr lines with 1_u symmetry.
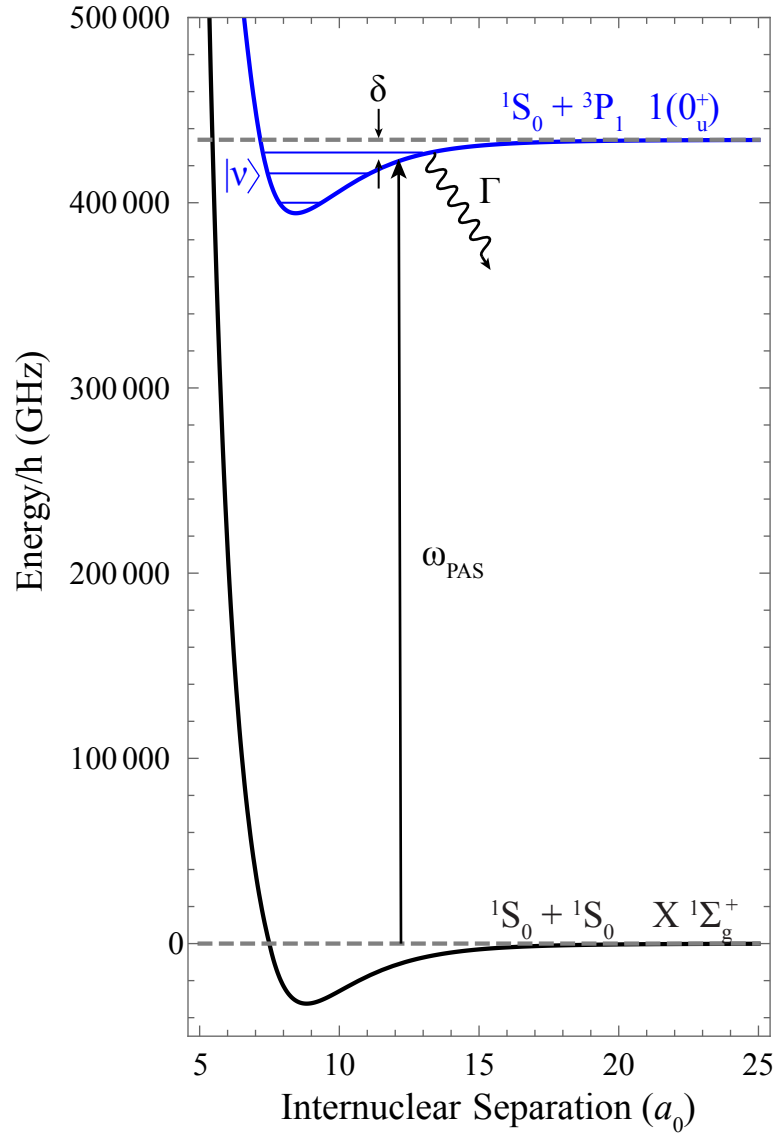
Figure 6.2: Schematic of a single photon photoassociation process. The solid black line is the $X^1\Sigma_g^+$ scattering potential of two ground state atoms as a function of the distance between the atoms. The blue solid line is the 0_u^+ potential corresponding to molecules consisting of one ground-state atom and one excited state atom. The photoassociation laser, with frequency ω_{PAS}, is detuned from the $^1S_0 + {}^3P_1$ dissassociation limit by δ. If δ is close to the binding energy of a bound state supported by the excited molecular potential, the photoassociation laser will induce the formation of molecules. The molecules will then decay to ground-state molecules or dissociate back to free atoms. After dissociation, the atoms acquire kinetic energy,leading to loss from the trap. By scanning the detuning, δ, we can measure the location of the bound molecular states and from this deduce the shape of the molecular potentials. In this work we denote the least bound state by $\nu = -1$, the second least bound state by $\nu = -2$, etc. The ground state potential (from [179]) and excited state potential (from [177]) are to scale, though the illustrated bound states are much deeper than those probed in this work.

In addition, Borkowski *et al.* constructed a mass-scaled model for all the bosonic isotopes. A mass-scaled model consists of a single potential that recreates the photoassocation spectra of all the bosonic isotopes of strontium simultaneously while only varying the molecular reduced mass for each isotope. Interestingly, in developing their model, Borkowski *et al.* discovered that they needed to include the potential curve of the $^1S_0 + {}^1D_2$ 0_u^+ $(^3\Sigma_u^+)$ state, which forms an avoided crossing with the $^1S_0 + {}^3P_1$ 0_u^+ $(^3\Pi_u^+)$ state at short range (see Fig. 6.3). This perturbing state was measured by Stein *et al.* [180] and theoretically described by Skomorowski *et al.* [173]. However, as Borkowski *et al.* pointed out, this mass-scaled, multi-channel model was insufficiently constrained given the known resonances in ^{84}Sr and ^{86}Sr.

In this work, we clear up these issues by measuring additional resonances in ^{84}Sr and ^{86}Sr, including more deeply bound states down to binding energies of $\simeq -5$ GHz, bringing the total known resonances up to seven for both ^{84}Sr and ^{86}Sr. In measuring the new lines, we discovered that some of the previously measured resonance positions could not be reproduced and measured new locations for those resonances. With these new spectra, we hope to build on the results in [177] and create a more accurate mass-scaled model that spans many GHz.

In this chapter, I will discuss our measurement of the new binding energies Sec. 6.3. Next, I will briefly review the theory of optical Feshbach resonances and discuss the measurement of the optical lengths, a measure of the photoassociation line strength, of the ^{84}Sr, 0_u^+ resonances in Sec. 6.4. Finally, I will conclude and discuss future photoassociation work in Sec. 6.5.
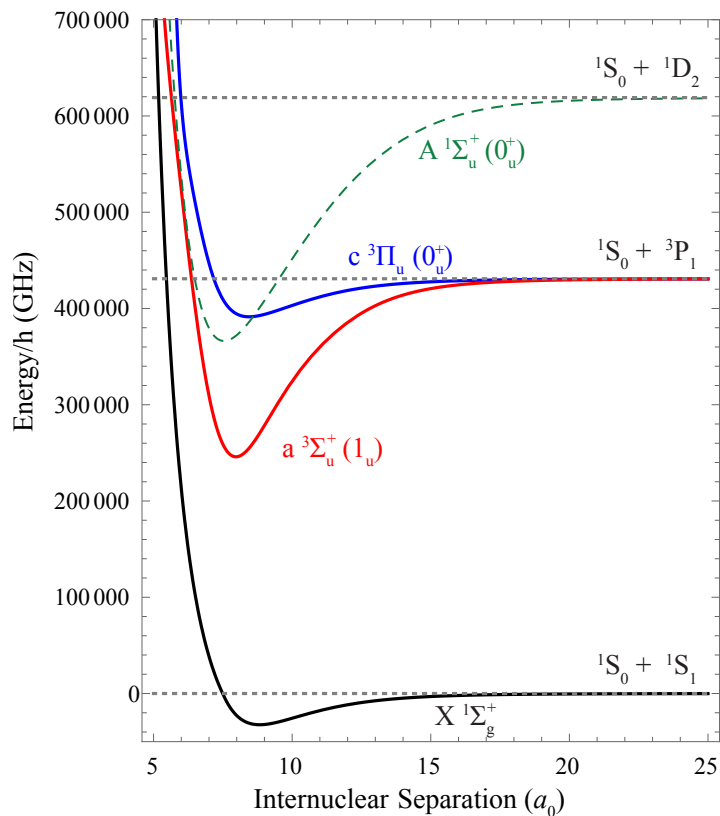
Figure 6.3: The three potential curves relevant to photoassociation relative to the $^1S_0 + {}^3P_1$ dissassociation limit in the Hund's case (a) configuration. The $^1\Sigma_u^+$ potential crosses the $^3\Pi_u$ potential at short range. Borkowski *et al.* showed that this crossing perturbs the $^3\Pi_u$ spectrum for ^{84}Sr. The $^1\Sigma_u^+$ potential parameters are from [173], the $^3\Pi_u$ and $^3\Sigma_u^+$ are from [177], and the ground state potential is from [179].

6.3 Measurement of Binding Energies in ^{84}Sr and ^{86}Sr

6.3.1 Experimental Procedure

Our experimental procedure follows the general recipe described in Ch. 3. For ^{86}Sr, we use a single beam optical dipole trap consisting of a pancake-shaped beam propagating along the horizontal plane with a vertical (horizontal) $1/e^2$ waist of 22.8 μm (228 μm). After evaporating for 1.0 s to a trap depth of approximately 2.5 μK, we have a sample consisting of $\simeq 10^6$ atoms at a temperature of about 150 nK and peak density of $\simeq 2 \times 10^{12}$ cm^{-3}. Due to the large s-wave scattering length of ^{86}Sr ($a_{\text{bg}} = 823\ a_0$ where a_0 is the Bohr radius [42]), the samples suffer from rapid three-body losses at larger densities. Therefore, we perform photoassociation of ^{86}Sr in a thermal gas as opposed to a BEC to maintain favorable signal-to-noise ratios from larger atom numbers.

Since the ^{84}Sr isotope can readily be evaporated to degeneracy (see Sec. 3.6.2 and [115, 125, 126]), we perform photoassociation of this isotope in a BEC. By using a BEC, we can ignore thermal lineshape effects [175] and the large density enhances the photoassociation signal. Our dipole trap for ^{84}Sr includes an additional crossing beam with a $1/e^2$ waist of 72 μm in addition to the horizontal beam mentioned above. After approximately two seconds of evaporation, we create a nearly pure BEC with a typical atom number of 10^5 atoms. Typical trap frequencies after evaporation are $\{\omega_x, \omega_y, \omega_z\} = 2\pi \times \{40, 40, 140\}$ Hz, and the BEC has a chemical potential, μ/h, of about 1 kHz. The peak density is about 10^{14} cm^{-3} and the final trap depth is also about 2.5 μK.

The photoassociation laser is referenced to a master laser operating near the 689-nm intercombination transition. We stabilize the master with a Pound-Drever-Hall lock to a very high finesse ($\mathcal{F} > 200{,}000$) cavity made from Ultra-Low-Expansion (ULE) glass. The cavity is operated in a temperature stabilized vacuum chamber in order to minimize thermal and pressure drifts. The linewidth of the master laser is ≤ 200 Hz, as determined

by measuring the joint linewidth of the master with another laser locked to a separate, similar cavity. We measured the long term drift of the cavity to be about 28 mHz/s by monitoring the $^1S_0 \rightarrow {}^3P_1$ transition frequency over several months. The photoassociation laser is stabilized relative to the master by an optical-phase-locked-loop (OPLL) [141]. This locking method gives us a great deal of flexibility, since we can vary the detuning of the PAS laser with respect to the atomic resonance over many GHz simply by changing the reference frequency supplied to the OPLL. The PAS laser is launched close to the experiment by a single-mode fiber and has a $1/e^2$ waist of 1.63 mm at the location of the atomic sample. We stabilize the intensity via feedback to an acousto-optical-modulator (AOM). All scans were either performed at zero magnetic field or with a small bias field of 200 mG parallel to the polarization of the photoassociation beam.

In order to avoid AC Stark shifts from the 1064-nm trapping beams, we turn on and off the dipole traps with a 50% duty cycle, period of 500 μs, peak trap depth of 5 μK, and apply the PAS laser while the 1064-nm beams are off. We vary the total amount of time the PAS laser is on from 10 to 500 ms in order to limit the maximum photoassociation atom number loss to $\approx$ 50% for the intensity and resonance under investigation. After applying the PAS laser, we measure the remaining atoms by absorption imaging using a 10 μs pulse from a beam resonant with the $^1S_0 \rightarrow {}^1P_1$ transition. To avoid systematic errors due to excessive optical depths, we limit the maximum optical depths of our ^{84}Sr BEC samples to $\leq$ 2.0 by allowing them to expand for 25 ms before imaging. We image our thermal ^{86}Sr samples after an expansion time of 12 ms.

6.3.2 Extracting Binding Energies and Uncertainties

We measured the binding energies of seven photoassociation resonances each for ^{84}Sr and ^{86}Sr. The results are summarized in Table 6.2. To determine these binding energies, we monitored atom number as the detuning of the PAS laser was varied. In the vicinity of a $^1S_0 + {}^3P_1$ molecular bound state, the photoassociative formation of molecules
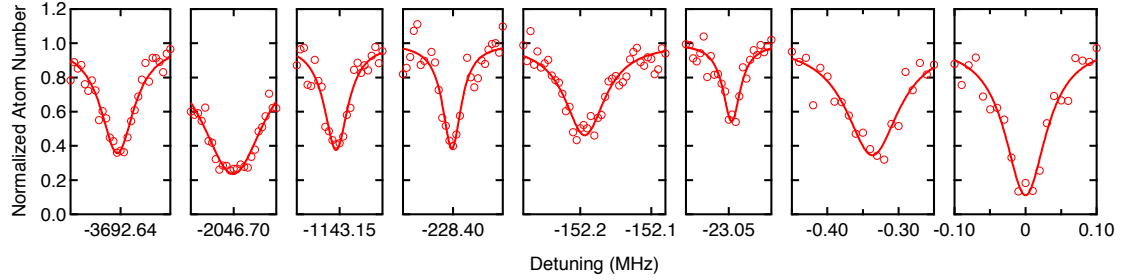
Figure 6.4: Example detuning scans across all the ^{84}Sr photoassociation resonances measured. The solid lines are Lorentzian fits to the data. The scan on the far right is the atomic $^1S_0 \rightarrow {}^3P_1$ transition used to calibrate the detuning values. The same horizontal scale is used for each plot. From left to right, the intensities used are 69, 24, 68, 4.6, 2.4, 0.66, 0.025, and 0.008 mW/cm^2 and the photoassociation light is applied for 70, 150, 200, 20, 100, 50, 3 and 3 ms.

leads to atom loss as the molecules quickly decay into ground state molecules or free atoms with enough kinetic energy to escape our shallow dipole trap. An example loss feature for each of the resonances we measured in ^{84}Sr and ^{86}Sr is shown in Figs. 6.4 and 6.5. Each scan is repeated at least three times and the results are averaged.

6.3.2.1   Fitting Thermal Lineshapes

For our thermal ^{86}Sr samples, the non-zero temperature will shift and broaden the photoassociation lineshapes. Since the temperatures of our samples are below the atomic recoil temperature, $T_R \simeq 460$ nK, we must take into account Doppler broadening as well [175]. This section will briefly describe the approach used, which can also be found in [177, 186], to account for these shifts and fit the resulting lineshapes.

We model the photoassociation loss process as $\dot{n} = -K_2 n^2$, where n is the atomic density and K_2 is the effective collision rate constant. In this model we assume that the photoassociation losses are much faster than other loss processes, such as one-body collisions with background gas particles. Integrating the differential equation gives

$$\int \dot{n}(\mathbf{r}) \, d^3\mathbf{r} = \dot{N} = -K_2 \int n(\mathbf{r}, t)^2 \, d^3\mathbf{r}. \tag{6.1}$$

For thermal atoms at temperature T, $n(\mathbf{r}) \propto \exp\left[-U(\mathbf{r})/k_B T\right]$, where $U(\mathbf{r})$ is the trap

129
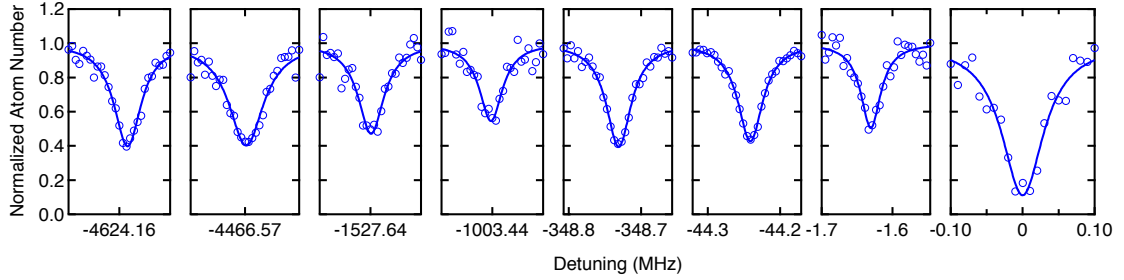
Figure 6.5: Example detuning scans across all the ^{86}Sr photoassociation resonances measured. The solid lines are Lorentzian fits to the data. The scan on the far right is the atomic $^1S_0 \rightarrow \ ^3P_1$ transition used to calibrate the detuning values. The same horizontal scale is used for each plot. From left to right, the intensities used are 18.5, 114, 5.7, 3.5, 3.4, 0.24, 0.035, and 0.008 mW/cm^2 and the photoassociation light is applied for 150, 500, 100, 100, 40, 30, 40 and 3 ms.

potential. For harmonic traps, the integral above can be evaluated to give

$$\int n(\mathbf{r}, t)^2 \ \mathrm{d}^3\mathbf{r} = \frac{1}{8} \left(\frac{m\bar{\omega}^2}{\pi k_B T} \right)^{3/2} N^2 \equiv C_{th} N^2, \tag{6.2}$$

where $\bar{\omega}$ is the geometric mean of the trap frequencies. We can integrate over time to yield an expression for the total atom number as a function of t, the time the photoassociation light is applied for,

$$N(t) = \frac{N_0}{1 + N_0 K_2 C_{th} t}. \tag{6.3}$$

Here, N_0 is the atom number with no photoassociation light applied. This expression can be re-arranged to yield

$$K_2 = \frac{8}{t} \left(\frac{1}{N(t)} - \frac{1}{N_0} \right) \left(\frac{\pi k_B T}{m\bar{\omega}^2} \right)^{3/2}, \tag{6.4}$$

which allows us to extract the measured collision rate from the measurements of atom number as a function of detuning.

Using the approach from [175], the collision rate can also be expressed as

$$K_2 = \frac{2k_B T}{hQ_T} \int_{-\infty}^{+\infty} \mathrm{d}y \ e^{-y^2} \int_0^{\infty} \mathrm{d}x \ x e^{-x^2} \mathcal{L}(\Delta, y, x^2) \tag{6.5}$$

130

where x and y are dimensionless variables and $Q_T = (2\pi \mu k_B T/h^2)^{3/2}$. The integral over x treats thermal shifts in the loss feature due to the relative velocity of the two atoms averaged over a Maxwell-Boltzmann distribution. The integral over y deals with the Doppler shifts due to the motion of the atoms relative to the laser, also averaged over a thermal distribution. The reduced mass of the molecule is half the atomic mass, $\mu = m/2$. The lineshape function is given by

$$\mathcal{L}(\Delta, y, x^2) = \frac{\eta \Gamma_{\text{mol}} \Gamma_{\text{stim}}}{(\Delta + y\Delta_D + x^2 \Delta_T - E_{rec}/\hbar)^2 + (\eta\Gamma_{\text{mol}}/4\pi)^2}, \tag{6.6}$$

where Δ is the photoassociation laser detuning from the photoassociation line center, $\Delta_T = k_B T/\hbar$ is the thermal width, $\Delta_D = k_{\text{las}}\sqrt{k_B T/m}$ is the Doppler width and $k_{\text{las}} = 2\pi/\lambda$ is the wavevector of the photoassociation laser. The natural linewidth of the excited molecular level is twice that of the atomic linewidth, or $\Gamma_{\text{mol}} = 2\Gamma_a = 2\pi \times 15$ kHz. The stimulated width, $\Gamma_{\text{stim}} = 2(\sqrt{2\mu x^2 k_B T}/\hbar)\Gamma_{\text{mol}}\ell_{\text{opt}}$, is much smaller than the molecular width for the parameters used here. The optical length, ℓ_{opt}, is a measure of the strength of the photoassociation resonance and will be discussed further in Sec. 6.4.2. The photon recoil leads to a constant shift of $E_{rec}/h = (\hbar k_{las})^2/4hm \simeq 2.4$ kHz. The parameter $\eta \geq 1$ is phenomenological and accounts for extra broadening typically measured in photoassociation experiments [40, 45, 48, 49, 177, 187].

When fitting the thermal lineshapes, the integral in Eq. (6.5) is evaluated numerically and truncated at arbitrarily selected large values of $x, |y| \leq 10$. An example loss feature that is fit using this method is shown in Fig. 6.6. Note that this analysis assumes that the temperature remains constant during the photoassociation process. We measure the temperature of the sample, as shown in Fig. 6.6(c), to ensure that the temperature is approximately constant for all detunings. Since the temperatures of our ^{86}Sr clouds are so low ($T \simeq 150 - 200$ nK), the thermal and Doppler broadening only result in shifts of a few kHz.
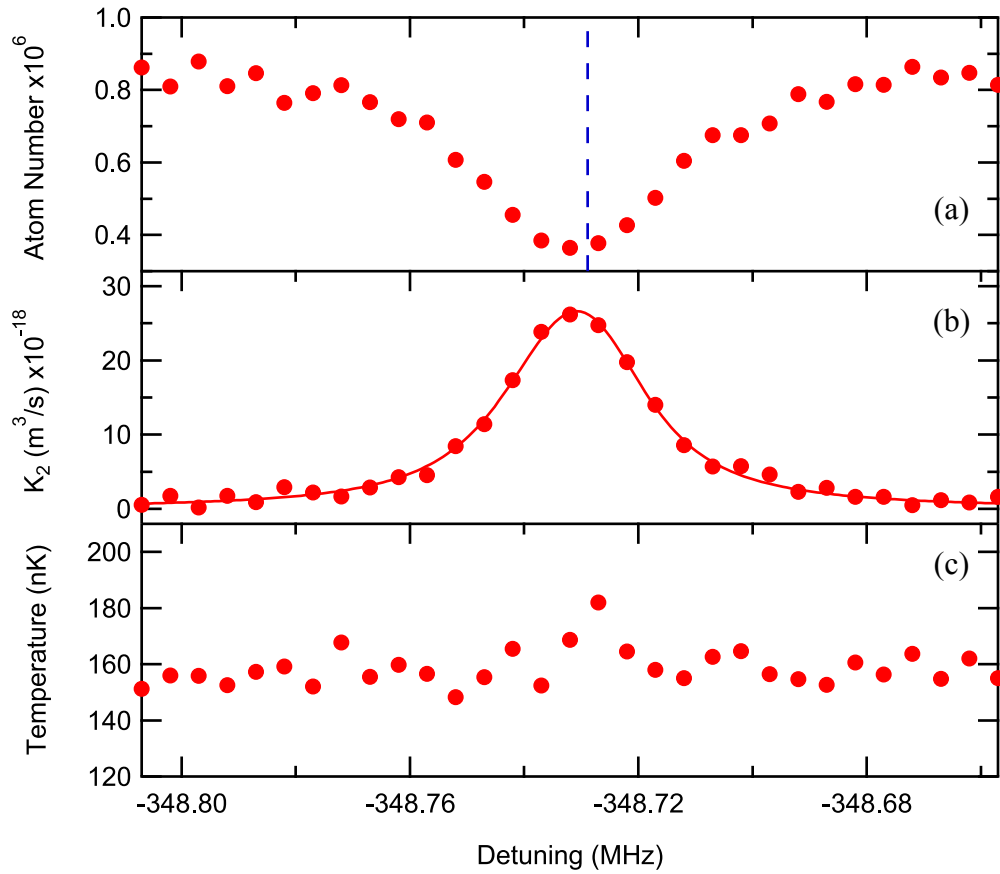
Figure 6.6: Photoassociation spectroscopy of the ^{86}Sr, $0_u^+ v = -3$ resonance. Atom number (a), the collision rate K_2 (b), and temperature (c) are shown with respect to the detuning of the photoassociation laser. The collision rate is calculated from the data in (a) using Eq. (6.4). The K_2 curve is fit using Eqs. (6.5) and (6.6) to extract the photoassociation line center. The fit result is shown by the solid line in (b) and the dashed line in (a) indicates the extracted binding energy of this resonance. The resonance is shifted by a few kHz from the minimum of the loss feature by thermal and Doppler effects. Since the temperature is invariant with respect to detuning, as shown in (c), the assumption of constant temperature required for this analysis is appropriate.

6.3.2.2 Fitting BEC Lineshapes

For the ^{84}Sr results, the PAS is performed on atoms in a BEC and the resulting lineshapes are symmetric. We do not need to consider thermal or Doppler broadening that leads to asymmetries and shifts as described above [175]. Therefore, we fit the atomic loss features to a simple Lorentzian curve to extract the binding energies. After fitting, we manually add in the correction due to photon recoil, $E_{rec}/h \simeq 2.4$ kHz. We also consider other sources of errors as described in the next section.

6.3.2.3 Error Sources

In order to assign uncertainties to the measured binding energies, we corrected or quantified a number of different sources of error. Though the long-term drift of our photoassociation laser is very small (28 mHz/s), we also observe intermediate timescale drifts on the order of 10s of kHz over a few hours, likely due to thermal fluctuations in the lab. In order to minimize errors due to these drifts of the photoassociation laser, we calibrate the absolute frequency by scanning over the atomic resonance before and after each scan of a photoassociation resonance. The typical laser drift is $\simeq 3$ kHz during these scans, which is similar to the typical statistical uncertainty associated with extracting the resonance position from the thermal lineshape or Lorentzian fits ($\simeq 2$ kHz). AC Stark shifts due to the ODT are eliminated by turning off the 1064 nm trapping beams while applying the PAS beam, as described in Sec. 6.3.1.

We did not perform a systematic investigation into the mean field shifts for our system. However, Stellmer *et al.* [50] measured mean field shifts for the $0_u^+, v = -3$ transition in a ^{84}Sr BEC to be about 2.4(5) mHz/atom. For our BECs with atom number $\approx 10^5$, this would correspond to shifts of about 250 Hz. We do not observe any dependence of the binding energies on the intensity of the PAS laser for the relatively low intensities used in this work. We estimate that AC Stark shifts due to the photoassociation laser

should be ≤ 500 Hz.

We also considered small errors in the RF frequencies generated by a direct-digital synthesizer (DDS) that are used to reference the OPLL lock of our photoassociation laser. By comparing the DDS to a commercial rubidium clock (SRS FS725), we measured a constant frequency error of 0.46 ppm, which resulted in corrections of ≤ 2.1 kHz to the measured binding energies.

Taking all these error sources into account, we conservatively estimate the uncertainty in our binding energies to be 10 kHz, which is dominated by laser drift and the statistical uncertainties of our fits.

6.3.3 Results

The measured photoassociation resonances are shown in Table 6.2. In order to assign symmetries and levels to the various observed lines, we compare the observed spacings and line strengths to expectations based on the molecular potential shapes. In general terms, the 0_u^+ potential tails off more gradually at large internuclear spacings compared to the 1_u potential (see the $^3\Pi_u$ (0_u^+) and $^3\Sigma_u^+$ (1_u) curves in Fig. 6.3). Therefore, there is a larger density of 0_u^+ bound states near threshold. In addition, the strength of the near-threshold 0_u^+ lines tend to be larger since the associated molecular wavefunctions extends to larger range and therefore have more overlap with the scattering wavefunction.

Most of our results are in good agreement with the previous measurements. However, there are several lines measured by other groups that we could not reproduce. We cannot say with certainty that the previous results were spurious, but we observe that given the very small saturation intensity of the $^1S_0 \rightarrow {}^3P_1$ atomic transition ($I_{\text{sat}} = 3$ μW/cm^2), a small amount of sideband noise on the photoassociation laser can cause losses that are easily confused as a photoassociation resonance. For instance, our PAS beam originates from the -1 diffracted order of a single-passed AOM operating at a frequency of Ω_{AOM}. When scanning the detuning of our PAS beam, we observe dips at detunings of $-\Omega_{AOM}$

Table 6.2: Photoassociation resonances for ^{86}Sr and ^{84}Sr. The last column compares the binding energies we measured to previous experimental results. We measured several new resonances, confirmed some previous measurements, but could not reproduce several lines observed by other experiments. *Given the proximity of the lines at -4624 and -4467 MHz, there is likely to be significant Coriolis mixing between these two states and the symmetry identification could be flipped.

			Binding Energy E_b/h (MHz)	
Isotope	Symmetry	Vibrational Level	Expt. (this work)	Expt. [177]
^{86}Sr	0_u^+	-1	-1.625(10)	-1.633(10)
	0_u^+	-2	-44.233(10)	-44.246(10)
	0_u^+	-3	-348.729(10)	-348.742(10)
	0_u^+	-4	-1527.645(10)	
	0_u^+	-5	-4466.572(10)*	
	1_u	-1	-1003.449(10)	-159.984(50)
	1_u	-2	-4624.155(10)*	
Isotope	Symmetry	Vibrational Level	Expt. (this work)	Expt. [50]
^{84}Sr	0_u^+	-1	-0.338(10)	-0.32(1)
	0_u^+	-2	-23.050(10)	-23.01(1)
	0_u^+	-3	-228.406(10)	-228.38(1)
	0_u^+	-4	-1143.161(10)	-1288.29(1)
	0_u^+	-5	-3692.645(10)	
	1_u	-1	-152.193(10)	-351.45(2)
	1_u	-2	-2046.703(10)	

and $-2\Omega_{AOM}$. We attribute the first dip to a small amount of non-diffracted light from the AOM being collected by the optical fiber, which is then resonant with the atomic transition at a detuning of $-\Omega_{AOM}$. We believe that the second dip can similarly be attributed to the small back-reflection of acoustic waves in the AOM crystal adding a small component of light whose frequency is upshifted, instead of downshifted, by the AOM and is therefore resonant with the atomic transition at a detuning of $-2\Omega_{AOM}$. With the potential for extremely small sidebands to cause significant atomic loss, it can be hard to identify and eliminate spurious signals. Since we were able to measure both the $\nu = -1$ and -2 1_u resonances for ^{86}Sr and ^{84}Sr, we can verify that the relative spacings are consistent with expectations, giving us more confidence in our results.

We have measured five new resonances, extending to binding energies of nearly 5 GHz, and corrected three lines that are likely to be spurious. An updated, theoretical treatment of these resonances is in progress, which should lead to more accurate mass-scaled and isotope-specific potentials.

6.4 Optical Feshbach Resonances

6.4.1 Background

Magnetic Feshbach resonances are an extremely useful tool that use the magnitude of a magnetic field to tune the strength of the atomic s-wave interactions [26]. The basic process, as illustrated in Fig. 6.7, concerns atoms colliding with energy E. Since we are dealing with ultra-cold atomic samples, $E \to 0$ as $T \to 0$. The background scattering length of two colliding atoms is determined by the properties of the background potential V_{BG}. Since $E > V_{BG}$ at long range, this potential is energetically accessible and is known as the open (or sometimes background or entrance) channel. A second molecular potential, V_c, supports a bound state at energy E_c. Since this potential is energetically forbidden at long ranges, it is therefore known as the closed channel. Assuming the magnetic moments

of these two molecular states are different, we can tune the energy offset between V_c and V_{BG} using a magnetic field. If we tune the bound state energy E_c close to E, the two channels will resonantly couple and the scattering length will diverge. Thus, the scattering length can be tuned to nearly any value by making small magnetic field changes in the vicinity of one of these magnetic Feshbach resonances [26].

For strontium and other elements with non-magnetic ground states, there are no magnetic resonances and the only available method of tuning interactions is optical Feshbach resonances (OFRs) [26]. OFRs work on the same principle, however instead of tuning E_c to be degenerate with E using a magnetic field, the two energies are coupled using an optical field. The schematic for this process is identical to that of photoassociation, shown in Fig. 6.2. One major difference compared to typical magnetic Feshbach resonances is that for OFRs, the closed channel is an excited state so there are decay processes that lead to atomic loss [26, 188]. The narrow linewidths of the intercombination transition of strontium and other alkaline-earth elements should help to limit the rate of this decay [185].

There are several advantages to optical Feshbach resonances over magnetic resonances. For instance, optical fields can be controlled with greater spatial and temporal precision than magnetic fields, potentially offering more flexibility. In addition, for magnetic Feshbach resonances, only the relative detuning between the scattering and bound states can be tuned through the magnitude of the magnetic field. For OFRs, both the detuning and coupling strength can be tuned through the frequency and intensity of the laser beam, potentially offering more flexibility. Unfortunately, interferences between multiple molecular resonances restrict the useful detuning range to values less than the separation between neighboring resonances [48, 188]. In addition, larger intensities lead to increased atomic and molecular losses. Therefore there are practical limits to the tuning range of OFR parameters.
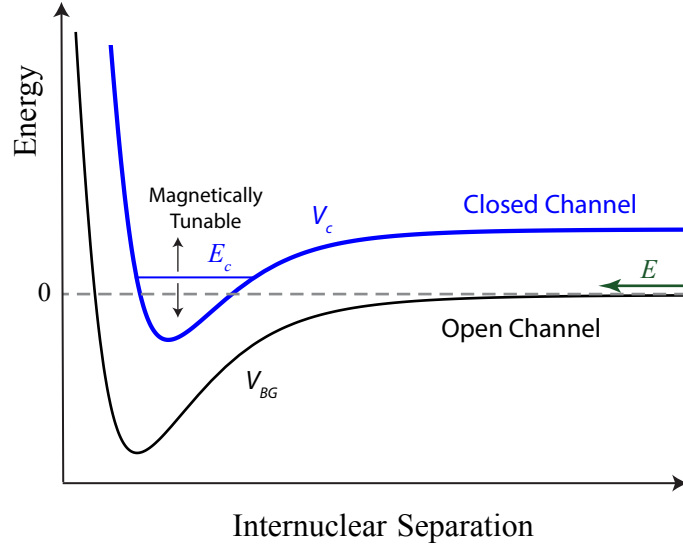
Figure 6.7: Magnetic Feshbach resonance schematic. The background scattering length of two colliding atoms is tuned by adjusting a closed channel bound state to be resonant with the scattering state.

6.4.2   Isolated Resonance Model of Optical Feshbach Resonances

The isolated resonance model [189] is a good description of the behavior of optical Feshbach resonances as long as the detuning is not large enough to be comparable to the distance between the resonance in question and an adjacent bound state [48, 188]. In this model [185, 188, 190], the scattering length is given by $a = a_{\mathrm{bg}} + a_{\mathrm{opt}}$ where the modification to the scattering length is

$$a_{\mathrm{opt}} = \frac{\ell_{\mathrm{opt}}\Gamma_{\mathrm{mol}}\Delta}{\Delta^2 + (\eta\Gamma_{\mathrm{mol}})^2/4},$$ (6.7)

and the two-body loss rate K_2 is given by

$$K_2 = \frac{4\pi\hbar}{\mu\alpha_{deg}} \frac{\eta\Gamma_{\mathrm{mol}}^2\ell_{\mathrm{opt}}}{\Delta^2 + (\eta\Gamma_{\mathrm{mol}} + \Gamma_{\mathrm{stim}})^2/4}.$$ (6.8)

The reduced mass μ, molecular width Γ_{mol}, and broadening factor η are the same as defined in Sec. 6.3.2.1. Here, the stimulated linewidth is given by $\Gamma_{\mathrm{stim}} = 2k\ell_{\mathrm{opt}}\Gamma_{\mathrm{mol}}$ where k is the wavenumber for the BEC or thermal sample. For a BEC, $k = \sqrt{21/8}/(2R_{\mathrm{TF}})$,

where R_{TF} is the Thomas-Fermi radius [49]. For a thermal gas, $k = \sqrt{2\mu E}/\hbar$, where E is the kinetic energy of the colliding atoms. The factor $\alpha_{deg} = 2$ (1) for BEC (thermal) samples accounts for the reduction of the inelastic scattering of a BEC compared to that of a thermal gas [175, 176, 191].

From these equations, we see that the optical length is an important parameter to describe the effects of a particular OFR. The maximum change in scattering length is $a_{\text{opt}} = \pm\ell_{\text{opt}}$ when $\Delta = \pm\Gamma_{\text{mol}}/2$ (and assuming $\eta = 1$). The optical length is a measure of the coupling between the ground, scattering state and the excited, bound state and is defined as

$$\ell_{\text{opt}} = \frac{\lambda^3}{16\pi c}\frac{f_{FC}}{k}f_{\text{rot}}I, \tag{6.9}$$

where $\lambda = 689.45$ nm is the wavelength of the atomic transition, the rotational factor $f_{\text{rot}} = 1$ for 0_u^+ resonances and $f_{\text{rot}} = 2$ for 1_u resonances, I is the intensity of the PAS laser, and f_{FC} is the Franck-Condon factor per unit energy [188]. The Franck-Condon factor is a measure of the overlap between the ground and excited molecular wavefunctions and is defined as

$$f_{FC} = \left| \int_0^\infty \phi_e(r)\phi_g(E,r)dr \right|^2, \tag{6.10}$$

where $\phi_e(r)$ is the excited bound molecular state wavefunction and $\phi_g(E,r)$ is the energy-normalized ground state scattering wavefunction. The energy-normalized wavefunction has the long-range form of

$$\phi_g(E,r) \xrightarrow{r\to\infty} \sqrt{\frac{2\mu}{\pi\hbar^2 k}}\sin[k(r - a_{\text{bg}})] \tag{6.11}$$

for s-wave collisions at low energies [185, 190]. Note that $f_{FC} \propto k$ for small k [188], so ℓ_{opt} is independent of temperature. The optical length is directly proportional to the photoassociation laser intensity, so the quantity ℓ_{opt}/I is a constant parameter for each resonance. We have measured the ℓ_{opt}/I value for the ^{84}Sr 0_u^+ states in order to characterize their properties as OFRs.

6.4.3 Measuring Optical Lengths for ^{84}Sr 0_u^+ States

To measure ℓ_{opt}/I and broadening factors for the ^{84}Sr 0_u^+ resonances, we performed photoassociation spectroscopy across each resonance using the procedure described in Sec. 6.3.1 for five different laser intensities. At each intensity, we scanned over the photoassociation resonance 4-6 times and averaged the results.

We start with the same loss equation for photoassociation loss used for a thermal gas in Sec. 6.3.2.1, $\dot{n}(\mathbf{r}) = -K_2 n(\mathbf{r})^2$ where n is the atomic density. Since the density distribution in a BEC is different than that of a thermal gas, after integrating over space the equation for total atom number has a slightly different form. For a BEC in the Thomas-Fermi approximation the total atom number changes according to [192]

$$\frac{d}{dt} \ln N = -C_2 K_2 N^{2/5}, \tag{6.12}$$

where

$$C_2 = \frac{15^{2/5}}{14\pi} \left(\frac{m\bar{\omega}}{\hbar a_{\text{bg}}^{1/2}} \right)^{6/5}. \tag{6.13}$$

In this expression, $\bar{\omega}$ is the geometric mean of the harmonic trap frequencies and a_{bg} is the atomic s-wave scattering length. The analytic solution to Eq. (6.12) is

$$N(t) = \frac{N_0}{\left(1 + \frac{2}{5} t N_0^{2/5} C_2 K_2 \right)^{5/2}} \tag{6.14}$$

with initial atom number N_0 and PAS laser application time t [45]. By combining Eqs. (6.14), (6.13), and (6.8), we can fit the loss features to extract ℓ_{opt} and η for each resonance and intensity. Since $\Gamma_{\text{stim}} \ll \Gamma_{\text{mol}}$ for the intensities used here, we ignore Γ_{stim} in the denominator of Eq. (6.8). There are other loss processes, such as one-body loss from collisions with background gas molecules or far off-resonant scattering from the atomic transition, that could complicate the analysis described here. We confirmed that those loss
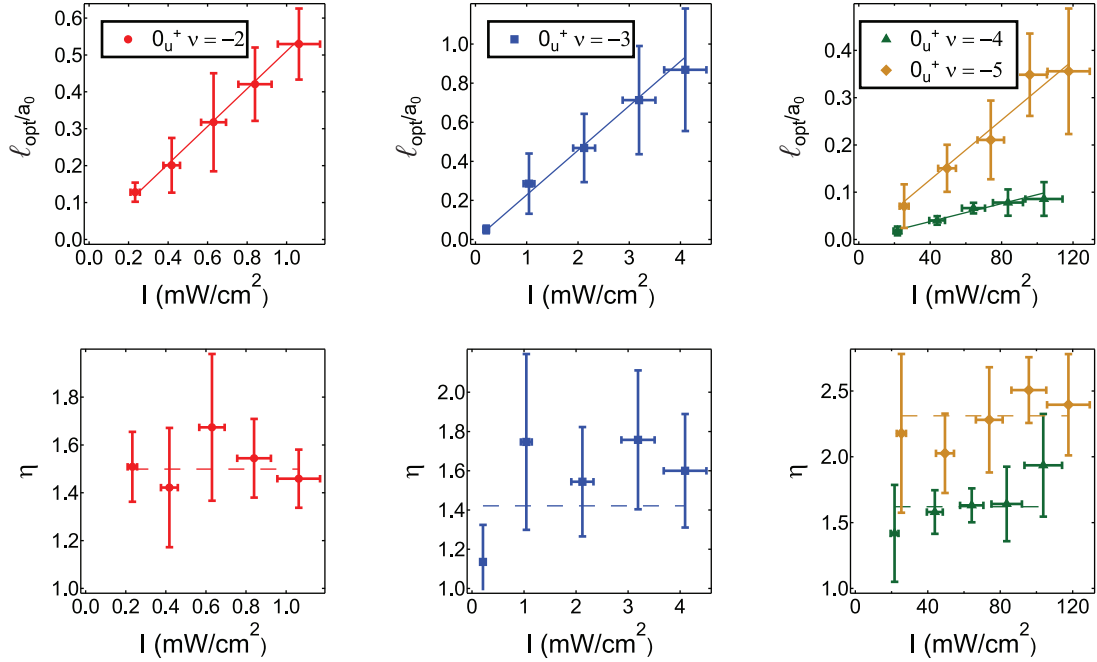
Figure 6.8: Optical lengths and η broadening factors for the ^{84}Sr 0_u^+, $\nu = -2$ to -5 resonances measured by fitting photoassociation loss curves to Eq. (6.14). Solid lines indicate linear fits whose slopes give the values for ℓ_{opt}/I reported in Table 6.3. Dashed lines indicate the weighted average values of η for each resonance.

processes were negligible for the parameters used in this study and we can safely use the simplified model above.

The extracted optical lengths and broadening factors for four ^{84}Sr 0_u^+ resonances are shown in Fig. 6.8. Due to its proximity to the atomic transition, we did not attempt to measure the 0_u^+, $\nu = -1$ optical length. For each resonance, ℓ_{opt}/I is extracted from the slopes in the top plots and η is extracted from the average of points in the bottom plots. The uncertainties include both systematic and statistical error sources, including uncertainties in the dipole trap frequencies, atomic scattering length and measured laser intensity and statistical errors from the fits added in quadrature. The statistical errors dominate the total uncertainty, followed by systematic errors in determing the laser intensity.

We calculated theoretical ℓ_{opt}/I values to compare to the measured values, as reported in Table 6.3. The theory values are based on numerical calculations of the ground and excited molecular wavefunctions using realistic potentials. More details on the cal-

Table 6.3: Measured ^{84}Sr optical lengths and broadening factors for four 0_u^+ resonances. The ℓ_{opt}/I measurements agree with a numerical estimate to better than 35%.

Vibrational Level	Binding Energy (MHz)	η	ℓ_{opt}/I $(a_0(\text{W/cm}^2)^{-1})$	
			Expt.	Theory
-2	-23.050(10)	1.50(8)	510(61)	334
-3	-228.406(10)	1.42(12)	228(42)	151
-4	-1143.161(10)	1.62(9)	0.95(12)	1.2
-5	-3692.645(10)	2.31(15)	3.16(52)	3.7

culations can be found in Appendix B. For the ground state scattering potential we used a Lennard-Jones potential of the form

$$V(r) = \frac{C_{12}}{r^{12}} - \frac{C_6}{r^6} - \frac{C_8}{r^8} - \frac{C_{10}}{r^{10}}. \tag{6.15}$$

The long-range C_6, C_8, and C_{10} coefficients are taken from [96] and the repulsive C_{12} [190] term was chosen to reproduce the ^{84}Sr experimentally determined scattering length ($a_{bg} = 123a_0$ [42]) and potential depth ($\simeq 32,400$ GHz [96]). We used the Numerov method to numerically integrate the Schrödinger equation with this potential and normalized the resulting wavefunction by matching it at long range to the energy-normalized form of Eq. (6.11). The excited molecular potentials were based on the ones used in Sec. III of [177]. To simplify the calculation, we used the adiabatic solution to the coupled two-channel potential by diagonalizing the potential for every distance r. The quantum defect parameters were re-optimized to approximately reproduce the updated bound states measured in Sec. 6.3. The binding energies and wavefunctions were calculated using the matrix Numerov method [193] with non-linear position scaling. The measured and calculated optical lengths match to better than 35%. The disagreement could be due to using the simplified adiabatic potentials instead of the full coupled-channel potentials or systematic errors in measuring the photoassociation atomic loss rate.

Measurements and calculations confirm that the line strength for the ^{84}Sr, $\nu = -2$

resonance is suppressed compared to the comparable resonances in ^{86}Sr and ^{88}Sr, for which $\ell_{\mathrm{opt}}/I \approx 10^4\ a_0(\mathrm{W/cm}^2)^{-1}$ [48, 177]. This is because in ^{84}Sr, the Condon point for this resonance ($R_c \simeq 150\ a_0$) is close to the background scattering length $123\ a_0$ and therefore a node in the scattering wavefunction [194, 195]. The optical lengths of the $\nu = -4$ and -5 resonances are also suppressed by nodes in the ground state scattering wavefunction near the classical turning points, as shown in Fig. 6.9. Contrary to the typical trend, the $\nu = -4$ state has a smaller ℓ_{opt}/I than the $\nu = -5$ state, which is also reproduced by the numerical calculation.

We observe that the η broadening factors are independent of laser intensity, which matches the behavior from a similar measurement in ^{174}Yb [45]. The source of the η broadening term is not clear. There could be some contribution to the broadening from systematic sources such as laser frequency drift and magnetic field noise. To minimize the effect of frequency drift of the PAS laser, the absolute detuning is calibrated before and after each group of scans by scanning over the atomic resonance. The absolute frequency drift is typically ≤ 5 kHz during the course of a measurement. Another potential broadening source is Doppler broadening due to BEC excitations from the dipole trap modulation discussed in Sec. 6.3.1. To estimate the magnitude of this effect, we calculated the average atomic velocity using the approach of [104] and determined the typical Doppler broadening to be ≤ 1 kHz. The residual broadening is likely due to additional molecular loss processes that have been measured in other experiments [40, 45, 48, 49, 177, 187], but lack a theoretical explanation.

6.5   Conclusion and Future Directions

We have presented an updated measurement of photoassociation resonances relative to the $^1S_0 + {}^3P_1$ dissassociation limit in ^{84}Sr and ^{86}Sr. In addition to measuring more deeply bound lines, our results correct three potentially spurious resonances in the literature. An updated theoretical treatement of the bosonic molecular potentials based on these findings
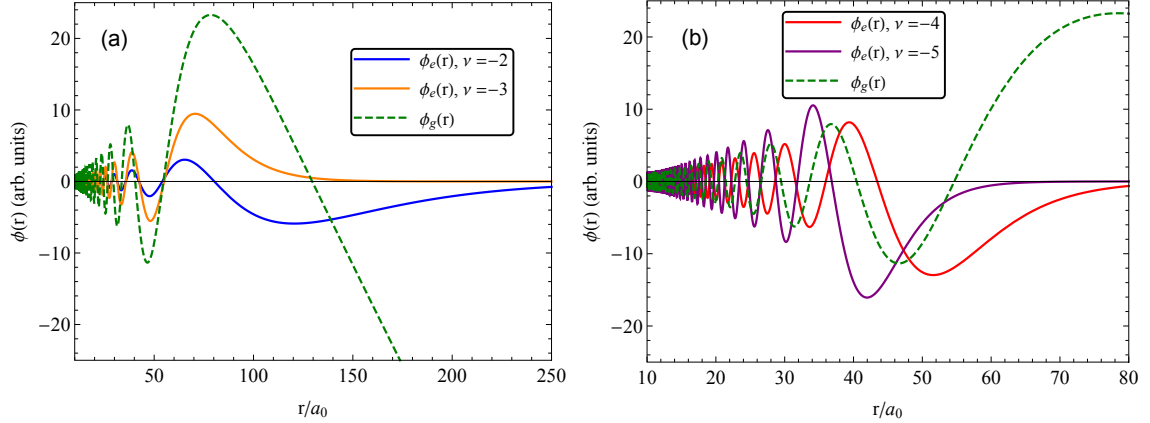
Figure 6.9: Numerically calculated excited and ground state molecular wavefunctions. The excited state wavefunctions are multiplied by 50 so that they are visible on the same scale as the ground state wavefunction. The ground state wavefunction has a node close to the classical turning point of the $\nu = -2, \; -4$, and -5 wavefunctions, reducing the associated Franck-Condon factors (see Eq. (B.1)) and optical lengths.

is underway. This improved theory, in addition to the optical length measurements, should guide future efforts to use optical Feshbach resonances to modify the scattering length or produce ground state molecules.

In the future, we may extend our studies to the subradiant photoassociation resonances of ^{84}Sr. Two previous studies [178, 194] have successfully probed these weak, electric dipole forbidden, transitions between the gerade ground state and gerade excited states in ^{174}Yb and ^{88}Sr. Since the electric dipole operator only connects states of opposite parity, these transitions are forbidden due to the Laporte selection rule [194]. However, in diatomic molecules they can acquire non-zero linewidths due to higher order magnetic-dipole and electric-quadrupole gerade-gerade transitions. Due to the subradiant nature of these transitions, they are much weaker and are characterized by much smaller linewidths (typically < 1 kHz) compared to those measured in this work [178]. In order to overcome the weak transition rates, the two previous studies increased the initial atomic density by starting from a Mott insulator in a 3D optical lattice or bound ground state molecule. We could take similar steps in our experiment and measure the ^{84}Sr 1_g binding energy spectrum.

A successful measurement of the ^{84}Sr gerade potentials could be combined with

the measurements in ^{88}Sr [178] to create a mass-scaled model applicable to the other strontium isotopes. This mass-scaled model would be particularly useful for studies of the photoassociation spectra of the fermionic ^{87}Sr isotope, which has not been successfully investigated at this time. For ^{87}Sr, the hyperfine interactions mix the gerade and ungerade states, so accurate mass scaled models of both symmetries are necessary to theoretically address the fermionic photassociation spectra. As illustrated by a similar study with ^{173}Yb [196], the spectrum is likely to be very complicated so a good theoretical understanding of the potentials will greatly aid the analysis. Despite the challenges, studying this spectrum should lead to important insights into the collisional properties of fermionic strontium. Since resonances corresponding to different total angular momentum are likely to be individually resolved [196], it may be possible to engineer spin-state dependent optical Feshbach resonances. Such a tool may be useful in a quantum simulation schemes as a method of controllably breaking the $SU(N)$ symmetry of the system.

Appendix A: The Polylogarithm Function

The polylogarithm function often arises when evaluating the spatial or momentum profiles of trapped atoms. This appendix will briefly discuss the definition, some of the properties, and methods of evaluating this function.

The polylogarithm is defined by a power series [197, Sec. 25.12]

$$\mathrm{Li}_n(z) = \sum_{k=1}^{\infty} \frac{z^k}{k^n}, \tag{A.1}$$

which is valid for $|z| \leq 1$. The function can also be defined using an integral representation,

$$\mathrm{Li}_n(z) = \frac{1}{\Gamma(n)} \int_0^{\infty} \mathrm{d}q \frac{q^{n-1}}{e^q/z - 1}, \tag{A.2}$$

where $\Gamma(n)$ is the Gamma-function. This representation is valid for $\mathrm{Re}(n) > 0$ and is real-valued for z real and $z < 1$. This integral is sometimes referred to as the Bose-Einstein integral whereas the closely related Fermi-Dirac distribution is described using

$$-\mathrm{Li}_n(-z) = \frac{1}{\Gamma(n)} \int_0^{\infty} \mathrm{d}q \frac{q^{n-1}}{e^q/z + 1}. \tag{A.3}$$

The limiting values are given by [100]

$$\mathrm{Li}_n(z) \xrightarrow{z \ll 1} z, \tag{A.4}$$

146

and

$$-\operatorname{Li}_n(-z) \xrightarrow{z \to \infty} \frac{1}{\Gamma(n+1)} \ln^n(z). \tag{A.5}$$

From the power series definition, it is clear that

$$\operatorname{Li}_n(1) = \zeta(n), \tag{A.6}$$

where $\zeta(n)$ is the Riemann zeta function. A handy relationship when evaluating integrals of polylogarithm functions is (see [198] for a proof)

$$\int_{-\infty}^{\infty} \operatorname{Li}_n\left(z e^{-a|x|^s}\right) \mathrm{d}x = 2\Gamma\left(1 + 1/s\right) a^{-1/s} \operatorname{Li}_{n+1/s}(z). \tag{A.7}$$

For the case when $s = 2$, [100]

$$\int_{-\infty}^{\infty} \operatorname{Li}_n\left(z e^{-ax^2}\right) \mathrm{d}x = \frac{\sqrt{\pi}}{\sqrt{a}} \operatorname{Li}_{n+1/2}(z). \tag{A.8}$$

Our image analysis is done in Igor Pro, which has no built-in polylogarithm evaluation function. When speed is not a concern, such as when only a small number of evaluations need to be performed, the polylogarithm can be computed by direct numerical integration of Eq. A.2. However, for applications that require many function evaluations, such as image fitting, we use several different methods to speed up evaluation. To evaluate the dilogarithm, or $\operatorname{Li}_2(z)$, used to fit the Fermi-Dirac density distribution (see Eq. (2.35)), we use a fast approximation based on [199]. For other polylogarithm orders, we pre-compute lookup tables that can be rapidly referenced when necessary. In the future we may want to transition our image analysis tasks to python for increased flexibility and speed. In python, the `mpmath` library implements a function to evaluate polylogarithm functions [200]. However, despite the inconvenience, it may still be preferable to use lookup tables as the `mpmath.polylog` function does not support arbitrary arguments and its evaluation speed can be $10^3\times$ slower than interpolating a lookup table.

Appendix B: Numerically Calculating Optical Lengths

This appendix will go into more detail about how we calculated the theoretical optical lengths for the ^{84}Sr 0_u^+ transitions shown in Table 6.3. The key ingredient to calculating the optical length (see Eq. 6.9) is to determine the Franck-Condon factor, which again is defined as

$$f_{FC} = \left| \int_0^\infty \phi_e(r)\phi_g(E,r)dr \right|^2, \tag{B.1}$$

where $\phi_e(r)$ is the excited bound molecular state wavefunction and $\phi_g(E,r)$ is the energy-normalized ground state scattering wavefunction. We will first work on calculating the ground state wavefunction.

B.1 Calculating the Ground State Wavefunction

B.1.1 Defining the Potential

Similar to the approach in [190], we will use a Lennard-Jones type potential for the ground state with the form

$$V_g(r) = \frac{C_{12}}{r^{12}} - \frac{C_6}{r^6} - \frac{C_8}{r^8} - \frac{C_{10}}{r^{10}}. \tag{B.2}$$

Though the repulsive, C_{12} term is not a realistic representation of the short range form of the potential, as we shall see, the wavefunction will oscillate rapidly at short range and the Franck-Condon factor will primarily depend on the long range portion of the wavefunction.

We ensure that the long range form of the potential is realistic by using $C_6 = 3164$ Ha a_0^6, $C_8 = 3.82 \times 10^5$ Ha a_0^8, and $C_{10} = 5.05 \times 10^7$ Ha a_0^{10} as measured by [96].[1] To determine the value of C_{12} to use, we select a value that yields a potential minimum, D_e, that approximately matches the experimentally measured value of $D_e/h \approx 32,400$ GHz [96]. Most importantly, we need to fine tune C_{12} to generate a scattering wavefunction that matches the ^{84}Sr experimentally measured s-wave scattering length of 123 a_0 [42]. We will describe the fine tuning process shortly.

B.1.2 Numerov's Method for Solving the Schrödinger Equation

Given the potential, the next step is to numerically solve the 1D time-independent Schrödinger equation,

$$\frac{-\hbar^2}{2\mu} \frac{d^2\psi(r)}{dr^2} + V_g(r)\psi(r) = E\psi(r), \tag{B.3}$$

where $\mu = m/2$ is the reduced mass of the molecule, $\hbar = 1$ in atomic units, E is the energy of the colliding atoms, and $\psi(r)$ is the wavefunction. We use the Numerov method, which is an algorithm for solving second-order differential equations of the form [193]

$$\psi''(r) = g(r)\psi(r). \tag{B.4}$$

For the Schrödinger equation, $g(r) = -2\mu(E - V_g(r))/\hbar^2$. Using a grid of points evenly spaced in r by a distance d and labeled by the index i, the solution to the differential equation is calculated using

$$\psi_{i+1} = \frac{\psi_{i-1}\left(12 - d^2 g_{i-1}\right) - 2\psi_i\left(5d^2 g_i + 12\right)}{d^2 g_{i+1} - 12} + O(d^6), \tag{B.5}$$

where $\psi_i = \psi(r_i)$ and likewise for g_i. It is important to select an appropriate grid spacing, d, to accurately capture the behavior of the wavefunction. The wavefunction will oscillate

---

[1]The calculation is performed using atomic units where the Hartree (Ha) is the unit of energy and the Bohr radius (a_0) is the unit of length.
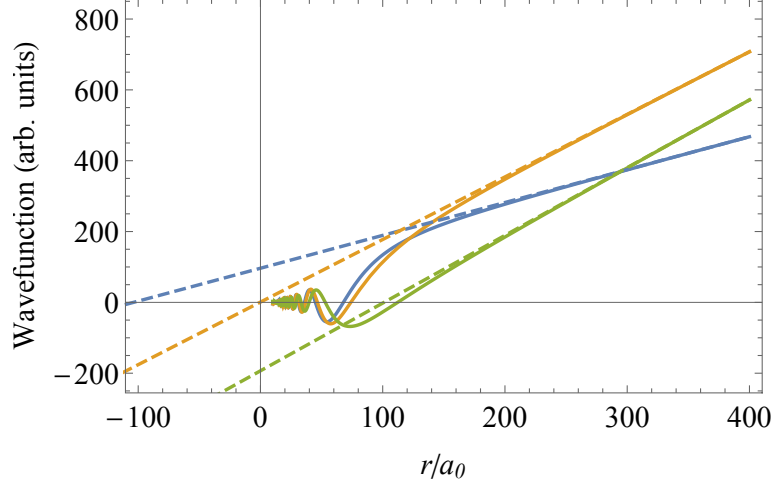
Figure B.1: Numerically calculated solutions to the ground state scattering wavefunctions (solid lines) with slightly different C_{12} values resulting in different scattering lengths. The scattering length of a wavefunction can be found by matching it to the point where the long-range form of the unperturbed wavefunction (see Eq. B.6) (dashed lines) crosses the horizontal axis. The blue, orange, and green traces have scattering lengths of -100, 0, and 100 a_0 respectively.

fastest at the minimum of the potential, V_{min}, so we find the de Broglie wavelength at that point, $\lambda_{min} = h/\sqrt{2\mu(E - V_{min})}$, and set $d = \lambda_{min}/10$ to ensure that there are at least 10 grid points for every oscillation of the wavefunction. We start the calculation at a minimum distance r_0 that is a couple periods inside the classically forbidden region of the wavefunction and initialize the calculation by selecting some small, but non-zero, value for r_0 and r_1. Some wavefunctions calculated in this manner are shown in Fig. B.1.

B.1.3 Tuning the Scattering Length

Now that we have a method of solving the Schrödinger equation, we return to the task of tuning the C_{12} parameter in the potential to match the measured scattering for ^{84}Sr. At long range, the s-wave scattering wavefunction has the plane wave form of

$$f_g(E, r) = \sqrt{\frac{2\mu}{\pi\hbar^2 k}} \sin\left[k(r - a_{bg})\right].$$

(B.6)

where $k = \sqrt{2\mu E}/\hbar$. In the limit of $k \to 0$, $f_g \propto r - a_{bg}$ at small r, so $f_g = 0$ at $r = a_{bg}$ and the scattering length can be interpreted as the horizontal intercept of the

150
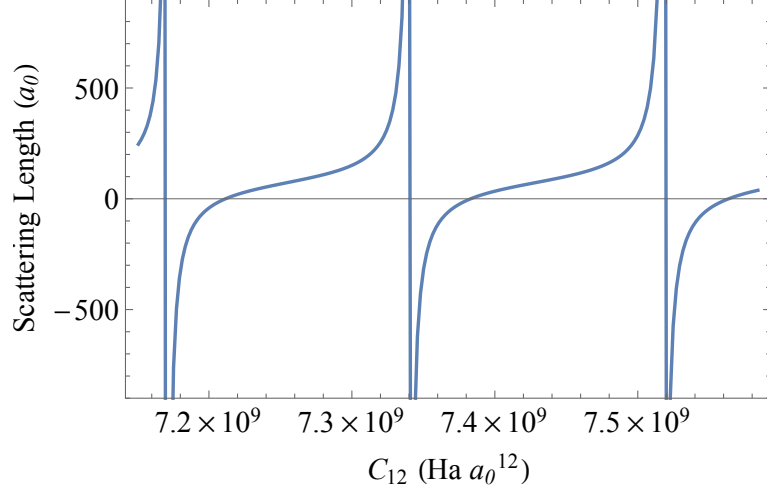
Figure B.2: The calculated scattering lengths as a function of the C_{12} parameter. The scattering wavefunctions were calculated at zero energy for a variety of values of C_{12}, showing a repeating, dispersive relationship. We use a value of $C_{12} \simeq 7.464 \times 10^9$ Ha a_0^{12} that reproduces the experimentally measured ^{84}Sr scattering length of 123 a_0.

unperturbed wavefunction. In order to determine the scattering length associated with a given wavefunction, we take the linear portion at long range and extrapolate back towards $r = 0$ to find the intercept, as illustrated in Fig. B.1. Since small changes to C_{12} will shift the phase of the wavefunction and therefore the scattering length, we map out the scattering length dependence on C_{12} in the vicinity of interest, as shown in Fig. B.2. Finally, we select a value of $C_{12} \simeq 7.464 \times 10^9$ Ha a_0^{12} where $a_{bg} = 123$ a_0.

B.1.4 Energy Normalizing the Wavefunction

The final step to calculating $\phi_g(E, r)$ for the Franck-Condon factor is to match our numerically integrated solution $\psi(E, r)$ to the energy normalized form of $f_g(E, r)$ given by Eq. B.6. We can write the numerical solution as

$$\psi(E, r) = Af_g(E, r) = A\sqrt{\frac{2\mu}{\pi\hbar^2 k}} \sin\left[k(r - a_{bg})\right].$$ (B.7)

So we need to determine the normalization constant A in order to calculate $\phi_g(E, r) = A^{-1}\psi(E, r)$. To efficiently find the normalization constant, we will use an approach based

151

on [201]. First, let us define the Wronskian operator,

$$W[y_1, y_2] = y_1 y_2' - y_2 y_1', \tag{B.8}$$

and two auxiliary functions

$$p(r) = \sin(kr)$$
$$q(r) = \cos(kr). \tag{B.9}$$

Using these definitions, we find that

$$W[\psi(E,r), p(r)] = A\sqrt{\frac{2\mu k}{\pi \hbar^2}} \sin(-k a_{\mathrm{bg}})$$
$$W[\psi(E,r), q(r)] = A\sqrt{\frac{2\mu k}{\pi \hbar^2}} \cos(-k a_{\mathrm{bg}}), \tag{B.10}$$

and the normalization constant is

$$A = \sqrt{\frac{\pi \hbar^2}{2\mu k}} \left(W[\psi(E,r), p(r)]^2 + W[\psi(E,r), q(r)]^2 \right)^{1/2}. \tag{B.11}$$

To find the normalization constant numerically, we calculate $\psi(E,r)$ out to very large r $(15,000\, a_0)$. The energy is determined by using the formula for the wavenumber of a BEC $k = \sqrt{21/8}/(2R_{\mathrm{TF}})$ [49] with $R_{\mathrm{TF}} \simeq 7.5\ \mu$m, which is a typical radius for our BECs. The normalization constant can easily be calculated according to Eq. (B.11) and we find that it converges at a distance of $r \approx 1,000\, a_0$.

B.2 Calculating the Excited State Wavefunction

B.2.1 Defining the Potential

To calculate the bound, excited-state molecular wavefunctions, we will first start with the two-channel potentials from Section III of [177]. The two channels correspond

Table B.1: Molecular $^1S_0 + {}^3P_1$ Potential Parameters. These parameters are used with Eq. (B.12) to define the molecular potentials in the Hund's case (a) representation. All values, except for the quantum defects, $\alpha(^{84}\text{Sr})$, are taken from [177]. The updated $\alpha(^{84}\text{Sr})$ values are tuned based on the updated binding energy spectrum of ^{84}Sr measured in Chapter 6 (see Fig. B.3).

Parameter	$^3\Sigma_u^+$	$^3\Pi_u$
A_0	1.29406314×10^2	5.78723038×10^6
A_1	-7.90551852×10^1	-3.46113235×10^6
A_2	1.87863441×10^1	7.79019763×10^5
A_3	-1.96979418×10^0	-7.85317879×10^4
A_4	$7.88636443 \times 10^{-2}$	3.01833743×10^3
γ	$7.61382806 \times 10^{-2}$	$1.34967817 \times 10^{-3}$
β	1.00	1.03238202
$\alpha(^{84}\text{Sr})$	0.045485	1.98930
C_{12}	-5.31841848×10^9	$-1.06415514 \times 10^{10}$
C_{10}	2.20495×10^8	5.24064×10^7
C_8	2.3574797×10^6	3.4156471×10^5
C_6	4.3015063×10^3	3.8683912×10^3
C_3	$1.52356615 \times 10^{-2}$	

to the Hund's case (c) 0_u^+ and 1_u states and are based on the *ab initio* calculations of the $^3\Sigma_u^+$ and $^3\Pi_u$ Hund's case (a) potentials from [173]. The Hund's case (a) potentials have the form of

$$
\begin{aligned}
V(r) =& e^{-\alpha r - \gamma r^2} \left(A_0 + A_1 r + A_2 r^2 + A_3 r^3 + A_r r^4 \right) \\
& - C_{12} f_{12}(r, \beta) r^{-12} - C_{10} f_{10}(r, \beta) r^{-10} - C_8 f_8(r, \beta) r^{-8} - C_6 f_6(r, \beta) r^{-6},
\end{aligned}
\tag{B.12}
$$

where the values of the various parameters are given in Table B.1 and $f_n(r, \beta)$ is the nth order Tang-Toennies damping function [202]

$$
f_n(r, \beta) = 1 - e^{-\beta r} \sum_{k=0}^{n} \frac{(\beta r)^k}{k!}.
\tag{B.13}
$$

These potentials are combined to give the corresponding Hund's case (c) representations by

$$V_{\text{tot}} = V_{\text{int}} + V_{\text{rot}}, \tag{B.14}$$

where

$$V_{\text{int}} = \begin{pmatrix} V(^3\Pi_u; r) - \frac{C_3}{r^3} & 0 \\ 0 & \frac{1}{2}\left(V(^3\Pi_u; r) + V(^3\Sigma_u^+; r)\right) + \frac{C_3}{2r^3} \end{pmatrix}, \tag{B.15}$$

and

$$V_{\text{rot}} = \frac{\hbar^2}{2\mu r^2} \begin{pmatrix} J(J+1) + 2 & -\sqrt{4J(J+1)} \\ -\sqrt{4J(J+1)} & J(J+1) \end{pmatrix}. \tag{B.16}$$

All the molecular states investigated in this work have $J = 1$. The final potential consists of a 2×2 matrix, with off-diagonal components arising from the rotational energy of the molecule.

Though it is possible to solve the Schrödinger equation with the full, multi-channel potential using numerical methods such as discrete variable representation (DVR) [203], we will simplify the problem by taking the adiabatic approximation, which consists of diagonalizing the potential for every value of r. The adiabatic approximation limits the accuracy of the resulting binding energies to a few MHz for most resonances, but is sufficient for our goal of estimating Franck-Condon parameters. I will refer to these potentials as $V_{\text{ad}}(0, r)$ and $V_{\text{ad}}(1, r)$ for the 0_u^+ and 1_u potentials respectively.

The potential parameters, shown in Table B.1, were determined by Borkowski *et al.* to reproduce the measured binding energy spectrum of ^{88}Sr [177]. For the spectrum of ^{84}Sr and ^{86}Sr, Borkowski *et al.* retained most of those parameters but tuned the two quantum defect parameters, α_Σ corresponding to the $^3\Sigma_u^+$ state and α_Π corresponding to the $^3\Pi_u$ state, to match the binding energy spectrum for each individual isotope. We took a similar approach and found new ^{84}Sr quantum defect parameters to more closely reproduce the updated binding energies that we measured in Chapter 6. The binding energies of the seven least bound resonances were calculated using the method that will
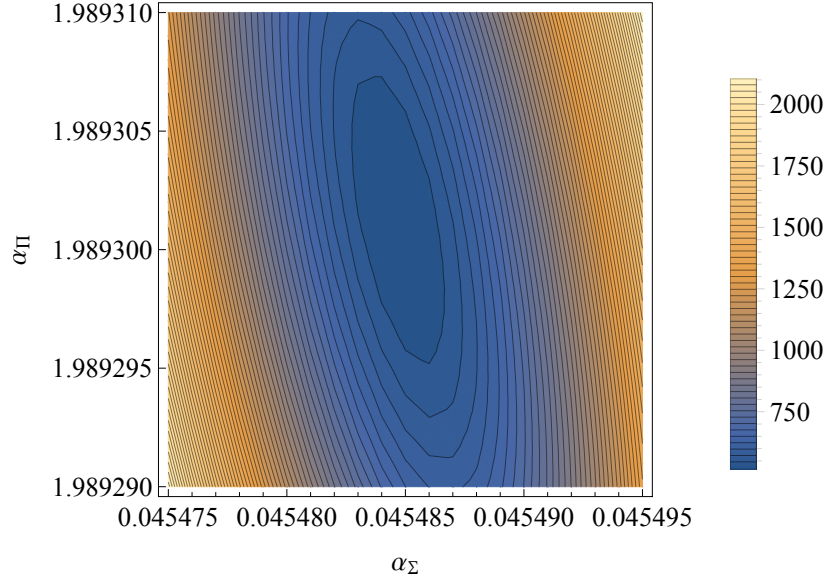
Figure B.3: The sum of the squared residuals are plotted with respect to the two quantum defect parameters, α_Σ and α_Π. The residuals come from comparing the calculated binding energies to the experimentally measured values. The adiabatic approximation limits the accuracy of this model to an average residual of about 6 MHz for the 7 photoassociation resonances measured.

be described in the next section. A 2D scan of the α_Σ and α_Π parameters mapping out the contours of the sum of the squared residuals is shown in Fig. B.3. The minimum is located at $\alpha = 0.045485$ and $\alpha_2 = 1.98930$, as reported in Table B.1, and we will use these values to define $V_{\text{ad}}(0, r)$ and $V_{\text{ad}}(1, r)$.

B.2.2 Matrix Numerov Method for Solving the Schrödinger Equation

We also use the Numerov method to calculate the bound states for the excited state potentials. In order to simultaneously calculate all of the bound states, we use a matrix method instead of the simpler algorithm described in Sec. B.1.2. As shown in [193], if we represent ψ as a column vector $(...\psi_{i-1}, \psi_i, \psi_{i+1}, ...)$, the Numerov representation of the Schrödinger equation can be written as a matrix equation

$$-\frac{\hbar^2}{2\mu}B^{-1}A\psi + V\psi = E\psi,\tag{B.17}$$

where the matrices A, B, and V are defined as $A = (\mathbb{I}_{-1} - 2\mathbb{I}_0 + \mathbb{I}_1)/d^2$, $B = (\mathbb{I}_{-1} + 10\mathbb{I}_0 + \mathbb{I}_1)/12$, $V = \text{diag}(...V_{i-1}, V_i, V_{i+1}, ...)$, and $\mathbb{I}_p$ is a matrix with 1s along the pth diagonal and 0s elsewhere. Then we can construct the Hamiltonian matrix

$$H = -\frac{\hbar^2}{2\mu} B^{-1} A + V \tag{B.18}$$

and determine all the binding energies and wavefunctions simultaneously by diagonalizing H.

For the molecular potentials under consideration, the wavefunction oscillate rapidly at short range near the potential minimum, and therefore require a small grid size in this region. However, for the weakly bound states that we are interested in, the wavefunctions also extend to long ranges, so with a linear grid the size of the matrix quickly becomes too large to be computationally manageable. Therefore, we will introduce a nonlinear scaling of the distance coordinate to allow for a large density of points at short range when the wavefunctions oscillate rapidly and a sparser density at long range when the wavefunctions oscillate slowly. This approach will allow us to capture the accurate behavior of the wavefunctions with moderately sized matrices.

B.2.3   Non-Linear Coordinate Transformation

To transform the coordinates from r to the new, non-linear coordinate y, we introduce the forward transform $y = u(r)$, where u is a monotonic, invertible function of r, and the inverse transform $r = U(y)$. We will transform the wavefunction from $\psi(r) \to \chi(y)$ using the scaling $\psi(r) = K(y(r)) \chi(y(r))$. The kinetic energy operator transforms according to [203]

$$T = -\frac{\hbar^2}{2\mu} \frac{d^2}{dr^2} = -\frac{\hbar^2}{2\mu} \left(\frac{1}{U'(y)^2} \frac{d^2}{dy^2} - \frac{U''(y)}{U'(y)^3} \frac{d}{dy} \right). \tag{B.19}$$

Since the Numerov algorithm can only be used to solve second-order differential equations with no first-derivative terms, we must select $K(y)$ such that there are no $\chi'(y)$ terms in the

Schrödinger equation after the coordinate transformation. Plugging these transformations into the Schrödinger equation yields

$$-\frac{\hbar^2}{2\mu}\left(\frac{1}{U'(y)^2}\frac{d^2}{dy^2} - \frac{U''(y)}{U'(y)^3}\frac{d}{dy}\right)K(y)\chi(y) + V[U(y)]K(y)\chi(y) = EK(y)\chi(y)$$
$$= [\chi''(y) \text{ terms}] + [\chi(y) \text{ terms}] + \chi'(y)\left(\frac{-\hbar^2 K'(y)}{\mu U'(y)^2} + \frac{\hbar^2 K(y)U''(y)}{2\mu U'(y)^3}\right) = EK(y)\chi(y).$$

(B.20)

So we must choose $K(y)$ to satisfy the differential equation

$$\frac{K'(y)}{U'(y)^2} + \frac{K(y)U''(y)}{2U'(y)^3} = 0.$$

(B.21)

The solution to this equation has the general form of

$$K(y) = C\sqrt{U'(y)},$$

(B.22)

where C is a constant of integration.[2]

Based on [203], we will select a scaling relationship of the form

$$y = u(r) = -2\sqrt{\frac{R_0}{r + R_s}},$$

(B.23)

where R_0 and R_s are tunable parameters. We somewhat arbitrarily use $R_0 = 10$ and $R_s = 0.01$, and we find the results to be insensitive to these parameters over a wide range of values. Therefore, the other scaling functions are

$$r = U(y) = -R_s + \frac{4R_0}{y^2}$$
$$K(y) = 2\sqrt{\frac{-2R_0}{y^3}}.$$

(B.24)

---

[2]An example of a non-linear coordinate transformation to solve the hydrogen atom can be found at http://www.physics.wisc.edu/~tgwalker/NumerovExamples/.

Plugging these equations into Eq. (B.20) gives the Schrödinger equation in our new coordinates

$$\frac{-\hbar^2 y^6}{128 R_0^2 \mu} \chi''(y) + \left(\frac{3\hbar^2 y^4}{512 R_0^2 \mu} + V[U(y)] \right) \chi(y) = E \chi(y). \tag{B.25}$$

This is similar to the original equation, except the kinetic energy term is multiplied by some additional factors and there is an additional term to the effective potential. The matrix Hamiltonian for the Numerov method is similar to Eq. (B.18) above and is given by

$$\tilde{H} = -\frac{\hbar^2}{128 R_0^2 \mu} \tilde{C} B^{-1} A + \tilde{V} + \frac{3\hbar^2}{512 R_0^2 \mu} \tilde{D} \tag{B.26}$$

where the matrices A and B are as defined above, $\tilde{C} = \text{diag}(...y_{i-1}^6, y_i^6, y_{i+1}^6, ...)$, $\tilde{V} = \text{diag}(...V[U(y_{i-1})], V[U(y_i)], V[U(y_{i+1})], ...)$, and $\tilde{D} = \text{diag}(...y_{i-1}^4, y_i^4, y_{i+1}^4, ...)$. Finally we are ready to solve the excited state potential by diagonalizing $\tilde{H}$.[3] For n grid points, since the diagonalization algorithm will return n eigenvalues and eigenvectors, we have to search the results to look for the eigenvalues (binding energies) that match the resonance in question. The resulting eigenvectors can be converted by to the original coordinates using $\psi(r) = K(y)\chi(y)$ and should be normalized in the usual method, $\int \psi(r)d^3\mathbf{r} = 1$.

B.3   Putting it all Together: Calculating the Optical Length

We can now calculate the energy-normalized ground state wavefunction, $\phi_g(E, r)$, using the methods described in Sec. B.1 and the excited state wavefunction, $\phi_e(r)$, using the methods described in Sec. B.2. To put it all together, we just need to calculate the Franck-Condon factor by numerically integrating Eq. (B.1), and then calculate the optical length according to

$$\ell_{\text{opt}} = \frac{\lambda^3}{16\pi c} \frac{f_{FC}}{k} f_{\text{rot}} I, \tag{B.27}$$

---

[3]Using a grid of 4000 points going out to a maximum distance of $r_{\text{max}} = 3000\ a_0$, the calculation takes about 2 minutes on a consumer laptop.

where λ = 689.45 nm is the wavelength of the atomic transition, the rotational factor f_{rot} = 1 for 0_u^+ resonances and f_{rot} = 2 for 1_u resonances, and, to obtain the correct units, I = 1 W/cm^2. The numerical results are shown in Table 6.3 and compared to the experimentally measured values.

Bibliography

[1] T. H. Maiman, "Stimulated Optical Radiation in Ruby," *Nature*, vol. 187, no. 4736, p. 493, 1960.

[2] A. Ashkin, "Acceleration and Trapping of Particles by Radiation Pressure," *Phys. Rev. Lett.*, vol. 24, no. 4, p. 156, 1970.

[3] D. Wineland and H. Dehmelt, "Proposed $10^{14}\Delta\nu < \nu$ laser fluorescence spectroscopy on TI$^+$ mono-ion oscillator, III," *Bull. Am. Phys. Soc.*, vol. 20, p. 637, 1975.

[4] T. W. Hänsch and A. L. Schawlow, "Cooling of gases by laser radiation," *Opt. Commun.*, vol. 13, no. 1, p. 68, 1975.

[5] A. Ashkin, "Trapping of atoms by resonance radiation pressure," *Phys. Rev. Lett.*, vol. 40, no. 12, p. 729, 1978.

[6] D. J. Wineland, R. E. Drullinger, and F. L. Walls, "Radiation-Pressure Cooling of Bound Resonant Absorbers," *Phys. Rev. Lett.*, vol. 40, no. 25, p. 1639, 1978.

[7] W. Neuhauser, M. Hohenstatt, P. Toschek, and H. Dehmelt, "Optical-sideband cooling of visible atom cloud confined in parabolic well," *Phys. Rev. Lett.*, vol. 41, no. 4, p. 233, 1978.

[8] W. D. Phillips and H. Metcalf, "Laser Deceleration of an Atomic Beam," *Phys. Rev. Lett.*, vol. 48, no. 9, p. 596, 1982.

[9] J. Prodan, A. Migdall, W. D. Phillips, I. So, H. Metcalf, and J. Dalibard, "Stopping Atoms with Laser Light," *Phys. Rev. Lett.*, vol. 54, no. 10, p. 992, 1985.

[10] V. S. Letokhov, V. G. Minogin, and B. D. Pavlik, "Cooling and trapping of atoms and molecules by a resonant laser field," *Opt. Commun.*, vol. 19, no. 1, p. 72, 1976.

[11] J. V. Prodan and W. D. Phillips, "Chirping the light-fantastic? Recent NBS atom cooling experiments," *Prog. Quantum Electron.*, vol. 8, no. 3-4, p. 231, 1984.

[12] W. Ertmer, R. Blatt, J. L. Hall, and M. Zhu, "Laser Manipulation of Atomic Beam Velocities: Demonstration of Stopped Atoms and Velocity Reversal," *Phys. Rev. Lett.*, vol. 54, no. 10, p. 996, 1985.

[13] S. Chu, L. Hollberg, J. E. Bjorkholm, A. Cable, and A. Ashkin, "Three-Dimensional Viscous Confinement and Cooling of Atoms by Resonance Radiation Pressure," *Phys. Rev. Lett.*, vol. 55, no. 1, p. 48, 1985.

[14] A. L. Migdall, J. V. Prodan, W. D. Phillips, T. H. Bergeman, and H. J. Metcalf, "First Observation of Magnetically Trapped Neutral Atoms," *Phys. Rev. Lett.*, vol. 54, no. 24, p. 2596, 1985.

[15] E. L. Raab, M. Prentiss, A. Cable, S. Chu, and D. E. Pritchard, "Trapping of Neutral Sodium Atoms with Radiation Pressure," *Phys. Rev. Lett.*, vol. 59, no. 23, p. 2631, 1987.

[16] S. Chu, J. E. Bjorkholm, A. Ashkin, and A. Cable, "Experimental Observation of Optically Trapped Atoms," *Phys. Rev. Lett.*, vol. 57, no. 3, p. 314, 1986.

[17] W. D. Phillips, "Nobel Lecture: Laser cooling and trapping of neutral atoms," *Rev. Mod. Phys.*, vol. 70, no. 3, p. 721, 1998.

[18] S. Chu, "Nobel Lecture: The manipulation of neutral particles," *Rev. Mod. Phys.*, vol. 70, no. 3, p. 685, 1998.

[19] A. Clairon, C. Salomon, S. Guellati, and W. D. Phillips, "Ramsey Resonance in a Zacharias Fountain," *Europhys. Lett.*, vol. 16, no. 2, p. 165, 1991.

[20] R. Wynands and S. Weyers, "Atomic fountain clocks," *Metrologia*, vol. 42, no. 3, p. S64, 2005.

[21] T. L. Nicholson, S. L. Campbell, R. B. Hutson, G. E. Marti, B. J. Bloom, R. L. McNally, W. Zhang, M. D. Barrett, M. S. Safronova, G. F. Strouse, W. L. Tew, and J. Ye, "Systematic evaluation of an atomic clock at 2×10^{-18} total uncertainty," *Nat. Commun.*, vol. 6, p. 6896, 2015.

[22] M. H. Anderson, J. R. Ensher, M. R. Matthews, C. E. Wieman, and E. A. Cornell, "Observation of Bose-Einstein Condensation in a Dilute Atomic Vapor," *Science*, vol. 269, no. 5221, p. 198, 1995.

[23] K. B. Davis, M. O. Mewes, M. R. Andrews, N. J. Van Druten, D. S. Durfee, D. M. Kurn, and W. Ketterle, "Bose-Einstein Condensation in a Gas of Sodium Atoms," *Phys. Rev. Lett.*, vol. 75, no. 22, p. 3969, 1995.

[24] B. DeMarco and D. S. Jin, "Onset of Fermi Degeneracy in a Trapped Atomic Gas," *Science*, vol. 285, no. 5434, p. 1703, 1999.

[25] I. Bloch, J. Dalibard, and W. Zwerger, "Many-body physics with ultracold gases," *Rev. Mod. Phys.*, vol. 80, no. 3, p. 885, 2008.

[26] C. Chin, P. Julienne, and E. Tiesinga, "Feshbach resonances in ultracold gases," *Rev. Mod. Phys.*, vol. 82, no. 2, p. 1225, 2010.

[27] I. M. Georgescu, S. Ashhab, and F. Nori, "Quantum simulation," *Rev. Mod. Phys.*, vol. 86, no. 1, p. 153, 2014.

[28] M. Saffman, T. G. Walker, and K. Mølmer, "Quantum information with Rydberg atoms," *Rev. Mod. Phys.*, vol. 82, no. 3, p. 2313, 2010.

[29] C. J. Foot, *Atomic Physics*. New York: Oxford University Press, 2005.

[30] A. Kramida, Yu. Ralchenko, J. Reader, and NIST ASD Team. NIST Atomic Spectra Database (ver. 5.2), [Online]. Available: http://physics.nist.gov/asd [2015, July 7]. National Institute of Standards and Technology, Gaithersburg, MD., 2014.

[31] H. Katori, T. Ido, Y. Isoya, and M. Kuwata-Gonokami, "Magneto-Optical Trapping and Cooling of Strontium Atoms down to the Photon Recoil Temperature," *Phys. Rev. Lett.*, vol. 82, no. 6, p. 1116, 1999.

[32] T. Mukaiyama, H. Katori, T. Ido, Y. Li, and M. Kuwata-Gonokami, "Recoil-Limited Laser Cooling of ^{87}Sr Atoms near the Fermi Temperature," *Phys. Rev. Lett.*, vol. 90, no. 11, p. 113002, 2003.

[33] T. Loftus, T. Ido, M. Boyd, A. Ludlow, and J. Ye, "Narrow line cooling and momentum-space crystals," *Phys. Rev. A*, vol. 70, no. 6, p. 063413, 2004.

[34] T. H. Loftus, T. Ido, A. D. Ludlow, M. M. Boyd, and J. Ye, "Narrow line cooling: Finite photon recoil dynamics," *Phys. Rev. Lett.*, vol. 93, no. 7, p. 073003, 2004.

[35] T. Kuwamoto, K. Honda, Y. Takahashi, and T. Yabuzaki, "Magneto-optical trapping of Yb atoms using an intercombination transition," *Phys. Rev. A*, vol. 60, no. 2, p. 745(R), 1999.

[36] T. Binnewies, G. Wilpers, U. Sterr, F. Riehle, J. Helmcke, T. E. Mehlstäubler, E. M. Rasel, and W. Ertmer, "Doppler Cooling and Trapping on Forbidden Transitions," *Phys. Rev. Lett.*, vol. 87, no. 12, p. 123002, 2001.

[37] R. Maruyama, R. H. Wynar, M. V. Romalis, A. Andalkar, M. D. Swallows, C. E. Pearson, and E. N. Fortson, "Investigation of sub-Doppler cooling in an ytterbium magneto-optical trap," *Phys. Rev. A*, vol. 68, no. 1, p. 011403(R), 2003.

[38] E. A. Curtis, C. W. Oates, and L. Hollberg, "Quenched narrow-line second- and third-stage laser cooling of ^{40}Ca," *J. Opt. Soc. Am. B*, vol. 20, no. 5, p. 977, 2003.

[39] S. Stellmer, B. Pasquiou, R. Grimm, and F. Schreck, "Laser cooling to quantum degeneracy," *Phys. Rev. Lett.*, vol. 110, no. 26, p. 263003, 2013.

[40] T. Zelevinsky, M. M. Boyd, A. D. Ludlow, T. Ido, J. Ye, R. Ciuryło, P. Naidon, and P. S. Julienne, "Narrow Line Photoassociation in an Optical Lattice," *Phys. Rev. Lett.*, vol. 96, no. 20, p. 203201, 2006.

[41] M. Kitagawa, K. Enomoto, K. Kasa, Y. Takahashi, R. Ciuryło, P. Naidon, and P. S. Julienne, "Two-color photoassociation spectroscopy of ytterbium atoms and the precise determinations of s-wave scattering lengths," *Phys. Rev. A - At. Mol. Opt. Phys.*, vol. 77, no. 1, p. 012719, 2008.

[42] Y. N. Martinez de Escobar, P. G. Mickelson, P. Pellegrini, S. B. Nagel, A. Traverso, M. Yan, R. Côté, and T. C. Killian, "Two-photon photoassociative spectroscopy of ultracold ^{88}Sr," *Phys. Rev. A*, vol. 78, no. 6, p. 062708, 2008.

[43] B. H. Mcguyer, C. B. Osborn, M. McDonald, G. Reinaudi, W. Skomorowski, R. Moszynski, and T. Zelevinsky, "Nonadiabatic effects in ultracold molecules via anomalous linear and quadratic zeeman shifts," *Phys. Rev. Lett.*, vol. 111, no. 24, p. 243003, 2013.

[44] M. Kahmann, E. Tiemann, O. Appel, U. Sterr, and F. Riehle, "Photoassociation spectroscopy of ^{40}Ca measured with kilohertz accuracy near the $^3P_1 + ^1S_0$ asymptote and its Zeeman effect," *Phys. Rev. A*, vol. 89, no. 2, p. 023413, 2014.

[45] M.-S. Kim, J. Lee, J. H. Lee, Y. Shin, and J. Mun, "Measurements of optical Feshbach resonances of ^{174}Yb atoms," *Phys. Rev. A*, vol. 94, no. 4, p. 042703, 2016.

[46] K. Enomoto, K. Kasa, M. Kitagawa, and Y. Takahashi, "Optical feshbach resonance using the intercombination transition," *Phys. Rev. Lett.*, vol. 101, no. 20, p. 203201, 2008.

[47] R. Yamazaki, S. Taie, S. Sugawa, and Y. Takahashi, "Submicron spatial modulation of an interatomic interaction in a Bose-Einstein condensate," *Phys. Rev. Lett.*, vol. 105, no. 5, p. 050405, 2010.

[48] S. Blatt, T. L. Nicholson, B. J. Bloom, J. R. Williams, J. W. Thomsen, P. S. Julienne, and J. Ye, "Measurement of Optical Feshbach Resonances in an Ideal Gas," *Phys. Rev. Lett.*, vol. 107, no. 7, p. 073202, 2011.

[49] M. Yan, B. J. Desalvo, B. Ramachandhran, H. Pu, and T. C. Killian, "Controlling Condensate Collapse and Expansion with an Optical Feshbach Resonance," *Phys. Rev. Lett.*, vol. 110, no. 12, p. 123201, 2013.

[50] S. Stellmer, B. Pasquiou, R. Grimm, and F. Schreck, "Creation of ultracold Sr_2 molecules in the electronic ground state," *Phys. Rev. Lett.*, vol. 109, no. 11, p. 115302, 2012.

[51] G. Reinaudi, C. Osborn, M. McDonald, S. Kotochigova, and T. Zelevinsky, "Optical Production of Stable Ultracold $^{88}Sr_2$ Molecules," *Phys. Rev. Lett.*, vol. 109, p. 115303, 2012.

[52] A. Ciamei, A. Bayerle, C. C. Chen, B. Pasquiou, and F. Schreck, "Efficient production of long-lived ultracold Sr_2 molecules," *Phys. Rev. A*, vol. 96, no. 1, p. 013406, 2017.

[53] S. Stellmer, R. Grimm, and F. Schreck, "Detection and manipulation of nuclear spin states in fermionic strontium," *Phys. Rev. A*, vol. 84, no. 4, p. 043611, 2011.

[54] B. J. DeSalvo, J. A. Aman, F. B. Dunning, T. C. Killian, H. R. Sadeghpour, S. Yoshida, and J. Burgdörfer, "Ultra-long-range Rydberg molecules in a divalent atomic system," *Phys. Rev. A*, vol. 92, no. 3, p. 031403(R), 2015.

[55] B. J. DeSalvo, J. A. Aman, C. Gaul, T. Pohl, S. Yoshida, J. Burgdörfer, K. R. Hazzard, F. B. Dunning, and T. C. Killian, "Rydberg-blockade effects in Autler-Townes spectra of ultracold strontium," *Phys. Rev. A*, vol. 93, no. 2, p. 022709, 2016.

[56] F. Camargo, J. D. Whalen, R. Ding, H. R. Sadeghpour, S. Yoshida, J. Burgdörfer, F. B. Dunning, and T. C. Killian, "Lifetimes of ultra-long-range strontium Rydberg molecules," *Phys. Rev. A*, vol. 93, no. 2, p. 022702, 2016.

[57] M. M. Boyd, *High Precision Spectroscopy of Strontium in an Optical Lattice: Towards a New Standard for Frequency and Time*. PhD thesis, University of Colorado, Boulder, 2007.

[58] A. Yamaguchi, S. Uetake, S. Kato, H. Ito, and Y. Takahashi, "High-resolution laser spectroscopy of a Bose-Einstein condensate using the ultranarrow magnetic quadrupole transition," *New J. Phys.*, vol. 12, p. 103001, 2010.

[59] U. Sterr, C. Degenhardt, H. Stoehr, C. Lisdat, H. Schnatz, J. Helmcke, F. Riehle, G. Wilpers, C. Oates, and L. Hollberg, "The optical calcium frequency standards of PTB and NIST," *Comptes Rendus Phys.*, vol. 5, no. 8, p. 845, 2004.

[60] M. Takamoto, F.-L. Hong, R. Higashi, and H. Katori, "An optical lattice clock," *Nature*, vol. 435, no. 7040, p. 321, 2005.

[61] A. D. Ludlow, M. M. Boyd, and J. Ye, "Optical atomic clocks," *Rev. Mod. Phys.*, vol. 87, no. 2, p. 637, 2015.

[62] N. Nemitz, T. Ohkubo, M. Takamoto, I. Ushijima, M. Das, N. Ohmae, and H. Katori, "Frequency ratio of Yb and Sr clocks with 5×10^{-17} uncertainty at 150 seconds averaging time," *Nat. Photonics*, vol. 10, no. 4, p. 258, 2016.

[63] S. L. Campbell, R. B. Hutson, G. E. Marti, A. Goban, N. D. Oppong, L. Sonderhouse, J. M. Robinson, W. Zhang, B. J. Bloom, and J. Ye, "A Fermi-degenerate three-dimensional optical lattice clock," *Science*, vol. 358, no. 6359, p. 90, 2017.

[64] A. Derevianko and M. Pospelov, "Hunting for topological dark matter with atomic clocks," *Nat. Phys.*, vol. 10, no. 12, p. 933, 2014.

[65] K. Van Tilburg, N. Leefer, L. Bougas, and D. Budker, "Search for Ultralight Scalar Dark Matter with Atomic Spectroscopy," *Phys. Rev. Lett.*, vol. 115, no. 1, p. 011802, 2015.

[66] Y. V. Stadnik and V. V. Flambaum, "Enhanced effects of variation of the fundamental constants in laser interferometers and application to dark-matter detection," *Phys. Rev. A*, vol. 93, no. 6, p. 063630, 2016.

[67] S. Kolkowitz, I. Pikovski, N. Langellier, M. D. Lukin, R. L. Walsworth, and J. Ye, "Gravitational wave detection with optical lattice atomic clocks," *Phys. Rev. D*, vol. 94, no. 12, p. 124043, 2016.

[68] F. Sorrentino, A. Alberti, G. Ferrari, V. V. Ivanov, N. Poli, M. Schioppo, and G. M. Tino, "Quantum sensor for atom-surface interactions below 10 μm," *Phys. Rev. A*, vol. 79, no. 1, p. 013409, 2009.

[69] N. Poli, F. Y. Wang, M. G. Tarallo, A. Alberti, M. Prevedelli, and G. M. Tino, "Precision measurement of gravity with cold atoms in an optical lattice and comparison with a classical gravimeter," *Phys. Rev. Lett.*, vol. 106, no. 3, p. 038501, 2011.

[70] A. O. Jamison, B. Plotkin-Swing, and S. Gupta, "Advances in precision contrast interferometry with Yb Bose-Einstein condensates," *Phys. Rev. A*, vol. 90, no. 6, p. 063606, 2014.

[71] M. M. Boyd, T. Zelevinsky, A. D. Ludlow, S. Blatt, T. Zanon-Willette, S. M. Foreman, and J. Ye, "Nuclear spin effects in optical lattice clocks," *Phys. Rev. A*, vol. 76, no. 2, p. 022510, 2007.

[72] M. Hermele, V. Gurarie, and A. M. Rey, "Mott insulators of ultracold fermionic alkaline earth atoms: Underconstrained magnetism and chiral spin liquid," *Phys. Rev. Lett.*, vol. 103, no. 13, p. 135301, 2009.

[73] A. V. Gorshkov, M. Hermele, V. Gurarie, C. Xu, P. S. Julienne, J. Ye, P. Zoller, E. Demler, M. D. Lukin, and A. M. Rey, "Two-orbital SU(N) magnetism with ultracold alkaline-earth atoms," *Nat. Phys.*, vol. 6, no. 4, p. 289, 2010.

[74] C. Xu, "Liquids in multiorbital SU(N) magnets made up of ultracold alkaline-earth atoms," *Phys. Rev. B*, vol. 81, no. 14, p. 144431, 2010.

[75] H. H. Hung, Y. Wang, and C. Wu, "Quantum magnetism in ultracold alkali and alkaline-earth fermion systems with symplectic symmetry," *Phys. Rev. B*, vol. 84, no. 5, p. 054406, 2011.

[76] S. R. Manmana, K. R. A. Hazzard, G. Chen, A. E. Feiguin, and A. M. Rey, "SU(N) magnetism in chains of ultracold alkaline-earth-metal atoms: Mott transitions and quantum correlations," *Phys. Rev. A*, vol. 84, no. 4, p. 043601, 2011.

[77] M. A. Cazalilla, A. F. Ho, and M. Ueda, "Ultracold gases of ytterbium: Ferromagnetism and Mott states in an SU(6) Fermi system," *New J. Phys.*, vol. 11, no. 6, p. 103033, 2009.

[78] M. Foss-Feig, M. Hermele, and A. M. Rey, "Probing the Kondo lattice model with alkaline-earth-metal atoms," *Phys. Rev. A*, vol. 81, no. 5, p. 051603(R), 2010.

[79] K. R. A. Hazzard, V. Gurarie, M. Hermele, and A. M. Rey, "High temperature thermodynamics of fermionic alkaline earth atoms in optical lattices," *Phys. Rev. A*, vol. 85, no. 4, p. 041604, 2012.

[80] M. E. Beverland, G. Alagic, M. J. Martin, A. P. Koller, A. M. Rey, and A. V. Gorshkov, "Realizing exactly solvable SU(N) magnets with thermal atoms," *Phys. Rev. A*, vol. 93, no. 5, p. 051601(R), 2016.

[81] M. E. Beverland, J. Haah, G. Alagic, G. K. Campbell, A. M. Rey, and A. V. Gorshkov, "Spectrum estimation of density operators with alkaline-earth atoms." arXiv:1608.02045, 2016.

[82] F. Gerbier and J. Dalibard, "Gauge fields for ultracold atoms in optical superlattices," *New J. Phys.*, vol. 12, p. 033007, 2010.

[83] N. R. Cooper, "Optical Flux Lattices for Ultracold Atomic Gases," *Phys. Rev. Lett.*, vol. 106, no. 17, p. 175301, 2011.

[84] A. Górecka, B. Grémaud, and C. Miniatura, "Synthetic magnetic fluxes on the honeycomb lattice," *Phys. Rev. A*, vol. 84, no. 2, p. 023604, 2011.

[85] A. V. Gorshkov, A. Rey, A. Daley, M. Boyd, J. Ye, P. Zoller, and M. Lukin, "Alkaline-Earth-Metal Atoms as Few-Qubit Quantum Registers," *Phys. Rev. Lett.*, vol. 102, no. 11, p. 110503, 2009.

[86] A. J. Daley, M. M. Boyd, J. Ye, and P. Zoller, "Quantum Computing with Alkaline-Earth-Metal Atoms," *Phys. Rev. Lett.*, vol. 101, no. 17, p. 170504, 2008.

[87] C. W. Bauschlicher Jr., S. R. Langhoff, and H. Partridge, "The radiative lifetime of the $^1D_2$ state of Ca and Sr: a core-valence treatment," *J. Phys. B At. Mol. Phys.*, vol. 18, no. 8, p. 1523, 1985.

[88] L. R. Hunter, W. A. Walker, and D. S. Weiss, "Observation of an Atomic Stark-Electric-Quadrupole Interference," *Phys. Rev. Lett.*, vol. 56, no. 8, p. 823, 1986.

[89] S. B. Nagel, P. G. Mickelson, A. D. Saenz, Y. N. Martinez, Y. C. Chen, T. C. Killian, P. Pellegrini, and R. Côté, "Photoassociative spectroscopy at long range in ultracold strontium," *Phys. Rev. Lett.*, vol. 94, no. 8, p. 083004, 2005.

[90] M. Yasuda, T. Kishimoto, M. Takamoto, and H. Katori, "Photoassociation spectroscopy of ^{88}Sr: Reconstruction of the wave function near the last node," *Phys. Rev. A*, vol. 73, no. 1, p. 011403(R), 2006.

[91] J. E. Sansonetti and G. Nave, "Wavelengths, transition probabilities, and energy levels for the spectrum of neutral strontium (SrI)," *J. Phys. Chem. Ref. Data*, vol. 39, no. 3, 2010.

[92] B. A. Bushaw and W. Nörtershäuser, "Resonance ionization spectroscopy of stable strontium isotopes and ^{90}Sr via $5s^2$ $^1S_0 \rightarrow 5s5p$ $^1P_1 \rightarrow 5s5d$ $^1D_2 \rightarrow 5s11f$ $^1F_3 \rightarrow$ Sr$^+$," *Spectrochim. Acta, Part B At. Spectrosc.*, vol. 55, no. 11, p. 1679, 2000.

[93] G. zu Putlitz, "Bestimmung des elektrischen Kernquadrupolmomentes des ungeraden stabilen Strontium-87-Kerns," *Zeitschrift für Phys.*, vol. 175, no. 5, p. 543, 1963.

[94] S. M. Heider and G. O. Brink, "Hyperfine structure of ^{87}Sr in the $^3P_2$ metastable state," *Phys. Rev. A*, vol. 16, no. 4, p. 1371, 1977.

[95] I. Courtillot, A. Quessada-Vial, A. Brusch, D. Kolker, G. D. Rovera, and P. Lemonde, "Accurate spectroscopy of Sr atoms," *Eur. Phys. J. D*, vol. 33, no. 2, p. 161, 2005.

[96] A. Stein, H. Knöckel, and E. Tiemann, "The $^1S +^1 S$ asymptote of Sr$_2$ studied by Fourier-transform spectroscopy," *Eur. Phys. J. D*, vol. 57, no. 2, p. 171, 2010.

[97] J. Coursey, D. Schwab, J. Tsai, and R. Dragoset, "Atomic Weights and Isotopic Compositions (version 4.1)." http://physics.nist.gov/Comp, 2015.

[98] D. A. Butts and D. S. Rokhsar, "Trapped Fermi gases," *Phys. Rev. A*, vol. 55, no. 6, p. 4346, 1997.

[99] C. J. Pethick and H. Smith, *Bose-Einstein Condensation in Dilute Gases*. Cambridge: Cambridge University Press, 2002.

[100] W. Ketterle and M. W. Zwierlein, "Making, probing and understanding ultracold Fermi gases," in *Ultracold Fermi Gases, Proceedings of the International School Phys. "Enrico Fermi", Course CLXIV* (M. Inguscio, W. Ketterle, and C. Salomon, eds.), pp. 95–287, Amsterdam: IOS Press, 2008.

[101] B. DeMarco, *Quantum Behavior of an Atomic Fermi Gas*. PhD thesis, University of Colorado, Boulder, 2001.

[102] U. Schneider, *Interacting Fermionic Atoms in Optical Lattices - A Quantum Simulator for Condensed Matter Physics*. PhD thesis, Johannes Gutenberg-Universitat, Mainz, 2010.

[103] G. M. Bruun and C. Clark, "Ideal gases in time-dependent traps," *Phys. Rev. A*, vol. 61, no. 6, p. 61601, 2000.

[104] Y. Castin and R. Dum, "Bose-Einstein Condensates in Time Dependent Traps," *Phys. Rev. Lett.*, vol. 77, no. 27, p. 5315, 1996.

[105] H. J. Metcalf and P. van der Straten, *Laser Cooling and Trapping*. New York: Springer-Verlag, 1999.

[106] P. D. Lett, W. D. Phillips, S. L. Rolston, C. E. Tanner, R. N. Watts, and C. I. Westbrook, "Optical molasses," *J. Opt. Soc. Am. B*, vol. 6, no. 11, p. 2084, 1989.

[107] T. Chanelière, J.-L. Meunier, R. Kaiser, C. Miniatura, and D. Wilkowski, "Extra-heating mechanism in Doppler cooling experiments," *J. Opt. Soc. Am. B*, vol. 22, no. 9, p. 1819, 2005.

[108] X. Xu, T. H. Loftus, M. J. Smith, J. L. Hall, A. Gallagher, and J. Ye, "Dynamics in a two-level atom magneto-optical trap," *Phys. Rev. A*, vol. 66, p. 11401(R), 2002.

[109] X. Xu, T. H. Loftus, J. W. Dunn, C. H. Greene, J. L. Hall, A. Gallagher, and J. Ye, "Single-Stage Sub-Doppler Cooling of Alkaline Earth Atoms," *Phys. Rev. Lett.*, vol. 90, no. 19, p. 193002, 2003.

[110] M. Yasuda and H. Katori, "Lifetime measurement of the $^3P_2$ metastable state of strontium atoms," *Phys. Rev. Lett.*, vol. 92, no. 15, p. 153004, 2004.

[111] A. Derevianko, "Feasibility of Cooling and Trapping Metastable Alkaline-Earth Atoms," *Phys. Rev. Lett.*, vol. 87, no. 2, p. 023002, 2001.

[112] P. G. Mickelson, Y. N. Martinez de Escobar, P. Anzel, B. J. DeSalvo, S. B. Nagel, A. J. Traverso, M. Yan, and T. C. Killian, "Repumping and spectroscopy of laser-cooled Sr atoms using the $(5s5p)^3P_2 - (5s4d)^3D_2$ transition," *J. Phys. B At. Mol. Opt. Phys.*, vol. 42, no. 23, p. 235001, 2009.

[113] P. G. Mickelson, *Trapping and Evaporation of Mixtures ^{87}Sr and ^{88}Sr Mixtures*. PhD thesis, Rice University, 2010.

[114] S. Stellmer, *Degenerate quantum gases of strontium*. PhD thesis, University of Innsbruck, 2013.

[115] S. Stellmer, R. Grimm, and F. Schreck, "Production of quantum-degenerate strontium gases," *Phys. Rev. A*, vol. 87, no. 1, p. 013611, 2013.

[116] S. Stellmer and F. Schreck, "Reservoir spectroscopy of $5s5p\ ^3P_2 - 5snd\ ^3D_{1,2,3}$ transitions in strontium," *Phys. Rev. A*, vol. 90, no. 2, p. 022512, 2014.

[117] S. B. Nagel, C. E. Simien, S. Laha, P. Gupta, V. S. Ashoka, and T. C. Killian, "Magnetic trapping of metastable $^3P_2$ atomic strontium," *Phys. Rev. A*, vol. 67, no. 1, p. 011401(R), 2003.

[118] H. J. Kluge and H. Sauter, "Levelcrossing experiments in the First Excited $^1P_1$ states of the Alkaline Earths," *Zeitschrift für Phys.*, vol. 270, no. 4, p. 295, 1974.

[119] B. Bushaw and B. Cannon, "Diode laser based resonance ionization mass spectrometric measurement of strontium-90," *Spectrochim. Acta Part B At. Spectrosc.*, vol. 52, no. 12, p. 1839, 1997.

[120] R. Grimm, M. Weidemüller, and Y. B. Ovchinnikov, "Optical dipole traps for neutral atoms," in *Adv. At. Mol. Opt. Phys.*, vol. 42, p. 95, 2000.

[121] R. Roy, A. Green, R. Bowler, and S. Gupta, "Rapid cooling to quantum degeneracy in dynamically shaped atom traps," *Phys. Rev. A*, vol. 93, no. 4, p. 043403, 2016.

[122] P. G. Mickelson, Y. N. Martinez De Escobar, M. Yan, B. J. Desalvo, and T. C. Killian, "Bose-Einstein condensation of ^{88}Sr through sympathetic cooling with ^{87}Sr," *Phys. Rev. A*, vol. 81, no. 5, p. 051601(R), 2010.

[123] S. Stellmer, M. K. Tey, R. Grimm, and F. Schreck, "Bose-Einstein condensation of ^{86}Sr," *Phys. Rev. A*, vol. 82, no. 4, p. 041602(R), 2010.

[124] G. Ferrari, R. Drullinger, N. Poli, F. Sorrentino, and G. Tino, "Cooling of Sr to high phase-space density by laser and sympathetic cooling in isotopic mixtures," *Phys. Rev. A*, vol. 73, no. 2, p. 023408, 2006.

[125] S. Stellmer, M. K. Tey, B. Huang, R. Grimm, and F. Schreck, "Bose-Einstein condensation of strontium," *Phys. Rev. Lett.*, vol. 103, no. 20, p. 200401, 2009.

[126] Y. N. Martinez de Escobar, P. G. Mickelson, M. Yan, B. J. DeSalvo, S. B. Nagel, and T. C. Killian, "Bose-Einstein Condensation of ^{84}Sr," *Phys. Rev. Lett.*, vol. 103, no. 20, p. 200402, 2009.

[127] M. K. Tey, S. Stellmer, R. Grimm, and F. Schreck, "Double-degenerate Bose-Fermi mixture of strontium," *Phys. Rev. A*, vol. 82, no. 1, p. 011608(R), 2010.

[128] V. D. Vaidya, J. Tiamsuphat, S. L. Rolston, and J. V. Porto, "Degenerate Bose-Fermi mixtures of rubidium and ytterbium," *Phys. Rev. A - At. Mol. Opt. Phys.*, vol. 92, no. 4, p. 043604, 2015.

[129] B. J. Desalvo, M. Yan, P. G. Mickelson, Y. N. Martinez De Escobar, and T. C. Killian, "Degenerate fermi gas of ^{87}Sr," *Phys. Rev. Lett.*, vol. 105, no. 3, p. 030402, 2010.

[130] W. Ketterle, D. S. Durfee, and D. M. Stamper-Kurn, "Making, probing and understanding Bose-Einstein condensates," in *Proceedings of the International School of Physics "Enrico Fermi," Course CXL* (M. Inguscio, S. Stringari, and C. E. Wieman, eds.), pp. 69–176, Amsterdam: IOS Press, 1999.

[131] D. S. Barker, *Degenerate Gases of Strontium for Studies of Quantum Magnetism*. PhD thesis, University of Maryland, 2016.

[132] K. J. Ross and B. Sonntag, "High temperature metal atom beam sources," *Rev. Sci. Instrum.*, vol. 66, no. 9, p. 4409, 1995.

[133] C. B. Alcock, V. P. Itkin, and M. K. Horrigan, "Vapor Pressure of the Metallic Elements," *Can. Metall. Q.*, vol. 23, no. 3, p. 309, 1984.

[134] M. Mantina, A. C. Chamberlin, R. Valero, C. J. Cramer, and D. G. Truhlar, "Consistent van der Waals Radii for the Whole Main Group," *J. Phys. Chem. A*, vol. 113, no. 19, p. 5806, 2009.

[135] H. C. W. Beijerinck and N. F. Verster, "Velocity distribution and angular distribution of molecular beams from multichannel arrays," *J. Appl. Phys.*, vol. 46, no. 5, p. 2083, 1975.

[136] J. A. Giordmaine and T. C. Wang, "Molecular beam formation by long parallel tubes," *J. Appl. Phys.*, vol. 31, no. 3, p. 463, 1960.

[137] M. Schioppo, N. Poli, M. Prevedelli, S. Falke, C. Lisdat, U. Sterr, and G. M. Tino, "A compact and efficient strontium oven for laser-cooling experiments," *Rev. Sci. Instrum.*, vol. 83, p. 103101, 2012.

[138] R. Senaratne, S. V. Rajagopal, Z. A. Geiger, K. M. Fujiwara, V. Lebedev, and D. M. Weld, "Effusive atomic oven nozzle design using an aligned microcapillary array," *Rev. Sci. Instrum.*, vol. 86, p. 023105, 2015.

[139] E. T. D. Hamamatsu Photonics K. K., "Hollow Cathode Lamps." https://www.hamamatsu.com/resources/pdf/etd/Hollow_TLS1014E.pdf, 2006.

[140] C. Javaux, I. Hughes, G. Lochead, J. Millen, and M. P. A. Jones, "Modulation-free pump-probe spectroscopy of strontium atoms," *Eur. Phys. J. D*, vol. 57, no. 2, p. 151, 2010.

[141] J. Appel, A. MacRae, and A. I. Lvovsky, "A versatile digital GHz phase lock for external cavity diode lasers," *Meas. Sci. Technol.*, vol. 055302, no. 20, 2009.

[142] B. Saxberg, B. Plotkin-Swing, and S. Gupta, "Active stabilization of a diode laser injection lock," *Rev. Sci. Instrum.*, vol. 87, no. 6, p. 063109, 2016.

[143] "ULE Corning Code 7972 Ultra Low Expansion Glass Advanced Optics and Materials." https://www.corning.com/media/worldwide/csm/documents/7972ULEProductInformationJan2016.pdf, 2016.

[144] "HPFS Fused Silica Industrial Grade." https://www.corning.com/media/worldwide/csm/documents/acc05106b701420999327978ea88a83b4.pdf, 2008.

[145] "Schott Optical Glass Data Sheets." http://www.schott.com/d/advanced_optics/ac85c64c-60a0-4113-a9df-23ee1be20428/1.1/schott-optical-glass-collection-datasheets-english-17012017.pdf, 2014.

[146] A. D. Ludlow, *The Strontium Optical Lattice Clock: Optical Spectroscopy with Sub-Hertz Accuracy*. PhD thesis, University of Colorado, Boulder, 2008.

[147] R. W. P. Drever, J. L. Hall, F. V. Kowalski, J. Hough, G. M. Ford, A. J. Munley, and H. Ward, "Laser Phase and Frequency Stabilization Using an Optical Resonator," *Appl. Phys. B*, vol. 31, no. 2, p. 97, 1983.

[148] E. D. Black, "An introduction to Pound-Drever-Hall laser frequency stabilization," *Am. J. Phys.*, vol. 69, no. 1, p. 79, 2001.

[149] E. C. Cook, P. J. Martin, T. L. Brown-Heft, J. C. Garman, and D. A. Steck, "High passive-stability diode-laser design for use in atomic-physics experiments," *Rev. Sci. Instrum.*, vol. 83, no. 4, p. 043101, 2012.

[150] R. W. Fox, L. Hollberg, and A. S. Zibrov, "Semiconductor diode lasers," in *Exp. Methods Phys. Sci.* (F. B. Dunning and R. G. Hulet, eds.), vol. 29C, ch. 4, pp. 78–102, Academic Press, Inc, 1997.

[151] J. Alnis, A. Matveev, N. Kolachevsky, T. Udem, and T. W. Hänsch, "Subhertz linewidth diode lasers by stabilization to vibrationally and thermally compensated ultralow-expansion glass Fabry-Pérot cavities," *Phys. Rev. A*, vol. 77, no. 5, p. 053809, 2008.

[152] A. D. Ludlow, X. Huang, M. Notcutt, T. Zanon-Willette, S. M. Foreman, M. M. Boyd, S. Blatt, and J. Ye, "Compact, thermal-noise-limited optical cavity for diode laser stabilization at 1×10^{-15}," *Opt. Lett.*, vol. 32, no. 6, p. 641, 2007.

[153] L. S. Ma, P. Jungner, J. Ye, and J. L. Hall, "Delivering the same optical frequency at two places: accurate cancellation of phase noise introduced by an optical fiber or other time-varying path," *Opt. Lett.*, vol. 19, no. 21, p. 1777, 1994.

[154] N. C. Pisenti, "Design and construction of a narrow-line clock laser for [87]Sr," 2015.

[155] K. Singer, S. Jochim, M. Mudrich, A. Mosk, and M. Weidemüller, "Low-cost mechanical shutter for light beams," *Rev. Sci. Instrum.*, vol. 73, no. 12, p. 4402, 2002.

[156] S. Friebel, C. D'Andrea, J. Walz, M. Weitz, and T. W. Hansch, "CO_2-laser optical lattice with cold rubidium atoms," *Phys. Rev. A*, vol. 57, no. 1, p. R20, 1998.

[157] B. Gadway, D. Pertot, R. Reimann, M. G. Cohen, and D. Schneble, "Analysis of Kapitza-Dirac diffraction patterns beyond the Raman-Nath regime.," *Opt. Express*, vol. 17, no. 2002, p. 19173, 2009.

[158] G. Reinaudi, T. Lahaye, Z. Wang, and D. Guéry-Odelin, "Strong saturation absorption imaging of dense clouds of ultracold atoms," *Opt. Lett.*, vol. 32, no. 21, p. 3143, 2007.

[159] K. Hueck, N. Luick, L. Sobirey, J. Siegl, T. Lompe, H. Moritz, L. W. Clark, and C. Chin, "Calibrating High Intensity Absorption Imaging of Ultracold Atoms," *Opt. Express*, vol. 25, no. 8, p. 8670, 2017.

[160] D. S. Barker, B. J. Reschovsky, N. C. Pisenti, and G. K. Campbell, "Enhanced magnetic trap loading for atomic strontium," *Phys. Rev. A*, vol. 92, no. 4, p. 043418, 2015.

[161] B. J. Bloom, T. L. Nicholson, J. R. Williams, S. L. Campbell, M. Bishof, X. Zhang, W. Zhang, S. L. Bromley, and J. Ye, "An optical lattice clock with accuracy and stability at the 10^{-18} level," *Nature*, vol. 506, no. 7486, p. 71, 2014.

[162] N. Hinkley, J. A. Sherman, N. B. Phillips, M. Schioppo, N. D. Lemke, K. Beloy, M. Pizzocaro, C. W. Oates, and A. D. Ludlow, "An Atomic Clock with 10^{-18} Instability," *Science*, vol. 341, p. 1215, 2013.

[163] T. Ido, Y. Isoya, and H. Katori, "Optical-dipole trapping of Sr atoms at a high phase-space density," *Phys. Rev. A*, vol. 61, no. 6, p. 061403(R), 2000.

[164] A. Traverso, R. Chakraborty, Y. N. Martinez De Escobar, P. G. Mickelson, S. B. Nagel, M. Yan, and T. C. Killian, "Inelastic and elastic collision rates for triplet states of ultracold strontium," *Phys. Rev. A*, vol. 79, no. 6, p. 060702(R), 2009.

[165] Y. N. Martinez de Escobar, P. G. Mickelson, M. Yan, and T. C. Killian, "Modification of atom scattering using an intercombination-line optical Feshbach resonance at large detuning." 2009.

[166] S. Stellmer, F. Schreck, and T. C. Killian, "Degenerate quantum gases of strontium," in *Annu. Rev. Cold Atoms Mol.*, vol. 2, ch. 1, pp. 1–80, World Scientific Publishing Co., 2014.

[167] K. Pandey, K. D. Rathod, S. B. Pal, and V. Natarajan, "Magnetic trapping of Yb in the metastable $^3P_2$ state," *Phys. Rev. A*, vol. 81, no. 3, p. 033424, 2010.

[168] J. R. Guest, N. D. Scielzo, I. Ahmad, K. Bailey, J. P. Greene, R. J. Holt, Z. T. Lu, T. P. O'Connor, and D. H. Potterveld, "Laser trapping of ^{225}Ra and ^{226}Ra with repumping by room-temperature blackbody radiation," *Phys. Rev. Lett.*, vol. 98, no. 9, p. 093001, 2007.

[169] S. De, U. Dammalapati, K. Jungmann, and L. Willmann, "Magneto-optical trapping of barium," *Phys. Rev. A*, vol. 79, no. 4, p. 041402(R), 2009.

[170] J. Grünert and A. Hemmerich, "Sub-Doppler magneto-optical trap for calcium," *Phys. Rev. A*, vol. 65, no. 4, p. 041401(R), 2002.

[171] H. G. Werij, C. H. Greene, C. E. Theodosiou, and A. Gallagher, "Oscillator strengths and radiative branching ratios in atomic Sr," *Phys. Rev. A*, vol. 46, no. 3, p. 1248, 1992.

[172] B. Bransden and C. Joachain, *Physics of Atoms and Molecules*. Harlow, England: Pearson Education Limited, 2nd ed., 2003.

[173] W. Skomorowski, F. Pawłowski, C. P. Koch, and R. Moszynski, "Rovibrational dynamics of the strontium molecule in the $A^1\Sigma_u^+$, $c^3\Pi_u$, and $a^3\Sigma_u^+$ manifold from state-of-the-art ab initio calculations." *J. Chem. Phys.*, vol. 136, no. 19, p. 194306, 2012.

[174] M. Kahmann, *Link between photoassociation and optical Feshbach resonances through the example of calcium*. PhD thesis, Leibniz Universität Hannover, 2014.

[175] R. Ciuryło, E. Tiesinga, S. Kotochigova, and P. S. Julienne, "Photoassociation spectroscopy of cold alkaline-earth-metal atoms near the intercombination line," *Phys. Rev. A*, vol. 70, no. 6, p. 062710, 2004.

[176] K. Jones, E. Tiesinga, P. D. Lett, and P. S. Julienne, "Ultracold photoassociation spectroscopy: Long-range molecules and atomic scattering," *Rev. Mod. Phys.*, vol. 78, no. 2, p. 483, 2006.

[177] M. Borkowski, P. Morzynski, R. Ciuryło, P. S. Julienne, M. Yan, B. J. Desalvo, and T. C. Killian, "Mass scaling and nonadiabatic effects in photoassociation spectroscopy of ultracold strontium atoms," *Phys. Rev. A*, vol. 90, no. 3, p. 032713, 2014.

[178] B. H. McGuyer, M. McDonald, G. Z. Iwata, M. G. Tarallo, W. Skomorowski, R. Moszynski, and T. Zelevinsky, "Precise study of asymptotic physics with subradiant ultracold molecules," *Nat. Phys.*, vol. 11, no. 1, p. 32, 2014.

[179] A. Stein, H. Knöckel, and E. Tiemann, "Fourier-transform spectroscopy of Sr_2 and revised ground-state potential," *Phys. Rev. A*, vol. 78, no. 4, p. 042508, 2008.

[180] A. Stein, H. Knockel, and E. Tiemann, "The states $1^1\Sigma_u^+$, $1^1\Pi_u$ and $2^1\Sigma_u^+$ of Sr_2 studied by Fourier-transform spectroscopy," *Eur. Phys. J. D*, vol. 64, no. 2-3, p. 227, 2011.

[181] T. Zelevinsky, S. Kotochigova, and J. Ye, "Precision test of mass-ratio variations with lattice-confined ultracold molecules.," *Phys. Rev. Lett.*, vol. 100, p. 043201, 2008.

[182] S. Kotochigova, T. Zelevinsky, and J. Ye, "Prospects for application of ultracold Sr_2 molecules in precision measurements," *Phys. Rev. A*, vol. 79, no. 1, p. 012504, 2009.

[183] K. Beloy, A. W. Hauser, A. Borschevsky, V. V. Flambaum, and P. Schwerdtfeger, "Effect of α variation on the vibrational spectrum of Sr_2," *Phys. Rev. A*, vol. 84, no. 6, p. 062114, 2011.

[184] A. Ciamei, A. Bayerle, B. Pasquiou, and F. Schreck, "Observation of Bose-enhanced photoassociation products," *Europhys. Lett.*, vol. 119, no. 4, p. 46001, 2017.

[185] R. Ciuryło, E. Tiesinga, and P. S. Julienne, "Optical tuning of the scattering length of cold alkaline-earth-metal atoms," *Phys. Rev. A*, vol. 71, no. 3, p. 030701(R), 2005.

[186] M. Yan, *Optical Feshbach Resonances and Coherent Photoassociation in a Strontium BEC*. PhD thesis, Rice University, 2013.

[187] M. Theis, G. Thalhammer, K. Winkler, M. Hellwig, G. Ruff, R. Grimm, and J. H. Denschlag, "Tuning the scattering length with an optically induced feshbach resonance," *Phys. Rev. Lett.*, vol. 93, no. 12, p. 123001, 2004.

[188] T. L. Nicholson, S. Blatt, B. J. Bloom, J. R. Williams, J. W. Thomsen, J. Ye, and P. S. Julienne, "Optical Feshbach resonances: Field-dressed theory and comparison with experiments," *Phys. Rev. A*, vol. 92, no. 2, p. 022709, 2015.

[189] J. Bohn and P. Julienne, "Semianalytic theory of laser-assisted resonant cold collisions," *Phys. Rev. A*, vol. 60, no. 1, p. 414, 1999.

[190] R. Ciuryło, E. Tiesinga, and P. S. Julienne, "Stationary phase approximation for the strength of optical Feshbach resonances," *Phys. Rev. A*, vol. 74, no. 2, p. 022710, 2006.

[191] H. T. C. Stoof, A. M. L. Janssen, J. M. V. A. Koelman, and B. J. Verhaar, "Decay of spin-polarized atomic hydrogen in the presence of a Bose condensate," *Phys. Rev. A*, vol. 39, no. 6, pp. 3157–3169, 1989.

[192] J. Söding, D. Guéry-Odelin, P. Desbiolles, F. Chevy, H. Inamori, and J. Dalibard, "Three-body decay of a rubidium Bose-Einstein condensate," *Appl. Phys. B Lasers Opt.*, vol. 69, no. 4, pp. 257–261, 1999.

[193] M. Pillai, J. Goglio, and T. G. Walker, "Matrix Numerov Method for Solving Schrödinger's Equation," *Am. J. Phys.*, vol. 80, no. 11, p. 1017, 2012.

[194] Y. Takasu, Y. Saito, Y. Takahashi, M. Borkowski, R. Ciuryło, and P. S. Julienne, "Controlled production of subradiant states of a diatomic molecule in an optical lattice," *Phys. Rev. Lett.*, vol. 108, no. 17, p. 173002, 2012.

[195] P. Julienne, "Cold binary atomic collisions in a light field," *J. Res. Natl. Inst. Stand. Technol.*, vol. 101, no. 4, p. 487, 1996.

[196] J. H. Han, J. H. Kang, M. Lee, and Y.-i. Shin, "Photoassociation spectroscopy of ultracold ^{173}Yb atoms near the intercombination line." arXiv:1710.03072, 2017.

[197] "*NIST Digital Library of Mathematical Functions*." http://dlmf.nist.gov/, Release 1.0.16 of 2017-09-18. F. W. J. Olver, A. B. Olde Daalhuis, D. W. Lozier, B. I. Schneider, R. F. Boisvert, C. W. Clark, B. R. Miller and B. V. Saunders, eds.

[198] I. Gotlibovych, *Degenerate Bose Gases in a Uniform Potential*. PhD thesis, University of Cambridge, 2014.

[199] D. Clamond, "Complex dilogarithm." https://www.mathworks.com/matlabcentral/fileexchange/10186-complex-dilogarithm, 2006.

[200] "Zeta functions, L-series and polylogarithms." http://docs.sympy.org/0.7.1/modules/mpmath/functions/zeta.html#polylog.

[201] B. P. Ruzic, C. H. Greene, and J. L. Bohn, "Quantum defect theory for high-partial-wave cold collisions," *Phys. Rev. A*, vol. 87, no. 3, p. 032706, 2013.

[202] K. T. Tang and J. P. Toennies, "An improved simple model for the van der Waals potential based on universal damping functions for the dispersion coefficients," *J. Chem. Phys.*, vol. 80, no. 8, p. 3726, 1984.

[203] E. Tiesinga, C. Williams, and P. Julienne, "Photoassociative spectroscopy of highly excited vibrational levels of alkali-metal dimers: Green-function approach for eigenvalue solvers," *Phys. Rev. A*, vol. 57, no. 6, p. 4257, 1998.